Characterising, understanding and predicting the performance of structural power composites

by

Maria Ivelinova Valkova

Department of Aeronautics
South Kensington Campus
Imperial College London
London SW7 2AZ
U.K.

This thesis is submitted for the degree of
Doctor of Philosophy of Imperial College London

February 2022

Abstract

Dramatic improvements in power generation, energy storage, system integration and light-weighting are needed to meet increasingly stringent carbon emissions targets for future aircraft and road vehicles. The electrification of transport could significantly reduce direct CO_2 emissions; however, battery energy and power density limitations pose a major technological barrier. The introduction of multifunctional structural power composites (SPCs), which simultaneously provide mechanical load-bearing and electrochemical energy storage, offers new possibilities. By replacing conventional materials with SPCs, electrical performance requirements could be relaxed, and vehicle mass could be reduced; however, for SPCs to outperform monofunctional systems, significant performance and reliability improvements are still required. The use of computational models to support experimental efforts has so far been overlooked, despite wide recognition of the benefits of such a combined approach.

The aim of this work was to develop predictive finite element models for structural supercapacitor composites (SSCs), and use them to investigate their mechanical, electrical, and electrochemical behaviour. A unit cell modelling technique was used to generate realistic mesoscale models of the complex microstructure of SSCs. The effects of composite manufacturing processes on the final performance of SSCs were investigated through characterisation and modelling of compaction and manufacturing defects. Numerical predictions of the elastic properties of SSCs were evaluated against data from the literature; and the presence of defects was shown to significantly degrade performance.

Motivated by the large series resistance of SSCs, direct conduction models were developed to better understand electrical charge transport. Based on investigations of various current collector geometries, design strategies for the mitigation of resistive losses were proposed. To enable analysis of the combined mechanical-electrochemical behaviour of SSCs, an ion transport user element subroutine was developed but could not be validated. Overall, this work demonstrates that substantial improvements in the mechanical and electrical properties of SSCs are possible through control of the composite microstructure. The models developed in this work provide guidance for the optimisation of manufacturing processes and the design of new SSC architectures, and underpin the future certification and deployment of these emerging materials.

Acknowledgements

I would like to thank my academic supervisors Prof Emile Greenhalgh, Prof Milo Shaffer and Dr Vito Tagarielli for making this research possible, for their insight, generosity, encouragement, and support throughout the past four years. I would also like to thank Prof Anthony Kucernak for his valuable advice on electrical and electrochemical analysis.

I would also like to thank my colleagues at the Structural Power Group: Natasha Shirshova, David Anthony, Sang Nguyen, Evgeny Senokos, Guocheng Qi, Francesca Pernice, Tomas Katafiasz, Alireza Razavi, Kalpana Balaskandan, Guohui Zhang, Victor Quan, Kaan Bilge and Habtom Asfaw for the help and encouragement they provided during this project.

The following sources of funding are gratefully acknowledged: Engineering and Physical Sciences Research Council (EPSRC) Future Composites Research Manufacturing Hub (EP/P006701/1), the EPSRC Beyond Structural project (EP/P007465/1), the European Office of Aerospace Research and Development (Institute of Education Grant FA9550-17-1-0251), the European Union Clean Sky 2 (Structural Power Composites for Future Civil Aircraft Project #738085) and the Royal Academy of Engineering (Chair in Emerging Technologies). The following organisations are gratefully acknowledged for supplying the materials used in this work: Chomarat, Oxeon and Gividi Fabrics.

The assistance and contributions of the following people is gratefully acknowledged: Joseph Meggyesi and Keith Wolstenholme for support with composites testing; Gary Senior and Jonathan Cole for support with composites characterisation; Mahmoud Ardakani for support with scanning electron microscopy; Dmitry Ivanov, Ollie Nixon-Pearson and Xuekun Lu for μCT scan acquisition; Sandy Fisher for advice on μCT visualisation; David Anthony for carbon aerogel monolith manufacture and physical characterisation, and help with CAG morphology interpretation; Samuel Humphry-Baker for help with nanoindentation; Sang Nguyen, Evgeny Senokos and Alireza Razavi for measurement and interpretation of electrical resistance; and Bo Yu for valuable discussions about composites characterisation and modelling.

I would like to thank my family and friends for their kindness, patience, and relentless support.

List of publications

Parts of the work presented in this thesis have been disseminated through written publications and oral presentations, listed below, as of February 2022.

Peer-reviewed journal publications

M. Valkova, D. B. Anthony, A. R. J. Kucernak, M. S. P. Shaffer, E. S. Greenhalgh. "Predicting the compaction of hybrid multilayer woven composite reinforcement stacks". *Composites Part A Applied Science and Manufacturing*, vol. 133, 105851, 2020.

M. Valkova, D. B. Anthony, A. R. J. Kucernak, M. S. P. Shaffer, E. S. Greenhalgh. "Predicting the mechanical behaviour of structural supercapacitor composites". *Composites Part A Applied Science and Manufacturing*, vol. 156, 106860, 2022.

Submitted journal manuscripts

M. Valkova, S. Nguyen, E. Senokos, S. Razavi, D. B. Anthony, A. R. J. Kucernak, M. S. P. Shaffer, E. S. Greenhalgh. "Current collector design strategies for mitigation of resistive losses in multifunctional structural power composites". 2022.

M. F. Pernice, G. Qi, E. Senokos, D. B. Anthony, S. Nguyen, M. Valkova, E. S. Greenhalgh, M. S. P. Shaffer, A. R. J. Kucernak. "Mechanical, electrochemical and multifunctional performance of a CFRP/carbon aerogel structural supercapacitor and its corresponding monofunctional equivalents". 2022.

Conference publications

M. Valkova, E. S. Greenhalgh, M. S. P. Shaffer, A. R. J. Kucernak, D. B. Anthony. "Predicting the consolidation of fabric-reinforced SPCs". *ICCM 22, 22nd International Conference on Composite Materials* (Melbourne, Australia), 11–16 August 2019.

E. S. Greenhalgh, M. Valkova, C. Lee, S. N. Nguyen, M. S. P. Shaffer, A. R. J. Kucernak. "Multifunctional design and predictive modelling for structural power" (poster). *Multifunctional Materials and Structures Gordon Research Conference* (Ventura, CA United States), 19–24 January 2020.

Declaration of originality

The work hereby presented is based on research carried out by the author at the Department of Aeronautics of Imperial College London, and it is all the author's own work except where otherwise acknowledged. No part of the present work has been submitted elsewhere for another degree or qualification.

Copyright declaration

Table of Contents

List of Figures

List of Tables

Nomenclature

Roman symbols

A	(m^2)	area
a	($/m$)	pore wall volume per unit volume of electrode
a	(m)	diameter of ion species
$\mathbf{B}$	(–)	displacement differentiation matrix
$C, \mathbf{C}$	(Pa)	elasticity tensor
C	(F)	capacitance
C_s	(F/m^2)	specific capacitance
CV	(–)	coefficient of variation
c	(mol/m^3)	concentration of ion species
D	(m^2/s)	diffusivity
d	(m)	diameter
E	(Pa)	elastic modulus
$E, \mathbf{E}$	(V/m)	electric field intensity, electric field intensity vector
F	(–)	deformation gradient
$\mathbf{F}$		vector of external loads
$\mathbf{G}$		vector of internal loads
G	(J/m^2)	toughness
H	(m)	Stern layer thickness
h	(m)	depth
i	(A)	electric current
$J, \mathbf{J}$	(–)	Jacobian, Jacobian matrix
$j, \mathbf{J}$	(A/m^2)	current density, current density vector
j_n	(A/m^2)	transfer current density
$\mathbf{k}, \mathbf{K}$	(Pa)	stiffness, element stiffness matrix, global stiffness matrix
k	(–)	stress concentration factor
L	(m)	length
$\mathbf{M}$		mass matrix
m_s	(kg/m^2)	areal mass
m_f	(–)	mass fraction
$N_\alpha, \mathbf{N}$	(–)	shape function, shape function matrix
$\mathbf{N}_s$	($mol/m^2 \cdot s$)	flux of ion species vector
P	(N)	applied force
P	(W)	power

P_{J}	(W)	volumetric Joule heat
p	(Pa)	applied pressure
$Q, \mathbf{Q}$		global field variables, global vector of nodal variables
$q, \mathbf{q}$		nodal field variables, element vector of nodal variables
q_s, Q_s	(C/m^2)	specific charge of electrode, specific charge of cell
$R, \mathbf{R}$		residual vector
R	(Ω)	resistance
S	(Pa)	contact stiffness
T	(K)	temperature
t	(s)	time
t	(m)	thickness
$\mathbf{u}$	(–)	vector of field variables
u	(m)	displacement
u	(m^2·mol/J·s)	ionic mobility
V	(m^3)	volume
V_f	(–)	fibre volume fraction
V_{R}	(V)	rated potential of supercapacitor cell
W	(m)	width
w	(–)	weighting factor in Gaussian quadrature
X_m	(Pa)	mean bundle strength
z	(–)	valence

Greek symbols

γ	(–)	shear strain
ε	(–)	normal strain
ε	(–)	porosity
ε_r	(–)	relative permittivity
κ	(S/m)	ionic conductivity
λ_{D}	(m)	Debye length
μ	(–)	friction coefficient
ν	(–)	Poisson's ratio
ρ	(kg/m^3)	volumetric density
ρ_f	(C/m^3)	free charge density
$\sigma^{\mathrm{E}}, \boldsymbol{\sigma}^{\mathbf{E}}$	(S/m)	volumetric electrical conductivity, electrical conductivity matrix
σ	(Pa)	normal stress
σ	(–)	standard deviation
τ	(Pa)	shear stress
ψ	(V)	electric potential

Coordinate systems

x, y, z	Cartesian coordinate system aligned with the warp yarn direction
$1, 2, 3$	Cartesian coordinate system aligned with the local fibre direction
ξ, η	natural coordinate system in 2D
x_i, y_i	integration point coordinates in Gaussian quadrature in 2D

Physical constants

e	(C)	elementary charge
F	(C/mol)	Faraday's constant
k_B	(J/K)	Boltzmann constant
N_A	(/mol)	Avogadro's number
R	(J/mol·K)	gas constant
ε_0	(F/m)	vacuum permittivity

Subscripts

a	active materials
b	bundle of broken fibres
C	contact
cc	current collector
cell	cell value
eff	effective value
e	electrode
f	fibre, frame, fingers
i	indenter
IL	ionic liquid
l	electrolyte phase, lateral direction
m	matrix
max	maximum
min	minimum
P	parallel
r	reduced
S	series
s	substrate, electrode surface, solid phase
s	ion species
sep	separator
SL	shear lag
t	transverse direction
total	total value

u ..... usable
W ..... Warburg
0 ..... initial (reference) value
∞ ..... bulk value

Superscripts

CNT ..... CNT-grafted
D ..... diffuse layer
DL ..... double layer
e ..... element
k ..... node
P ..... pyrolised
St ..... Stern layer
total ..... total value

Decorations above

* ..... carbon aerogel-modified, coefficient

Abbreviations

AC ..... activated carbon, alternating current
BADGE ..... bisphenol A diglycidyl ether
C ..... carbon fabric
CAG ..... carbon aerogel
CDM ..... continuum damage mechanics
CF ..... carbon fibre
CLT ..... classical laminate theory
CMC ..... ceramic matrix composite
CNT ..... carbon nanotube
CPD ..... critical point drying
CV ..... cyclic voltammetry
CZM ..... cohesive zone method
DAFF ..... directly attributable fibre failures
DC ..... direct current
DEF ..... defects
DL ..... electric double layer
EC ..... equivalent circuit
EDLC ..... electrochemical double layer capacitor
EIS ..... electrochemical impedance spectroscopy
EMIM-TFSI ..... 1-ethyl-3-methylimidazolium bis(trifluoromethylsulfonyl)imide
ESR ..... equivalent series resistance

EV	electric vehicle
FEA	finite element analysis
FEM	finite element model
G	glass fabric
GCD	galvanostatic charge discharge
GF	glass fibre
HPC	high performance computing
hUC	hybrid unit cell
ICL	Imperial College London
IL	ionic liquid
IP	in-phase
MF	multifunctional
OP	out-of-phase
PB	Poisson-Boltzmann equation
PBC	periodic boundary condition
PGS	pyrolytic graphite sheet
PNP	Poisson-Nernst-Planck equation
RC	resistor-capacitor
RF	resorcinol-formaldehyde
RIFT	resin infusion under flexible tooling
RT	room temperature
RVE	representative volume element
SAM	slice array model
SBC	structural battery composite
SC	supercapacitor
SEM	scanning electron microscope
SPC	structural power composite
SSC	structural supercapacitor composite
STR	structural
TLM	transmission line method
TRL	technology readiness level
UC	unit cell
UD	unidirectional
UEL	user-defined element subroutine
WFRC	woven fabric-reinforced composite
μCT	X-ray micro-computed tomography

1 Introduction

As one of the fastest growing sources of greenhouse gas emissions [1], growing by about 5% per year before 2020 [2], the aviation sector looks to emerging disruptive technologies [3] to future-proof aircraft against increasingly stringent sustainability targets, such as Europe's 2050 net zero carbon target [4]. Meanwhile, the electrification of road vehicles, which are responsible for 74% of CO_2 emissions in the transport sector [5], is proceeding at rapid pace: sales of electric vehicles (EVs) have been steadily rising across Europe [6], and are beginning to outstrip those of internal combustion and hybrid engine vehicles [7].

However, the full benefits of electrification are currently beyond reach due to the relatively low specific energy of batteries, compared to that of aviation and automotive fuel. Feasibility analyses have suggested that at least a four-fold increase in the specific energy of battery packs and additional power augmentation will be required to enable the fully electric-powered short range (<600 nmi) flight of Airbus A320-sized aircraft [8]. Meanwhile in typical EVs, such as the Tesla Model S (85 kWh), to deliver a 265 mi range the battery pack constitutes over 28% of the total vehicle weight [9]. The relatively slow historic rate of increase in battery specific energy (4% per year [8]) has driven the aviation [10,11] and automotive [12–14] industries to consider alternative lightweighting strategies, such as multifunctional materials. These technologies promise a considerable reduction in vehicle mass and emissions, and thus, closely align with commercial and legislative roadmaps [4,15].

Composite materials, which integrate the properties of multiple constituents, have been identified as an ideal platform for the creation of multifunctional materials [16]. Structural multifunctional composites are an emerging class of composite materials with the ability to perform various non-structural functions in addition to their structural role, for example, structural health monitoring, self-healing, actuation, thermal and electrical transport, energy harvesting and/or storage. Structural power composites (SPCs), such as structural batteries (SBCs) [17] and structural supercapacitors (SSCs) [18], which store energy electrochemically, are of particular relevance to the transport sector. Indeed, BAE Systems, Tesla and Lamborghini have all announced development of SPC technologies [13,14,19].

The Structural Power Group at Imperial College London (ICL) [16,20] has led the development of truly multifunctional SSCs, successfully demonstrating laminated devices at both the laboratory and component scales. The longstanding goal of this research has been to advance the mechanical and electrochemical performance of SSC devices, such that the commercially viability of the technology can be demonstrated through mass savings and system-level efficiency improvements. Further performance improvements are necessary to reach this goal.

To date, the development of SSC devices and their constituents has almost exclusively relied on experimental research, proving time intensive and costly. Computational analysis techniques, such as finite element modelling, promise to accelerate the development and deployment of SSCs by enabling virtual testing and performance prediction. However, truly predictive device-level models are yet to be demonstrated: there is an urgent need for their development. In contrast to SBCs, for which coupon-level experimental data from full cell devices has only become available recently [21], comprehensive measurements from SSCs have existed for some time [22,23]. This data offers an immediate opportunity for the experimental validation of predictive models of SSCs, thus motivating a focus on their development.

It is anticipated that the electrochemical and mechanical properties of SSCs and other emerging multifunctional hybrid composites are strongly dictated by their micro- and mesostructure. The development of realistic models of SSCs must therefore be informed by a careful study of the microstructure and, in particular, how it is affected by the presence of nanocarbons, structural electrolyte, interply hybridisation, and the composite fabrication route. Upon successful validation of their predictive capability, such computational models can be used to further investigate structure-property relationships in SSCs. Most importantly, these findings can guide improvements to the design of SSCs, and to SSC manufacturing practices.

It is well understood [24] that advancing the state-of-the-art in SSCs requires reconciling the often competing and/or coupled objectives of simultaneously maximising the mechanical and electrochemical performance. It therefore follows that multiphysics models would be best suited to supporting technological advancement; however, a multiphysics modelling framework for SSCs is yet to be proposed. It is anticipated that such a predictive capability would be valuable not only in the present research and development

phase, but would also underpin later phases of testing and certification of multifunctional materials and components in commercial applications.

The research gaps relating to the computational modelling of SSCs, outlined above, are examined in detail in Chapter 3. This thesis aims to address these research gaps through the following Phases of work:

Phase 1: using numerical simulations of reinforcement compaction to generate realistic mesoscale finite element models of the architecture of structural supercapacitors;

Phase 2: developing the first truly predictive mechanical models of structural supercapacitors and using them to examine structure-property relationships;

Phase 3: using electric conduction models to analyse the performance of current collectors and suggest improvements in their design;

Phase 4: developing an ion transport finite element subroutine to enable a new mechanical-electrochemical analysis workflow.

Each work phase above constitutes a novel contribution to the research and development of SSCs, as well as the wider field of composites research.

The thesis is organised as follows: in Chapter 2, literature relevant to each of the Phases is reviewed. In Chapter 3, the research gaps are identified and discussed, providing the motivation for the research plan; the thesis scope and structure of the thesis are presented. Chapters 4 to 7 address the respective Phases above, detailing the development and analysis of predictive models of the compaction, mechanical, current collection and electrochemical behaviour of SSCs. Chapter 8 contains a detailed discussion of the research findings from these Phases, and contrasts the results with the background literature. The chapter closes with a summary of the novel achievements and impact of this thesis. In Chapter 9, the conclusions of this thesis are summarised. In Chapter 10, the implications of this thesis on the future development of SSCs are discussed, and topics for future investigation are suggested.

2 Predictive modelling for structural supercapacitors: literature review

2.1 Introduction

This thesis was completed in the context of ongoing research efforts by the Structural Power Group at Imperial College London (hereafter referred to as 'the Group') to develop structural supercapacitors (SSCs) [16,20]. This review chapter is structured as follows: Section 2.2 offers an introduction to structural power composites, focusing on the present state-of-the-art in SSCs, and discusses the challenges in their development. Sections 2.3 to 2.6 review experimental and computational research relevant to SSCs, focusing in turn on reinforcement compaction, and mechanical, electrical, and electrochemical performance aspects, providing background information where necessary. In Chapter 3, the research gaps are identified, which motivated the research plan for this thesis.

2.2 Structural supercapacitor composites

2.2.1 State-of-the-art in architecture and performance

This Section aims to provide a brief overview of the state-of-the-art in structural supercapacitor composites, which has been reviewed in detail by other researchers [18,25,26]. Two main design approaches have been taken in the development of composite structures with electrochemical energy storage functionalities. The earliest efforts followed a 'multifunctional structure' approach, embedding thin-film electrochemical devices within structural composite laminates [27]. This approach continues to be used today [28–30], perhaps most recently demonstrated in Tesla's 'structural battery pack', in which adhesively bonded commercial battery cells function as the core layer of a sandwich floor structure [13]. As others have noted [24] however, the performance gains offered by this approach are limited, since the functional requirements are addressed separately in the design: that is, the multifunctional laminate is composed of monofunctional plies.

An alternative philosophy, pioneered by the US Army Research Laboratory [31,32], has led to the development of structural power composites, such as structural batteries [17]

and structural supercapacitors [18]. These composite materials are considered truly multifunctional materials since all constituents and plies are designed to possess dual functionality. This concept promises far greater performance gains; however, it also poses the much more difficult task of developing new constituent materials and successfully integrating them into a multifunctional composite.

In the short term, challenges related to scaling up the production of SPCs, and achieving low variability in cell performances, mean that SPCs are likely to initially find use alongside traditional energy storage devices in low voltage, low production volume applications, for example, a single cell powering the lights on a small drone, bicycle, or scooter. In the medium term, it is anticipated that early adopters of SPCs would be unmanned aerial vehicles and light leisure vehicles, such as electric scooters, where safety and certification barriers to entry are lower. SPCs are then expected to gradually enter service in automotive vehicles and commercial aircraft by replacing secondary or parasitic structures, for example, using multi-cell SPC constructions in cabin panels, flooring, seats, galley, or shelving to power infotainment systems and provide auxiliary power supply. SPCs are not expected to solely power EVs; however, they could be used alongside batteries to provide peak power, load levelling and regenerative energy harvesting.

Within SPCs, 'laminated' and 'fibre level' [33] cell architecture concepts have emerged. The Structural Power Group at ICL [16,20] has led the development of SSCs, employing the former architectural scheme, in which a 'cell' is formed of three plies, in a layup mirroring that of a conventional supercapacitor. A supercapacitor (SC) is an electrical energy storage system, which consists of a pair of high surface area porous electrodes, internally separated by a thin electrically insulating but ionically permeable (that is, porous) membrane and externally connected by highly conductive current collectors, with an electrolyte filling the pore volume of the electrodes and separator [34].

In present generation SSCs developed at ICL (Figure 2.1), a carbon fibre fabric coated with nanostructured carbon aerogel (CAG) [22,35] serves as a structural electrode. Early work on SSCs focused on carbon nanotube- (CNT) grafted carbon fabric electrodes [20,36]; however, CAG-modified fabrics were later demonstrated to be superior [16] due to higher surface area (ca. 160 m^2/g, compared to ca. 45 m^2/g for CNTs), and consequently, capacitance. Typically, copper tape with conductive adhesive is applied to the external surface of each electrode to provide current collection. The structural separator layer

features a thin glass fibre fabric, though materials such as non-woven polyethylene or polyester sheets have also been used [23]. The plies share a bicontinuous structural electrolyte, consisting of a structural epoxy resin and ionic liquid (IL) blend, which phase separates upon crosslinking [16,20,37]. Due to the relatively high viscosity of the resin mixture, and the low vapour pressure of the IL, the structural electrolyte is filmed. The cell is then consolidated via a resin film infusion route and cured under vacuum [38].

Various research groups [37,39–42] have since adopted this approach to SSC design and manufacture, producing what can be described as hybrid fabric-reinforced multifunctional laminates. An alternative laminated concept has been proposed [43,44], in which macroscale (several mm wide) through-thickness perforations are introduced into SSCs, consisting of CNT sheet electrodes and solid polymer electrolyte. The SSCs were embedded inside a carbon fibre composite, with the structural resin-filled perforations acting as transverse reinforcement for improved shear performance of the multifunctional laminate. This concept falls somewhat short of being a truly multifunctional material.

Overall, SSC research is still at a low technology readiness level (TRL), primarily focused on laboratory-scale device concept demonstration and constituent-level development of electrodes (carbon-based [37,40,41,43] and metal oxide-based [40,42,45]) and electrolytes (conductive polymers [40] and ionic liquid blends [41,45]), rather than on addressing scale-up issues and practical applications. The performance of SSCs has been measured in terms of characteristics such as the specific energy and power densities (normalised by total device mass, though this convention is not always followed in the literature), and tensile and shear elastic moduli.

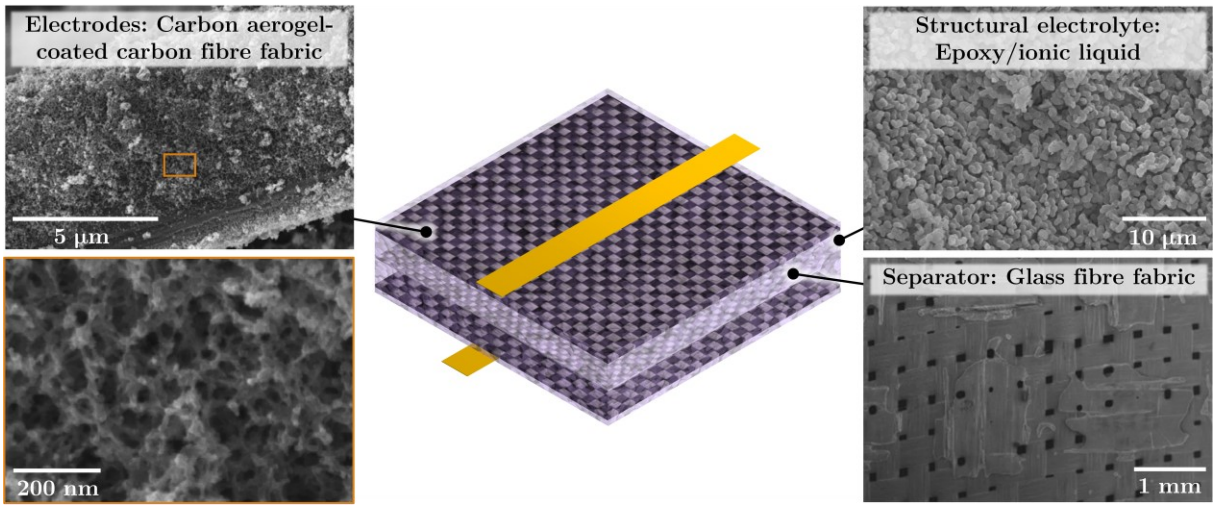

Figure 2.1. Schematic of architecture of structural supercapacitors developed at Imperial College London.

Despite their importance in most applications, properties such as mechanical strength and toughness, as well as long-term electrochemical cyclability, are usually neglected in the literature. Whilst neglecting these properties may be reasonable (even preferable) to progress in early stages of development and performance ranking, this carries risks for later stages of design and deployment.

Near-term performance targets of 5 Wh/kg and 1 kW/kg have been proposed for the electrochemical properties of SSCs, while tensile Young's modulus and matrix-dominated properties of SSCs have been targeted within 80% and 50%, respectively, of those typical of woven composites [46]. The performance targets proposed for the ionic conductivity and Young's modulus of the structural electrolyte were 1 mS/cm and 1 GPa [16].

SSC laminates fabricated during a recent ICL project [47] achieved some of the highest device-level performance reported in the literature to date [18], including energy and real power densities of 93 mWh/kg and 5.2 W/kg (Table 2.4), respectively, and tensile and shear moduli of 32.9 GPa and 1.7 GPa (Table 2.3). The structural electrolyte system used in these laminates was a 35% v/v blend of IL/epoxy, which achieved an ionic conductivity and Young's modulus of 0.3 mS/cm and 800 MPa, respectively (neat properties). This data makes clear that electrochemical performance is still systematically lower than what is required for deployment. It is worth noting that the specific electrochemical properties of the equivalent semi-structural (that is, containing IL only) SSC devices were more than an order of magnitude higher than those of the multifunctional devices above.

2.2.2 Challenges for development and performance

For comparison, state-of-the-art commercial monofunctional symmetric supercapacitors achieve energy densities (normalised by cell mass) of up to 7.5 Wh/kg and power densities up to 41 kW/kg [34]. Multifunctional efficiency analysis has shown [48] that to achieve a mass-saving multifunctional design, the properties of SSCs should be no more than an order of magnitude lower than those of conventional devices or structures. Performance improvement thus continues to be the principal challenge in the development of SSCs.

Development challenges stem from the fact that the architecture and combination of constituents (described in the previous Section) employed to enable and enhance

multifunctionality are unconventional to both structural composite and electrochemical energy storage solutions. This novelty poses unique developmental challenges related to manufacture, performance tradeoffs and analysis. When considering performance, it is widely agreed that a holistic approach to achieving mechanical and electrochemical objectives is required since these are often coupled and/or conflicting [49]. For instance, increasing the electrolyte volume fraction in the multifunctional matrix simultaneously improves energy density and reduces mechanical rigidity. Improved understanding of the structure-property relationships at both the constituent and device scales is required to design SSCs with an optimal and tailored balance of properties.

To date, the development of SSC constituents and devices has tended to be experimental. However, total reliance on such experimental research can not only be time-consuming and expensive, but also impractical since many of the constituents are continually under development with limited quantities available for testing. Computational models can considerably reduce the experimental burden through rapid virtual testing. Over the last decade, finite element modelling (FEM) has been established as a powerful technique for the analysis of the mechanical and electrochemical behaviours, respectively, of conventional composites and supercapacitors. The technique remains unused in the analysis and optimisation of SSCs. This, and other research gaps, are discussed in Chapter 3, while the remainder of this Chapter reviews the relevant literature.

2.3 Compaction of woven fabric reinforcements

2.3.1 Background and characterisation

Woven reinforcements are widely used in composite manufacture due to their improved formability, lower cost, and handleability, over those of unidirectional (UD) prepregs [50]. The availability of a wide variety of weaves permits considerable control over the fabric forming characteristics, such as drapability, permeability and compressibility [50,51]. In the fabrication of SSC and other SPCs, dry woven fabric preforms have been the preferred architecture of the fibre reinforcements to provide the necessary stability and robustness under repeated handling and aggressive processing conditions, documented elsewhere [16]. To satisfy the electrochemical property requirements in SPCs [20,37,45], carbon and glass fabrics have been layered (Section 2.2.1), resulting in interply hybrid woven composites.

During the preforming and consolidation stages of manufacturing woven fabric-reinforced composites (WFRCs), the fabric architecture undergoes complex dimensional changes. These deformation mechanisms have been widely studied [52–55] and include changes in the local fibre orientation, volume fraction and interyarn gaps, yarn flattening and nesting between adjacent plies. Pressure is applied during consolidation to obtain composite parts with high fibre content and minimal defects. The structural integrity of WFRC components is strongly influenced by their micro- and mesostructure, hence considerable efforts have been dedicated to their prediction via preforming and compaction process modelling (outlined in Section 2.3.2).

There is no standard test procedure for the evaluation of fabric compressibility (also referred to as compaction). Typically, an out-of-plane compression test is performed in a mechanical test machine. Researchers have used linear or exponential data fitting [56–59] or inverse parameter identification algorithms [57,60] to evaluate the transverse compressive stiffness of the fabric yarns, which is an essential input property for compaction models. However, the repeatability of compaction experiments has been questioned: a recent compaction benchmark exercise [61] highlighted large scatter in measurements between the twenty six benchmark participants. The study identified choice of test fixture and the load and displacement measurement methods as the key factors responsible for variation. Consequently, two measures to improve the accuracy and repeatability of dry fabric compaction tests were suggested: the use of direct thickness measurement methods instead of crosshead displacement to eliminate machine compliance errors, and the use of compression platens with a spherical seating to ensure parallelism.

2.3.2 Modelling

Models for the compaction of fibrous reinforcements were originally developed for the textile industry [62] and later adopted by composites researchers [63,64] to describe the properties of randomly-oriented and aligned fibre networks. These early semi-empirical and analytical models were based on fibre bending analysis, typically taking the form of a power law between the applied pressure and fibre volume fraction. Numerical models were later proposed [65] for the compaction of woven fabrics, in which the three-dimensional fabric architecture was explicitly considered, alongside the experimentally measured compression and bending properties of yarns. Fabric compaction has been primarily studied through mesoscale finite element (meso-FE) models [66], which simulate periodic ‘unit cell’

(UC) representations through periodic boundary conditions [67]. The UC can be constructed from measurements of the fabric or composite geometry. These methodologies have enabled the analysis of the mechanical behaviour (and other physical attributes important to composite manufacturing) of a wide variety of fabric reinforcements.

Subsequent investigation into fabric compaction modelling have highlighted the importance of lateral yarn interactions and material non-linearity [68], in accurately reproducing the actual response. More complex hypo-elastic [57,69] and hyper-elastic [52,70] constitutive models of fabric yarns have also been introduced, which are typically implemented as user material subroutines for commercially available finite element codes. However, the above models rely on parameters requiring inverse parameter identification based on several mechanical tests, and their predictive accuracy is not always guaranteed. Compaction simulations of multilayer fabric preform stacks [57] have demonstrated a large influence of the in-plane offset between adjacent plies, or ply offset (further discussed in Section 2.4.2.2), on the effective compressibility of fabric stacks.

2.4 Mechanical performance of SSCs

2.4.1 Background and characterisation

2.4.1.1 Constituent level

Multifunctional matrix

Bicontinuous structural electrolytes have been developed based on blends of structural epoxy and ionic liquid electrolyte [20,71,72] with the aim of providing a good combination of mechanical and electrochemical properties, typically characterised by their Young's modulus and ionic conductivity. Figure 2.2 summarises the reported performance of different (neat) structural electrolytes. It is known that these properties are highly sensitive to the ratio of the phases, and understanding of microstructure-property relationships in the neat resins has progressed. However, fractographic analysis has indicated that the microstructure formed within SSC devices (*in situ*) differs from that of the neat material [20]. That study reported a high degree of heterogeneity, with a liquid dominated phase close to the fibres and structural dominated phase at interstitial sites in the fabric, as well as voidage at the carbon/glass ply interface, closed porosity and sheathing of fibres by the structural phase. Understanding of these *in situ* effects on matrix microstructure, and the resulting mechanical and electrochemical properties is lacking.

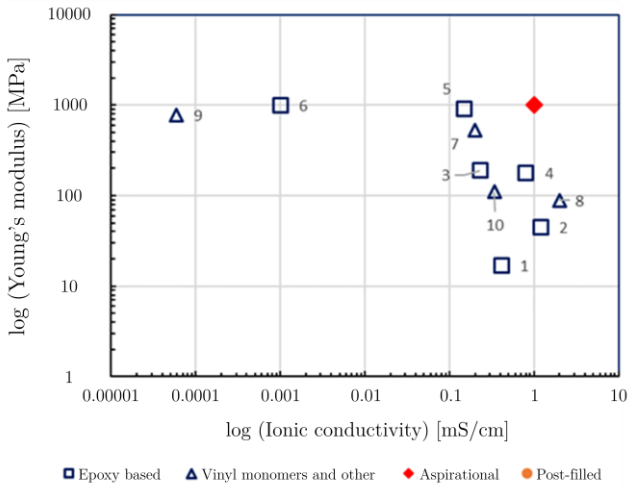

Figure 2.2. Multifunctional performance of structural electrolytes in the literature [72].

Carbon aerogel

Carbon aerogel (CAG) is a monolithic organic material consisting of an interconnected nanoporous network of carbon particles [73]. CAG is synthesised through pyrolysis of organic aerogels, which are produced through a sol-gel polymerisation of a precursor, such as resorcinol-formaldehyde (RF) [73]. CAG offers a range of attractive properties, including high porosity, low density, high electrical conductivity, high surface area and good thermal and specific mechanical properties [74], which can be controlled through the synthesis conditions. It has been reported that even slight variations in these conditions may cause considerable changes in the nanostructure, and consequently, the physical and mechanical properties [75].

The steps involved in the processing of CAG for the ICL SSCs consist of vacuum-assisted resin infusion under flexible tooling (RIFT) of the RF precursor mixture, which crosslinks under vacuum, followed by solvent exchange, drying and pyrolysis, as detailed elsewhere [47]. Carbon fibres (CFs) can be introduced in the RIFT step [76], as is the case in ICL SSCs [22], where carbon fabrics have been used as fibrous reinforcements for the structural electrodes. This has the effect of shape-stabilising the CAG and improving the mechanical integrity, handleability and in-plane electrical conductivity of the resulting CAG-modified carbon fabric (CAG/CF) [77].

In the absence of CFs, monolithic CAG is produced, though a poor sample survival rate (approximately 1 in 10) has been reported as a result of brittle fracture during solvent removal and pyrolysis [78]. This has been attributed to high surface tension effects causing partial collapse of the porous structure [79]. Therefore, only small specimen sizes (up to 10

mm across) have been successfully produced, and mechanical characterisation of monolithic CAG is very challenging [80]. Monolithic CAG samples and their polymer composites have been successfully characterised only under uniaxial compression [75,78]. In a previous ICL project developing High Performance Ductile Composite Technology (HiPerDuCT), polymer composite samples composed of ca. 63 vol. % dense monolithic CAG (dry CAG monolith density 1.59 g/cm^3) and epoxy resin exhibited a near five-fold increase in compressive modulus over epoxy, a moderate decrease (–11%) in strength, and a brittle cleavage failure with a large reduction (–91%) in failure strain (0.35%) [78] (Table 2.1).

An alternative characterisation technique, widely used in the study of silica and graphene aerogel monoliths and other nanocomposites [81–83], is instrumented indentation, also known as nanoindentation. During a nanoindentation test, load is applied normal to the sample surface through an indenter. The applied load and indenter penetration depth are continuously recorded, allowing the elastic, time-dependent and fracture properties of the material to be determined from this data [84]. By virtue of the small loads applied (< 1 N), the technique is non-destructive, and requires small quantities of material: it can be performed on thin film specimens, provided they are of sufficient thickness to avoid substrate effects [85–87]. These advantages make nanoindentation an attractive technique for the evaluation of the mechanical properties of CAG in future.

For fibre composites, nanoindentation may also be used to measure the *in situ* matrix properties, provided the constraining effect of the fibres can be minimised by performing indentations parallel to the fibre direction and away from fibres [88]. For epoxy/CF composites, the *in situ* matrix modulus has been shown to be ca. 30% larger than the neat value [88], whilst in some ceramic matrix composites, a significantly reduced *in situ* matrix modulus has been observed, attributed to porosity and inclusion of softer embedded phases [89].

Polymer composites based on CAG/CF fabrics have been mechanically characterised using standard test methods, including short beam (interlaminar) shear, longitudinal tension and longitudinal compression [90] (Table 2.1). This research demonstrated improvements in compressive stiffness, and compressive and interlaminar shear strengths when CAG-modified fabrics were used with a soft multifunctional matrix. However, CAG modification was detrimental to tensile, compressive and interlaminar shear strengths (with a small positive effect on stiffnesses) when used with a structural epoxy,

with researchers suggesting poor fibre-matrix interfacial shear strength as a possible cause [73,90]. A 10% decrease in the tensile strength of control samples produced using pyrolised CFs, and a 50% decrease in that of CAG/CF samples, compared to baseline CF composite samples was considered an indication of process-induced damage to the outer surfaces of CFs [73].

If CAG can be conceptualised as the matrix material, which transfers load between fibres, CAG/CF fabrics could be classed as a carbon/carbon composite. Polymer-infiltrated CAG/CF may share some similarities with ceramic matrix composites (CMCs), since the failure strain of the CAG/epoxy matrix material (0.35% from monolith tests [78]) is lower than that of the CFs typically used (ca. 1.5%, [91]). In CMCs, the naturally brittle ceramic matrix is reinforced with fibres to improve the toughness by encouraging repeated crack deflection along the fibre/matrix interfaces [92,93]. The latter is achieved when these interfaces (or interphases) are relatively weak [94].

Table 2.1. Reported influence of CAG on mechanical properties of structural composites.

Matrix	Fibres	CAG loading†	Fibre volume fraction (%)	Test condition	Modulus (GPa)	Strength (MPa)	Ref.
PEGDGE	C	–	57.1	Short beam/ interlaminar shear	–	3.4 ± 0.1	[90]
PEGDGE	C*	5.4 vol. %	55.7		–	14.0 ± 0.4	
PRIME	C	–	56.3		–	60.5 ± 1.9	
PRIME	C*	5.0 vol. %	56.5		–	43.0 ± 1.1	
PEGDGE	C	–	57.1	Compression	16.6 ± 1.5	50.4 ± 3.8	
PEGDGE	C*	5.4 vol. %	55.7		60.5 ± 3.6	174.8 ± 9.2	
PRIME	C	–	54.4		62.0 ± 1.0	634.6 ± 16.2	
PRIME	C^P	–	56.1		60.3 ± 0.5	453.1 ± 17.1	
PRIME	C*	5.0 vol. %	55.3		63.9 ± 0.5	331.2 ± 9.3	
PRIME	C	–	54.4	Tension	62.6 ± 0.7	813.2 ± 4.3	
PRIME	C^P	–	56.1		64.8 ± 0.7	729.5 ± 22.1	
PRIME	C*	5.0 vol. %[a]	55.3		65.3 ± 0.5	409.0 ± 7.1	
PRIME	–	–	–	Compression	2.78 ± 0.2	84.4 ± 1.0	[78]
PRIME	– (CAG)	62.6 vol. %	–		15.8 ± 2.9	74.5 ± 9.4	

C refers to as-received carbon fibre fabric (CF); C^P refers to pyrolised CF; C* refers to CAG-modified CF; CAG refers to carbon aerogel monolith; [a] indicates assumed value; † refers to laminate value.

2.4.1.2 Device/laminate level

Woven composites

Typical protocols for the mechanical characterisation of SSC laminates consist of 0°/90° tensile and compressive and ±45° tensile (in-plane shear) tests [20,47,48], although bending tests have also been performed [44,95]. The failure of conventional woven composites under these load conditions has been widely studied [96,97], and is considered

more complex than that of UD laminates due to the weave architecture and interactions between the yarns [98]; it features damage mechanisms, including intralaminar failure of the yarns, cracking in neat matrix pockets, and interlaminar failure of the yarn/yarn and yarn/matrix interfaces [67,99]. A review of the experimental literature [98] compared the failure of woven and cross-ply UD architectures, concluding that in woven composites crack initiation and damage progression occurs at a lower and narrower range of strains (0.2–0.4% compared to 0.4–0.8%). As a result, the tensile strength of carbon/epoxy woven composites is typically 60–90% of that of equivalent UD composites.

The tensile failure sequence in carbon/epoxy woven composites has been well studied and can be summarised as follows [98]: damage initiates as fibre/matrix debonding and transverse matrix cracks within the 90° yarns, concentrated near yarn intersections where crimp and shear stresses are highest and strain concentrations exist; at higher strains, crack length and density increase; eventually, delamination cracks and transverse cracks in matrix pockets also develop; final failure is controlled by fibre breakage or delamination.

Under in-plane shear, failure evolves as follows [98]: transverse cracks initiate around 1% strain; failure proceeds through distributed shear damage within the yarns [99] and delamination cracks between warp and weft yarns due to shear stresses, and between plies; scissoring mechanisms allow large global shear deformations to be reached [98]. In both load cases, crack development is periodic due to the fabric architecture, whilst final failure is controlled by fibre breakage or delamination [98,99].

The matrix- and interface- dominated properties of woven composites can be particularly affected by the presence of voids [100]. The effects of voids have been most often studied by short beam shear experiments, from which it has been reported that:

- voids act as initiation sites for intralaminar cracks, which subsequently propagate and become interlaminar cracks [101];
- void shape and size matters: crack formation and strength degradation are more severe in composites with large, sharp-cornered or high aspect ratio voids due to stronger stress concentrations, which lower crack initiation stress [101,102].

Experimental studies have linked a 10% void content to 18% and 56% reductions in tensile stiffness and strength, respectively, in biaxial woven laminates [103]. Under in-plane shear, tests on cylindrical UD carbon/epoxy specimens found 60% and 70% reductions in modulus and strength, respectively, at 5% void fraction.

Structural supercapacitor composites

The mechanical performance of the SSCs, which are the focus of this thesis, were recently characterised in 0°/90° and ±45° tensile tests [47] (Table 2.3). The experiments were designed to isolate the influence of CAG and structural electrolyte on the device performance, by analysing four different laminates, summarised in Table 2.2.

Laminates containing pure epoxy matrix were considered monofunctional (structural only) since they contained no electrolyte (that is, they had no electrical energy storage function). The research showed that the measured initial tensile and in-plane shear moduli of the structural laminates were relatively insensitive to the introduction of CAG, but reductions of ca. 20% and 47%, respectively, were observed for multifunctional laminates, compared to the baseline (Figure 2.3). The failure behaviour was also severely affected by these constituents, with severe reductions in tensile strength and maximum shear stress associated with CAG (ca. −69% and −20%, respectively, compared to the baseline) and structural electrolyte (ca. −72% and −55%, respectively).

Table 2.2. SSC laminates tested in Ref. [47].

Sample name	Electrodes	CAG modification	Matrix	Sample code
Baseline	C	No	BADGE	CGC STR
Pyrolised	C^P	No	BADGE	C^PGC^P STR
CAG-modified	C*	Yes	BADGE	C*GC* STR
Multifunctional	C*	Yes	BADGE/41 wt. % IL	C*GC* MF
Semi-structural	C*	Yes	IL	—

C refers to as-received biaxial carbon fibre fabric (CF); C^P refers to pyrolised CF; C* refers to CAG-modified CF; CAG refers to carbon aerogel monolith; STR refers to structural laminates; MF refers to multifunctional laminates; a indicates assumed value.

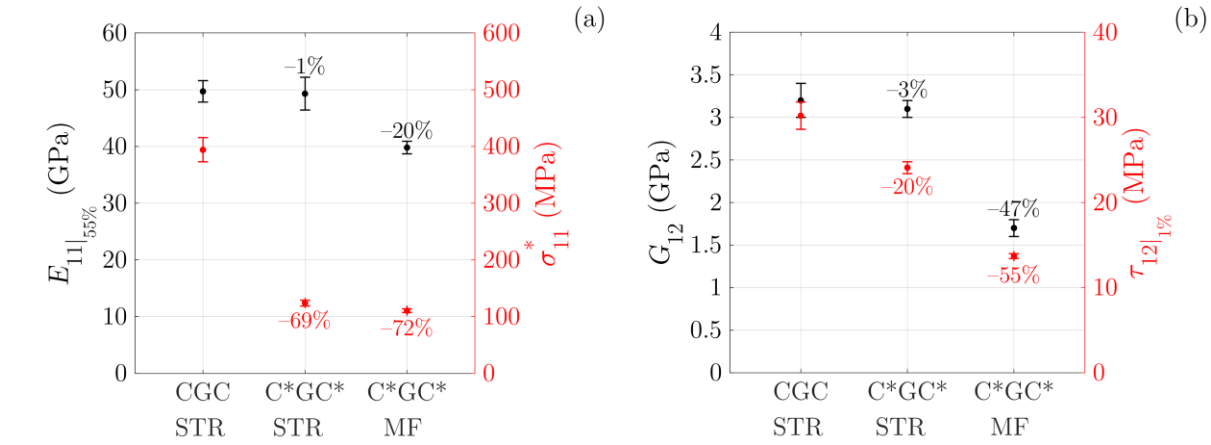

Figure 2.3. Mechanical performance of SSC laminates tested in Ref. [47].

The authors reported a number of differences in the tensile fracture surfaces during some limited fractographic studies. Unlike the baseline material configuration specimens, in which the fibre bundles had fractured at different planes, the CAG-modified structural and multifunctional laminates presented a much more brittle and flat fracture morphology with much larger fibre zones having fractured on the same plane, initiating from the same local failure event. Mirror-mist-hackle morphologies [104] on the fibre ends were similar across all material configurations, consistent with negligible degradation of fibre strengths due to the high temperature processing. It was reported that the morphology of the structural electrolyte matrix corresponded to that observed for bulk matrix prepared with lower IL content.

Failure modes under in-plane shear were also disparate across the three material configurations: baseline specimens presented a single fracture location oriented at 45° across the specimen width, which was associated with off-axis intralaminar splitting prior to fibre failure. In contrast, the CAG-modified structural specimens presented localised fracture indicating there had been no off-axis intralaminar splitting or delamination prior to fibre failure.

The multifunctional specimens presented extensive delamination between the plies, leading to isolated final failures of each ply, after extensive scissoring deformation and off-axis intralaminar splitting. In both loading conditions, the fracture morphologies of CAG-modified specimens were consistent with good bonding and load transfer between carbon fibres and CAG, and brittle failure of the CAG; whilst those of the multifunctional laminates suggested poor wetting/interface of the CAG with epoxy.

The authors hypothesised that the brittle tensile fracture of CAG-containing specimens could have been caused by a high CAG/CF bond strength, inhibiting fibre debonding and pull-out (Cook-Gordon process [105]). In the shear case, the strong CAG/CF interface was believed to have been responsible for the localised damage by inhibiting secondary fracture mechanisms, such as ply splitting and delamination, which would have distributed damage development and isolated the yarns.

However, the authors noted that further investigations were required to determine the causes of the strength reduction and improve the failure performance. In the multifunctional laminates, the lower initial tensile and shear stiffnesses were attributed to the compliant structural electrolyte, which was also thought to have promoted ply splitting

and delaminations. Under in-plane shear the soft matrix between the yarns explained the extensive scissoring deformation of the fabrics, whilst large interlaminar voids further promoted delamination, explaining the change in failure mode compared to the structural CAG specimens.

These recent findings somewhat contradict earlier reports on the in-plane shear behaviour of similar structural and multifunctional composites (10 wt. % IL) based on CAG/CF and GF fabrics [22,23] (Table 2.3). For the multifunctional laminates, increases in both in-plane shear modulus and strength (ca. 220% and 60%, respectively, in [22]) were demonstrated compared to the baseline. Similar improvements associated with CAG were also reported for structural composites with a soft epoxy matrix (PEGDGE), while properties were unchanged for composites with structural epoxy resin (BADGE) [22].

The authors reported that for all laminates, failure occurred by matrix damage accumulation, followed by delamination between the carbon and glass plies. Similar morphologies were observed in all laminates, displaying good fibre/matrix adhesion, matrix plasticity and ductile failure, indicating good infusion of epoxy into the CAG. Later work investigating multifunctional laminates with an alternative matrix (MTM57/ 45 wt. % IL) also reported shear modulus and strength improvements associated with CAG (ca. 340% and 190%, respectively, in [23]), though poor matrix wetting was observed between in the specimens without CAG, which could have attributed to the large apparent increase.

Table 2.3. Reported effect of CAG and matrix on structural properties of ICL SSCs.

Sample code	Matrix	CAG loading (fabric)	Fibre volume fraction (%)	Test condition	Modulus (GPa)	Strength (MPa)	Ref.
$[C/G]_s$ STR	BADGE	–	45.0	In-plane shear	4.38 ± 0.06	25.9 ± 2.2	[22]
$[C*/G]_s$ STR	BADGE	9.5 wt. %	40.7		5.05 ± 0.21	26.2 ± 0.5	
$[C/G]_s$ STR	PEGDGE	–	47.2		0.20 ± 0.01	5.83 ± 0.14	
$[C*/G]_s$ STR	PEGDGE	9.5 wt. %	42.0		0.91 ± 0.06	8.88 ± 0.12	
$[C/G]_s$ MF	PEGDGE / 10 wt. % IL	–	47.2		0.27 ± 0.01	5.36 ± 0.07	
$[C*/G]_s$ MF	PEGDGE / 10 wt. % IL	9.5 wt. %	42.0		0.90 ± 0.06	8.71 ± 0.11	
$[C/G]_s$ MF	MTM57 / 45 wt. % IL	9.5 wt. %	–	In-plane shear	0.18 ± 0.01	2.22 ± 0.21	[23]
$C*/G]_s$ MF	MTM57 / 45 wt. % IL	9.5 wt. %	–		0.79 ± 0.05	6.36 ± 0.79	
CGC STR	BADGE	–	44.2	In-plane shear	3.2 ± 0.2	30.2 ± 1.6†	[47]
C*GC* STR	BADGE	15.3 wt. %	43.0		3.1 ± 0.1	24.1 ± 0.7†	
C*GC* MF	BADGE / 41 wt. % IL	15.5 wt. %	45.5		1.7 ± 0.1	13.7 ± 0.3†	
CGC STR	BADGE	–	44.2	Tension	40.0 ± 1.5	394.0 ± 21.3	
C*GC* STR	BADGE	15.3 wt. %‡	43.0		38.6 ± 2.3	123.9 ± 5.2	
C*GC* MF	BADGE / 41 wt. % IL	15.5 wt. %	45.5		32.9 ± 0.9	110.4 ± 3.3	

C and G refer to as-received biaxial carbon fibre fabric (CF) and biaxial glass fibre fabric (GF), respectively; C* refers to CAG-modified CF; IL refers to EMIM-TFSI; † shear stress at 1% shear strain; ‡ unpublished data.

2.4.2 Modelling

2.4.2.1 Constituent level

Multifunctional matrix

In the wider background literature on interpenetrating composite matrices, analytical models have also been used for the prediction of the mechanical and physical properties. These models have been outlined in detail by other researchers [106], therefore the discussion here will focus on their relevance. The analytical models are typically derived from volumetric rules of mixtures, however, more complex models based on representative volume elements, which explicitly account for the geometric parameters of the interpenetrating network [107] have also been developed. As each model represents a specific idealisation of the geometry, phase connectivity and stress state of the composite system, they offer varying levels of predictive accuracy for different examples of real systems. When these models are taken together, predictive uncertainty can be substantial since upper and lower bound predictions can differ considerably for a given volume fraction [106]. Therefore, the accuracy of a particular model can only be verified by comparisons with experimental data (ideally over a range of volume fractions), the availability of which can be limited. Finally, few insights about desirable morphological features of structural electrolytes can be obtained from these models provide due to the limited flexibility in the geometric representations assumed.

Computational analyses have been used to complement experimental development of multifunctional bicontinuous structural electrolytes for structural power applications. A topology optimisation scheme [108] has been developed, combining mechanical finite element analysis with an electrical resistance network model, and using a multi-objective optimisation function to define the desired balance of effective mechanical stiffness and ionic conductivity. The scheme was used to identify optimal bicontinuous microstructures for a range of solid volume fractions and weighting factors, producing a series of multifunctional Pareto fronts. The numerical predictions were validated through compression and impedance spectroscopy experiments performed on macroscale 3D printed specimens; however, their predictive accuracy is yet to be demonstrated at finer length scales relevant to structural electrolytes.

A numerical study [109] has recently addressed the latter, comparing the properties reported for structural electrolytes in the literature with those predicted from simulations.

Various classes of random computer-generated bicontinuous geometries were considered, mimicking the experimentally observed morphologies. Properties were evaluated across a range of porosities using structural and mass diffusion simulations. These models predicted effective stiffnesses in the correct order of magnitude, however predictions of ionic conductivities were less accurate, with the authors suggesting that more complex diffusion models for ionic liquids would be needed. Whilst there are indications that numerical simulations may in future be able to predict the properties of structural electrolytes more accurately, at present their applicability in predicting the properties at higher length scales (for example, device-level) is limited.

Carbon aerogel

Hierarchical composites featuring carbon nanoreinforcements such as CNTs and CAG have shown promise in improving composite stiffness and strength, however the structure-property relationships, and mechanisms of load-transfer and damage are not fully understood. Both analytical and numerical models can be used as investigative and predictive tools for the mechanical and physical properties of CAG. At present, such modelling techniques appear not to have been applied to examine CAG or CAG-modified composites; however, silica aerogels have been widely studied via three-dimensional numerical simulations [110–114]. In these works, cluster algorithms are commonly used to produce random-generated skeletal particle networks, with which the microstructural dependence of the elastic [110,112,113] and failure properties [111,112,114] can be evaluated. It should be noted that the relevance of these models to optimising CAG synthesis conditions is somewhat limited, since nanostructures are difficult to produce in a controllable manner. Previous research at ICL [78] has indicated that shrinkage during drying and pyrolysis can severely affect the density and morphology of the final network.

The required input properties for the above models include the average particle radius or statistical particle size distribution, particle overlap lengths and neck geometry, and particle coordination numbers, which govern the network morphology, and contact stiffness between the particles. A serious drawback of applying such nano–scale simulations to study real system is the need for precise knowledge of particle radii, requiring extensive characterisation of statistical particle size distributions using high resolution scanning electron microscopy. The feasibility of using such a model to predict the mechanical properties of CAG is somewhat questionable, as this would and the elastic properties have

been shown to be extremely sensitive to even small (1 nm) variations in average particle radius [111], which would imply a high degree of uncertainty in the resulting predictions. Furthermore, as these models are restricted to very small volumes of material (on the order of 100 nm), multiscale methods would be required for the simulation of aerogel-modified fibre composites [111]. The analytical models discussed in the previous Section could conceivably be applied to obtain less computationally-intensive first approximations of the properties of CAG monoliths. However, the remaining need for experimental verification significantly diminishes the value of such modelling methodologies over direct measurement methods.

2.4.2.2 Device-level

Structural supercapacitor composites

Computational modelling has rarely been applied in the analysis and development of SSC devices (or laminates). Progress in this field appears to have been hindered by a lack of experimental mechanical data on the constituent materials. The only published work used the multiscale generalised method of cells [115] to simulate the elastic response of fabric-reinforced SSC coupons reported elsewhere [22,48]. In the absence of experimental data on the structural electrolyte, its elastic properties were calibrated using the coupon test data; direct predictions of the elastic response of the laminates were therefore not possible. Carbon aerogel was not considered in the study, likely for the same reason, despite its strong influence on properties (Section 2.4.1).

Woven composites

The SSCs of interest in this thesis are based on woven fabrics, and therefore suitable modelling strategies can be identified from woven composites research, where the majority of analyses have been performed numerically [67]. As the predictive accuracy of mechanical models relies not only on good knowledge of the constitutive properties but also on accurate representation of the laminate geometry [66,116,117], meso-FEM (introduced in Section 2.3.3) has been established as a powerful technique for the prediction of mechanical behaviour.

By explicitly considering the complex undulating three-dimensional architecture of woven fabrics, mesoscale FEM has improved upon early analytical models based on classical laminate theory [118–120] and orientation averaging [121–123] that employ highly idealised representations of the architecture and loading conditions. These models are generally unsuitable for the prediction of matrix-dominated elastic properties, strength

prediction, damage progression or defect modelling [124]. Though it is more computationally intensive, mesoscale FEM is robust enough to investigate these issues.

Various mesoscale geometric modelling techniques have been employed, such as the method of cells previously used in the simulation of SSCs [115]. Alternative methods, which utilise X-ray imaging [125–127] or preform simulations [70,128], have been demonstrated for the generation of highly realistic unit cell (UC) geometries, enabling more accurate predictions of elastic and non-linear behaviour, and progressive damage [128,129]. The advantage of the preform simulation route is that it allows the complex geometry of the interaction zones between the nested yarns to be automatically captured without the need for extensive laminate characterisation. This enables the complex mesoscale stress state within the yarns near these zones to be correctly captured [117], and allows interfacial debonding of the yarn/yarn and yarn/matrix interfaces to be incorporated in progressive damage analyses [116]. When yarn input data for these models is obtained from micromechanical predictions, rather than direct measurement of representative yarn UD specimens, these mesoscale fabric composite models could be considered multiscale [117].

For mesoscale UC models of fabric composites, periodic boundary conditions (PBCs) are typically applied to model in-plane deformations. Further improvements in computational efficiency have been achieved by exploiting internal symmetries, to create reduced unit cells [130,131]. One potential disadvantage of the use of such boundary conditions is that free edge effects (that is, deviations from the stress distribution in an infinite laminate) present in real laminates are neglected. Meso-FE investigations have however shown that free edge effects are confined to a narrow region [132].

Some researchers have pointed out that the choice of out-of-plane boundary conditions is also important [132,133] and implies different assumptions about the laminate thickness. Out-of-plane PBCs imply an infinitely thick laminate, whilst free surfaces imply finite thickness, and the stress distributions obtained from models employing the two conditions can differ significantly [132]. In the latter, out-of-plane and shear stresses in the surface plies are amplified, and these free surface effects propagate to the midplane even in thick (sixteen-ply) laminates [132]. The above authors further noted that the exact magnitudes of both free edge and finite thickness effects are dependent on the weave geometry, ply offset (discussed below) and location in the weave [132]. These findings are relevant to SSCs since typically ‘single cell’ laminates consisting of three or four plies have

been investigated, and the effects of scaling up the laminate thickness on the measured mechanical properties are unknown at present.

Researchers have also recognised that meso-FE models of multilayer fabric composites, which treat the composite geometry deterministically, fail to account for the arbitrary variation in the interply shift (also referred to as ply offset or stacking configuration) that is unavoidably introduced during production [134]. Differences in the ply offset have been shown both experimentally [135] and numerically [134,136] to govern the stress distribution and failure behaviour of fabric composites, due to differences in the through-thickness and shear support provided by adjacent layers. Therefore, it has been suggested [136] that the effect of ply offset should be considered in mesoscale mechanical models of fabric laminates. Idealised bounds for the ply offset have been proposed, for example in-phase and out-of-phase stacking of adjacent fabric layers [136], as well as other intermediate [134] or random cases. It is notable that the numerical studies of ply offset have considered only idealised uncompacted laminate geometries, neglecting the complex nesting in compacted stacks and the associated differences in the local yarn and fibre packing (Section 2.3).

Few studies have attempted to numerically predict the effects of voids on the elastic properties of fabric composites [137,138]. These studies have focused on predicting elastic properties, simulating voids by randomly discounting individual elements from the meso-scale UC. In the case of biaxial woven fabric composites, for the same void content, meso-FE simulations predicted negligible reductions in longitudinal tensile and in-plane shear stiffnesses [137], contradicting experimental findings, which have found significant reductions [103] (reviewed in Section 2.4.1.2). A possible cause of this disagreement could be the assumption of small, randomly dispersed voids in the meso-FE studies, in contrast to the large, localised voids reported for laminates with high void volume fractions. These works make clear that predicting the effects of voids on elastic properties alone is a complex and challenging issue, and accurate prediction of the failure properties of laminates containing large voids is therefore judged unlikely at present.

Approaches for modelling progressive damage in woven composites include continuum damage mechanics (CDM), in which the effective mechanical properties of finite elements are degraded according to level of damage, with various failure initiation and propagation criteria available; and the cohesive zone method (CZM), which allows pre-

defined crack surfaces to be modelled, whose opening is governed by linear elastic fracture mechanics [67]. The failure behaviour of woven composite UCs under tensile and in-plane shear loads was comprehensively modelled by McLendon and Whitcomb [99] using a multiscale approach. That work combined CDM and CZM to capture distributed and localised damage types, respectively. Initial shear damage of the matrix was considered small and diffuse compared to the UC size, therefore CDM was used, whilst at normal and shear stress levels corresponding to formation of larger discrete matrix cracks, as well as cracks in matrix pockets and interfacial yarn/yarn and yarn/matrix delaminations, CZM was used.

The predicted tensile failure sequence was as follows: damage was initiated as discrete transverse cracks in 90° yarns, followed by neat matrix cracks, transverse cracks in 0° yarns, and some yarn/yarn delaminations in the vicinity of transverse cracks [99]. At higher strains, neat matrix cracks were deflected along the yarn/matrix interfaces, until the first fibre failure was reached. Shear damage in the yarns was minor under this condition. Under in-plane shear, distributed shear damage dominated the response, developing first near tow edges at intersections. Tow decohesion increased with load, promoting matrix cracks and yarn/matrix delaminations. The simulation became unstable around 6% shear strain.

SSC laminates are a specialised example of glass/carbon 'interply hybrid' fabric composites. The mechanical performance of structural interply hybrid fabric composites has been widely studied. Improvements in tensile strain [139], flexural failure [140–142], and penetration [140] and impact [143–145] resistance have been experimentally demonstrated. Ply-level finite element analysis (FEA) has been used to predict the layup-dependent impact response [143,144]. However, due to a lack of data, delamination criteria used in these models tend to rely on unrealistic assumptions and/or parameter calibration. The fabric architecture has also not yet been explicitly considered, perhaps due to the difficulty in constructing a suitable mesoscale UC.

2.5 Current collection in SSCs

2.5.1 Background

For charge to flow through an electrochemical cell, the electrical resistance of the cell components must be overcome, resulting in an electric potential drop. The latter is

proportional to the current density and is assumed to obey Ohm's law, expressed in matrix form as:

$$\mathbf{J} = \boldsymbol{\sigma}^{\mathbf{E}} \cdot \mathbf{E} \quad , \tag{2.1}$$

where $\mathbf{J}$ is the current density, $\boldsymbol{\sigma}^{\boldsymbol{E}}$ is the volumetric electrical conductivity, and $\mathbf{E}$ is the electric field intensity, defined as the gradient of electric potential, ψ:

$$\mathbf{E} = -\nabla\psi \quad . \tag{2.2}$$

The electrical power (also known as Joule heat, P_J) dissipated through this process is expressed, per unit volume, by Joule's law [34]:

$$\frac{dP_{\mathrm{J}}}{dV} = \mathbf{J} \cdot \mathbf{E} = \mathbf{E} \cdot \boldsymbol{\sigma}^{\mathbf{E}} \cdot \mathbf{E} \quad . \tag{2.3}$$

The loss of useful power due to internal electrical resistance (also referred to as equivalent series resistance, ESR) has a direct impact on the power performance and energy efficiency of the electrochemical cell [146], whilst the generated heat can lead to thermal stress and expansion, self-discharge, accelerated ageing, and overvoltage damage in cell packs [147]. Measures to reduce ESR include modifying the geometric parameters of the cell, as well choosing cell materials with low intrinsic and contact resistivities [148]. The area-normalised ESR of commercial supercapacitors is typically on the order of a few $\Omega.\mathrm{cm}^2$ [149].

In supercapacitors, current collectors serve to transport electrons to and from the electrode/electrolyte interfaces to charge the cell or supply power to the external circuit. In conventional (monofunctional) supercapacitors and batteries, current collectors double as supportive substrates, onto which the (typically less conductive) active layer is deposited. Continuous metallic foil current collectors are therefore used; however, their mass can be substantial: more than 10% of total mass [150], and could be considered parasitic as they do not contribute to the capacitance.

In SSCs, CAG-modified carbon fibre electrodes have been developed to provide high specific mechanical properties alongside high specific capacitance and electrochemical stability. In contrast to the active layers used in conventional devices, SSC electrodes are self-supported and possess structural integrity; therefore, there is an opportunity to reduce parasitic mass by using current collectors which only partially cover the electrode surface. Consequently, common practice within the research community dictates using a narrow ($\leq$ 2 cm wide) copper strip along one edge of each electrode to provide current collection [20] (Figure 2.4(a)).

However, in the above current collector configuration, the path of charge carriers through the electrode is lengthened, which can negatively impact the cell ESR, especially if the conductivity of the electrodes is poor. Figure 2.4(b) presents the area-normalised ESR of a commercial supercapacitor (BCAP0150 2.7V 150F, Maxwell [149,151]) compared to those of semi-structural SSCs developed at ICL. From the data, it is apparent that:

(i) the normalised ESR of freestanding semi-structural SSC devices is at least an order of magnitude higher than those of off-the-shelf monofunctional systems, contributing to poor power-performance competitiveness;
(ii) the SSC current collector configuration can have a major influence on the cell ESR;
(iii) even for laboratory-scale SSC cells, charge collection inefficiencies increase dramatically with device area (as has been noted elsewhere [148,152,153]), posing a major obstacle to the eventual scale-up of this technology.

Since there are practical limitations to changing the cell materials (at least in the near term), examining the design of current collectors offers opportunities to reduce ESR and parasitic mass, thereby improving overall cell performance.

This line of research is further motivated by the recent demonstration of a screen printing technique for the application of thin (10 μm) current collectors onto carbon fibre structural electrodes used in structural batteries [154]. The screen-printed current collector strips showed similar performance to conventional copper strip collectors. The high dimensional accuracy of this technique [154] could enable the exploration of more complex alternative current collector geometries.

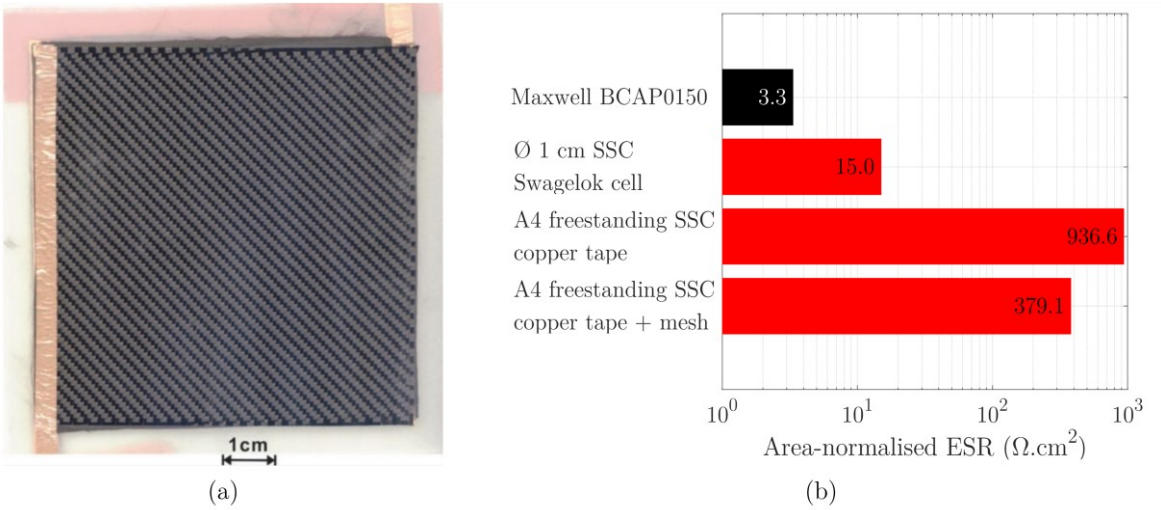

Figure 2.4. (a) Freestanding SSC device with copper strip current collectors [20], and (b) area-normalised equivalent series resistance of a commercial supercapacitor and multifunctional SSC devices (unpublished data by the Group).

2.5.2 Current collector modelling and optimisation

The problem of designing lightweight and power-efficient current collectors for SSCs could be considered analogous to that in solar cells [155–157], where series resistance was originally linked to low energy conversion efficiencies [152]. In that context, area (rather than mass) minimisation is relevant, since shading losses incurred by top contact current collectors must be balanced with resistive losses to maximise energy conversion efficiency [152]. As a result, current collectors with 5–10% area coverage [157] have been developed, which take the form of metallic grids with parallel strips or 'busbar and fingers' grids [155].

For these simple geometries, analytical solutions for the minimum spacing [157] and width [155] of the grid elements have been derived based on the maximum allowable power/voltage loss. It should be noted that these solutions are based on 1D and 2D treatments, which assume idealised current distributions oriented perpendicular to the grid elements, and neglect contact losses and substrate losses in the through-thickness (transverse) direction, both of which are expected to be important in SSCs.

Mitigation of resistive losses through current collector design remains an active area of development for many other electrochemical devices with low conductivity substrates/electrodes, such as fuel cells, electrolysers, and redox flow batteries, where access to reactants/removal of products require a grid current collector. Current collector design has been widely studied both experimentally [152,158,159] and computationally [153,160–162] in relation to laboratory-scale solar cells, fuel cells and water-splitting devices, though these investigations have also been limited to simple geometries, such as parallel strips or simple mesh grids. There is agreement across the experimental studies on the most important factors for electrical performance: the geometric feature size (for example, spacing between metallic strips [160]) and the quality of the current collector electrode contact [148,158]. It should be noted that parasitic mass was not considered in any of these works, therefore there remains a need to link electrical performance to lightweighting issues.

Finite element models have been extensively used in the context of scaling-up water splitting devices [153,160,161], as a means to assess the impact of voltage losses associated with current collection. Analyses were commonly performed over a 2D domain, following one of two approaches. The first approach considers the through-thickness cross-section of the device to be the analysis domain of interest [160], and implicitly assumes that the geometry and boundary conditions are uniform in-plane. The approach is analogous to that

taken in physics-based 1D electrochemical simulations of SCs [163–165] (reviewed in Section 2.6.3.3), and allows the relative resistance contributions from all cell components to be studied. However, due to the implicit assumption of a uniform planar current collector geometry, this type of model is unsuitable for current collector design. Researchers studying lithium-ion batteries, circumvented this problem by coupling a 1D electrochemical model with a 2D current collection model, to study thermal and mechanical stress distributions [166], examining the influence of end tab placement.

The second modelling approach is based on the assumption that the electrode (also referred to as the substrate) is sufficiently thin and conductive to produce a negligible potential drop through-thickness [153], allowing the electrode surface geometry to be exactly modelled in 2D [153,160,161]. However, in real electrochemical devices where electrodes have finite thickness, the current distribution cannot be expected to remain constant through-thickness, particularly for non-uniformly distributed current collectors. Regardless of the approach, the existing research agrees that resistive losses may significantly impair performance, particularly as devices are scaled-up, unless the combined effects of geometry and conductivity are addressed [161].

3D analyses appear to be rare, despite the obvious benefits of increased accuracy and flexibility, but likely due to the computational expense associated with full electrochemical analyses. It is however possible to consider the problem of electric conduction in isolation from electrochemical processes, and this approach has been used in 3D simulations, evaluating the potential of gold grid current collectors in mitigating resistive losses in water splitting devices [162]. This type of analysis appears particularly relevant in the context of SSCs, due to the complex architecture of the carbon fabric electrodes, and the anisotropy in their electrical conductivity [90].

2.5.3 Electrical conductivity characterisation

Since current collection models rely on input data parametrising the conductivities of the cell materials, it is pertinent to review how these can be obtained from standard measurements. The most common method for the measurement of contact and substrate conductivity is the Transmission Line Method [167]. In this method, contact strips are placed across a rectangular substrate at several positions x along its length, as shown in Figure 2.5.

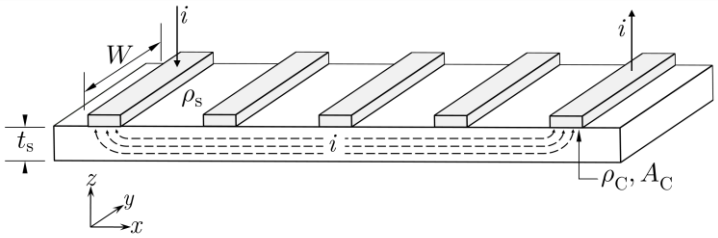

Figure 2.5. Conductive substrate with contact strips, and electric current across them during transmission line resistance measurement.

Current is introduced through the contact strips and the potential drop is measured across contact pairs, allowing the resistance to be calculated. To minimise parasitic resistances, a four-point contact measurement should be used [167]. The measured resistance includes contributions from the substrate and the contact resistances at the contact interfaces:

$$R_{\text{total}}(x) = R_{\text{s}}(x) + 2R_{\text{C}} = \frac{\rho_{\text{s}} x}{W t_{\text{s}}} + \frac{2\rho_{\text{C}}}{A_{\text{C}}} \quad , \tag{2.4}$$

where W is the sample width, t_s is the substrate thickness, and A_C is the area of one contact strip. Eqn. (2.4) assumes (i) negligible current in the transverse (z) direction, and (ii) negligible current in unprobed intermediate contacts. The latter assumption is only strictly true when contact resistivity is higher than substrate resistivity, or when the contact strips have negligible width. The contact and substrate resistivities may then be found by inspection of the y-axis intercept and gradient, respectively, of the plot of R_T against L.

2.6 Electrochemical and multiphysics performance of SSCs

2.6.1 Background

Depending on the dominant mechanism of energy storage, SCs can be classed as:

(i) *Electrochemical Double Layer Capacitors* (EDLCs), which store charge electrostatically,

(ii) *pseudo-capacitors*, which feature additional fast reversible redox (Faradaic) reactions,

(iii) *asymmetric or hybrid capacitors*, which combine storage mechanisms by mixing electrode types [168].

As the majority of SSCs developed within the Group at ICL belong to type (i), this section will focus on the relevant background, using the terms SC and EDLC interchangeably. In EDLCs, energy is stored by the capacitive deionisation of an electrolyte and the subsequent electrostatic adsorption of the mobile ions in the diffuse layer onto the surfaces of the polarised electrodes (Figure 2.6), to counteract their electronic charge [169].

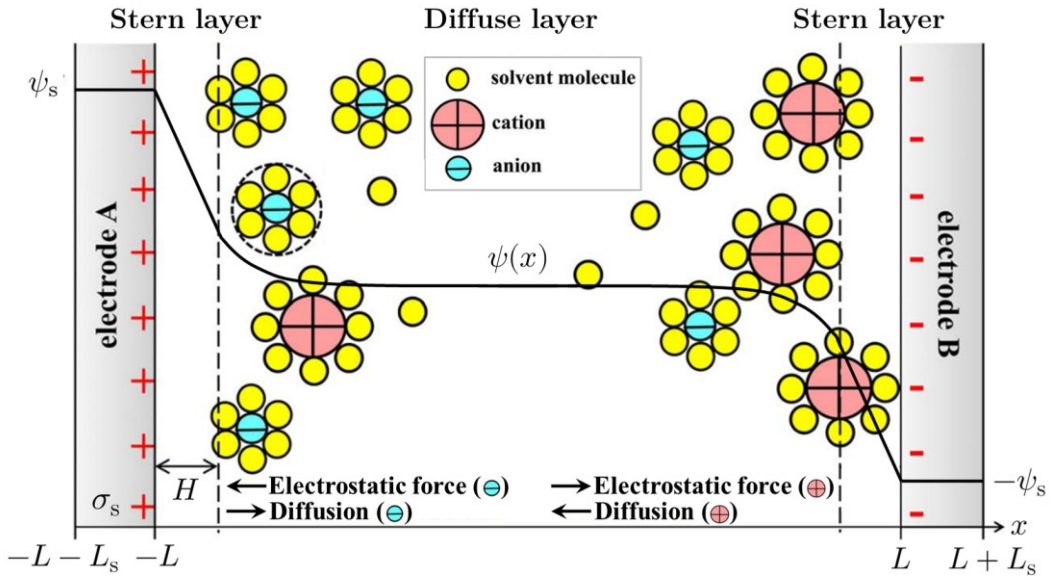

Figure 2.6. Schematic of an EDLC, showing the Stern and diffuse layers (adapted from [165] to show domain boundary labels and boundary conditions).

DL refers to the layer of excess/deficit electrons and counter-ions that is continually accumulated and released at each electrode/electrolyte interface during charge and discharge. The counter charges are separated by a thin dielectric region (Stern layer), generating an electric field, in which electric potential energy is stored. Upon discharge, the ions are desorbed and current flows through the external circuit.

The performance of an EDLC is determined by the composition and morphology of the electrodes, current collectors, separator, electrolyte, and the overall cell design. To maximise electrochemical performance, electrodes should have a high electrical conductivity, large surface area, a suitable pore structure for ion transport and charge storage, and good thermal and chemical stability. Consequently, carbon in its various forms (for example, activated carbon, CNTs, templated carbons, carbon aerogels and graphene [165]) is a commonly used. The separator must be thin and highly porous to minimise the total cell impedance and maximise power density, yet robust enough to prevent short circuits. The ideal electrolyte should have a high ionic conductivity and dielectric constant, a wide potential and temperature window, in addition to safety, low cost and toxicity. Aqueous, organic, and ionic liquid electrolytes have been developed for SCs, each offering distinct benefits and drawbacks.

Since energy storage is achieved by an electrostatic phenomenon rather than an electrochemical reaction [170], EDLCs benefit from fast process kinetics, resulting in greater power density and longer cycle life compared to rechargeable batteries [171].

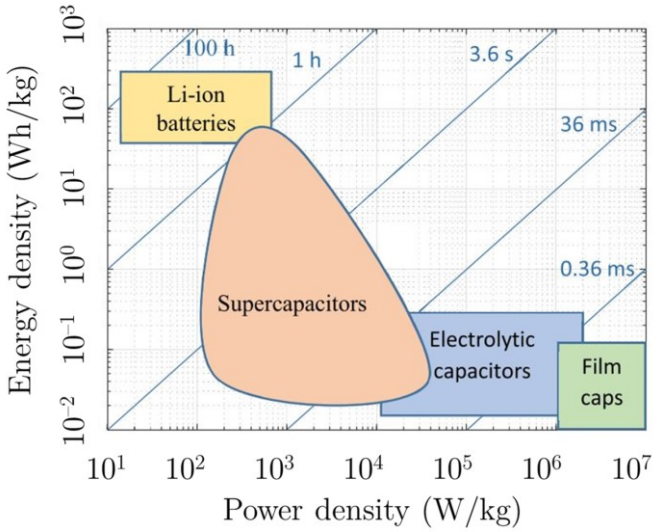

Figure 2.7. Ragone plot for different electrical energy storage systems (cell level performance) [34].

Thanks to the use of high surface area porous electrodes and ultra-thin separators [34], EDLCs usually offer greater energy density, compared to those of conventional electrolytic and dielectric capacitors. SCs thus bridge the performance gap between batteries and conventional capacitors in terms of specific energy and power density (Ragone plot, Figure 2.7). Current state-of-the-art commercial SCs reach energy and power densities (normalised by packaged weight), respectively, on the order of 10 Wh/kg and 10 kW/kg, compared to 100 Wh/kg and 1 kW/kg for batteries [34,171,172].

There has been increased interest in the research and development of SCs in response to the expansion of the EV market, wireless consumer electronics, smart grid management and renewable energy sectors [171]. Common applications of SCs include filtering, AC-DC smoothing, load levelling, emergency power systems, surge power storage, low to high power conversion, and peak or pulse power. When used in conjunction with batteries, fuel cells or combustion engines, SCs can extend their lifetime, while reducing size and weight by relaxing maximum power requirements. In low energy-high power applications, SCs can replace batteries entirely, and are particularly well suited to applications powered by intermittent energy sources, energy harvesting and regeneration [165], and harsh temperature environments, for example, aerospace, oil and gas or renewables [34,173].

Individual SC cells have low voltage ratings, typically below 2.7 V per cell, dictated by the electrolyte stability window. For most practical applications, multiple SC cells must be connected in series to increase the voltage, and/or in parallel to increase total capacitance. Like batteries, they require voltage balancing protection circuits to prevent

degradation and catastrophic over-voltages. Unlike batteries, where the discharge voltage is relatively constant, capacitors and supercapacitors exhibit a voltage drop during discharge and DC-DC converters are required to maintain a steady power output. Further improvements in capacitance and high voltage operation, coupled with a steady decline in prices are expected to contribute to the rapid growth of the supercapacitor market, projected at $5 billion in 2025 [170]. The largest uptake of supercapacitors is expected to be in the transportation sector for engine-starting, burst power for stop-start processes, electrical system augmentation, regenerative breaking, torque augmentation, and hybrid electric drives for mass transit, trucks and electric trains [34,170].

2.6.2 Characterisation

2.6.2.1 Electrochemical characterisation

The state-of-the-art in the architecture and electrochemical performance of ICL SSCs (reviewed in Section 2.2.1) has shown continuous improvements over the last decade (Table 2.4). The electrochemical properties of SCs and SSCs are characterised in the same way, through parameters such as specific capacitance, area-normalised ESR, specific power and energy densities, and Coulombic and energy efficiencies. The most commonly used electrochemical characterisation methods are Galvanostatic Charge Discharge (GCD), Cyclic Voltammetry (CV), and Electrochemical Impedance Spectroscopy (EIS). Details of the methods and data processing are outlined in Appendix A.

An influence of the composite consolidation method (hot-press vs autoclave) and consolidation pressure on energy density has been demonstrated in laminate-type structural capacitors [174]. In that work, a six-fold increase in energy density was achieved by increasing the laminate consolidation pressure from 3.5 bar to 13.8 bar. The performance improvement was attributed to the straightening of the crimp in the woven fabric separators and reduction of void content. For semi-structural ICL SSCs, experimental work has also demonstrated a dependence of electrochemical performance on the pressure applied during tests (unpublished data). For monofunctional supercapacitors, researchers found an important contribution to ESR due to contact resistance between the electrodes and current collectors forms, which was reduced by 40% when a pressure of 2.5 bar was applied [148]. Overall, discussion of pressure dependence in the background literature is rare. To achieve higher power and energy densities, it is imperative that the sources of loss, and the reasons for pressure dependence are identified.

Table 2.4. Reported electrochemical properties of ICL SSCs.

Electrodes	Separator	Matrix	Current collectors	ESR (kΩ.cm2)	Capacitance (mF/g)	Energy density* (mWh/kg)	Power density* (mW/kg)	*Applied voltage (V)	Ref.
C^{CNT}	G	MTM57 / IL + 4.6 M LiTFSI	copper adhesive tape (side strip)	383	10‡	10.1‡	31.5‡	2.7	[20,24]
C^{a}	G	PEGDGE / IL + 0.1 M LiTFSI	copper adhesive tape (side strip)	746	52‡	1.4‡	2680‡	2	[175]
C*	PP	PEGDGE / 10 wt. % IL	copper adhesive tape (side strip)	1.72	603†	0.84‡	32.8‡	0.1	[22]
C*	G	PEGDGE / 10 wt. % IL	copper adhesive tape (side strip)	14.7	71†	0.099‡	3.84‡	0.1	[22]
C*	G	BADGE / 41 wt. % IL	n/a (Swagelok cell)	0.080	212‡	93‡	5200‡	2.7	[47]
C*	G	IL	n/a (Swagelok cell)	0.015	1731‡	1405‡	301000‡	2.7	[47]

C and G refer to as-received biaxial carbon fibre fabric (CF) and biaxial glass fibre fabric (GF), respectively; C* refers to CAG-modified CF; C^{CNT} refers to CNT-grafted CF; C^{a} refers to activated CF; IL refers to EMIM-TFSI; PP refers to polypropylene membrane;
† normalised by electrode mass; ‡ normalised by cell mass; * calculated at applied voltage indicated.

2.6.2.2 Multiphysics characterisation

The mechanical-electrochemical characterisation of SSCs has received relatively little attention. *In situ* GCD measurements have been performed during four point bending tests of a structural composite with SSC interleaves embedded at the compression, tension and neutral planes [43]. Changes in energy density in the tension and compression planes were linked to changes in ESR due to local transverse loads. It was hypothesised that the local load state may also affect the electrolyte infiltration of the electrodes.

Initial failure occurred at interleaf edges, and local buckling of the SSCs plies was observed, however the composite retained 93% and 69% of its power and energy densities, respectively. In follow up work [44], development of extensive delamination between the electrodes and current collectors was identified as the main mechanism of electrochemical degradation under three-point bending. For CNT-based SSCs, tensile testing with *in situ* GCD has linked capacitance degradation to plastic deformation, with failure of the electrochemical functions preceding the complete mechanical failure [41]; however, the exact mechanisms of electrochemical degradation were not identified.

2.6.3 Modelling

2.6.3.1 Electric double layer theories

The structure and properties of the electric double layer, which forms at the electrode/electrolyte interface, has been extensively studied [176]. The theory used most often to describe the structure of the electric double layer is the Gouy-Chapman-Stern model, which expresses the specific capacitance of the double layer as a series combination of those arising in the Stern and diffuse layers, illustrated in Figure 2.6:

$$\frac{1}{C_s^{\mathrm{DL}}} = \frac{1}{C_s^{\mathrm{St}}} + \frac{1}{C_s^{\mathrm{D}}} \quad . \tag{2.5}$$

This expression combines the earlier models of Helmholtz and Gouy-Chapman for the respective layers. In the Helmholtz model, the capacitance C_s^{St} arises due to the separation of the countercharges by the charge-free Stern layer:

$$C_s^{\mathrm{H}} = \frac{\varepsilon_0 \varepsilon_r}{H} \quad , \tag{2.6}$$

where ε_0 is the vacuum permittivity, ε_r is the relative permittivity of the solvent, and H is the Helmholtz (Stern) layer thickness, which is approximated as half the unsolvated ion radius a ($H = a/2$) [169]. This is the simplest capacitance model and neglects the voltage

dependence of capacitance. In the diffuse layer model of Gouy-Chapman, the distribution of charge is governed by diffusion and electrostatic forces, and capacitance is expressed as:

$$C_s^{\mathrm{D}} = \frac{\varepsilon_0 \varepsilon_r}{\lambda_{\mathrm{D}}} \cosh\left(\frac{ze\psi_{\mathrm{D}}}{2k_{\mathrm{B}}T}\right) \quad , \tag{2.7}$$

where z is the charge number, e is the elementary charge, k_{B} is the Boltzmann constant, ψ_D is the potential drop across the DL. λ_D is the Debye length:

$$\lambda_{\mathrm{D}} = \sqrt{\frac{\varepsilon_0 \varepsilon_r k_{\mathrm{B}} T}{e^2 N_{\mathrm{A}} z^2 c_\infty}} \quad , \tag{2.8}$$

where N_{A} is the Avogadro number and c_∞ is the bulk electrolyte concentration. Since the ions were treated as non-interacting point charges, the specific capacitance was overpredicted by the model [34]. A correction for the finite size and packing of ions was later introduced to the above by the Bikerman model [165]. For ionic liquids, which researchers consider to be molten salts, a multilayer model has been proposed to better reproduce the structure of the DL [176].

2.6.3.2 Equivalent circuit models

Equivalent circuit (EC) models aim to represent the overall global behaviour of a supercapacitor cell using resistor-capacitor (RC) circuits of varying complexity. The chosen EC model can provide quick estimates of performance parameters such as impedance and capacitance by applying parameter fitting algorithms to experimental data.

The most basic EC model consists of an ideal capacitor representing DL capacitance, in series with a resistor element (R_{S}, also referred to as ESR) as a lumped representation of the ohmic resistances of the electrolyte and electrode [177]. In the more commonly applied Randles' circuit [178] (Figure 2.8), an additional parallel resistance, R_{P}, representing self-discharge current leakage, and a Warburg impedance element, Z_{W}, representing frequency-dependent diffusion resistance, are connected in parallel with the capacitance. The physical interpretation of the elements has been somewhat inconsistent and has been contested in the literature (as discussed in Refs. [165,179,180]).

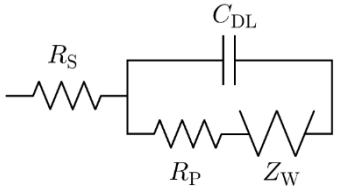

Figure 2.8. Randles' circuit model of an EDLC [178].

Progressive ion diffusion in EDLCs with porous electrodes has been modelled by EC models with multiple RC branches with different time constants [181], or transmission line models [182], as an attempt to more closely resemble the physical structure of the cell. Finally, the high frequency response has been modelled using dynamic models combining series-connected capacitor and RC groups [34].

The common drawback of all EC models is their limited application. They are primarily used to interpret raw experimental data, and can reproduce the results for a given cell under typical electrochemical characterisation methods. However, they cannot extrapolate the response of arbitrary EDLC cells under arbitrary operating conditions, or to provide design rules since model parameters typically have limited direct physical meaning [165,183].

2.6.3.3 Physics-based models of conventional SCs

Until recently, the research and development of EDLCs had been pursued mostly experimentally [165], however there has been a growing interest in the use of numerical simulations as a means to simultaneously drive performance improvements, and to cut down development time and cost by enabling rapid interrogation of the available design space. In contrast to EC models, physics-based continuum models use a detailed description of the complex and coupled interfacial and charge transport processes to compute the local spatial and spatiotemporal distributions of electric potential and ion concentration. Thus, in principle they allow the electrochemical performance of EDLCs to be evaluated without the need for assembling and characterising a physical cell.

Numerous works have simulated the equilibrium [184] and dynamic [169,179] behaviour of EDLCs, performing parametric analyses to understand the influence of key electrode and separator parameters (surface area, thickness, electrode particle radius, conductivity, porosity and tortuosity), electrolyte properties (bulk concentration, permittivity, diffusivity and ion diameter), and cell operating conditions (frequency, current density and voltage window).

Steady-state models

Equilibrium (steady state conditions, corresponding to zero flux) models of EDLCs involve the solution of the Poisson-Boltzmann (PB) equation to compute the charge distribution, from which an estimate of the cell specific capacitance can be obtained.

Poisson's charge conservation equation (obtained from the differential form of Gauss' law $\nabla . \boldsymbol{E} = \frac{\rho_f}{\varepsilon_0 \varepsilon_r}$) governing the potential distribution is stated as:

$$\nabla^2 \psi = -\frac{\rho_f}{\varepsilon_0 \varepsilon_{\mathrm{r}}} \quad , \tag{2.9}$$

where $\mathbf{E} = -\nabla\psi$ is the electric field, ε_0 and ε_r are the absolute and relative permittivities, and ρ_f is the free charge density, given by:

$$\rho_f = \sum_s \; ez_s c_s \quad , \tag{2.10}$$

where e is the elementary charge and s refers to the ion species. Gouy and Chapman combined the above with the Boltzmann distribution $c_i = c_\infty \exp\left(-ez_i\psi/k_{\mathrm{B}}T\right)$ to obtain:

$$\nabla^2 \psi = \frac{2ezc_\infty}{\varepsilon_0 \varepsilon_{\mathrm{r}}} \sinh\left(\frac{ez\psi}{k_{\mathrm{B}}T}\right) \quad , \tag{2.11}$$

where k_{B} is the Boltzmann constant and a symmetric monovalent electrolyte is assumed [165]. The potential distribution may be obtained numerically from the PB equation:

$$\psi = 2\frac{k_{\mathrm{B}}T}{ez} \ln\left(\frac{1 + \exp\, -x\kappa \;\; \tanh\left(\frac{ez\psi_s}{4k_{\mathrm{B}}T}\right)}{1 - \exp\, -x\kappa \;\; \tanh\left(\frac{ez\psi_s}{4k_{\mathrm{B}}T}\right)}\right) \quad . \tag{2.12}$$

For small potentials [164], the Debye-Hückel approximation, $\nabla^2\psi = \lambda_{\mathrm{D}}^{-2}\psi$, may be applied to obtain a closed form solution for the potential. In the modified PB model (MPB) [165], steric corrections (accounting for the finite size of ions) are applied to the charge distribution:

$$\nabla^2 \psi = \begin{cases} 0 & \text{in the Stern layer} \quad , \\ -\dfrac{2ezN_{\mathrm{A}}c_\infty \sinh\left(\frac{ez\psi}{k_{\mathrm{B}}T}\right)}{\varepsilon_0 \varepsilon_{\mathrm{r}} \left(1 + 4a^3 N_{\mathrm{A}} c_\infty \sinh^2\left(\frac{ez\psi}{2k_{\mathrm{B}}T}\right)\right)} & \text{in the diffuse layer} \quad . \end{cases} \tag{2.13}$$

Transient models

In transient physics-based models of supercapacitors, a system of coupled partial differential equations (PDEs, typically 1D) are solved numerically for the electrolyte domain to compute the evolution of electric potential, $\psi(\boldsymbol{x},t)$, and concentration of ion species, $c_s(\boldsymbol{x},t)$ [165,185]. The system of governing equations is referred to as the Poisson-Nernst-Planck (PNP) equations and comprises Poisson's charge conservation equation (Eqn. (2.9)), the mass conservation equation, and the Nernst-Planck equation governing ion transport [164,183]. The Nernst-Planck equation states that, in a dilute electrolyte, in the absence of bulk fluid motion, the flux (expressed in vector form) of the ion species s, $\boldsymbol{N}_s$, is given by:

$$\mathbf{N}_s = -D_s \nabla c_s - z_s u_s F c_s \nabla\psi \quad , \tag{2.14}$$

where D is the diffusivity, z is the valence, u is the mobility, F is the Faraday constant. The first term on the right-hand side of Equation (2.14) corresponds to diffusion flux (Fick's law) and the second to electrostatic migration (electromigration). For dilute solutions, the ion mobility is proportional to its diffusivity and is given by the Nernst-Einstein relation [186]:

$$u_s = \frac{D_s z_s}{RT} \quad , \tag{2.15}$$

where R is the gas constant and T is the temperature.

Finally, the mass conservation statement governing the concentration of ion species reads:

$$\frac{\partial c_s}{\partial t} = -\nabla \cdot \mathbf{N}_s \quad . \tag{2.16}$$

The electrolyte current density due to the flow of ions, **J**, is expressed as:

$$\mathbf{J} = -F \sum_s z_s \mathbf{N}_s \quad . \tag{2.17}$$

The electric potential in the electrode domain is governed by Ohm's law and charge conservation:

$$\nabla \cdot \left(\sigma_{\mathrm{e}}^{\mathrm{E}} \nabla \psi \right) = 0 \quad , \tag{2.18}$$

where $\sigma_{\mathrm{e}}^{\mathrm{E}}$ is the electrical conductivity of the electrode material. The simultaneous Eqns. (2.9), (2.10) and (2.14) are coupled and must be solved numerically. If the current collector is considered explicitly, its potential is also governed by Eqn. (2.18), with conductivity $\sigma_{\mathrm{cc}}^{\mathrm{E}}$.

In the PNP model, ions are treated as non-interacting point charges and the Stern layer is neglected. This assumption leads to an overprediction of the surface concentration and capacitance, limiting the validity of this model to dilute electrolytes and low surface potentials. In the modified PNP model (MPNP) [165,183], a correction has been proposed to account for steric effects (that is, the finite size of ions and the presence of the Stern layer) thereby extending its validity. In this case, the Poisson's equation (Eqn. (2.9)) is rewritten as:

$$\nabla^2 \psi = \begin{cases} 0 & \text{in the Stern layer} \quad , \\ -\dfrac{\rho_f}{\varepsilon_0 \varepsilon_{\mathrm{r}}} & \text{in the diffuse layer} \quad . \end{cases} \tag{2.19}$$

It follows that the electric potential profile in the Stern layer is linear. Additionally, assuming a symmetric monovalent electrolyte containing ion species with identical diameter and diffusion coefficient, a correction term is added to the transport equation (Eqn. (2.14)):

$$\mathbf{N}_s = -D\nabla c_s - z_s u_s F c_s \nabla \psi - \frac{D N_{\mathrm{A}} a^3 c_i}{1 - N_{\mathrm{A}} a^3 \left(c_1 + c_2 \right)} \nabla \left(c_1 + c_2 \right) \quad . \tag{2.20}$$

In 1D, the Poisson's equation (Eqn. (2.9)) in the PNP model is a second order PDE in space, requiring two boundary conditions each for the potential and ion concentrations. At the electrode/current collector interface, a zero-ion flux boundary condition is prescribed. The electric potential boundary condition takes the general form:

$$\psi\ -L-L_{\mathrm{s}},t\ =\psi_{\mathrm{s}}(t)\quad \text{and}\quad \psi\ L+L_{\mathrm{s}},t\ =-\psi_{\mathrm{s}}(t)\quad . \tag{2.21}$$

Its exact form depends on the experiment being simulated, such as CV, EIS or GC, outlined in Appendix A.1. For further detail on boundary conditions, see Appendix A.2. Zero electric potential and uniform bulk concentration are typically assumed as initial conditions:

$$\psi\ x,0\ =0\ \ \text{and}\ \ c_s\ x,0\ =c_{s,\infty}\quad . \tag{2.22}$$

Derivation of the finite element formulations of the PNP and MPNP models for EDLCs in 1D and 2D have been described by Lim [164]. That work showed that the presence of the Stern layer must be included for accurate numerical predictions of electric double layer capacitance and energy density. Explicit modelling of the Stern layer can result in computationally expensive meshes, therefore alternative boundary conditions have been established to account for this layer, whilst simplifying the computational domain [187]. In addition to steric corrections in the modified PNP model [165], porous electrode (Appendix A.3) and concentrated electrolyte solution theories [186] have been developed to extend model validity.

Models for hybrid asymmetric electrochemical devices, such as lithium ion capacitors, have also been developed, which could be of relevance to the future design of hybrid structural power composites. In these models, separate charge storage mechanisms are assumed in each electrode [163,188].

Physics-based models are typically used to simulate standard electrochemical experiments, for comparison with real cells and estimation of performance parameters such as specific capacitance, time constant, impedance and frequency response. Due to their complexity and cost, transient analyses have been typically restricted to 1D [179,189], pseudo-1D models with a spherical particle domain [169], and simple 3D cell geometries [190]. These models have been useful not only in identifying the key design parameters and rules for EDLCs, but also in supporting the physical interpretation of standard electrochemical characterisation data [179].

The physics-based models described above are based on continuum theory and do not explicitly model interactions at the atomic level. Much finer atomistic level structures in

the charge density field can be resolved by molecular dynamics and density functional theory models, which simulate the motion and interactions of systems composed of individual atoms or groups [171]. Although these simulations are limited to short length and time scales, molecular dynamics calculations of transport properties and double layer dimensional properties can be used to parametrise volume averaged models, such as the modified PNP model, and good overall agreement has been demonstrated between the two modelling approaches [191].

2.6.3.4 Multiphysics models

No multiphysics models of structural supercapacitors exist yet. This section will briefly review multiphysics models used to study of monofunctional supercapacitors, as well as multifunctional composites with piezoelectric or electrochemical energy storage functionalities.

In monofunctional supercapacitors, heat dissipation arises due to the intrinsic resistance of the cell materials (irreversible) and ordering of ions in the DL (reversible) [192]. Excessive heating should be avoided in SCs as it can lead to thermal stress and expansion, self-discharge, accelerated ageing, and overvoltage damage in packs [147]. Electro-thermal models based on system-level [192–194] and physics-based [147] approaches have been developed to predict heat generation in SCs and inform thermal management strategies. As present, the effects of thermal expansion and mechanical loading on the electrochemical response of SCs have not been numerically investigated, though efforts to investigate these issues have recently been made in the context of lithium-ion batteries [195,196].

Progress has been made in modelling the behaviour of piezoelectric [197–199] and structural battery composites [200–203]. A sequentially coupled electro-mechanical model of CNT/polymer composites was recently implemented in Abaqus FEA by Matos *et al.* [199]. Inclusion of electrical tunnelling conduction across adjacent CNTs was achieved through a user element subroutine (UEL), enabling simulations of the changes in effective resistance in response to elastic deformation. In mesoscale models of woven piezoresistive composites, the effect of damage on the electrical response was simulated based on the electro-elastic constitutive equations combined with stress-based failure criteria.

In embedded batteries [201] and structural micro-batteries [200,203] coupled mechanical-electrochemical models have been developed to analyse the effects of ion intercalation, heat generation and mechanical load. In the former, porous electrode theory and concentrated electrolyte theories were employed in a one-dimensional battery model, whilst in the latter 2D microcomposite models were implemented in the COMSOL FEA suite [202]. A similar methodology was also used to simulate intercalation induced matrix and interface cracking in structural micro-batteries [202].

These works indicate that similar methodologies could be applied to analyse the coupled mechanical-electrochemical response of structural supercapacitors, though the complex three-dimensional architecture of these devices may present additional challenges to model development.

3 Research plan

3.1 Research gaps and motivation

Phase 1: Compaction modelling and characterisation

As discussed in Section 2.3.1, reinforcement compaction has important implications for the mechanical properties of fabric-reinforced composites. For multifunctional SPCs, the level of compaction also influences electrochemical performance parameters such as equivalent series resistance, and hence power density and energy density [44], through its effect on the electrode and separator thicknesses, and the contact resistance at the electrode/current collector interface [148]. These relationships are yet to be quantified in the context of SSCs. Previous SSC studies have suggested that interply hybridisation may disrupt efficient fibre packing in the preform stack [48], however no further analysis has been presented.

The impact of CAG modification on the compressibility and final morphology of SPCs is also not yet understood. From research into CNT-modified carbon fibre fabrics [204,205] it could be hypothesised that compressibility will be hindered in the CAG-modified fabric, with potential detrimental effects on the mechanical properties and power performance of multifunctional composites. Previous research at ICL appears to support this hypothesis as the fibre volume fraction of CAG-modified SSC laminates manufactured was consistently lower than that of laminates using as-received fabric (ca. –5% absolute difference) [22]. An experimental investigation of the compressibility of SSC reinforcements is therefore needed.

The accuracy of numerical predictions of the mechanical and electrochemical performance of SPCs will rely on realistic geometric representations of their internal geometry. Compaction simulations have been demonstrated as effective pre-processing tools for the generation of realistic FE models [116]. Hybrid woven stacking sequences have not received attention in mesoscale fabric modelling, despite intensive research in this area (Section 2.3.2). Multilayer compaction models [56,57,70] have been restricted to mono-fabric (hereafter referred to as monolithic) stacks, perhaps due to the difficulty in applying the UC modelling technique to more complex stacking sequences. A lack of simulation tools

has also hindered investigations of the performance of hybrid WFRCs in both conventional structural and multifunctional applications. Development of mesoscale compaction models for hybrid fabric stacks will therefore be helpful in the study of their compressibility and final morphology. Modelling the latter will be relevant for later structural analyses of SSCs.

Phase 2: Mechanical modelling and characterisation

It is evident from the review of the state-of-the-art in SSCs (Section 2.2) that a combined experimental-computational approach has great potential to accelerate the development of SSCs with improved mechanical properties. By enabling rapid and systematic virtual testing, predictive models could significantly reduce the experimental burden and timescales for technological advancement.

A review of previous efforts to model the mechanical response of SSCs (Section 2.4.2) has shown that research has been largely focused on constituent-level modelling of structural electrolytes [108,109] and analysis of the stiffness-conductivity tradeoff. These works have provided valuable insights to matrix developers, however, only limited conclusions about the performance of SSCs at higher length scales (for example, device- or component-level) can be drawn from their findings. On the other hand, the only available device-level mechanical model of SSCs [115] has been of limited utility as it is unable to make direct performance predictions. Due to a lack of data on the mechanical properties of the structural electrolyte and CAG, the model relies on device-level experimental data for material parameter calibration, and neglects the presence of CAG, despite clear indications in the literature of the importance of the latter.

It is these unique constituents and architecture (reviewed in the previous Chapter), which distinguish SSCs from structural battery composites, for which models have been recently developed [206–208]; and from conventional structural composites, for which mechanical models are widely available. These laminate features complicate not only the prediction of mechanical performance, but also the interpretation of experimental results. Recent tensile and in-plane shear experiments SSC laminates [47] have reported a lack of improvement in the elastic moduli, alongside considerable reductions in tensile strength and shear strain to failure of CAG-modified composite laminates, even when used alongside a structural epoxy matrix. These findings were contrary to previous reports of a stiffening effect associated with CAG [24,209], indicating that current understanding of the mechanical behaviour of SSCs is incomplete (Section 2.4.1). These experimental results

provide both a motivation for the development of predictive device-level models, and an opportunity to validate them. Detailed microstructural and fractographic characterisation of the tested laminates could uncover new information about their microstructure, which could support model development.

It is imperative that the lack of experimental data on the material properties of CAG used in SSCs is addressed to enable the model development. Nanoindentation (Section 2.4.1) stands out as an attractive technique for the characterisation of the elastic properties of CAG, since it can be used on relatively small specimens, which are more likely to survive specimen preparation [78], and in which the probability of critical defects is lower, reducing the likelihood of premature failure during the tests. Anticipated challenges in the preparation of specimens with fibre orientations parallel to indentation direction (Section 2.4.1), and risk of damage during machining, motivate the use of monolithic CAG samples for these experimental measurements.

Mesoscale fabric stack compaction simulations (Section 2.3.2) could be used to generate realistic finite element device-level models to enable more accurate prediction of the linear and non-linear mechanical response [210,211] of SSCs. By explicitly representing the complex composite architecture of SSCs, mesoscale models would improve on previous work, which employed geometric idealisations through the method of cells [115]. It is envisaged that the predictive capability of the models could be validated against the recent experimental data [47]; and that the models could be used to:

(i) examine the effects of constituent properties on properties at higher length scales;
(ii) help explain the apparent contradictions in the reported effects of CAG modification;
(iii) identify the factors presently limiting SSC performance, to drive improvements.

Such predictive methods represent an important step toward the timely and successful deployment of SSCs, as structural analysis of digital twins is expected to play an essential role in the design and certification of multifunctional components.

Phase 3: Current collection performance analysis

The gravimetric mechanical properties and power density of the SSCs developed by the Group at ICL is presently limited by high internal resistance and parasitic weight (Section 2.5.1). Despite recognition that the spacing and geometry of copper current collectors is fundamentally determined by the in-plane conductivity of the electrodes and

the active current densities generated [16], a careful design of the current collector configuration is yet to be carried out; however, there are clear indications that power performance may have been severely limited as a result of neglecting to optimise current collection (discussed in Section 2.2.2).

The mass of non-optimised metallic current collectors can have further detrimental impact on gravimetric mechanical and electrochemical performance. The high conductivity and electrochemical stability of metallic foils traditionally used as current collectors come at the cost of density: 5.8 and 1.7 times that of carbon fibre, for copper and aluminium, respectively [212]. A material breakdown analysis of a Li-ion plug-in hybrid electric vehicle battery pack [150] found that the metallic current collectors were responsible for about 14% of the overall cell mass. A similar analysis of the BCAP0150 commercial supercapacitor [149], found the mass fraction in that system to be about 10%. In a recent demonstrator application of SSCs (a composite C-beam) developed by the Group (unpublished work), current collectors accounted for 16% of the packaged cell mass, and the ratio of current collector to active materials (including two electrodes, separator and matrix filling the pores) was 53%.

Clearly, to maximise the light-weighting benefits afforded by the concept of SSCs, the tradeoff between internal resistive losses and parasitic mass must be considered. Such a tradeoff has not been of concern to developers of conventional batteries and supercapacitors, since in those devices continuous metallic foils are used simultaneously as supportive substrates for the active materials and as current collectors [150]. It is worth noting that, with the increasing adoption of electric vehicles, factors such as parasitic mass, material cost and sustainable resource use are expected to rise in importance in the near term. Analogous mass-performance tradeoff problems can nevertheless be found in related fields, such as solar cell and water splitting devices (as reviewed in Section 2.6.2).

The design of mass- and power- efficient current collectors for structural supercapacitors could be addressed through numerical direct current conduction models. Considering the aligned architecture of the carbon fabric electrodes, their substantial thickness, and the need to determine the current distribution across the cell area, it seems appropriate to model this system as a fully three-dimensional domain. The implementation of such a model within a finite element package would be relatively fast, flexible, and inexpensive. By automating the model generation process, current distributions and heat

dissipation contributions could be rapidly evaluated for a variety of current collector and cell geometries and operating conditions, enabling the identification of successful strategies for the mitigation of resistive losses. This approach would allow the exploration of current collectors, which are more geometrically complex or have a greater number of hierarchy levels than typically studied geometries (Section 2.6.2).

Geometries of potential interest include several families of space-filling fractal grids, which have been previously studied in the context of turbulence enhancement [213]. These grids are expected to perform well in the present application, since their hierarchical network architecture could be leveraged to achieve efficient current collection with a minimal amount of current collector material. Finally, new strategies for improving the contact properties between the electrodes and current collectors, such as selective masking of designated areas during the manufacture of CAG-modified fabric electrodes (Section 2.2.1), could be assessed through experimental and numerical studies. At present, current collection issues have received limited attention in the context of structural power [154]; therefore, this work could be a valuable contribution to the wider research community. The findings could be of relevance to other energy storage applications where lightweighting is desirable, for instance, EV or drone battery packs.

Phase 4: Electrochemical and multiphysics modelling

In contrast to purely electrochemical devices, where structural integrity is important only in so far as safety and lifetime are concerned, structural load bearing is a fundamental requirement for SPCs. This structural requirement presents an additional dimension to the design problem, requiring the conciliation of the often antagonistic and/or coupled mechanical and electrochemical performance objectives [24] (Section 2.2.2). The size and complexity of the design problem makes it impractical to rely on experimental research alone, and calls for a combined experimental-numerical approach.

It has also been recognised that a holistic approach to modelling and designing SSC must be established, and that simulation packages and material databases must evolve to meet the demands of multifunctional design [25]. A segregated approach to the analysis of mechanical and electrochemical behaviour carries a risk of slow and inefficient progress, as a result of contradictory design recommendations obtained from the individual analyses. Therefore, a long term aspiration for research in this field is the development of an

integrated multiphysics modelling framework for the analysis of multifunctional performance.

Such a framework would significantly reduce experimental burden and development time by enabling the identification of promising design strategies early on. In the long term, the availability of predictive multifunctional models will be essential to the commercial deployment of SSCs in aviation, where physical verification of components and aircraft is being progressively replaced by virtual tests [214]. With these end users in mind, it is prudent to implement multiphysics analysis capabilities within existing software packages, which the key players in the aviation industry recognise as part of their practice, such as Abaqus FEA [215]. This software already supports coupled thermal-electrical-structural analyses; however, elements are not yet available for ion transport simulation. Such an element could be implemented through a user-defined element subroutine, similar to the recent work of Matos *et al.* [199] (Section 2.6.3.4).

3.2 Thesis scope

The overarching aim of this thesis is to establish predictive tools, based on the finite element method, for the mechanical, electrical, and electrochemical behaviour of SSCs, and to use these to complement experimental efforts to advance multifunctional performance.

Following the review of the literature (Chapter 2), a research plan consisting of four Phases was identified (outlined in Section 3.1). Phase 1 (Chapter 4) focuses on the experimental characterisation of the compressibility of the fabrics used in SSCs, and the development of a mesoscale model for the compaction of hybrid multilayer fabric stacks. Phase 2 (Chapter 5) draws on the outcomes of Phase 1 and focuses on the development of a realistic mechanical model of SSCs, with which the effects of the constituent materials and the presence of defects on the composite elastic properties are evaluated. Detailed microstructural characterisation of SSC laminates is used to inform model development and experimental interpretation. In Phase 3 (Chapter 1), the influence of current collection on the multifunctional performance of SSCs is investigated through experimental conductivity characterisation and electrical simulations, with the aim of identifying more efficient current collector designs. Finally, Phase 4 (Chapter 7) details the development of a user element subroutine for the Abaqus FEA suite to enable simulations of ion transport in SSCs.

The models developed towards these Phases serve as valuable new tools for the analysis of SSC performance and complement experimental research to accelerate their deployment.

3.3 Thesis outline

The remainder of this thesis comprises four technical chapters, outlined below, addressing each of the aforementioned aspects of predictive modelling for SSCs. The results presented in these chapters are discussed in detail in Chapter 8, drawing connections across the different Phases, and contrasting the findings with the background literature. In Chapter 9, the conclusions of this thesis are summarised. Its implications and recommendations for future work are discussed in Chapter 10.

Chapter 4 Compaction analysis and prediction

In Chapter 4, the compressibility of the carbon and glass woven dry fabrics used in SSCs, as well as multilayer stacks of these fabrics, is characterised in out-of-plane compression experiments, using a direct thickness measurement method. The effect of CAG modification on compressibility is likewise quantified. A new mesoscale finite element model for the compaction of hybrid multilayer fabric stacks is proposed, considering periodic unit cells with different ply offsets. A non-linear elastic constitutive model is implemented for the yarns, which is calibrated from the single layer experimental data. The multilayer model predictions are validated against the experimental data, and optical and X-ray μCT microstructural observations. The model is intended to provide information about the compacted geometry and attainable fibre volume fraction of hybrid multilayer stacks and serves as a pre-processor for the generation of realistic unit cell models of SSCs.

Chapter 5 Mechanical performance analysis and prediction

In Chapter 5, a new finite element model for the prediction of the mechanical response of SSC laminates is developed. The model considers quasi-mesoscale unit cells with different ply offsets, which are generated from the compaction simulations (Chapter 4) via a novel geometry reconstruction algorithm. To support model development, for the first time, nanoindentation is used to characterise the elastic modulus of monolithic CAG, and detailed microstructural characterisation of untested SSC laminates is performed using optical, scanning electron and X-ray μCT imaging. The mechanical model is used to perform virtual tests, which isolate the effects of CAG modification, structural electrolyte, and

defects on the elastic behaviour of SSCs. In conjunction with the micrographs, the numerical predictions of elastic properties are compared with experimental data from the literature. Experimental findings on the longitudinal tensile failure properties of CAG-modified laminates are reexamined, with the help of additional fractographic analysis, and in light of the background literature.

Chapter 6 Current collection performance analysis and prediction

In Chapter 6, the key conductivity parameters governing the electrical power dissipation due to internal resistance in the structural electrodes and current collectors in SSCs are identified and characterised. A new three-dimensional model of electrical charge transport is developed based on the experimental data. Models considering various current collector geometries are used to analyse the tradeoffs between resistive power losses and parasitic mass across a range of system parameters, including device area. The numerical studies are used to identify current collector designs, which simultaneously minimise resistive power losses and current collector mass. The predictions of the total area-normalised resistance are compared with experimental data from Swagelok cell and A4 sized freestanding SSC devices.

Chapter 7 Electrochemical and multiphysics modelling

In Chapter 7, an original ion transport simulation workflow is proposed to introduce new multiphysics capabilities within the Abaqus FEA software suite, which are relevant to SSCs. A user element subroutine is developed based on the governing equations for ion transport in supercapacitors, guided by the software documentation. A two-dimensional ion transport element is implemented via a FORTRAN subroutine, which is called in a reconfigured combined thermal-electrical analysis procedure. Initial testing of the simulation workflow is performed to guide future development efforts.

4 Compaction analysis and prediction

4.1 Introduction

There is, at present, a lack of understanding of the effects of carbon-aerogel modification of carbon fibre fabric electrodes, and the hybridisation of structural electrode and separator fabrics, on the final geometry and fibre distribution of structural supercapacitor composites. This chapter addresses the knowledge gap through experimental and computational compaction studies, with the following aims:

- to experimentally determine the effects of hybridisation and carbon aerogel-modification on the compaction response of multilayer stacks combining the glass and carbon dry woven fabrics used in structural supercapacitors;
- to develop a compaction finite element model, applicable to structural supercapacitors and other hybrid woven fabric-reinforced composites, to predict the compacted mesoscale geometry and fibre distribution of the fabrics.

The chapter is organised as follows: Section 4.2 details the experimental characterisation of the compressibility of the dry fabric reinforcements used in structural supercapacitors, and imaging of a hybrid woven laminate. Sections 4.3 presents the two-step development of the compaction model: firstly, a unit cell model of each fabric ply was constructed, in which the yarn constitutive behaviour was governed by a non-linear relation calibrated using the obtained experimental data. These constitutive relations were subsequently used to simulate the compaction behaviours of monolithic and hybrid stacks of these fabrics. An original hybrid unit cell was proposed to model the latter. Section 4.4 compares the model predictions with the experimental compaction results and the microstructural observations. The main findings of these studies are summarised in Section 4.5, and later discussed in Chapter 8. An additional outcome of this work is the generation of realistic geometric models of the fabric stacks, which can serve as a starting step for the development of accurate mechanical and electrochemical models of structural supercapacitors, and other composites with a similar architecture.

4.2 Materials and characterisation methods

4.2.1 Mechanical characterisation of fabric compressibility

Three different fabrics were used in this study, including two as-received fabrics: a 200 g/m² conventional carbon fibre plain weave (C-WEAVE™ 200P 3K HS, Chomarat [216]) made with Toray FT300B carbon fibres, and a finer, thinner 53 g/m² spread tow glass fibre plain weave (1086, Gividi Fabrics srl [217]) made with E-glass fibres, and a CAG-modified version of the carbon fibre plain weave (ca. 230 g/m², 15.1 wt. % CAG). The CAG modification process was outlined in Section 2.4.1.

This choice of materials was motivated by their use as the electrode and separator reinforcement in SSCs investigated by the Group [47]. Specimen nomenclature is introduced here to refer to single plies (monolayers) of the carbon and glass fabrics as C and G, respectively, while the CAG-modified carbon fabric is referred to as C*. Surface scans of the fabrics C and G are shown in Figure 4.1(a) to (c) and the fabric specifications are presented in Table 4.1.

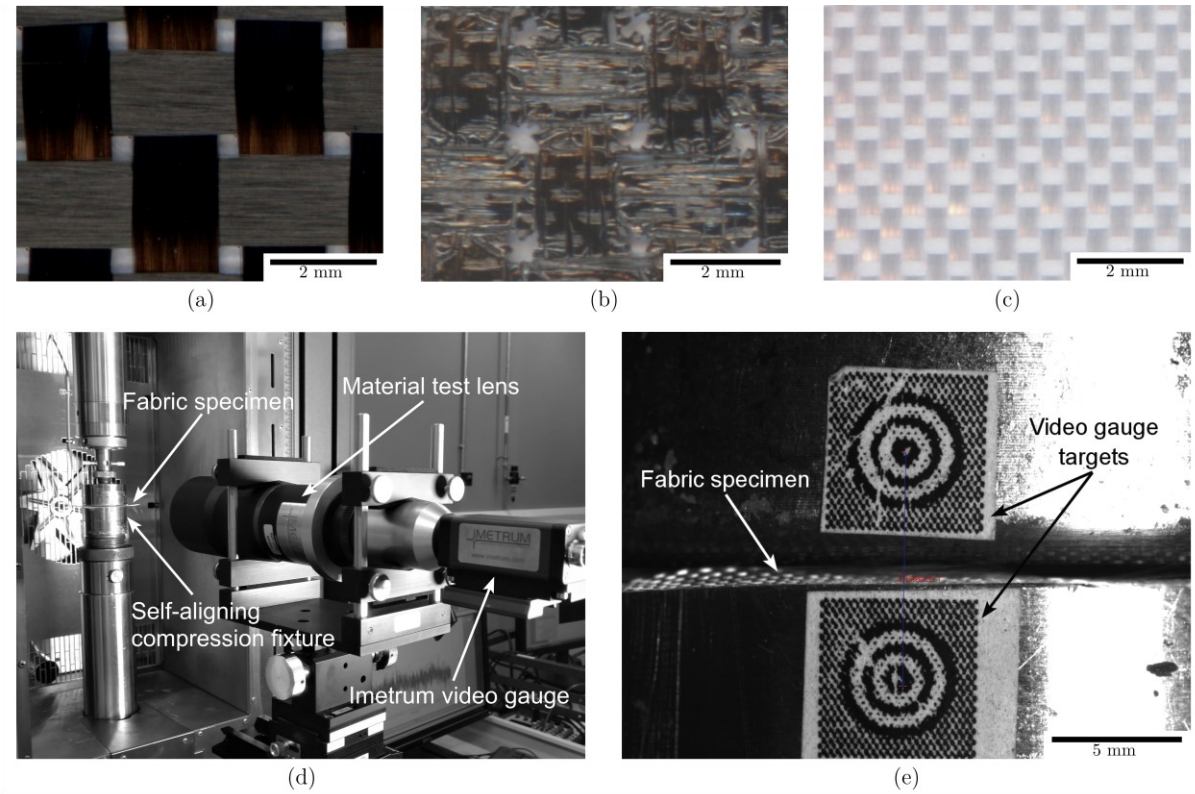

Figure 4.1. Surface scans of the fabrics (a) C, b) C* and (c) G; (d) out-of-plane compression test setup; (e) video gauge image capture.

Table 4.1. Fabric specifications [216,217].

Fabric	Weave	Areal mass (g/m^2)	Fibre type	Fibre modulus (GPa)	Fibre density (g/cm^3)	Filaments /yarn
Carbon, C	Plain	200	FT300B (PAN)	230	1.75	3000
Glass, G	Plain	53	E glass	71	2.55	200
CAG/Carbon, C*	Plain	230	FT300B (PAN)	230†	1.75†	3000

† indicates assumed value.

Table 4.2. List of compression specimens.

Code	Number of fabric layers	Fibre mix	Stacking sequence	Number of specimens
C	1	–	$[0^\circ_C/90^\circ_C]$	6
G	1	–	$[0^\circ_G/90^\circ_G]$	6
CC	2	Monolithic	$[0^\circ_C/90^\circ_C]_2$	6
GG	2	Monolithic	$[0^\circ_G/90^\circ_G]_2$	6
CG	2	Hybrid	$[0^\circ_C/90^\circ_C/0^\circ_G/90^\circ_G]_T$	6
CGC	3	Hybrid	$[0^\circ_C/90^\circ_C/0^\circ_G/90^\circ_G / 0^\circ_C/90^\circ_C]_T$	6
GCG	3	Hybrid	$[0^\circ_G/90^\circ_G / 0^\circ_C/90^\circ_C/0^\circ_G/90^\circ_G]_T$	6
C*	1	–	$[0^\circ_{C^*}/90^\circ_{C^*}]$	3
C*GC*	3	Hybrid	$[0^\circ_{C^*}/90^\circ_{C^*}/0^\circ_G/90^\circ_G / 0^\circ_{C^*}/90^\circ_{C^*}]_T$	3

The compressibility experiments were performed by applying out-of-plane compressive load to fabric specimens via parallel platens. Parallelism between the platens was ensured by using a two-part 50 mm diameter self-aligning compression fixture with a spherical seating (Figure 4.1(c)). Specimens with dimensions 60×60 mm were cut from the fabrics and placed centrally on the fixture. In addition to the monolayer specimens, C, G and C*, the compressibility behaviour of multilayer specimens with the following stacking sequences were studied: C2, G2, CG, GCG, CGC and C*GC* (Table 4.2). The hybrid CGC and C*GC* stacks were of particular interest in this work, reflecting the architecture of electrochemical SPCs.

All specimens were inspected for uniformity and alignment before testing and care was taken to ensure good alignment of the fibre directions. However, it was impossible to eliminate all misalignments; some fabric shear and/or ply misalignment (ca. < 2°, estimated from the minimum angle of misalignment resolvable by the naked eye) was likely to have still been present. The test was performed on an Instron 5969 universal testing machine fitted with a 50 kN load cell, calibrated within –0.25% error in compression in the 0.5 to 2 kN force range. The experiments were performed in displacement-control at a rate of 1 mm/min, used in previous studies [61]. The specimens were loaded up to a pressure of 1

MPa, corresponding to an applied force of about 2 kN, and immediately unloaded by returning the crosshead to its initial position. The specimens were loaded only once, and the first compression cycle was taken to represent realistic forming conditions. Irreversibility during subsequent loading-unloading cycles was not considered in the computational part of this work, however cycling data was nevertheless gathered and analysed for information purposes (Appendix C.1). At least six specimens were tested per stacking sequence for specimens containing the as-received C and G fabrics only, and three specimens were tested for specimens containing the C* fabric.

The vertical distance between the platens was recorded (Figure 4.1(d)) by an Imetrum Video Gauge system. A General Purpose Lens (ISM-LENS-GP006, 50 mm focal length, 0.12 μm typical displacement resolution, with 80 pixels equal to 2.0 mm) or a Material Test Lens (IMT-LENS-MT051, 0.394 magnification, 190 mm working distance, 0.070 μm typical displacement resolution, with 80 pixels equal to 1.1 mm), both from Imetrum Ltd, was fitted to the camera (IMT-CAM027) depending on the total thickness of the specimen. This optical measurement method eliminated the need for any additional machine compliance calibrations (discussed in Section 2.3.1). The calculation of the total fibre volume fraction at a given applied pressure, $V_{\mathrm{f}}^{\mathrm{total}}(p)$, was adapted from [57] for hybrid fabric stacks,

$$V_{\mathrm{f}}^{\mathrm{total}}\ p\ = \frac{1}{t\ p}\left(\frac{n_{\mathrm{C}}\ m_{s,\mathrm{C}}}{\rho_{\mathrm{C}}} + \frac{n_{\mathrm{G}}\ m_{\mathrm{s,G}}}{\rho_{\mathrm{G}}}\right) \quad , \tag{4.1}$$

where $t(p)$ is the specimen thickness (defined as the vertical distance between the platens) at the applied pressure p, n is the number of fabric layers, m_s is the fabric areal mass, ρ is the density of fibres and additional subscripts C and G refer to the respective fibre type.

4.2.2 Imaging techniques

Optical microscopy was used for the geometric characterisation of C and G in their undeformed state. The samples were prepared by casting pieces cut from the fabric in polyester casting resin/hardener system (KLEER-SET 11 10 82/9, MetPrep Ltd), taking care to align the fabric orientation with the through thickness sample direction. The surface of the cast specimens was polished following cure, with 0.006 μm Silica particles used in final polishing step. Cross-sections with approximate widths of 20 mm were prepared along both the warp and weft directions for each fabric and imaged in a Zeiss Axio Imager.M2m optical microscope.

Both optical microscopy and μCT were used to qualitatively evaluate the geometry of the CGC model. A CGC composite panel was manufactured by resin infusion under flexible tooling using epoxy resin containing bisphenol A diglycidyl ether monomer with isophorone diamine hardener (Sigma-Aldrich, GB) in a 4:1 weight ratio [218]. The panels were cured according to the manufacturer's instructions. A diamond wire saw was used to cut samples for imaging from the cured panel. For optical microscopy, five samples with in-plane dimensions of 20×20 mm were prepared using the procedure described above.

For μCT imaging, three samples with approximate in-plane (xy) dimensions of 10×10 mm were stacked in the through-thickness (z) direction and secured with tape. The scan was performed at the National Composites Centre, GB using a Nikon X-Tek 320 kV electron beam machine. During the μCT scan, X-rays generated by an X-ray source were transmitted through the sample to a detector, which recorded their intensity. A series of planar X-ray projection images (radiographs) were collected during one rotation of the specimen, allowing cross-sectional slices to be later reconstructed.

The beam voltage and current used in the scan were 60 kV and 103 μA. The voxel size was 6.065 μm with 3141 radiographs acquired during one full rotation. The Metris CT Pro software was used to generate a volume reconstruction from the radiographs using a filtered back-projection reconstruction algorithm. Additional manipulation, segmentation and visualisation was performed in VG Studio Max 2.1 and Avizo 9.4. The results are discussed in Section 4.4.2.

4.3 Compaction model development

4.3.1 Monolayer fabric compaction model

4.3.1.1 Geometric model

In mesoscale fabric modelling [66], the individual fibres and their interactions are not modelled discretely. Instead, the yarns are treated as solid continua with homogenised material properties that are isotropic in the plane of the yarn cross-section. It should be noted that the resulting stress-strain fields within the yarn should not be interpreted as those at the microscale. It is assumed that the yarns' local shape, spacing, contact interactions, fibre orientation and fibre volume fraction are sufficient to represent the mechanical and kinematic behaviour of the fabric. This modelling approach was used in the present model and the following commonly applied geometric assumptions were adopted:

(i) the weaves were balanced, with identical geometric and material properties of the warp and weft yarns, ignoring any potential process-induced variabilities [68];

(ii) in the absence neighbouring yarns, yarn cross-sections were elliptical [219];

(iii) in the undeformed plain weave fabric, yarn paths were sinusoidal [220].

These validity of these assumptions was supported by optical micrographs of the undeformed fabric (Figure 4.2(a) and (b)), allowing the fabric model to be constructed from the average measured values of the three basic parameters: yarn width, pitch (distance between the centres of adjacent parallel yarns), and thickness (Table 4.3). The geometry was generated in Abaqus/CAE through the Abaqus scripting interface (Figure 4.2(c) and (d)). Idealised yarn volumes were constructed by spline extrusions of the cross-section along the yarn paths. This approach commonly suffers from undesirable volumetric interpenetrations in the nominal geometry [221], except when applied to very sparse fabrics. Here, the interpenetrations were resolved by a procedure proposed elsewhere [116], consisting of a fictitious thermal contraction-expansion step with activated contact interactions between the yarns during expansion, which introduced a more realistic spatial variability in the geometry at no additional computational cost.

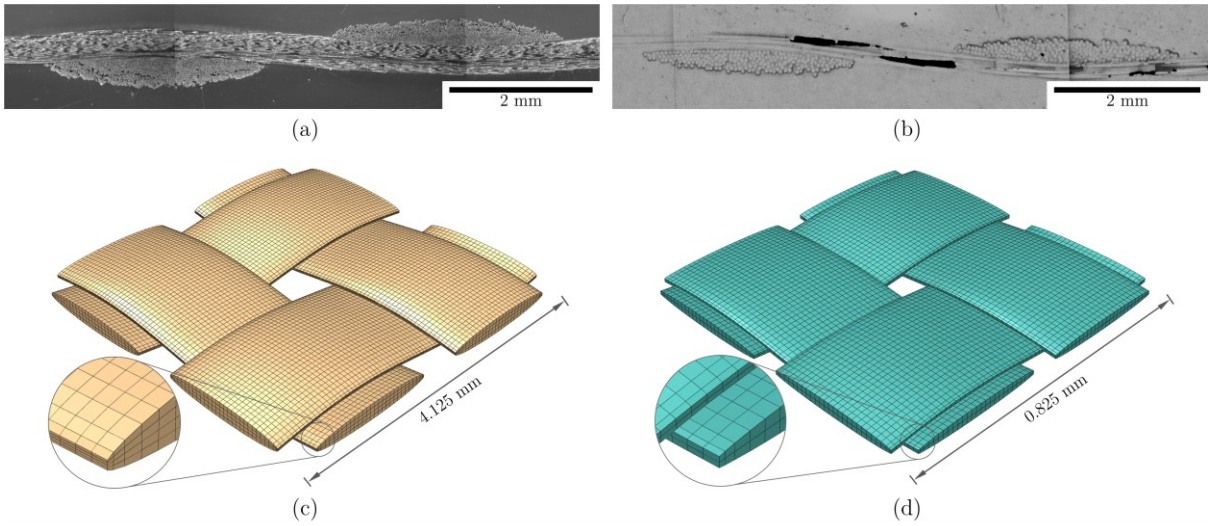

Figure 4.2. Optical micrographs of the fabric cross-sections: (a) C and (b) G; fabric monolayer unit cell geometry and mesh: (c) C and (d) G.

Table 4.3. Mean geometric parameters of the undeformed fabrics.

Fabric	Width (mm)	Height (mm)	Pitch (mm)	Intrayarn fibre volume fraction (%)
Carbon, C	1.557 (±0.047)	0.200 (±0.009)	2.018 (±0.087)	46.9
Glass, G	0.347 (±0.056)	0.028 (±0.004)	0.419 (±0.019)	49.7

Parentheses indicate one standard deviation.

4.3.1.2 Domain discretisation and boundary conditions

A structured hexahedral mesh was constructed by partitioning the yarn volumes such that the elements preserved the local longitudinal and transverse directions of the yarn. The automatic periodicity of the resulting mesh facilitated the application of in-plane periodic boundary conditions through multi-point constraint equations [222]. In these equations, the nodal displacement degrees of freedom of pairs of equivalent nodes on opposite thorough-thickness faces of the unit cell were linked through those of a fictitious master node. Out-of-plane compressive load was simulated using a coupling constraint, linking the out-of-plane displacement degrees of freedom of a pair of steel platens on either side of the fabric UC to those of an additional master node.

The fabric deformation was modelled in a large displacement framework (geometrically non-linear analysis). Contacts were modelled using a global surface-to-surface contact algorithm. A 'hard' contact definition was specified for the normal contact behaviour. Tangential contact behaviour was described by a global penalty friction formulation with an assumed interyarn friction coefficient of 0.2 for C [223,224] and 0.5 for G [68,225]. Convergence difficulties due to contact non-linearity are common to this type of problem [226,227] and in the present case necessitated the use of the Abaqus/Explicit dynamic solver. Care was taken to ensure that all the analyses were performed in a quasi-static regime by controlling the rate of applied displacement and mass scaling, and monitoring the relevant strain and kinetic energy outputs.

Linear and quadratic tetrahedral elements were avoided because of their overly stiff bending response and poor accuracy, and higher computational expense and poor performance in contact problems, respectively, in comparison to linear hexahedral elements. Full integration elements with incompatible modes (C3D8I), which avoid the shear locking problems (high stiffness in bending problems due to parasitic shear) of standard first order full integration elements (C3D8) and the hourglassing problems of first order reduced integration elements (C3D8R), could not be used in combination with the user-defined material subroutine (Section 4.3.1.3). Therefore, C3D8R elements, commonly used in mesoscale fabric simulations [56], were selected. Enhanced hourglass control was used and care was taken to ensure the artificial energy dissipation of the model was acceptably low. Care was also taken to produce high-quality approximately rectangular elements; however, some element skewing at the yarn edges was unavoidable due to the

elliptical yarn cross-section. It must be highlighted that parallelogram- and trapezium-shaped elements with skew angles as low as 10° suffer substantial loss of accuracy [228], with significant implications for the accuracy of fabric forming simulations. In the present work, a very fine mesh was used to minimise such skew.

4.3.1.3 Constitutive model

Achieving consistency between the mechanical behaviour of a fabric mesoscale model with that observed in experiments is challenging. Owing to the weave, dry fabrics exhibit a quasi-continuous behaviour [229] at both the yarn and fabric scales, despite discontinuities at the fibre scale. It is widely accepted that yarns should be modelled as transversely isotropic [56], and that their fibrous structure gives rise to a number of unique mechanical characteristics: tensile and bending stiffnesses are decoupled, while the transverse, bending and shear stiffnesses are small in comparison to the tensile stiffness [69]. Geometric non-linearity, evolving contact boundary conditions between yarn and tool surfaces, and material non-linearity are all important. Material non-linearity during compaction takes the form of increased transverse and shear stiffness arising due to the increased fibre packing, and hence, increased number of fibre to fibre contacts.

Sensitivity study

To inform the constitutive model definition, a preliminary sensitivity study (Figure 4.3) was performed on the five elastic constants needed to describe the transversely isotropic constitutive model (E_1, E_2, G_{12}, ν_{12} and ν_{23}) and the interyarn friction coefficient (μ) to determine their influence on the simulated compaction response. The response was most sensitive to the transverse modulus (E_2), which justified the use of a non-linear transverse modulus determined inversely from the compression experiments, with all remaining elastic constants adopted from the literature (Table 4.4). The study also showed that to avoid hourglass instabilities a minimum value of 1 MPa was required for G_{12}. The hourglass effect was evidenced by discontinuities in the force-displacement response alongside the characteristic mesh deformations.

User material subroutine

A non-linear relationship between the local (intrayarn) fibre volume fraction, V_f, and transverse modulus, E_2, was implemented through a user-defined material subroutine (VUMAT). The element-wise intrayarn fibre volume fraction was introduced as a solution

dependent variable and calculated based on the initial intrayarn fibre volume fraction, $V_{f,0}$, and the element volume change, which was represented by the element Jacobian, J:

$$V_f = \frac{V_{f,0}}{J} \quad . \tag{4.2}$$

The Jacobian was obtained from the deformation gradient, F, as $J = \det(F)$. The initial fibre volume fraction (Table 4.3) was computed from the fabric areal mass, fibre density, unit cell side length, L, and idealised yarn volume in the UC, $V_{\text{yarns},0}$, according to:

$$V_{f,0} = \frac{m_s \, L^2}{\rho \, V_{\text{yarns},0}} \quad . \tag{4.3}$$

Adopting the methodology used in previous works [57,65,70], the non-linear transverse modulus of the yarns was assumed to follow a bi-exponential relation:

$$E_2 = a\exp(bV_f) + c\exp(dV_f) \quad , \tag{4.4}$$

where E_2 is measured in Pa, while a, b, c and d are fitting coefficients. The coefficients a and b control the low-pressure response, while c and d control the high-pressure response. An iterative inverse procedure was used to obtain the values of the coefficients (Table 4.5) by minimising the error between the experimental and numerical compressibility responses for each of the two fabric monolayers. Once the iterative procedure had been completed, the coefficient c was adjusted to account for the theoretical maximum value of transverse modulus. A semi-analytical procedure was used to determine this value (briefly outlined below). A mesh convergence analysis (Figure 4.4) indicated solution convergence with 2142 elements per yarn for both fabrics.

Maximum transverse modulus of a fibre bundle

Hexagonal packing of straight and parallel fibres with circular cross-sections and constant diameters, which achieves the theoretical maximum fibre volume fraction of 91%, was assumed as an idealised case representing the maximum transverse modulus of the fibre assembly. A 3D representative volume element (RVE) of such a fibre bundle was generated. The RVE had a rectangular cross-section in the transverse plane (yz) and the third dimension (x) was specified as an arbitrary small value. The fibres were modelled as parallel transversely isotropic elastic bodies in hard contact. Manufacturer's datasheet and literature values of the elastic constants were assumed (Table 4.6).

Symmetry boundary conditions were applied at the xz boundary surfaces, through multi-point constraints on the displacement degrees of freedom. Displacements were fixed on one yz surface and free on the opposite surface, allowing for axial Poisson's expansions. Compression was applied via prescribing displacements on the xy boundary surfaces.

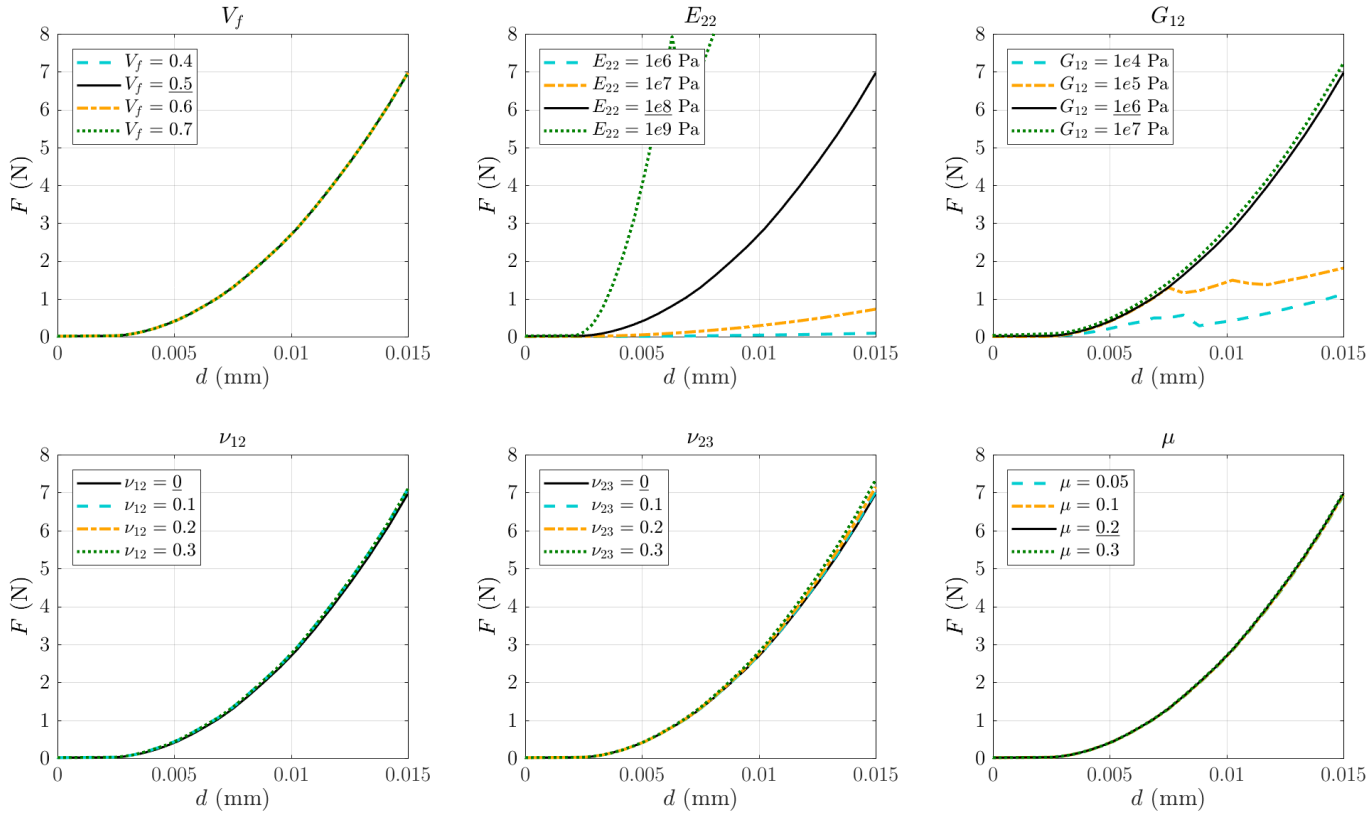

Figure 4.3. Sensitivity of the compaction response of the C monolayer model to the elastic properties of the yarns and the interyarn friction. Nominal parameter values underlined in the legends.

Table 4.4. Yarn constitutive model parameters.

E_1 (Pa)	E_2 (Pa)	G_{12} (Pa)	ν_{12} (—)	ν_{23} (—)
$V_f E_{1,f}$	$a\exp(bV_f) + c\exp(dV_f)$	1×10^6	0	0
[68,227]	[57,65,70]	[58,224]	[54,58,70,226]	[54,58,70,226]

Square brackets indicate references.

Table 4.5. Non-linear transverse stiffness coefficients.

Fabric	a (Pa)	b (—)	c (Pa)	d (—)
Carbon, C	0.45	23.14	2.4×10^{-15}	61.20
Glass, G	187.76	14.09	33.9×10^{-16}	65.60

Table 4.6. Fibre specifications and semi-analytical maximum transverse modulus of fibre bundle.

Fibre type	d_f (μm)	$E_{1,f}$ (GPa)	$E_{2,f}$ (GPa)	$G_{12,f}$ (GPa)	$G_{23,f}$ (GPa)	$\nu_{12,f}$ (—)	$\nu_{23,f}$ (—)	$E_{2,max}$ (GPa)
FT300B (PAN)	7	230	15	27	7	0.26	0.26	2.5
	[91]	[91]	[230]	[230]	[230]	[231]	**	
E glass	5	73	73	30	30	0.23	0.22	17.2
	*	[230]	[230]	[230]	[230]	[230]	**	

* and ** indicate measured and assumed values, respectively.

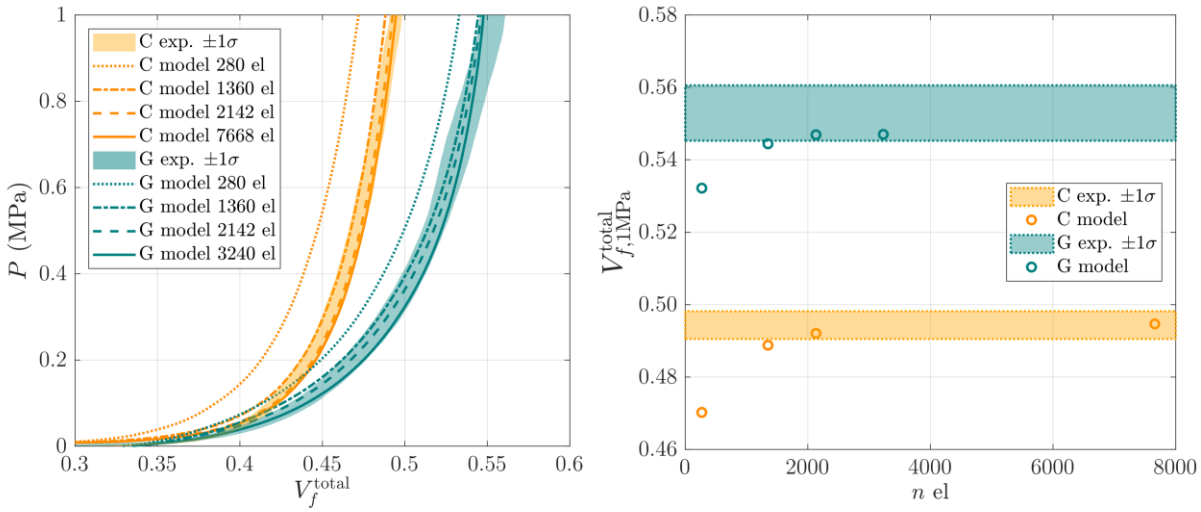

Figure 4.4. Mesh convergence analysis for monolayer compaction, with experimental comparison.

4.3.2 Multilayer fabric compaction model

4.3.2.1 Monolithic unit cell

Models of the bilayer monolithic stacks C_2 and G_2 were generated to permit comparison between the compaction behaviour of monolithic and hybrid stacking sequences, and to provide additional model validation datasets. Interply nesting is a key feature of multilayer fabric stacks and has a significant influence on the compaction behaviour [54]. The relative in-plane ply offset of the fabric plies determines the size and position of the yarn contact regions through which compressive load transfer occurs, and consequently, the effective compressibility of the stack.

The concept of phase difference between the nominally sinusoidal yarn paths was adopted to describe the ply offset (nesting configuration) [57]. To account for the potential range of effective compressibilities, the limit cases representing minimum and maximum possible nesting were considered: in-phase (IP) and 90° out-of-phase (90°OP). The two cases are alternatively described as no in-plane offset between adjacent fabric plies, and an offset equal to 25% of the UC length, respectively (Figure 4.5).

The alignment of the contact points (that is, yarn densification regions) in the IP model was expected to yield a compressibility response equivalent to that of the monolayer. In the 90°OP model, the multitude and spread of contact regions across the UC was expected to result in more uniform yarn densification and higher total fibre volume fraction at a given applied pressure, relative to the IP model and monolayer cases.

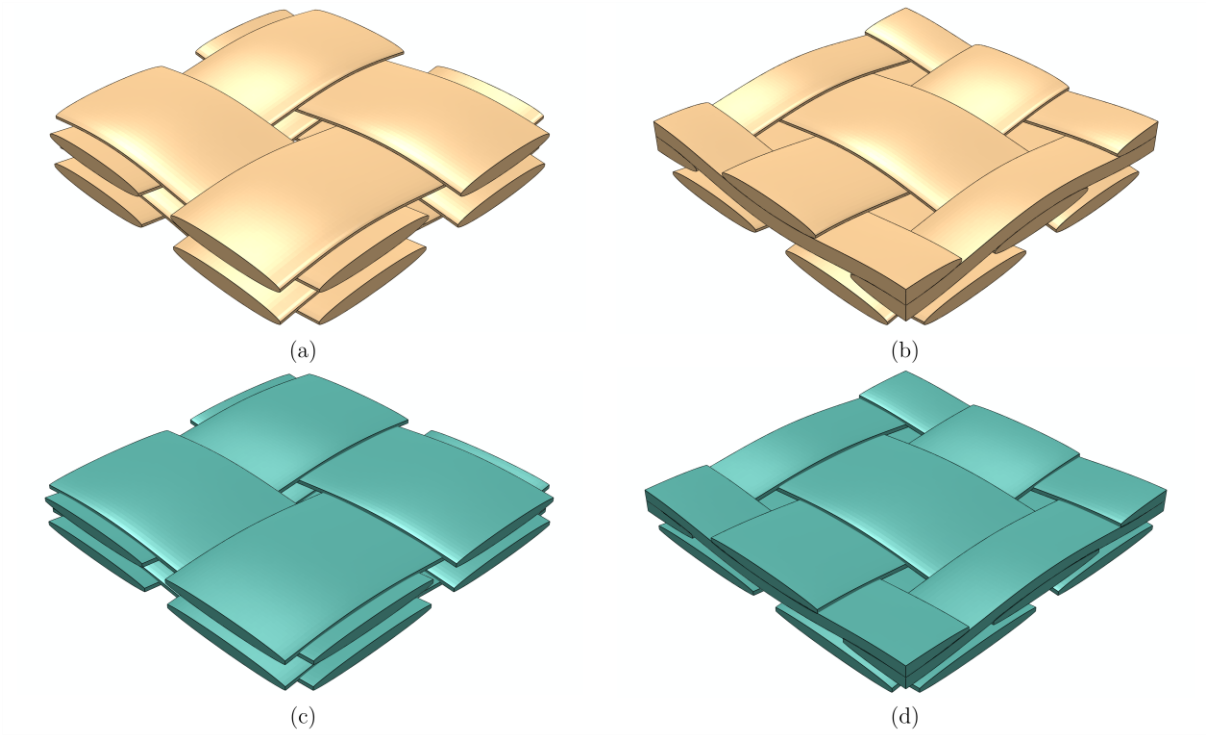

Figure 4.5. Monolithic multilayer fabric stack models: (a) CC_{IP}, (b) $CC_{90°OP}$, (c) GG_{IP} and (d) $GG_{90°OP}$.

This methodology enabled comparison with the experimentally determined compressibility ranges, where an arbitrary variation of ply offsets was present. The constitutive models of the C and G yarns were those obtained from the previously described initial calibration performed on the monolayer models (Section 4.3.1.3), while boundary conditions and remaining model parameters were kept the same. Additionally, the equivalence of the in-phase model to an 180° out-of-phase model [136] was verified by comparison between their respective compressive responses.

4.3.2.2 Hybrid unit cell

The major challenge associated with constructing a unit cell model of a hybrid woven reinforcement stack, or hUC model, stems from the dissimilar unit cell dimensions of the constituent fabrics. Consider the unit cells of two balanced fabrics A and B, UC_A and UC_B, with unique side lengths, $L_A \neq L_B$. To construct a mesoscale hUC of a multilayer stack consisting of the two fabrics, periodicity of the hUC geometry must be ensured.

Strictly speaking, a periodic hUC can only be generated by the tessellation of UC_A and UC_B, such that the side length of the hUC, L_{hUC}, represents the least common multiple of those of the constituent unit cells, that is, $L_{hUC} = n_A L_A = n_B L_B$, where $n_A, n_B \in \mathbb{N}$. The number of required tessellations is then $n_A^2 + n_B^2$ for a hybrid bilayer. In most cases, strict

enforcement of this requirement would render the hUC mesh size impractical for mesoscale analysis. It is therefore desirable to make suitable approximations to reduce the computational domain where possible.

The approach proposed here was to approximate the in-plane geometric parameters of the fabrics to minimise the number of tessellations required for a periodic hUC. Firstly, values of L_A and L_B were modified within the range of specimen variability (mean $\pm 1\sigma$), such that their least common multiple, and hence n_A and n_B, were minimised (Figure 4.6). To satisfy the modified UC size, yarn width and pitch were adjusted by selecting values from their respective ranges of variability, as close as possible to the mean.

Using the modified geometric parameters (Table 4.7) allowed hUCs containing fabrics C and G to be constructed with a 1:5 tessellation ratio (Figure 4.7). The absolute differences in the initial intrayarn volume fraction between the modified and the original geometries were –0.66% and +0.62% for the C and G fabrics respectively, hence no additional adjustment was deemed necessary to maintain a similar total fibre volume fraction. IP and 90°OP nesting of the C layers was considered in the CGC model.

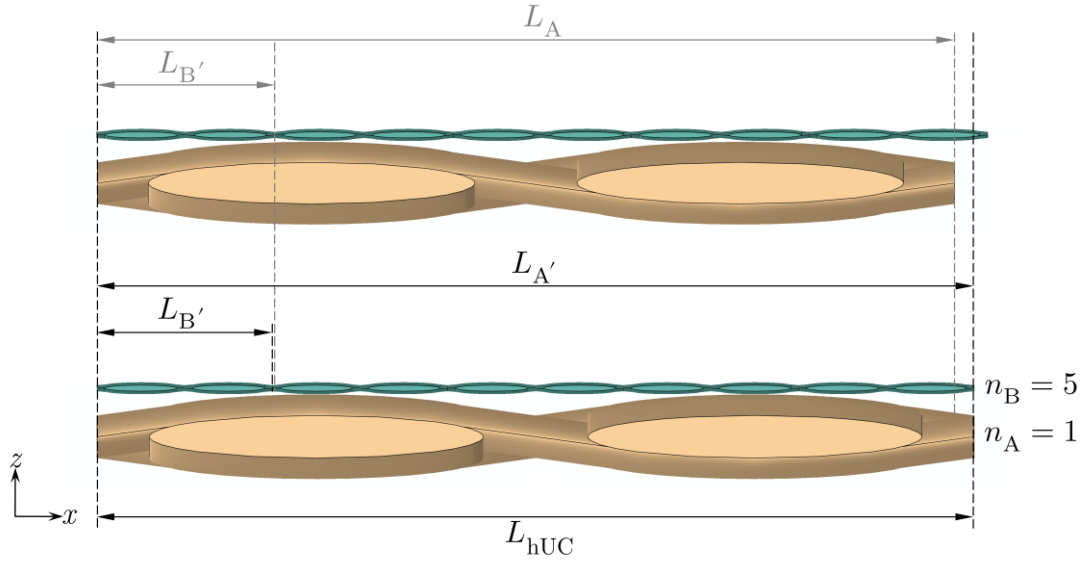

Figure 4.6. Geometric approximation used to construct hybrid multilayer fabric stack models with 1:5 tessellation ratio.

Table 4.7. Modified geometric parameters in hUC models.

Fabric	Width (mm)	Pitch (mm)
Carbon, C	1.5500	2.0625
Glass, G	0.3395	0.4125

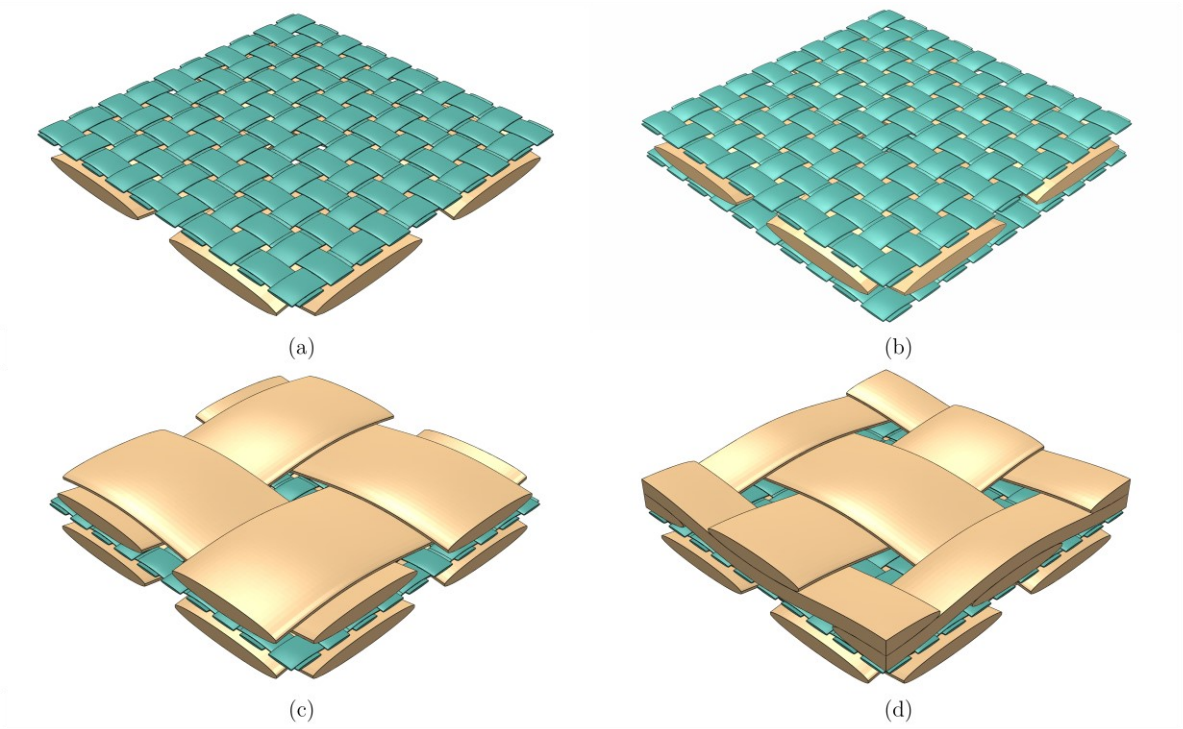

Figure 4.7. Hybrid multilayer fabric stack models: (a) CG, (b) GCG, (c) CGC_{IP} and (d) $CGC_{90°OP}$.

4.4 Compaction model results

4.4.1 Compressibility response comparison

The measured pressure versus fibre volume fraction curves (Figure 4.4 and Figure 4.8) are presented as an experimental range, calculated from the mean and standard deviation ($\pm 1\sigma$) for each stacking sequence, based on at least six specimens. The curves follow the same characteristic non-linear response reported in the literature [57,68,70]. The low initial compression resistance was attributed to a dominance of yarn bending and decrimping deformation mechanisms [54,60], while the sharp increase in compressive stiffness at higher applied compressive strains was attributed to increasing fibre packing density. The observed increase in compression resistance was approximately biexponential in the pressure range studied ($R^2 > 0.98$ in all cases).

In the single layer experiments (Figure 4.4) the initial fibre volume fractions of the undeformed fabrics were approximately 32% and 29%, respectively for C and G. C presented a more rigid compression response ($V_{f,C}^{total}$ 1 MPa $= 49.5\%$) compared to G ($V_{f,G}^{total}$ 1 MPa $= 55.3\%$). Both monolithic multilayer stacks, C_2 and G_2 (Figure 4.8(a)), showed increases in compressibility relative to the respective monolayer responses

(V_{f,C_2}^{total} 1 MPa $= 54.0\%$ and V_{f,G_2}^{total} 1 MPa $= 57.3\%$). The relative increase in fibre volume fraction was attributed to nesting of the plies [57], and was more pronounced for C_2 (8.7%), than G_2 (3.6%). The measured compressibility curve ranges for the three hybrid stacking sequences (Figure 4.8(b)) fell between those of the monolayers C and G. Stacking sequence CG, in which the mass fraction of C ($m_{f,C}$) was 79%, displayed the least compliant response ($V_{f,CG}^{total}$ 1 MPa $= 50.1\%$), and was dominated by the compressibility of C. Sequence GCG ($m_{f,C} = 88\%$) displayed an intermediate response ($V_{f,GCG}^{total}$ 1 MPa $= 51.9\%$), indicating an increased influence from the more compliant G plies. CGC was the most compliant on average ($V_{f,CGC}^{total}$ 1 MPa $= 52.4\%$).

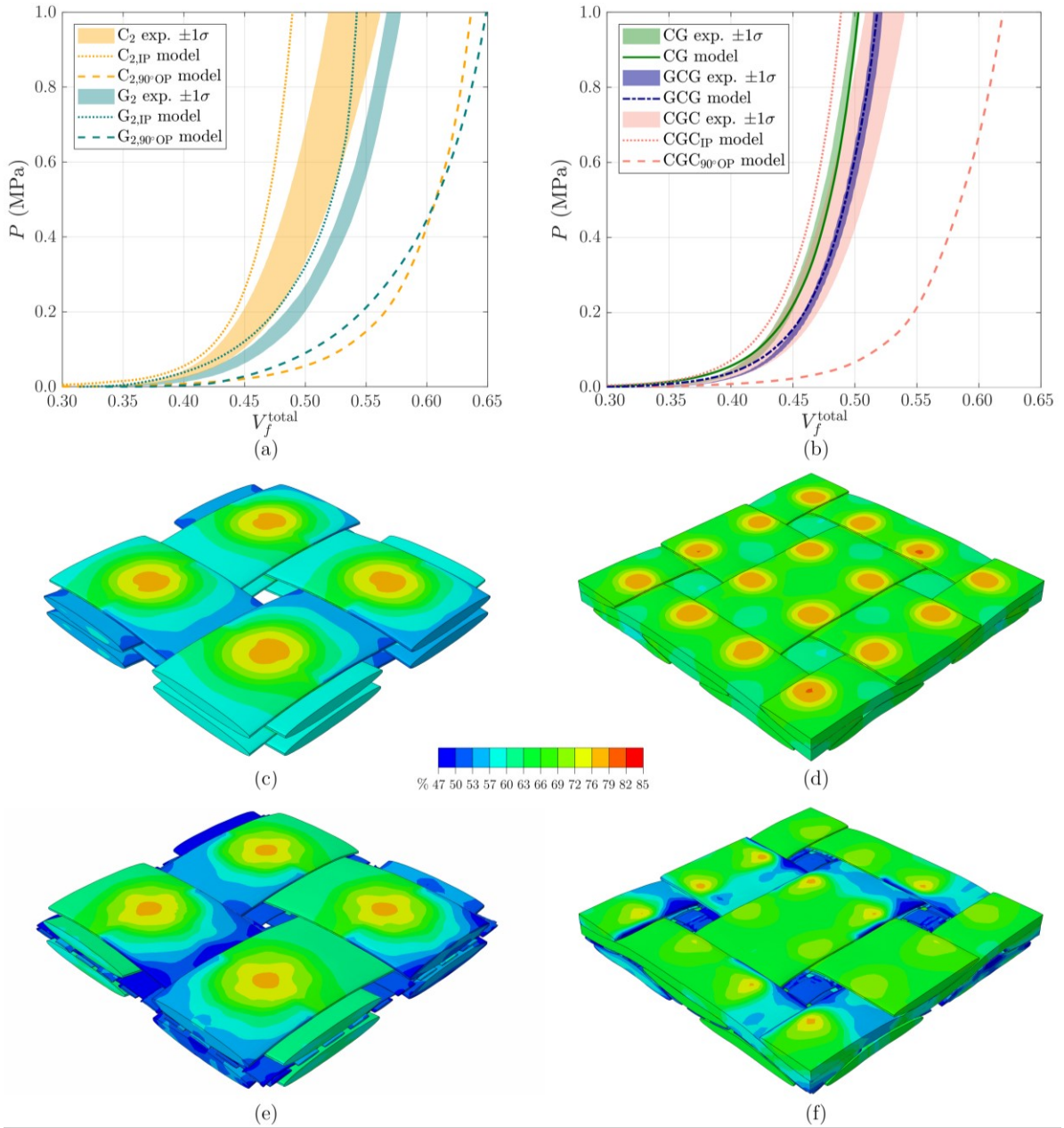

Figure 4.8. Measured and predicted compaction responses: (a) monolithic, and (b) hybrid stacks. Predicted fibre volume fraction: (c) CC_{IP}, (d) $CC_{90°OP}$ (0.6 MPa); (e) CGC_{IP}, (f) $CGC_{90°OP}$ (0.3 MPa).

4.4.2 Meso-structure comparison

A volumetric reconstruction was obtained from the μCT scan of the hybrid CGC/epoxy specimen based on the local X-ray attenuation characteristics within each voxel (Figure 4.9(a)). High intensity voxels represented glass yarns, mid-intensity voxels represented carbon yarns and resin pockets, and the lowest intensities were associated with free volume. Mutually orthogonal slices through the panel (Figure 4.9(b)) showed that the periodicity of the mesostructure was retained after compaction. Through-thickness waviness of the G fabric was a key meso-structural feature. Although the morphology of the samples was relatively uniform, some local geometric variation, and shear distortion of the G fabric (ca. 3°) were also present. A 4.2×4.2 mm region of interest containing one full hUC was extracted from each sample. Orthogonal slices (Figure 4.10) from the laminate midplane (xy), were used to qualitatively assess the accuracy of the predicted geometry.

Statistical μCT analysis was considered outside the scope of this work. To aid visualisation, a 'representative' hUC (Figure 4.10(b)) was volume segmented by defining threshold intensity values for the glass yarns and free volume. Segmentation of the carbon yarns from the pure epoxy regions was not possible due to the relatively low contrast between their respective grey values. Nevertheless, carbon yarns were still distinguishable by the orientations of carbon fibre bundles in the xy plane. The characteristic through thickness 'footprint' of the glass yarns at the laminate midplane slice (Figure 4.11(d)) was used to qualitatively assess the model mesostructure predictions (Figure 4.11(a) to (c)).

Cross-sectional optical micrographs obtained from the same panel (Figure 4.9(c)) were used to complement the μCT observations, providing greater detail of the internal morphology. To aid visualisation and provide additional means of comparison, carbon yarns and glass yarns were segmented by tracing the yarn contours (Figure 4.11(h)). Laminate midplane cuts (Figure 4.11(a) and (b)) and cross-sections (Figure 4.11(e) and (f)) from the models showed that the compacted geometries from the two ply offset limit cases were not representative of the physical specimen. These findings motivated the analysis of a third geometric configuration, $CGC_{36°OP}$, with a phase shift of 36° (a ply offset of 10% of the UC length) between the C plies in both the warp and weft directions, based on the average ply offsets observed in the physical μCT specimen (a total of six measurements, two per sample). The results of the CGC36°OP model (Figure 4.11(c) and (g)) yielded a more accurate geometric representation of the panel.

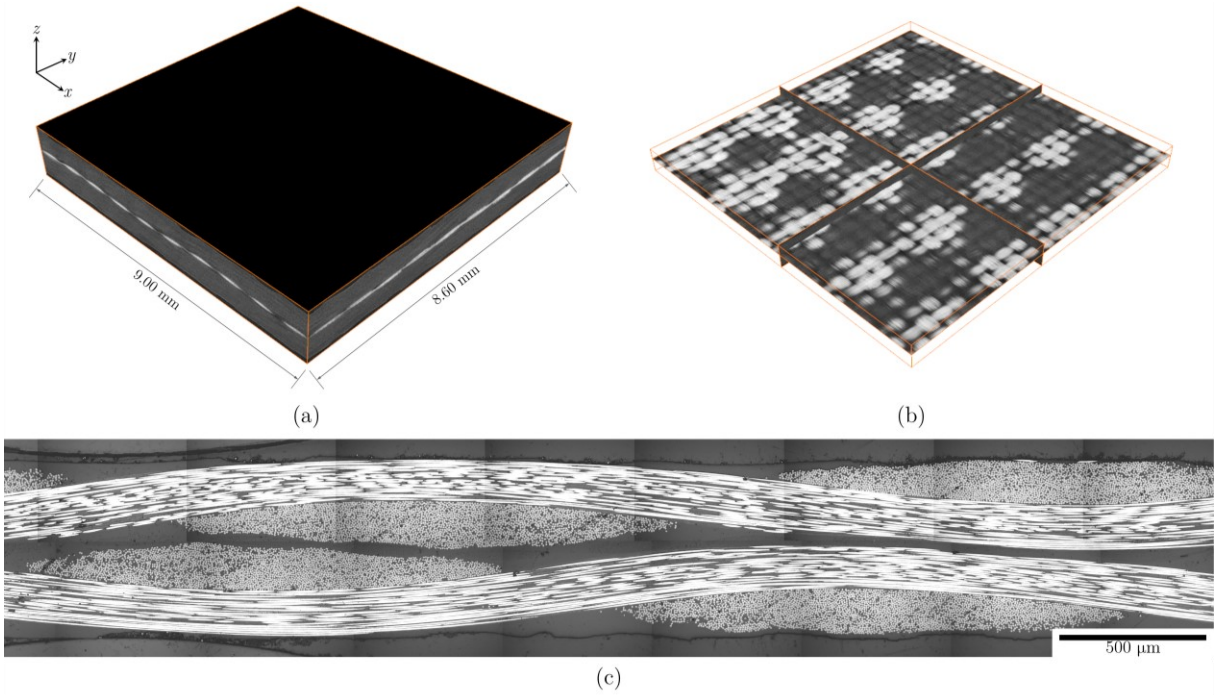

Figure 4.9. Three-point perspective projection of (a) volume reconstruction, and (b) orthogonal slices (midplanes: xy, xz, yz) obtained from the μCT scan of the CGC/epoxy laminate (four complete hUCs); (c) optical micrograph of the CGC/epoxy laminate cross-section (one representative hUC).

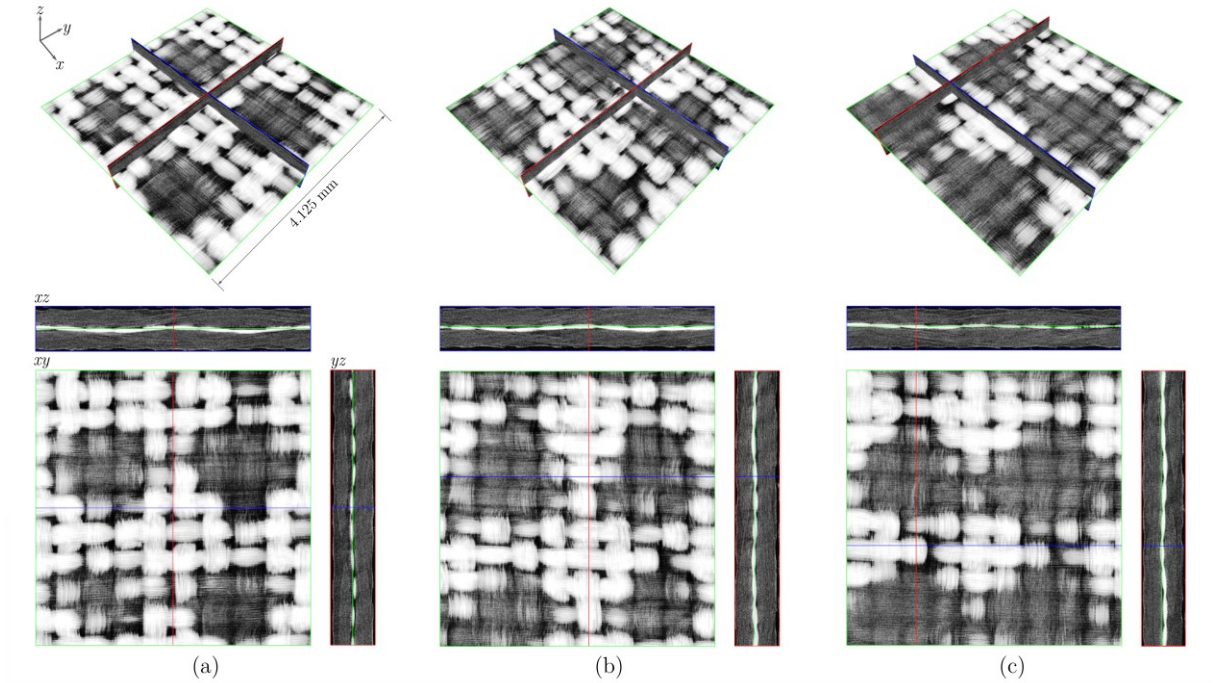

Figure 4.10. Three-point perspective (above) and third-angle multiview orthographic (below) projections of orthogonal slices (midplanes xy, xz, zy) obtained from the μCT scan of the CGC/epoxy laminate (one representative hUC from each sample).

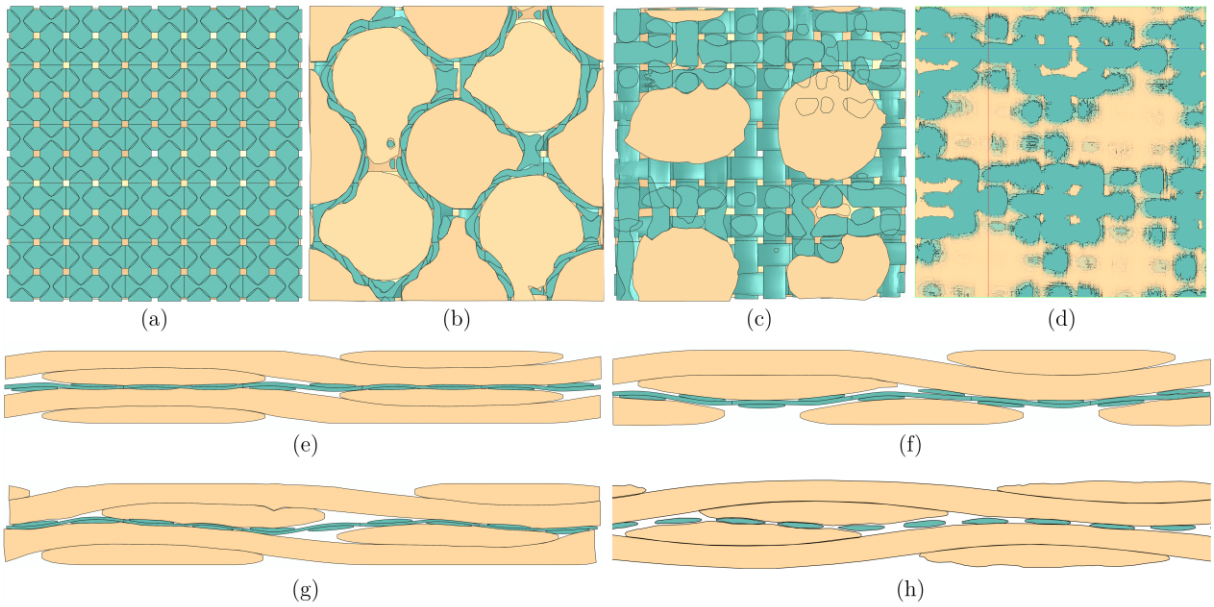

Figure 4.11. Predicted midplane slices through (a) CGC_{IP}, (b) $CGC_{90°OP}$ and (c) $CGC_{36°OP}$ models; (d) segmented midplane slice extracted from the CGC/epoxy μCT scan (manually segmented and colourised); Predicted cross-sections through (e) CGC_{IP}, (f) $CGC_{90°OP}$ and (g) $CGC_{36°OP}$ models; (h) optical micrograph of the CGC/epoxy cross-section (manually segmented and colourised).

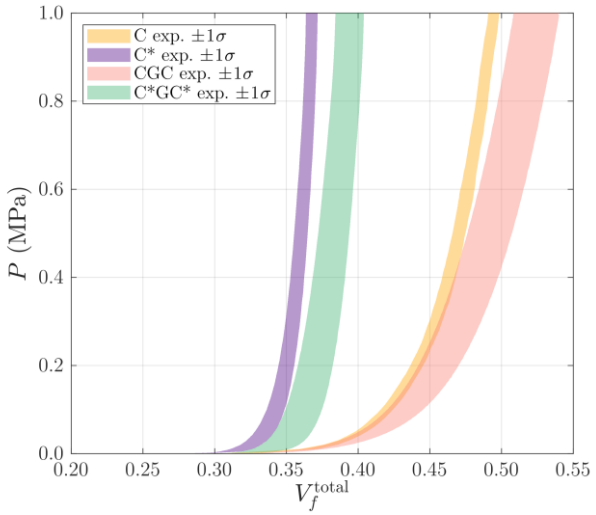

Figure 4.12. Experimental compressibility of as-received (C and CGC) and CAG-modified (C* and C*GC*) fabric monolayers and device stacks.

4.4.3 Effect of CAG modification

Figure 4.12 illustrates the effect of CAG modification on compressibility. The CAG-modified specimens C* and C*GC produced a more rigid response compared to the as-received, with the absolute value of average total fibre volume fractions at 1 MPa falling by ca. 13% in the C* and C*GC* specimens (V_{f,C^*}^{total} 1 MPa $= 36.8\%$ and $V_{f,C^*GC^*}^{total}$ 1 MPa $= 39.4\%$). The average initial fibre volume fractions fell slightly by 3% and 2%, respectively. The measurement scatter for the modified stacks was low ($CV_{C^*} = 0.15\%$ and $CV_{C^*GC^*} = 2.5\%$).

4.5 Summary of results

An original mesoscale compaction model was proposed and validated for dry multilayer fabric stacks with hybridised stacking sequences. This hybrid unit cell model (hUC) extends beyond existing models, which have been restricted to monolithic stacking sequences. Focusing on the fabrics used in SSC laminates, the numerical model was validated against compressibility experiments performed on monolithic and hybrid fabric stacks. The main findings of the present chapter were as follows:

- Both the numerical and experimental results demonstrated that the in-plane ply offset has a major influence on the compressibility responses and internal morphologies of the multilayer stacks, contributing to experimental variability thereof.
- Hybridisation of the fabric stacking sequence may inhibit nesting, leading to a reduction in the attainable total fibre volume fraction at a given compaction pressure, compared to those obtained from monolithic stacking sequences.
- The experimental results confirmed that a substantial loss of compressibility occurs as a result of CAG-modification.

These results are discussed in detail in Section 8.1. The model additionally serves as an automatic pre-processor for the generation of realistic finite element representations of the compacted geometry of SSCs, serving as a starting point for the analysis of their mechanical response in Chapter 5.

5 Mechanical performance analysis and prediction

5.1 Introduction

There is a strong need for realistic device-level mechanical models of structural supercapacitor composites, which consider their complex woven composite architecture and the combined response of their non-conventional constituents. These models would assist in the analysis and interpretation of experimental results [47] and direct the development of structural supercapacitors with improved mechanical performance. The aims of this chapter were therefore:

- to develop a finite element model for the mechanical response of structural supercapacitor composite laminates;
- to measure the elastic modulus of carbon aerogel to provide model input data;
- to revisit the laminates under investigation and perform additional microstructural characterisation to support model development and interpretation of experimental results reported in the literature;
- to validate the predictive capability of the developed models against experimental data.

The chapter is organised as follows: the experimental characterisation techniques used are outlined in Section 5.2, with the experimental results presented in Section 5.3. The development of the finite element model is detailed in Section 5.3.2, followed by the numerical predictions of the elastic properties in Section 5.5, focusing on the effects of carbon aerogel, structural electrolyte, and defects. The main findings are briefly summarised in Section 5.6. The findings and their implications are discussed in Chapter 7. Due to a present lack of available data on the non-linear mechanical behaviour of constituent materials, the work in this Chapter was constrained to elastic behaviour prediction; however, in future, the models developed in this work can be readily adapted to study the non-linear behaviour of supercapacitors, including damage development and failure.

5.2 Materials and characterisation methods

5.2.1 Materials

5.2.1.1 Composite laminates

The nomenclature introduced in Chapter 2 (Table 2.2) is adopted to describe the laminates investigated in this Chapter. The laminates were produced using the fabrics listed in Chapter 4 with two different matrix systems: a structural epoxy resin, bisphenol A diglycidyl ether monomer (BADGE, D3415, Sigma-Aldrich, GB) cross-linked with isophorone diamine hardener (118184, Sigma Aldrich, GB) in a 4:1 weight ratio; and a multifunctional resin composed of epoxy resin and 34 vol. % ionic liquid 1-Ethyl-3-methylimidazolium bis(trifluoromethylsulfonyl)imide (EMIM-TFSI, 11291, Sigma-Aldrich, GB [47]). The nomenclature STR and MF is used in this Chapter to refer to laminates using the structural and multifunctional matrix systems, respectively.

Details of the laminate manufacture are briefly summarised here. The STR laminates were fabricated by laying up the fabrics on a hot plate and infusing the stack with the structural resin mixture under a RIFT process. The laminates were cured under vacuum using the following temperature cycle: 60°C for 1 hour, 80°C for 2 hours and 120°C for 2 hours, followed by cool down to room temperature. The MF laminates were produced by filming the structural electrolyte onto a backing paper, and placing the C* and G fabrics onto the uncured structural electrolyte films to impregnate each layer. The three pre-impregnated plies were laid up on the hot plate and cured in the same way as the STR laminates, allowing phase separation to complete.

In summary, three types of laminates were investigated: (a) the baseline structural laminate CGC STR, (b) the CAG-modified structural laminate C*GC* STR, and (c) the CAG-modified multifunctional SSC laminate C*GC* MF. The structural laminates were modelled to validate the FE modelling methodology, and to examine in isolation the influence on mechanical performance of variables such as CAG, structural electrolyte, and defects.

5.2.1.2 Carbon aerogel monolith

To generate input material data for the FE models mechanical models of the CAG-modified laminates, the elastic modulus of CAG was measured by nanoindentation (see Section 2.4.1.1). For this purpose, monolithic CAG samples were produced by vacuum-

assisted aging of a resorcinol-formaldehyde-water mixture placed in a rectangular mould. The aged aerogel was solvent exchanged using acetone, followed by critical point drying and pyrolysis. The sample dimensions were 12.13×12.07×2.36 mm, measured using a digital calliper. Visually and under scanning electron microscopy (Section 5.3.2), the surfaces of the monolith sample (post pyrolysis) appeared to have been smooth and flat. Further details of the manufacture and physical characterisation of the CAG monolith are given in Appendix C.3.

5.2.2 Imaging techniques

Optical microscopy, scanning electron microscopy and micro X-ray computed tomography (μCT) were used to examine the microstructure of the untested CGC STR, C*GC* STR and C*GC* MF laminates. The imaged samples were cut using a diamond wire saw from the same laminates, from which the test coupons in Ref. [47] had been made. To enable safe specimen handling and imaging, the ionic liquid was removed from the C*GC* MF samples by washing in ethanol for 24 hours. For the optical and scanning electron microscopy, both through-thickness and in-plane sample cross-sections were prepared, with approximate in-plane sample dimensions of 20×20 mm and 10×10 mm, respectively. The approximate in-plane dimensions of the μCT samples were 10×10 mm. Optical and X-ray μCT imaging were performed according to the procedures outlined in Section 4.2.2. A partial analysis of these datasets, focusing on the CGC STR laminates, was previously presented in Chapter 4. The fracture surfaces of representative composite coupons tested to failure under longitudinal tension and in-plane shear in Ref. [47] were also imaged using a scanning electron microscope (SEM). A diamond wire saw was used to prepare samples from the coupons by cutting across the coupon width, at a small distance (5 to 10 mm) from the fracture surfaces, taking care to avoid handling-induced damage.

Scanning electron microscopy of the untested composite samples and fracture surfaces was performed using a variable pressure scanning electron microscope (S3700N-II, Hitachi High-Tech GmbH) in secondary electron emission modes, at acceleration voltages of 5 to 15 kV. During scanning electron microscopy, an electron beam raster scanned the specimen surface under observation and images were produced by recording the intensity of secondary electrons scattered by the specimen surface. Electrical grounding was provided through an aluminium mounting stub to dissipate the electric charge accumulated on the sample surface. Bonding to the stub was achieved through a conductive

carbon adhesive disc. To improve surface conductivity, the samples were further coated with gold using a K550X Sputter Coater using a plasma current and chamber pressure of 40 mA and 0.15 mbar, respectively. The target distance and deposition time were ca. 30 mm and 25 s, respectively, resulting in a gold film thickness of approximately 5 nm [232]. Silver DAG paint was used to ensure good electrical contact from the observed surface to the stub (all scanning electron microscopy consumables from Agar Scientific).

Additional scanning electron microscopy was performed on the CAG monolith and C* fabric to compare their morphologies at high magnifications. Sample preparation was as follows: the monolith sample was fractured using a safety knife, exposing the internal cross-sections for imaging; the C* sample was prepared by carefully pulling a yarn out of the fabric edge to reveal the fracture surface at the yarn/yarn crossover interface. Carbon black-loaded epoxy (Double Bubble, Loctite) and carbon discs were respectively used to attach the monolith fragments and C* fabric to aluminium test stubs. Prior to imaging, the specimens were left to dry in a programmable vacuum oven (Memmert VO400) at elevated temperature (40 °C) and reduced pressure (500 mbar) for four days. Both specimens were imaged uncoated, and imaging was performed in a high resolution field emission gun SEM (LEO Gemini 1525, Carl Zeiss NTS GmbH), operating in secondary electron emission mode at 5 kV.

5.2.3 Mechanical characterisation of monolithic carbon aerogel

Characterisation of the *in situ* elastic properties of CAG (that is, in the carbon fabric) was not possible due to the compliant nature of the underlying dry carbon fabric substrate, its complex architecture, undulating surface, and the presence of surface and sub-surface defects (see Appendix C.2 for preliminary indentation experiments on CAG-modified fabric samples and Section 5.3.1 for further discussion of defects). Anticipated challenges in the machining of microcomposite specimens with suitable fibre orientations (discussed in Section 2.4.1.1) further indicated that characterisation of monolithic specimens was a reasonable alternative approach to obtain the elastic properties of CAG, avoiding the above problems. The monolithic CAG sample described in Section 5.2.1.2 was tested dry (that is, not infused with resin) due to the high likelihood of fracture under the pressure applied during RIFT [78]. It was deemed reasonable to assume that the Young's modulus of the dry CAG monolith would provide a conservative estimate of that of the

CAG backfilled with epoxy or structural electrolyte, provided (as was expected to be the case) that the modulus of CAG was significantly higher than those of the other phases.

Instrumented nanoindentation (described in Section 2.4.1.1) was performed using a Micromaterials NanoTest Platform 3l. In this system, load was applied through an electromagnetically actuated pendulum, to which the indenter is attached. A capacitive system was used to measure indentation depth, by monitoring the change in capacitance resulting from the movement of a capacitor plate attached to the arm of the pendulum. A Vickers diamond indenter tip (ML/VICKERS 171-590-510 / C-0022682, Synton-MDP) was used, with a maximum tip diameter and maximum indentation depth of 2.5 mm and 20 μm, respectively. The CAG monolith sample was bonded to an aluminium stub using a thin layer of epoxy (Double Bubble, Loctite), allowing the adhesive to become tacky before bonding to minimise the ingress of epoxy into the CAG pores. The specimen surface, which had a smooth visual appearance, was left unpolished to avoid damage or premature fracture.

A series of indentations were performed in load-control mode at seven maximum indentation loads between 5 mN and 100 mN at a rate of 1 mN/s. This load range was chosen so as to avoid cracking of the specimen, which was observed to occur at loads of about 250 mN in the preliminary microindentation tests (see Appendix C.2). As per standard measurement procedures [233], the indentation test sequence included a five second dwell at peak load and a 60 second dwell period for thermal drift correction (accounting for thermal deformations in the indenter and apparatus). Ten indentations were performed at each maximum load, spaced 200 μm apart. The load-penetration depth curves were recorded and analysed by the method of Oliver and Pharr [234] (identified in Section 2.4.1.1), which is summarised here for clarity. Modelling the sample and indenter system as a series combination of springs, the reduced modulus of the system, E_r, is given by [85]:

$$\frac{1}{E_{\mathrm{r}}} = \left(\frac{1-\nu^2}{E}\right) + \left(\frac{1-\nu_{\mathrm{i}}^2}{E_{\mathrm{i}}}\right) \quad , \tag{5.1}$$

where E and ν are the Young's modulus and Poisson's ratio of the specimen, and subscript i denotes the indenter material (diamond). From elastic contact theory, for a rigid indenter of known shape in contact with a homogenous isotropic half-space [85]:

$$E_{\mathrm{r}} = \frac{S\sqrt{\pi}}{2\sqrt{A}} \quad , \tag{5.2}$$

where $A = A\ h$ is the contact area of the indenter as a function of the indentation depth, h, and S is the initial stiffness of unloading (also known as the contact stiffness):

$$S = \left.\frac{dP}{dh}\right|_{P_{\max}} \quad . \tag{5.3}$$

The elastic modulus of the specimen may thus be obtained using the maximum penetration depth, $h_{\max}$, and the contact stiffness recorded for a given peak load, $P_{\max}$.

The following assumptions about the specimen geometry and structure were made:

a) A continuum approximation of the monolith was assumed and surface roughness effects were neglected, since the diameter of the indentations was much larger (at least two orders of magnitude) than the pore width, which has been previously determined to be less than 40 nm (unpublished data by the Group).

b) The indentation depths used in this work were at least three orders of magnitude smaller than the sample thickness, therefore the substrate effect (see Section 2.4.1.1) was assumed negligible.

c) The pore structure and mechanical properties of the monolith were assumed to be homogeneous throughout the sample, and representative of those of the CAG in the C* fabric.

The above assumptions are discussed in Section 5.3.2.

Prior to the CAG monolith indentation tests, frame compliance and area function calibration were performed, to correct for the compliance of the testing equipment and indenter tip rounding, respectively. The calibrations were performed according to the instrument manual [233] using a fused silica reference sample. The frame compliance was determined as $1/K_{\mathrm{f}} = 0.328$ nm/mN. The Young's modulus measurements obtained for the fused silica reference sample were in excellent agreement with the literature value in the depth range 0.4 to 1.2 μm (Figure 5.2), therefore this same range was used to calculate the mean modulus of the CAG monolith.

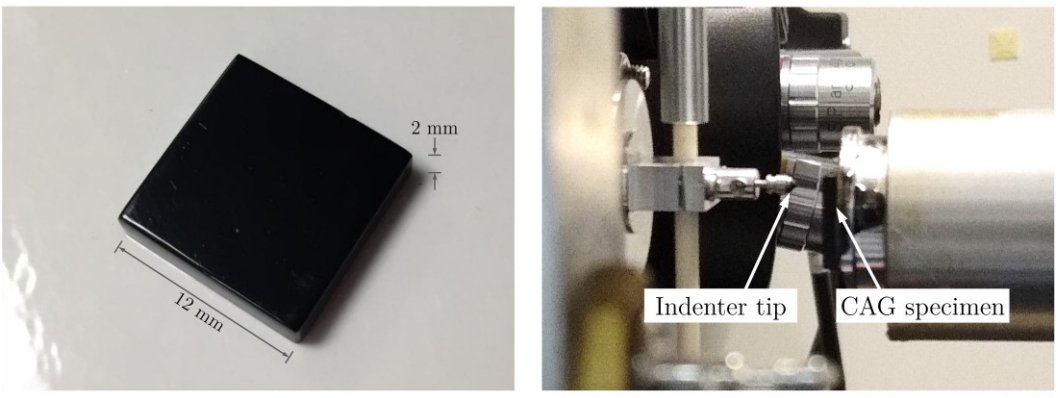

Figure 5.1. (a) CAG monolith specimen, and (b) nano-indentation experiment setup.

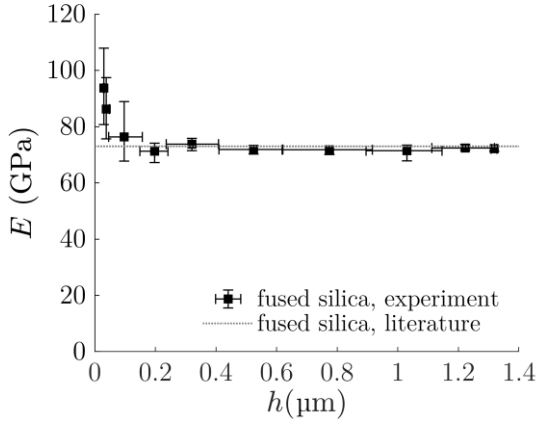

Figure 5.2. Young's modulus versus indentation depth for fused silica reference sample.

5.3 Experimental results

5.3.1 Imaging of untested composite laminates

5.3.1.1 Structural laminates

Optical micrographs of the through-thickness and in-plane cross-sections of the CGC STR and C*GC* STR laminates were obtained (Figure 5.3 and Figure 5.5). In the C*GC* STR laminate (Figure 5.3(b) and Figure 5.4), an abundance of fibre-free transverse bands was observed in the intrayarn regions, which were not present in the baseline laminate (Figure 5.3(a)). They will be referred to as 'cracks' in the following, though it should be noted that they were backfilled with epoxy during RIFT. The crack distribution was approximately periodic, with, on average, each yarn split into three segments. It has been reported that monolithic CAG fragments during solvent removal and pyrolysis [78] due to surface tension effects causing partial collapse of the porous structure [79].

From the large width of the transverse cracks (often up to 50 μm across in the samples analysed) and their smooth morphology, it was concluded that the cracks were formed under a similar collapse process during the CAG-modification process, that is, they were process-induced 'pre-cracks', which were backfilled during the subsequent resin infusion. A second type of pre-cracking was also observed between adjacent yarns at yarn crossover points (Figure 5.4) and will hence be referred to as interyarn delaminations. This type of cracking affected all yarns in the analysed samples, and also appeared to have been backfilled with epoxy resin.

The C*GC* STR laminates also presented dark regions with severe fibre chipping in the interior of the carbon yarns (Figure 5.3(b), Figure 5.4 and Figure 5.5(b)). Since the

polishing conditions, fibre content and polymer were identical to those of the baseline laminate, these features were considered to have been consistent with intrayarn voidage as a result of incomplete impregnation of the carbon yarns. To eliminate polishing damage as the cause of this voidage, the non-destructive μCT scans were scrutinised (Figure 5.6). Visual inspection of the reconstructed volumes confirmed the presence of both transverse cracks and intrayarn voids across all the yarns in all the C*GC* STR laminate samples.

The void area fraction could not be reliably measured from the micrographs, since this type of analysis is prone to section- and location-bias [100], which can only be minimised by analysing a large number of cross-sections. It was hoped that μCT image analysis could instead be used, since it is regarded as the most accurate technique for the characterisation of void content, morphology and distribution [100]. However, the technique relies on adequate image acquisition and post-processing, and in this case the scan quality was degraded by: (i) 'partial-volume effects' linked to the limited spatial resolution (6 μm voxel), resulting in CT values, which reflected an average attenuation value for the materials in each voxel [235], and (ii) 'beam hardening' or 'streaking' artefacts due to the inclusion of the highly attenuating glass fibres within lower attenuation carbon-based constituents [235]. Overall, the limited resolution and scan quality identification of the different material phases extremely challenging and prevented void content measurement through automatic segmentation techniques, such as thresholding or texture classification.

The scanned volumes were instead inspected manually to determine the size and distribution of the voids. Based on visual inspection of fourteen yarns, it was determined that voids were elongated along the fibre direction, and were present along 83 ± 11% of the yarn length, though the variability across the specimen was large ($CV = 0.6$). On average, voids were distributed in three separate areas across the yarn cross-sections. The distribution appeared to have been related to the number of transverse cracks in the yarn, though causality could not be determined. The void width was not measured due to the large variation and coalescence, particularly in the central yarn segments.

It was also important to determine which material phases were present in the intrayarn voids, that is, whether there was an absence of epoxy or CAG or both. Analysis of the optical and μCT imaging was inconclusive due to insufficient resolution and 'partial volume' effects; therefore, the polished cross-section samples were further examined using scanning electron microscopy (Figure 5.7 and Figure 5.8).

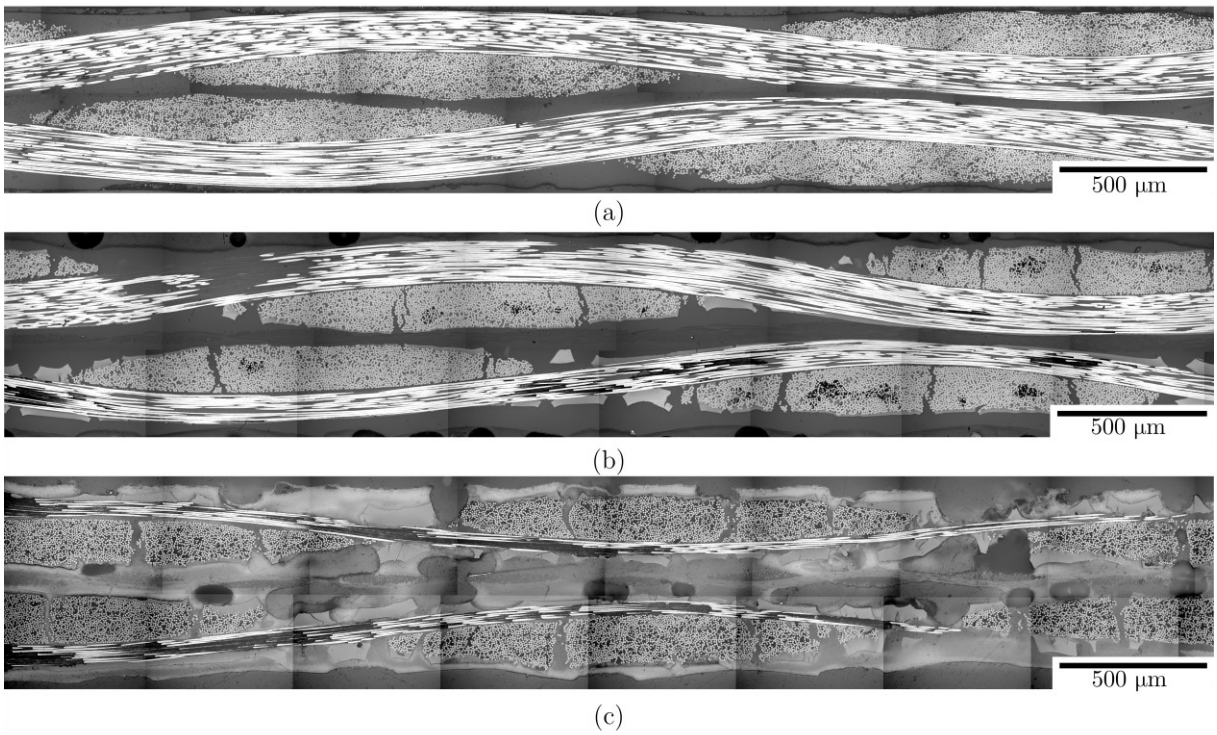

Figure 5.3. Optical micrographs of (a) baseline (CGC STR), (b) CAG-modified (C*GC* STR), and (c) multifunctional (C*GC* MF) laminate cross-sections (one representative UC).

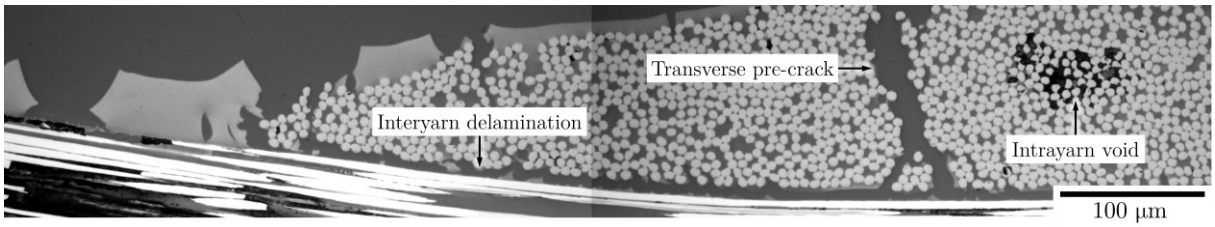

Figure 5.4. Optical micrographs of C*GC* STR laminate cross-sections, showing detail of the defects.

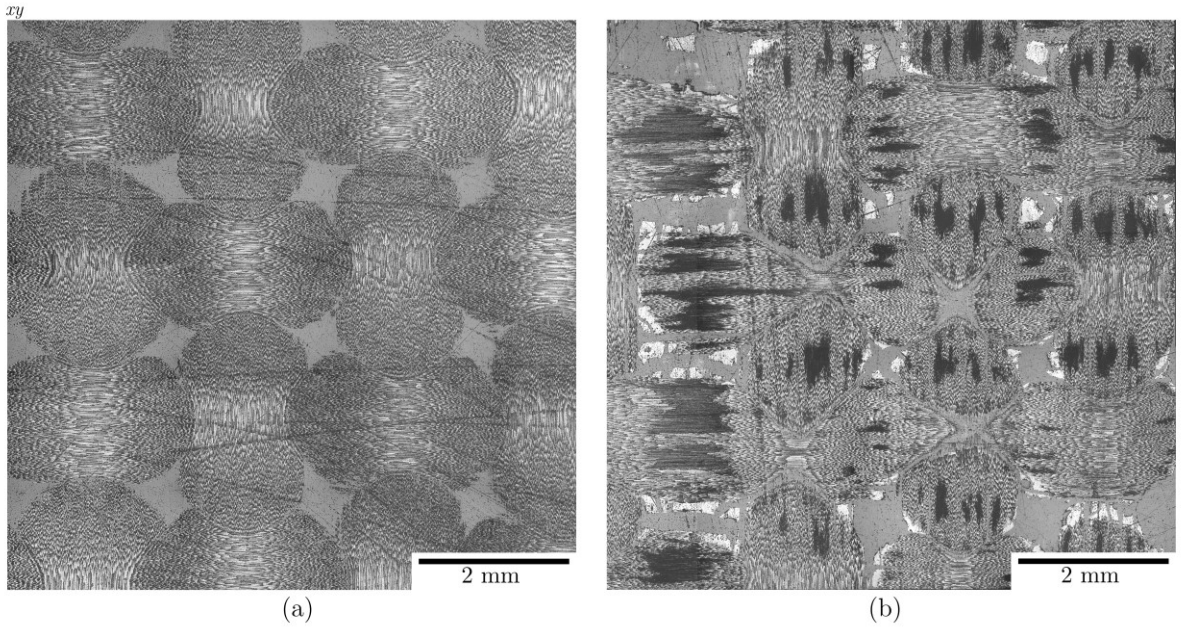

Figure 5.5. Optical micrographs of (a) CGC STR, and (b) C*GC* STR laminates, showing planar cross-sections through a carbon ply.

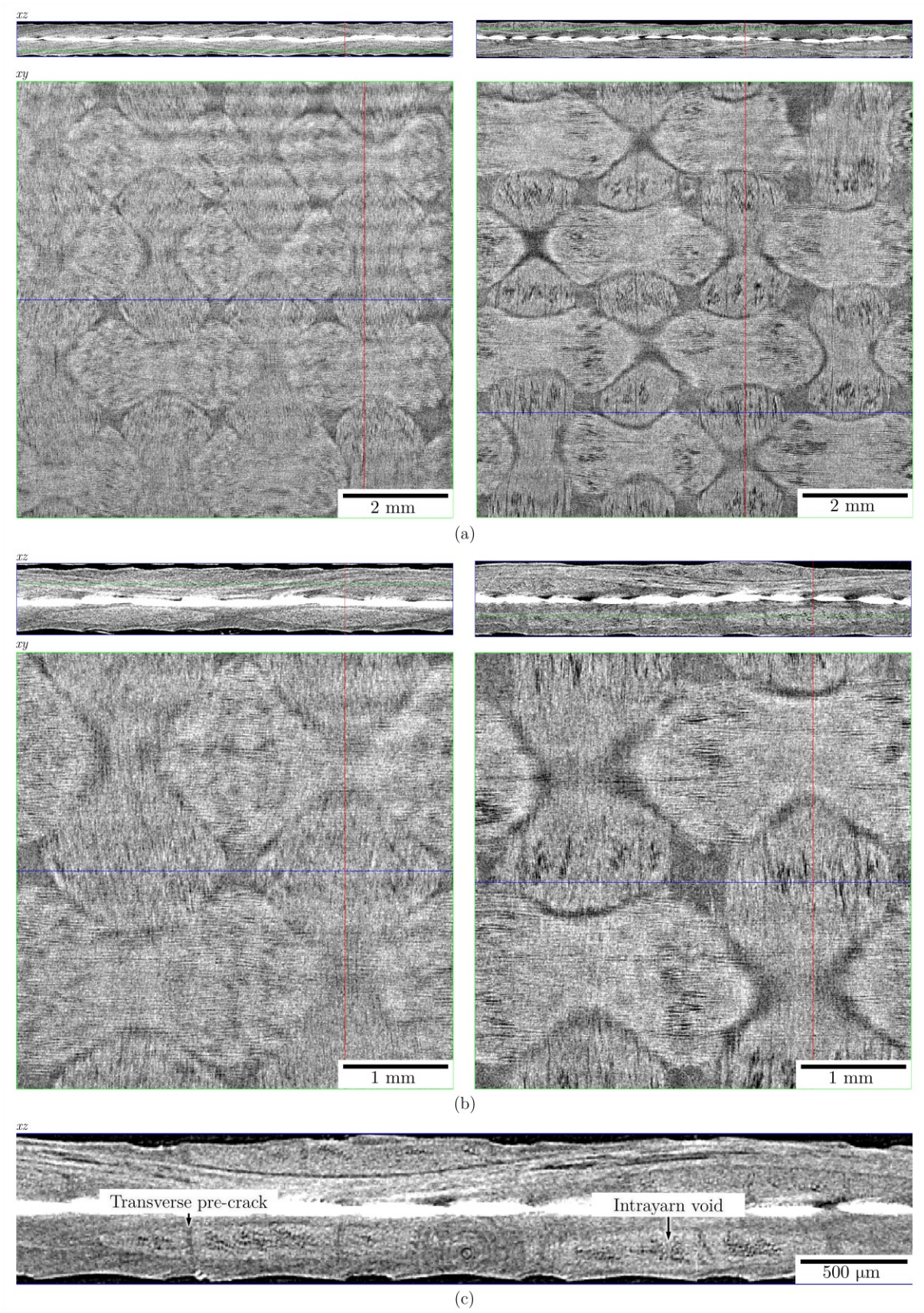

Figure 5.6. (a) Orthogonal projections from the CGC STR (left) and C*GC* STR (right) µCT reconstructions, containing: (a) four UCs, and (b) one UC; (c) detail of defects in C*GC* STR sample.

The void distribution agreed with that observed under μCT (Figure 5.6). Surface inspection revealed broken dry fibres near what were thought to be the peripheral regions of the interyarn voids, whilst towards the interior of the voids, large fibre segments had been removed during the polishing process. Crenulations were visible on the surfaces of the broken fibres, and they appeared devoid of any matrix, even at high magnifications at which the porous structure of CAG would be observable under scanning electron microscopy.

This morphology suggested an absence of both CAG and epoxy in the intrayarn voids. This hypothesis is consistent with recent fractographic analysis of the laminates [47], which reported poor wetting of the CAG-modified yarns with epoxy resin, indicating that epoxy infusion of the CAG nanopores may have been poor, leaving the interior yarn regions dry. The edges of an untested composite specimen (originally cut using a dry diamond saw, between sacrificial plates) were additionally observed under scanning electron microscopy. Across the edge surface, the 90° carbon yarns displayed large regions of fibres, which appeared to be poorly supported by matrix (Figure 5.9).

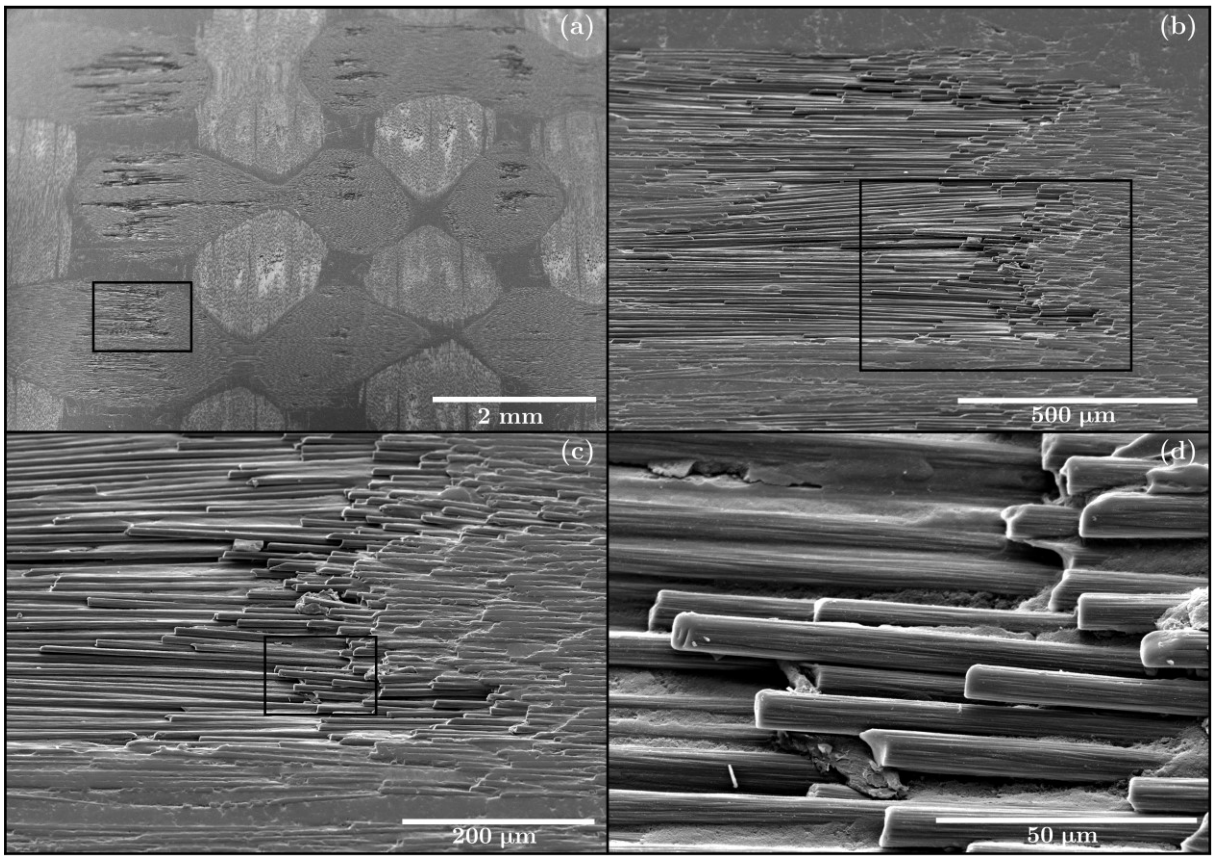

Figure 5.7. Scanning electron micrographs of the polished cross-section through the C*GC* STR laminate (35° surface tilt), showing transverse cracks and interyarn voids with fibres devoid of matrix.

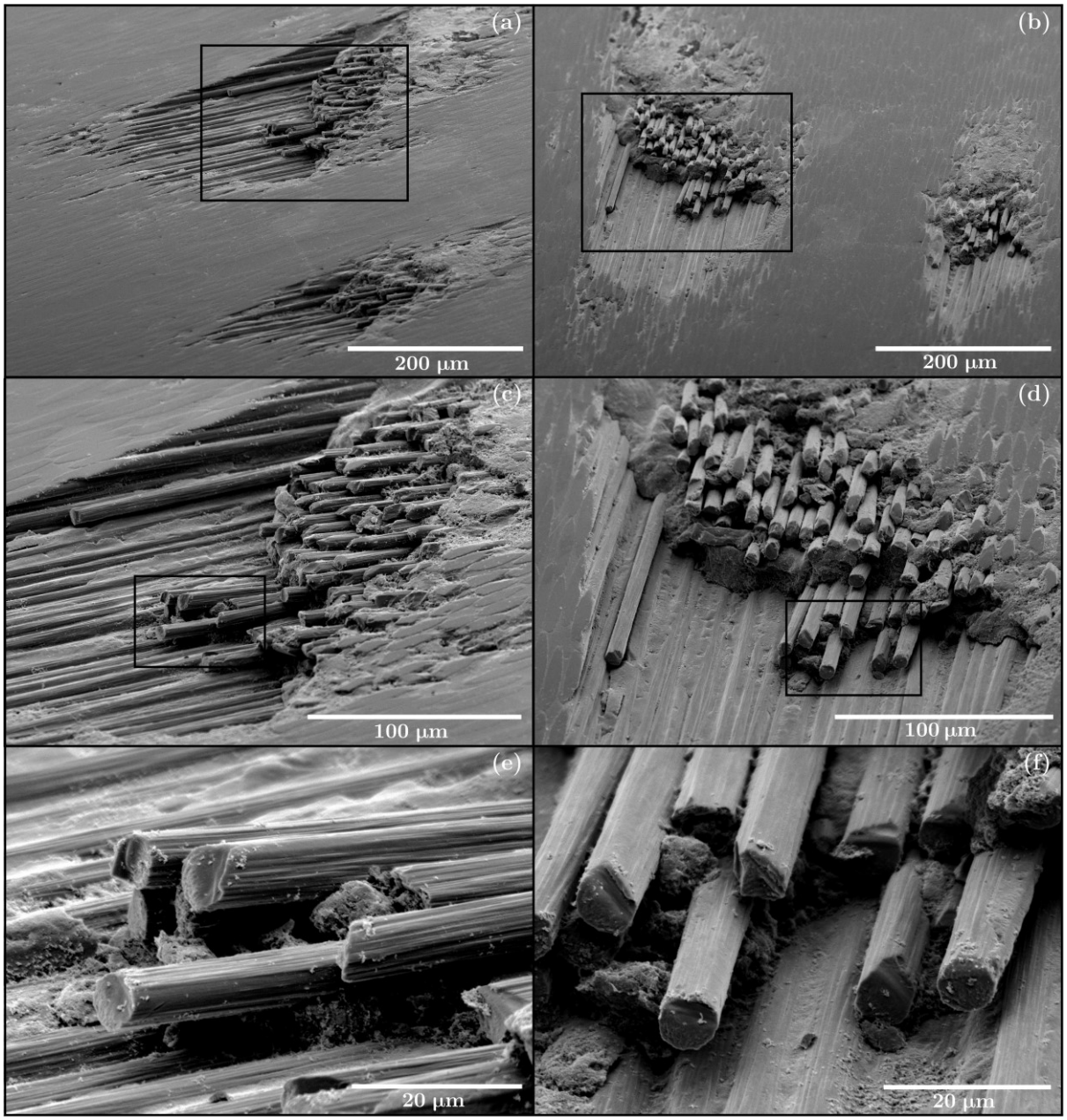

Figure 5.8. Scanning electron micrographs of the polished cross-section through the C*GC* STR laminate (50° surface tilt), showing interyarn voids with fibres devoid of matrix.

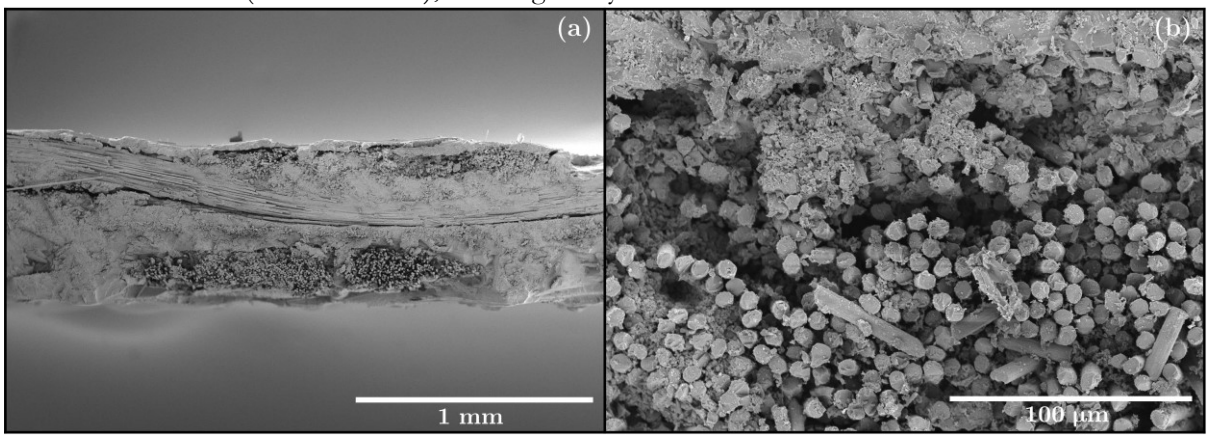

Figure 5.9. Scanning electron micrographs of the cut edge of an untested C*GC* STR composite coupon with 0/90° fibre orientation (no surface tilt), showing interyarn voids.

5.3.1.2 Multifunctional laminates

Optical microscopy of the C*GC* MF cross-sections (Figure 5.3(c)) revealed, in addition to back-filled transverse cracks in the carbon yarns, many interlaminar voids. These were either spherical or elongated in the interlaminar plane, with a maximum observed length ca. 900 μm, and a local radius ranging from 15 μm to more than 50 μm. The micrographs were manually segmented to highlight the void distribution (Figure 5.10). The rounded edges of the voids indicated they could have been filled with either air or IL, as a result of air entrapment or phase separation of the structural electrolyte, respectively [104].

Based on analysis of a limited number of samples, the largest voids appeared to have been localised near the interstitial regions of the carbon fabrics, resembling the typical void morphology for fabric composites manufactured via liquid composites moulding [236,237]. Scanning electron microscopy (Figure 5.11) confirmed that the interlaminar voids were also elongated in the orthogonal direction. The presence of the CAG and polishing debris prevented evaluation of the intrayarn matrix microstructure. Unlike the C*GC* STR samples, the MF samples showed no clearly identifiable regions of intrayarn voidage, though it can be assumed that voids associated with CAG infusion were present.

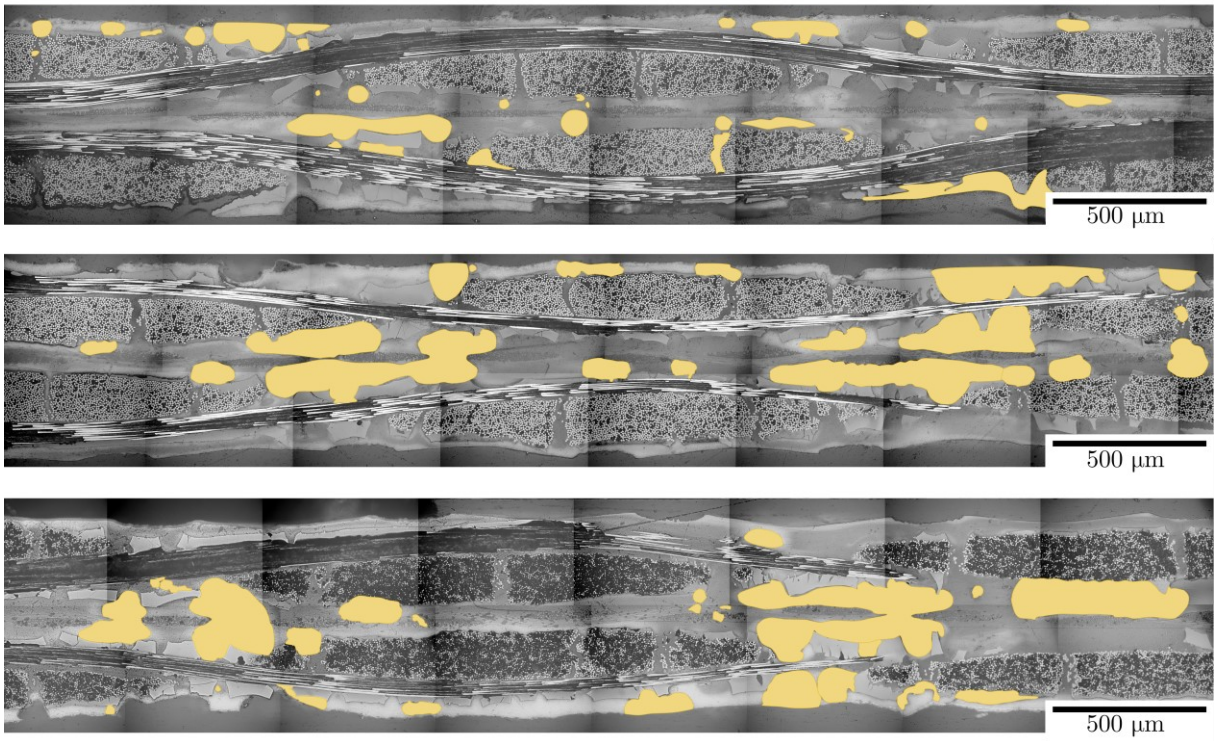

Figure 5.10. Optical micrographs of C*GC* MF laminate cross-sections, showing matrix voidage (highlighted in yellow).

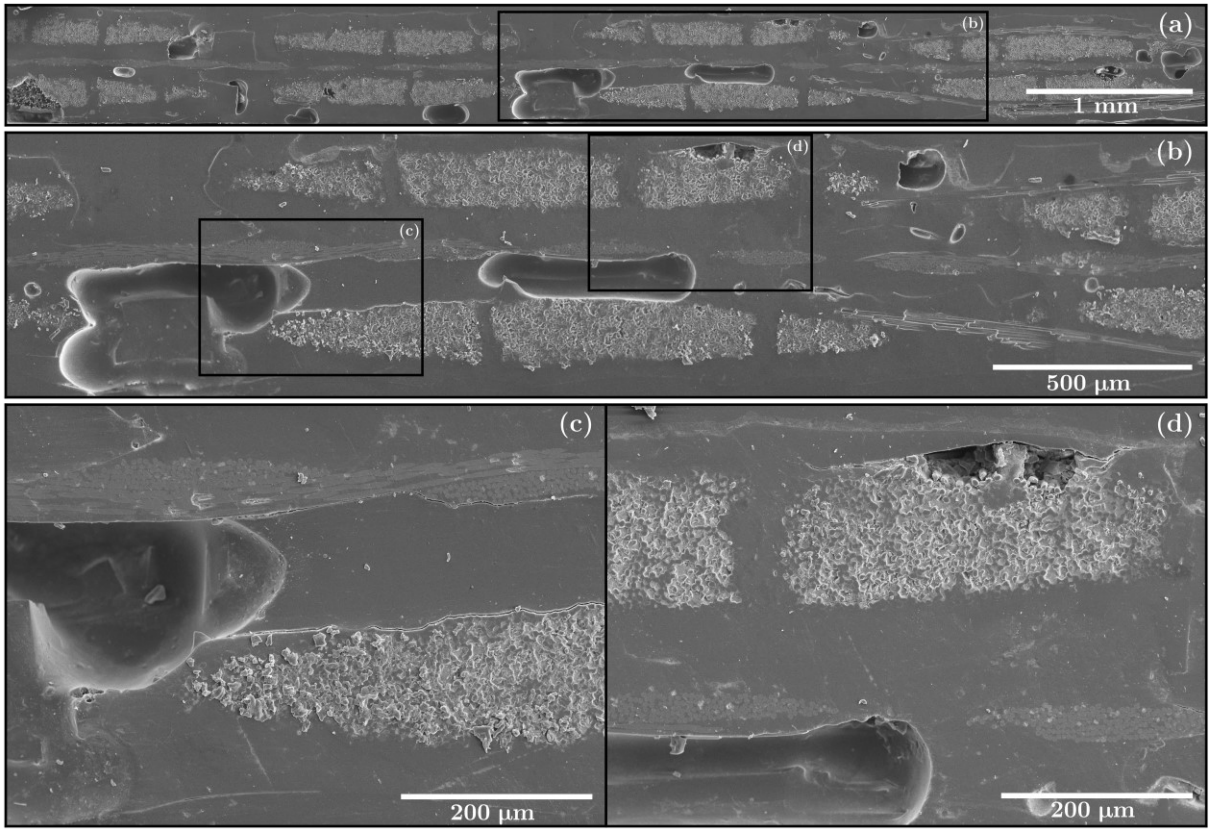

Figure 5.11. Scanning electron micrographs of a through-thickness cross-section of the C*GC* MF laminate (no surface tilt), showing large scale voids in the structural electrolyte.

5.3.2 Imaging of tensile fracture surfaces

To provide further insights into the composite microstructure, scanning electron microscopy was also performed on the fracture surfaces of a C*GC* STR composite specimen with 0/90° orientation, which had been tested to failure under tensile load [47]. The fracture morphology across the specimen is shown in Figure 5.12(a), with detail of the carbon ply shown in Figure 5.12(b). The latter image was centred on a 0° carbon yarn near the top surface of the specimen, and adjacent to the glass fibre ply.

The CAG skin layer on the lower surface of this carbon yarn was mostly intact, indicating a relatively strong interface between CAG and carbon fibre (or skin and core of the yarn). The surface of the CAG skin was smooth, suggesting a poor interface between the carbon and glass ply (inset in Figure 5.12(a)). In Figure 5.12(b), an epoxy-filled transverse pre-crack was observed separating the carbon yarn into two segments, left and right. The right segment presented a flat fracture surface, indicative of brittle fracture with very limited fibre debonding in this region, which has been linked to a strong fibre/matrix interface [104,238] with a large interfacial debond energy [94].

The left segment presented a mixed failure morphology, with the peripheral regions showing the flat morphology described above; and a central region presenting a broom-like failure, indicative of a weak fibre/matrix interface [94,104,238] or possibly a complete absence of any matrix. The latter morphology is consistent with poor infusion of both CAG precursor and epoxy in this region, agreeing with the previous observations on the untested laminates (Section 5.3.1.1). The ductile cohesive failure of the lower fracture surface of the epoxy-filled transverse pre-crack indicated the presence of a continuous region of epoxy across the carbon/glass ply interface in the vicinity of the pre-crack. A matrix pocket near an interstitial site within the lower carbon ply was also observed to have failed cohesively (lower left of Figure 5.12(a)).

Within the region shown in Figure 5.12(b), the global direction of failure appears to have been right-to-left: proceeding from the right segment, through the transverse crack, to the left segment and upper region of epoxy. This sequence is evidenced by 'riverline' features [104] in the upper half of the pre-crack region. Local fibre failures, marked (1), appear to have triggered failure in the surrounding CAG skin and/or fibres, indicated by the orientation of radial riverlines in the CAG skin, and that of the radial 'mirror-mist-hackle' morphology at the fibre ends, respectively. The latter is otherwise known as directly attributable fibre failures (DAFFs) [104]. The continuity of the fracture plane in the right half of the image suggests that these regions failed together in a brittle manner with little fibre debonding or pull-out. The significance of this planar morphology is further discussed in Section 8.2.3.

Additional riverline features in the upper portion of the epoxy matrix indicate failure of this region propagated from the sharp corners of the CAG skin regions, marked (2), possibly via delaminations at their interface. Additionally, riverlines in the epoxy near the top fibre marked (1) suggest failure of the epoxy in that region directly propagated from the CAG skin to the left. Fibre disbonds were also seen near the periphery of yarn segments, marked (3), however, given the fracture plane was continuous across these cracks, they are likely to have formed as secondary damage.

Whilst it was possible to differentiate between regions of pure epoxy and regions containing CAG, it was difficult to determine whether the latter also contained epoxy. Differences in local matrix texture and hue near the periphery of the yarn segments, marked (4), suggest partial infusion of epoxy into the CAG.

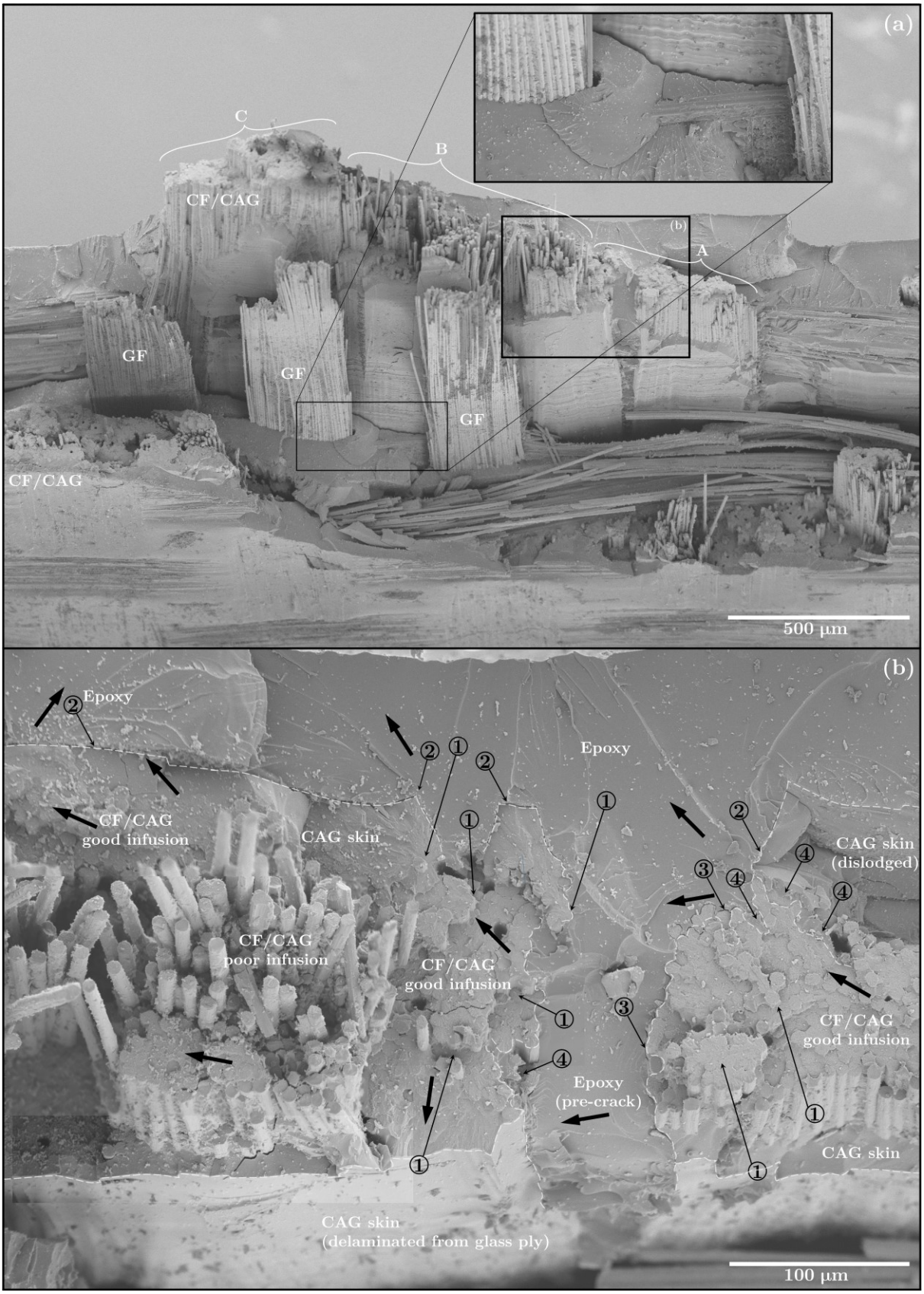

Figure 5.12. Scanning electron micrograph of the longitudinal tensile fracture surface of a C*GC* STR test coupon with 0/90° fibre orientation, showing (a) fracture morphology across all plies, with inset showing ply interface (ca. 60° surface tilt), and (b) fracture morphology across the carbon ply, annotated to show features of interest, perimeter of CAG skin (dash line) and directions of crack growth (ca. 20° surface tilt, stitched).

After the brittle failure of the yarn region in the right half of Figure 5.12(b), marked A in Figure 5.12(a), failure is likely to have propagated right-to-left through the rest of the yarn, with two distinct failure regions apparent from the later micrograph. Region B presented a broom-like failure morphology, in stark contrast to region C, which presented a flat fracture surface. The shape and location of region B closely agreed with the previous X-ray observations (Section 5.3.1.1), supporting the hypothesis that this region was poorly infused with CAG and epoxy.

Comparison of the failure morphologies of the 90° carbon yarns of the upper and lower carbon plies also revealed two distinct failure morphologies. In the top ply the fracture surface was relatively flat fracture surface with fibres surrounded by matrix, whilst the lower ply (Figure 5.12(a), bottom right) failure was again broom-like, with unsupported fibres

5.3.3 High magnification scanning electron microscopy of CAG

Scanning electron microscopy was used to assess whether a skin/core morphology was present in the CAG monolith specimen (described in Section 5.2.1) and the dry CAG-modified carbon fabric (C*). The microstructure near the upper surface of the monolith specimen (Figure 5.13, right) showed no significant difference to that in its core (Figure 5.13, left), with both regions presenting a bicontinuous microstructure. This absence of a skin/core structure differed from findings from the HiPerDuCT project [78], though this was not surprising as the precursor and drying procedures differed (D. Anthony, personal communication, 1 Sept 2021).

The observed morphology of the C* fabric was consistent with those observed during previous studies by the Group [22,209], presenting a bicontinuous microstructure, which slightly varied across the specimen. The microstructure of CAG surrounding fibres near the yarn/yarn interface (Figure 5.14, left) was compared with that within the CAG layer on top of the fabric (Figure 5.14, right). The microstructure in both regions was skeletal, however in the latter there was greater apparent tortuosity. Comparisons were complicated by differences in the manner the two surfaces were generated: by sliding a yarn out in the former, and during drying of gelled precursor in the latter. The two regions were also imaged at different angles: the former was observed perpendicularly, whilst the latter was observed obliquely, which possibly contributed to an apparent difference in texture by increasing shadowing and contrast [104], enhancing the appearance of surface relief.

Finally, the morphology of the monolithic CAG (Figure 5.13) was compared to that of the *in situ* CAG in the dry C* fabric (Figure 5.14). The microstructures across both specimen types presented bicontinuous features, with a subtle difference in the apparent tortuosities. As variation in the local apparent tortuosity had also been observed across the C* fabric, this difference was considered to be within the range of microstructural variability within the fabric (D. Anthony, personal communication, 1 Sept 2021). The monolith was therefore deemed suitable for further mechanical characterisation (Section 5.3.4) to enable initial estimates for the elastic properties of the CAG-modified SSC laminates (Section 5.5).

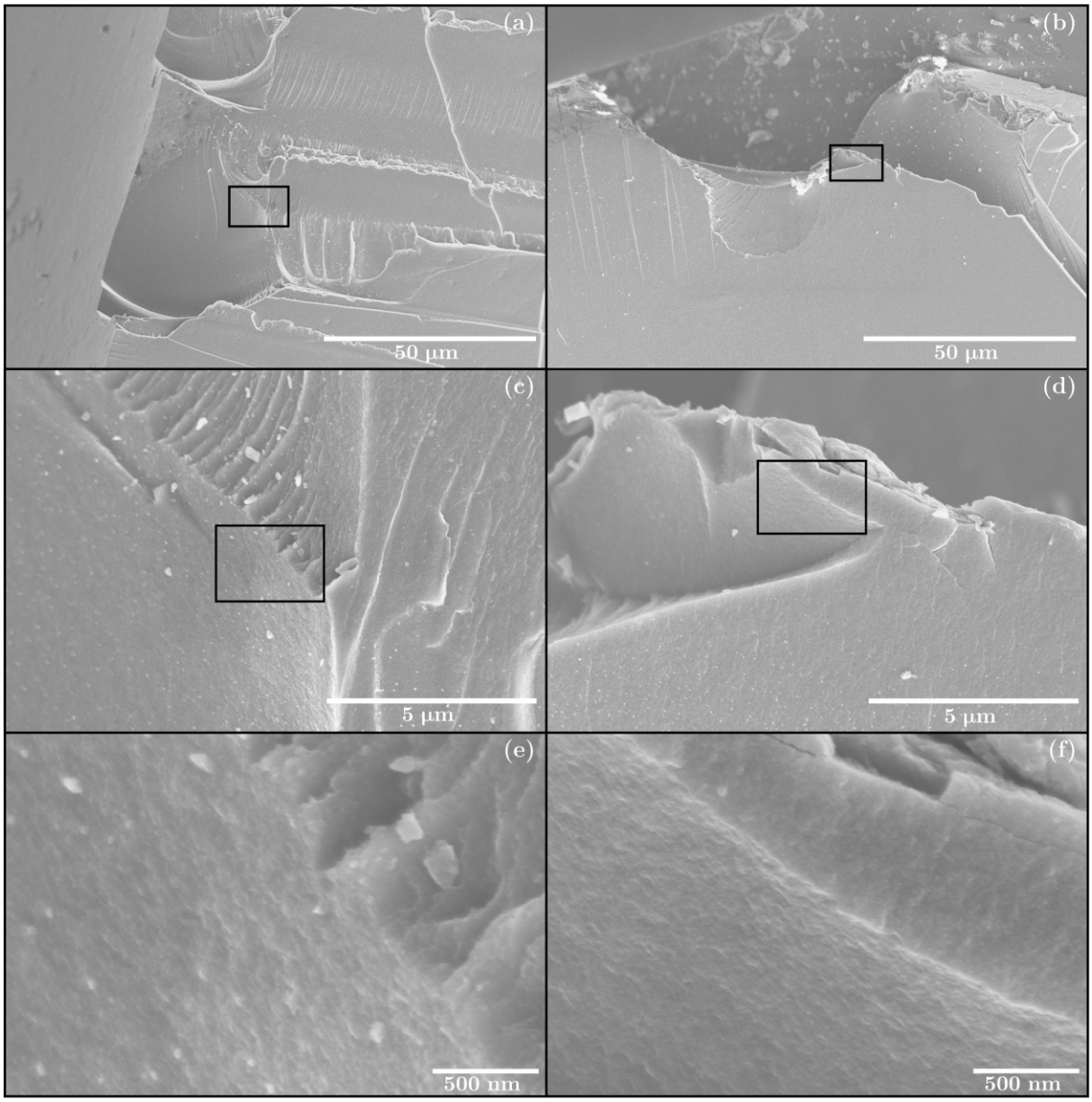

Figure 5.13. Scanning electron micrographs of the fracture surfaces of the CAG monolith, showing: (a), (c) and (e) a region near the centre of the specimen; and (b), (d) and (f) a region near the top surface.

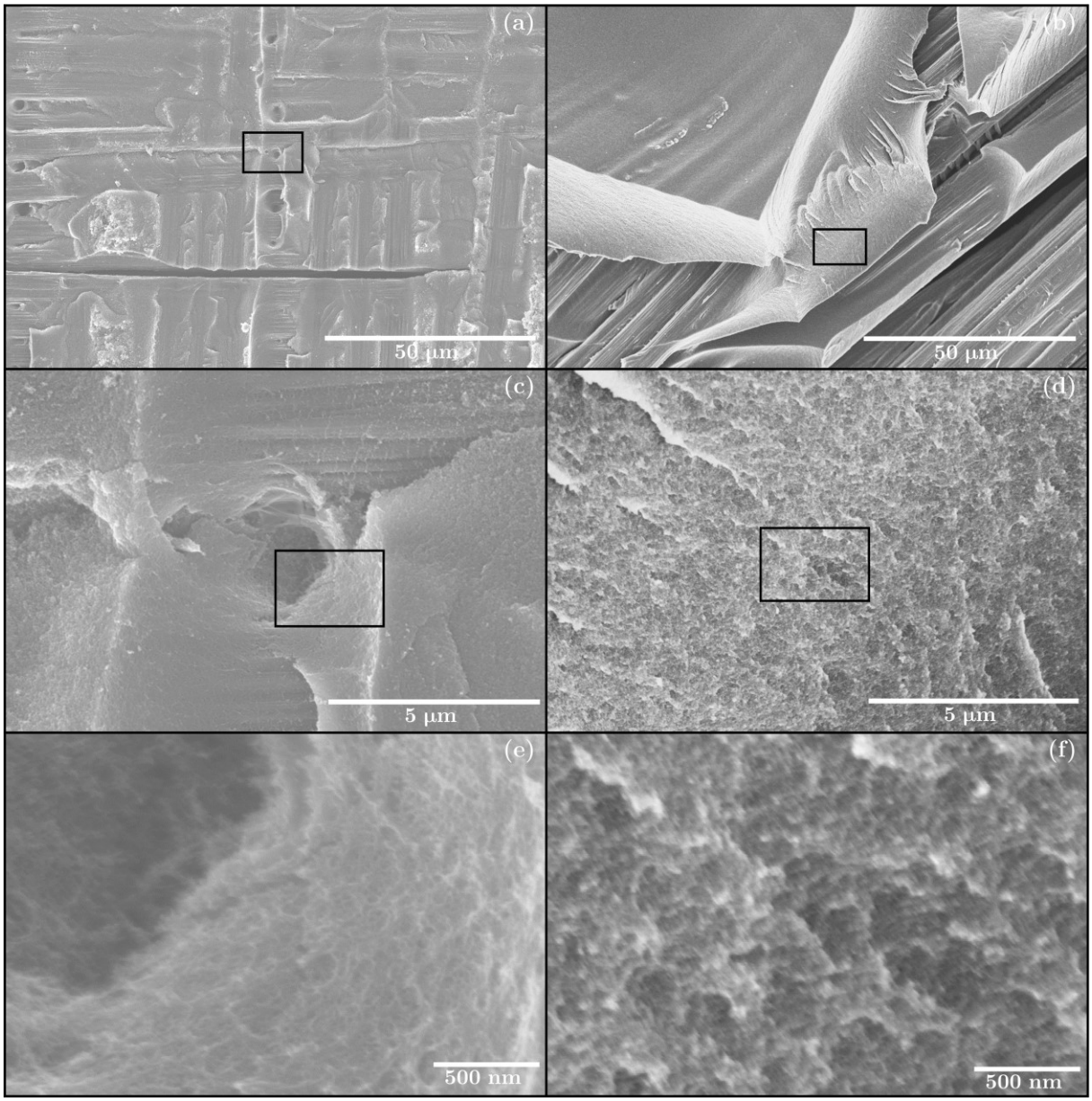

Figure 5.14. Scanning electron micrograph of the internal surfaces of the dry C* fabric, showing: (a), (c) and (e) a region near the fibres; and (b), (d) and (f) a thicker CAG layer on top of the fabric

5.3.4 CAG compliance characterisation by nanoindentation

Load-indentation depth curves characteristic of brittle solids were obtained for the monolithic CAG (Figure 5.15(a)) [85]. The Young's modulus was calculated according to the procedure outlined in Section 5.2.2 across a range of indentation maximum loads (Figure 5.15(b)). An average Young's modulus of 23.1 ± 1.7GPa for the CAG monolith was measured in the 0.4 to 1.2 μm depth range, whilst the average hardness was 3.8 ± 0.4 GPa (plot omitted for brevity). This modulus value was approximately eight and thirty times higher than those of the epoxy and structural electrolyte, respectively (Table 5.1), justifying its direct use in the model parametrisation (Section 5.4.4).

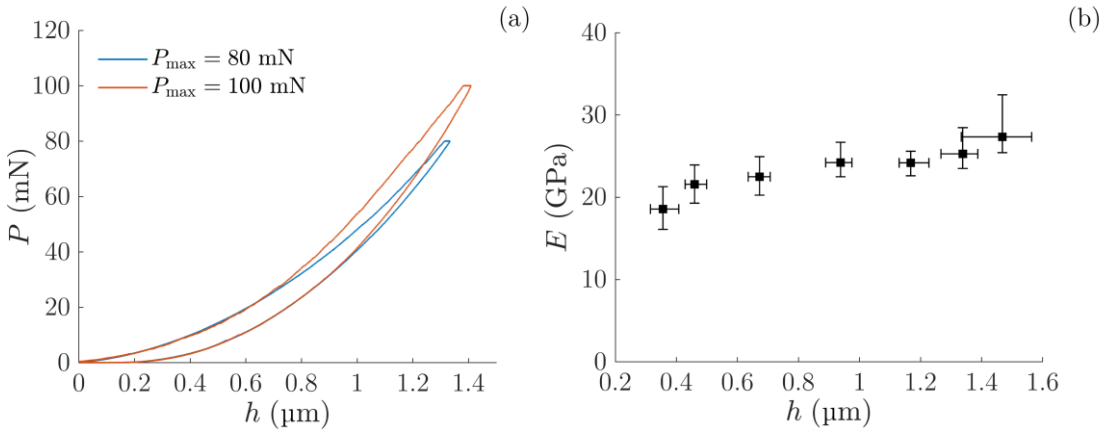

Figure 5.15. (a) Typical indentation curves for 80 mN and 100 mN peak loads, and (b) measured Young's modulus versus indentation depth for the CAG monolith.

5.4 Computational model development

5.4.1 Geometry

5.4.1.1 Reinforcement compaction

The procedure for generating realistic mesoscale unit cell models of the composite laminates (Section 5.2.1.1) is depicted in Figure 5.16. With the aim of reducing pre-processing and computational effort, a quasi-mesoscale modelling approach was taken, in which the architecture of the carbon fabric was represented at the mesoscale, whilst the finer glass ply was modelled as a homogenised continuous layer with transversely isotropic material behaviour. The final thickness of the reinforcement stack was 536 µm, chosen to match the averaged local thickness of the C*GC* STR laminate, as measured from optical micrographs of the through-thickness cross-sections (Section 5.3.1, Figure 5.3).

Considering the high sensitivity of the internal morphology to ply offset (previously demonstrated in Section 4.4.2), and its likely influence on composite elastic properties, several ply offset models of equal thickness were considered. Unit cells were generated with the in-phase (IP), 90° out-of-phase (90°OP) ply offsets introduced in Chapter 3, as well as the symmetric 180° out-of-phase (180°OP) case (Figure 5.17). Following the observations reported by De Carvalho [136], it was assumed that, for a given laminate thickness (volume fraction), these models would provide a representative limiting range of elastic properties. Experimental results from physical specimens with arbitrary ply offsets could then be expected to fall within this limiting range. However, it should be noted that in that work only the IP and 180°OP configurations were considered.

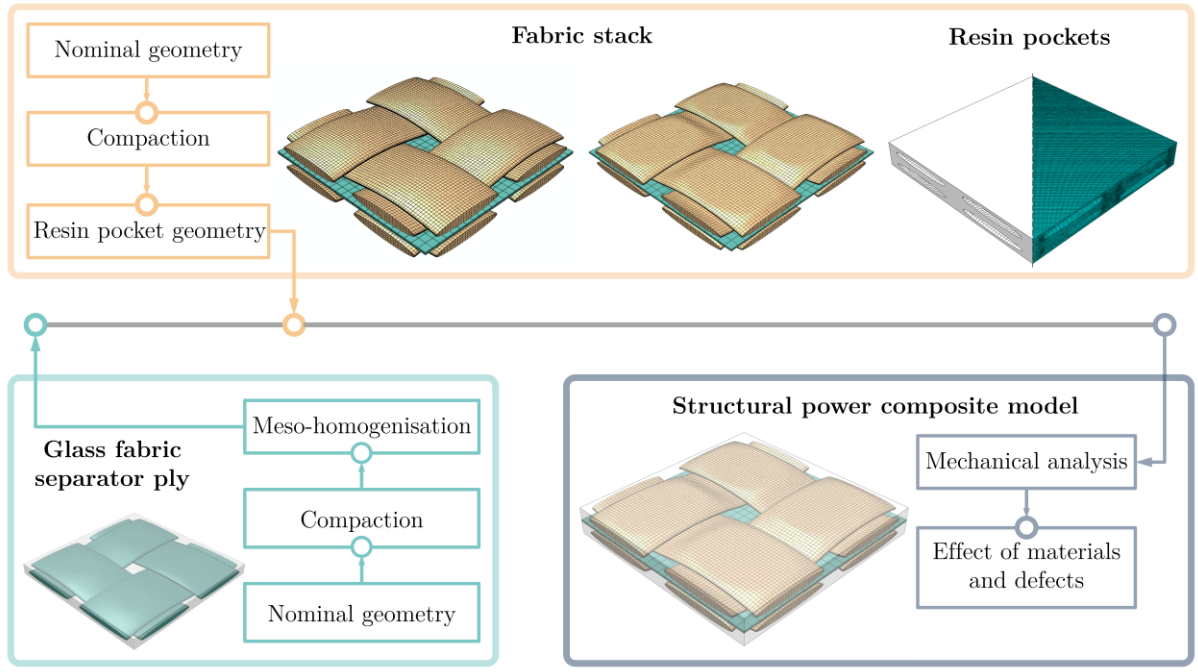

Figure 5.16. SSC mechanical model generation and analysis workflow.

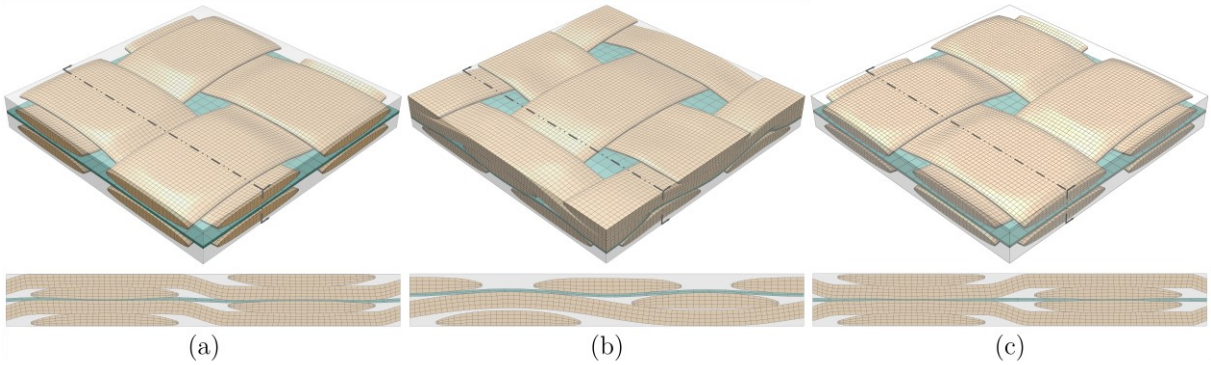

Figure 5.17. SSC unit cell geometries with (a) IP, (b) 90°OP and (c) 180°OP ply offsets.

The geometry of the laminate reinforcements was obtained from a compaction simulation, following a slightly modified version of the methodology described in Chapter 4, where the glass ply was modelled as a transversely isotropic continuous layer (Figure 5.16). In all geometric configurations, the glass ply thickness and the total thickness of the compacted reinforcements were chosen to match their corresponding average values in the C*GC* STR laminate (50.6 μm and 536 μm, respectively), as measured from the micrographs (Figure 5.3).

5.4.1.2 Compacted reinforcement geometry reconstruction

Following the fabric stack compaction simulation, it was necessary to import the deformed yarns as solid geometric objects in a new model. Abaqus CAE 2017 did not support this workflow: parts could be accurately imported from an output database only as

orphan meshes (meshes with no associated parent geometry [222]), which were unsuitable for the geometric Boolean operations required to construct the matrix pockets. A geometry reconstruction algorithm was therefore developed, in which element edge information was read from the output database of the compaction model and used to construct a wire skeleton of each yarn. Closed wire loops on the external yarn surface were detected and covered with shell faces. Finally, the yarn shell was converted to a solid volume.

5.4.1.3 Resin pocket geometry

The matrix pockets occupying the space around the yarns were constructed by performing a Boolean cut operation between a nominal matrix volume and the geometric reconstructions of the yarns. The nominal matrix volume was generated with in-plane dimensions exactly matching the UC dimensions of the compacted fabric stack. To reproduce the observed laminate microstructures (Figure 5.3) and simplify model generation, the thickness of the matrix was increased by 5 μm on either side of the fabric stack. The total fibre volume fraction of the UC models was 43.6%, closely matching the reported values [47].

To overcome errors in the Boolean operations (associated with small voids and overclosures at contacting interfaces), a yarn contact zone detection algorithm inspired by the work of Wehrkamp-Richter [116] was developed, based on a logical statement performed for each yarn pair, comparing the distance between arbitrary surface node pairs with a user-defined radius of separation. For yarn pairs with multiple contact zones, a K-means clustering algorithm [239] was additionally implemented to group the nodes according to their respective zone. A convex hull algorithm [240] was then used to construct a 2D closed perimeter encompassing the nodes from each group, which subsequently defined a solid extrusion, linking the yarns at their respective contact zones.

Once the Boolean cut was performed, the modified yarn geometries were discarded from the model and replaced by the orphan meshes of the compacted yarns. The procedure was validated by visual inspection of the contact zone and resulting geometry. The Boolean cut procedure remained prone to failure when applied to the 90°OP model due to the highly three-dimensional contact surfaces between the carbon yarns and the glass ply. To circumvent this issue, and to maintain uniformity, for all configurations the embedded element technique (described in Section 5.4.3) was instead applied to the glass ply, which was justified by the relatively small volume occupied by the glass ply (5%).

5.4.2 Domain discretisation

The carbon and glass yarns were re-imported as orphan meshes, and therefore retained the periodic meshes used in the earlier compaction simulation (Section 4.3.1). Solid first order elements with incompatible modes (C3D8I) were used. The carbon ply was meshed with 2142 elements per yarn and four elements through the thickness, with a 60 μm average element edge length, based on the previous mesh refinement study (Chapter 4). Since the yarns were re-imported as orphan meshes from the compaction simulation, they retained their periodic mesh structure. Based on mesh refinement studies, which showed a negligible change in the effective elastic moduli (<1.5%) when the mesh density was doubled in every direction, the glass ply was meshed with 1250 (25×25×2) elements.

The matrix pockets were discretised using solid quadratic tetrahedral elements (C3D10). To ensure a periodic matrix mesh of sufficient quality could be generated, it was necessary to use elements with an average edge length of 30 μm, resulting in meshes containing ca. 1.20×10^6 elements in the IP and 180°OP cases, and 0.85×10^6 elements in the 90°OP case. Solution convergence was verified by demonstrating a negligible change (<0.1%) in the effective moduli obtained from models generated with an average edge length of 40 μm. The periodic matrix meshes were created as follows:

- An initial matrix mesh was constructed by 'edge seeding', enforcing a specified number of elements to be formed along the side edges of the matrix volume, and allowing an automated solid tetrahedral mesh to be generated accordingly.
- Offset shell mesh copies of the external faces of the above mesh were generated via the 'Mesh Edit' toolbox (only one surface was copied per face pair).
- The initial mesh was discarded, and the offset shell mesh copies were transferred back onto the external surfaces of the matrix, ensuring paired faces received identical surface meshes. A solid tetrahedral mesh was generated, respecting the periodic surface meshes.

5.4.3 Boundary conditions and loads

The contact detection algorithm (Section 5.4.1.3) was applied to the carbon yarns to define the interactions in the yarn/yarn and yarn/matrix contact regions by defining pairs of corresponding 'master' and 'slave' contact surfaces. A surface-to-surface tie constraint formulation was applied for the elastic simulations performed in this work. An embedded

region constraint [222] was used to constrain the nodal displacements of the glass ply to those of the embedding matrix mesh. Due to rotational symmetry in the xy plane, four displacement-controlled load cases were sufficient to perform elastic homogenisation (detailed in Section 5.4.5): the normal and shear global strains $\varepsilon_{11}, \varepsilon_{33}, \gamma_{12}$ and γ_{23}. These strains were applied though in-plane periodic boundary conditions. The implementation combined (i) multi-point constraint equations [222] (Appendix B.1) linking the displacements of individual boundary node pairs through those of a set of imaginary master nodes, and (ii) displacement boundary conditions defined at the master nodes, specifying the global displacement state. To prevent over-constraining the model, slave nodes used in pre-existing tie constraints and multi point constraint equations were excluded from further constraints. To simulate the experiments in Ref. [47]:

- out-of-plane rotations were constrained by setting the out-of-plane master node displacements to zero;
- periodic Poisson strains were permitted by setting the relevant master node displacements to an unspecified value ('UNSET');
- laminate surfaces were allowed to deform freely (free surface).

Implicit in the use of the free surface boundary condition is that a 'single SSC cell' (or its structural equivalent) was simulated. To understand the influence of free surface effects [132,133] (see Section 2.4.2.2) on the mechanical properties of the system investigated here, 'double cell' and 'infinitely thick' stacks were additionally simulated. In both cases, in-plane periodicity was retained; however, the out-of-plane boundary condition was replaced by either: (i) a free surface and a symmetry surface condition; or (ii) a periodic boundary condition, respectively. The results of these additional studies are reported in Appendix B.2.

5.4.4 Constitutive model

5.4.4.1 Resin pockets

A homogenous isotropic elastic material model was specified for the resin pockets, with using the engineering constants of the structural (STR) or multifunctional (MF) matrix systems, as appropriate. Literature values of the properties of these systems were used (Table 5.1). The bulk properties of the structural electrolyte (34 vol.% EMIM-TFSI) were estimated by linear interpolation of literature data [241] available for the 33 vol.% and 35 vol.% EMIM-TFSI formulations.

A parametric study was performed in which the value of the Young's modulus of the structural electrolyte, $E_{\mathrm{m,MF}}$, was set to 150 MPa, 300 MPa, 1500 MPa. A second parametric study was also performed to understand the influence of the Young's modulus of the CAG, $E_{\mathrm{m,CAG}}$, on the elastic response. In this study, the nominal value of $\boldsymbol{E_{\mathrm{m,MF}}}$ was used, whilst the value of $E_{\mathrm{m,CAG}}$ was set to 5 GPa, 10 GPa and 35 GPa.

5.4.4.2 Carbon yarns

The carbon yarns were modelled as homogenous transversely isotropic continua (the approach used in Chapter 4). The local fibre orientation and fibre volume fraction within each element was obtained from the compaction simulation (Chapter 4). The elastic properties within each yarn element were calculated according to the Chamis micromechanics equations [242], using literature values for the elastic properties of the carbon fibres (Table 4.6) and the matrix (Table 5.1), at the corresponding fibre volume fraction and orientation.

In the model without CAG (CGC), the properties of the STR matrix were assumed for the matrix material. Since CAG functioned as a stiff reinforcement filling the space between the fibres [24], in the models with CAG (C*GC*), CAG was conceptualised as the matrix material within the yarns. The elastic modulus measured from nanoindentation of the CAG monolith (Section 5.3.4) was assumed for the matrix material in the C*GC* models.

A set of defect-containing (DEF) models were generated to assess the effect of the back-filled transverse pre-cracks observed in the C*GC* laminates (Section 5.3.1) on mechanical properties. The distribution of these fibre free bands was approximated in the model as periodic and equispaced across the yarn width. In both the warp and weft yarns, the fibre-free bands were specified as one-element-wide (66 μm), such that 10% of the nominal yarn volume was fibre-free (Figure 5.18). These elements were assigned the material properties of the global matrix system (STR or MF). The nominal yarn cross-section was assumed unchanged by the presence of the pre-cracks, and the yarn segments were assumed to have been uniformly densified. A constant fibre volume fraction scaling factor was applied to the yarn segments, such that the same total fibre volume fraction was maintained across all the models.

Table 5.1. Elastic properties of the matrix materials.

Matrix material	E_m (GPa)	ν_m (–)
STR	2.74 [243]	0.34 [244]
MF	0.76 [241]†	0.30*
CAG	23.12	0.30*

† and * indicate interpolated and assumed values, respectively.

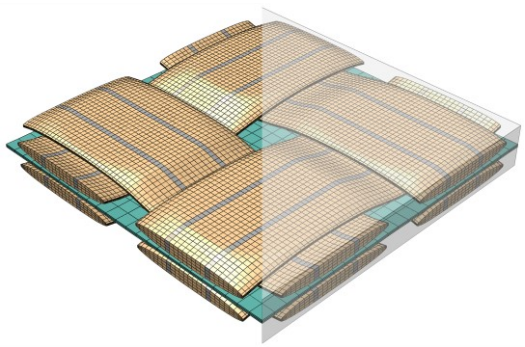

Figure 5.18. SSC unit cell model with transverse pre-cracks shown in grey (DEF).

5.4.4.3 Glass ply

A mesoscale UC model of the glass fibre composite ply was generated following the workflow described in the previous Sections, with a thickness equal to the average measured from optical micrographs of the composite laminates (50.6 μm). Glass plies made with structural and multifunctional resin were considered (denoted G STR and G MF, respectively). The ply-level properties were obtained by the meso-homogenisation procedure detailed in Section 5.4.5. The resulting five elastic constants obtained for each matrix configuration (Table 5.2) were used to define the elastic constitutive response of the homogenised transversely isotopic glass ply in the composite laminate models.

5.4.5 Post-processing, experimental and analytical comparisons

For the meso-homogenisation step, the generalised elastic constitutive relation between stresses and strains (Hooke's law) was assumed [245]:

$$\sigma_i = C_{ij}\varepsilon_j \qquad i,j = 1 \ldots 6 \quad , \tag{5.4}$$

where contracted (Voigt) notation is used: σ_i are the principal stress components ($\sigma_{11}, \sigma_{22}, \sigma_{33}, \tau_{12}, \tau_{13}, \tau_{23}$ in tensor notation), ε_j are the principal strains ($\varepsilon_{11}, \varepsilon_{22}, \varepsilon_{33}, \gamma_{12}$, γ_{13}, γ_{23} in tensor notation) and C_{ij} is the elasticity tensor. The homogenised principal strains $\varepsilon_i = 0.1\%$ were individually applied to the UCs through the periodic boundary conditions (Appendix B.1). The internal stress components were volume-averaged over the UC:

$$\bar{\sigma}_i = \frac{1}{V}\int_V \sigma_i dV \tag{5.5}$$

to obtain the homogenised elastic moduli (E_{11}, E_{22}, E_{33}, G_{12}, G_{13}, G_{23}). To correct for the embedment of the glass ply, the volume and stresses of the embedding matrix elements were discounted from the above. The Poisson's ratios (ν_{ij}) were calculated as:

$$\nu_{ij} = -\frac{\varepsilon_j}{\varepsilon_i} \qquad i,j = 1,2,3 \quad . \tag{5.6}$$

The predicted properties were compared against experimental data (Table 5.3).

Additionally, a comparison was made with the predictions made by a modified version of the slice array model (SAM) developed by Naik and Ganesh [120] for the in-plane elastic properties of plain weave fabric composites. The model utilises sinusoidal shape functions for the meso-scale geometry of the weave, accounting for gaps between adjacent yarns, elliptical yarn cross-sections and matrix pockets. The effective elastic constants are averaged over a series of slices through the unit cell, first idealising each slice as a four-ply laminate. The slices are then assembled via classical laminate theory (CLT).

In the present implementation of the SAM, the Chamis micromechanics equations were used to calculate the local elastic properties of the yarns based on the fibre and matrix properties. A uniform fibre volume fraction was assumed within the yarns (64.5% and 53% for the carbon and glass yarns, respectively), such that the total volume fraction of the unit cells matched those in the FE models. The ply thicknesses were uniform, and based on the thicknesses in Section 5.4.1.1. The carbon and glass plies were assembled by CLT to obtain the effective elastic properties of the SSC laminates.

Table 5.2. Elastic properties of homogenised glass fibre composite ply.

System	$E_{11} = E_{22}$ (GPa)	E_{33} (GPa)	G_{12} (GPa)	$G_{13} = G_{23}$ (GPa)	ν_{12}	$\nu_{13} = \nu_{23}$
G STR	13.17	6.28	2.48	1.17	0.10	0.14
G MF	10.85	1.80	0.76	0.34	0.15	0.05
G $MF_{150\ MPa}$	8.43	0.37	0.15	0.07	0.25	0.01
G $MF_{300\ MPa}$	9.54	0.73	0.30	0.14	0.21	0.02
G $MF_{1500\ MPa}$	11.90	3.41	1.45	0.67	0.11	0.08

Subscripts refer to the Young's modulus of the structural electrolyte used in the parametric study.

Table 5.3. Experimental data on the mechanical properties of composite laminates in Ref. [47].

System	V_f^{total} (%)	E_{11} (GPa)	σ_{11}^* (MPa)	G_{12} (GPa)	$\tau_{12}\vert_{\gamma_{12}=1\%}$ (MPa)
CGC STR	44.2	40.0	394.0	3.2	30.2
C*GC* STR	43.0	38.6 (–4%)	123.9 (–69%)	3.1 (–3%)	24.1 (–20%)
C*GC* MF	45.4	32.9 (–18%)	110.4 (–72%)	1.7 (–47%)	13.7 (–55%)

5.5 Computational model results

5.5.1 Effect of ply offset

The homogenised tensile and in-plane shear moduli, E_{11} and G_{12}, were calculated for the IP, 90°OP and 180°OP ply offset models (Figure 5.19(a) and (b), Table 5.4). The difference between the maximum and minimum values obtained was largest in the C*GC* MF configuration (19% for E_{11} and 51% for G_{12}). The IP model presented the lowest E_{11}, while the 90°OP and 180°OP performed similarly (relative difference within 4%). The 90°OP case had the highest G_{12}, while the IP and 180°OP responses were similar.

5.5.2 Comparison with analytical predictions

The numerical predictions were those of the slice array model (SAM) described in Section 5.4.5 (Figure 5.19(a) and (b), Table 5.4). The analytically predicted E_{11} were systematically lower than the corresponding FE predictions, but within 10% of the values from the IP model. Conversely, the analytical G_{12} predictions were close to the maximum predicted by the FE models, lying within 10% of the corresponding 90°OP model results.

5.5.3 Effect of constituents and defects

The minimum and maximum values of the numerical predictions in Table 5.4 were used to calculate an average and indicative range for each material configuration, plotted in Figure 5.19(c) and (d) against the experimental measurements (average ± one standard deviation) and analytical SAM predictions. CAG modification was predicted to increase the E_{11} and G_{12} of the structural laminates by 13% and 225%, respectively, relative to the baseline laminate. Improvements were retained in the presence of pre-cracks (DEF) (+11% and +105%), as well as in the multifunctional laminates with pre-cracks (+1% and +16%).

For the baseline structural laminate, good agreement was achieved with the tensile experiment, with the IP model providing the closest prediction (−4%). The shear modulus of the baseline laminate was slightly underpredicted, with the closest prediction made by the 90°OP model (−9%). The CAG-modified DEF models overpredicted E_{11} by +22% and +32% in the structural and multifunctional cases, respectively. Overprediction was even more severe for G_{12} (+81% and +82%), although the error was significantly reduced compared to the defect-free models (+180% and +280%).

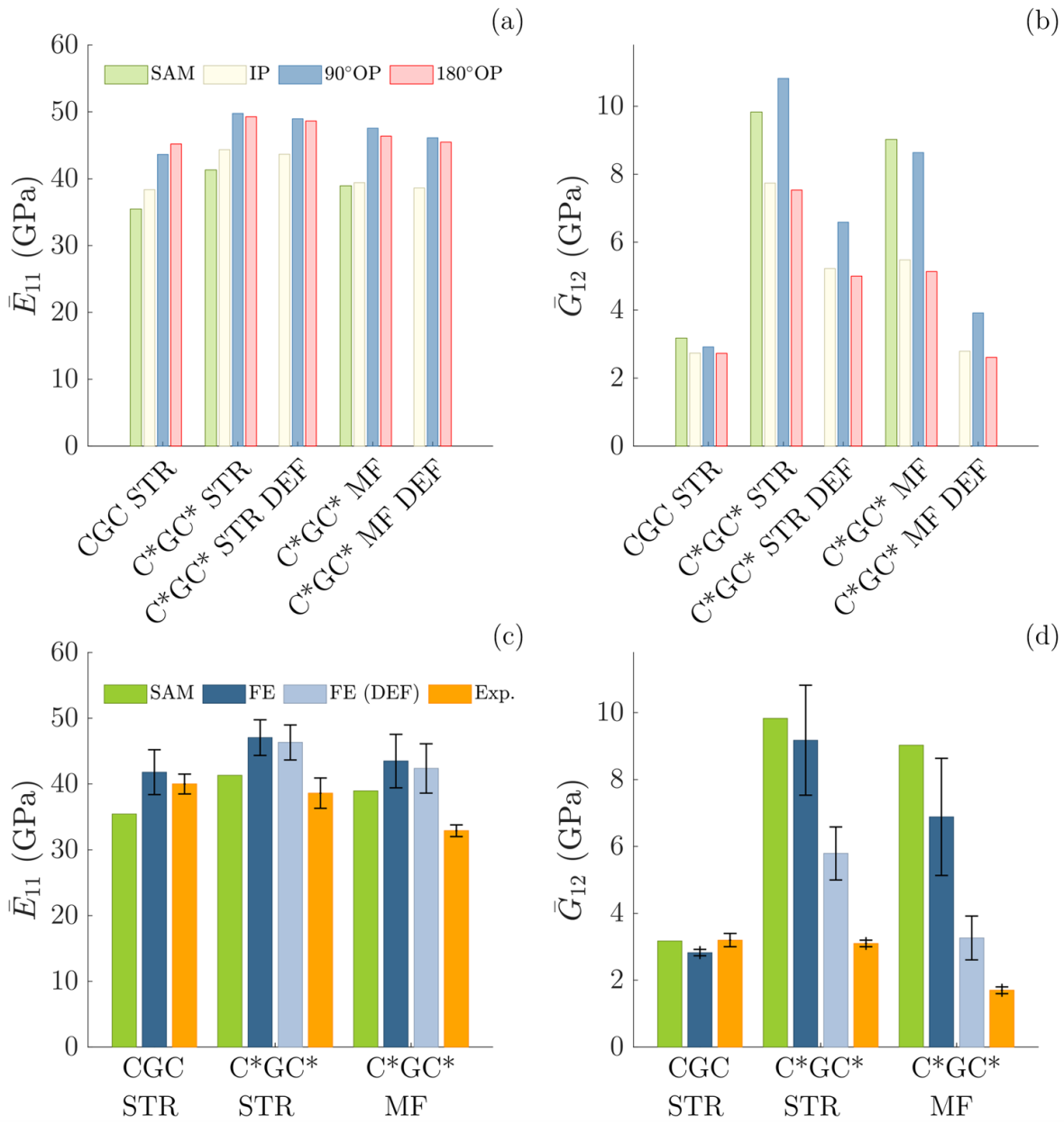

Figure 5.19. Predicted homogenised tensile and in-plane shear moduli, $\overline{E}_{11}$ (left) and $\overline{G}_{12}$ (right) for the SSC laminates: (a) and (b) effect of ply offset and constituent materials; (c) and (d) comparison with experimental data from literature [47].

Table 5.4. Predicted homogenised tensile and in-plane shear moduli for the SSC laminates with different ply offsets and constituent materials.

Laminate type	E_{11} (GPa)				G_{12} (GPa)			
	Analytical	Numerical			Analytical	Numerical		
	SAM	IP	90°OP	180°OP	SAM	IP	90°OP	180°OP
CGC STR	35.4	38.4	43.6	45.2	3.2	2.7	2.9	2.7
C*GC* STR	41.3	44.3	49.8	49.3	9.8	7.7	10.8	7.5
C*GC* STR DEF	–	43.7	49.0	48.6	–	5.2	6.6	5.0
C*GC* MF	38.9	39.4	47.6	46.4	9.0	5.5	8.6	5.1
C*GC* MF DEF	–	38.6	46.1	45.5	–	2.8	3.9	2.6

The effect of the elastic modulus of the structural electrolyte ($E_{m,MF}$) on the effective elastic properties of the multifunctional laminate are seen in Figure 5.20(a) and (b). Experimental values were plotted as a range to indicate uncertainty in the *in situ*/effective matrix modulus. G_{12} was more sensitive to the value of $E_{m,MF}$, doubling over the 150 MPa to 1.5 GPa range, compared to a 12% increase in E_{11}.

The effect of the elastic modulus of the CAG ($E_{m,CAG}$) (assuming the nominal value of $E_{m,MF}$) is shown in Figure 5.20(c) and (d). Once again, G_{12} displayed greater sensitivity than E_{11}; however, the effect was also dependent on the presence of pre-cracks. In the 5 GPa to 35 GPa range, $\overline{G}_{12}$ increased by 144% and 79% in the pristine and pre-cracked cases, respectively, whilst $\overline{E}_{11}$ increased by 14% and 11%.

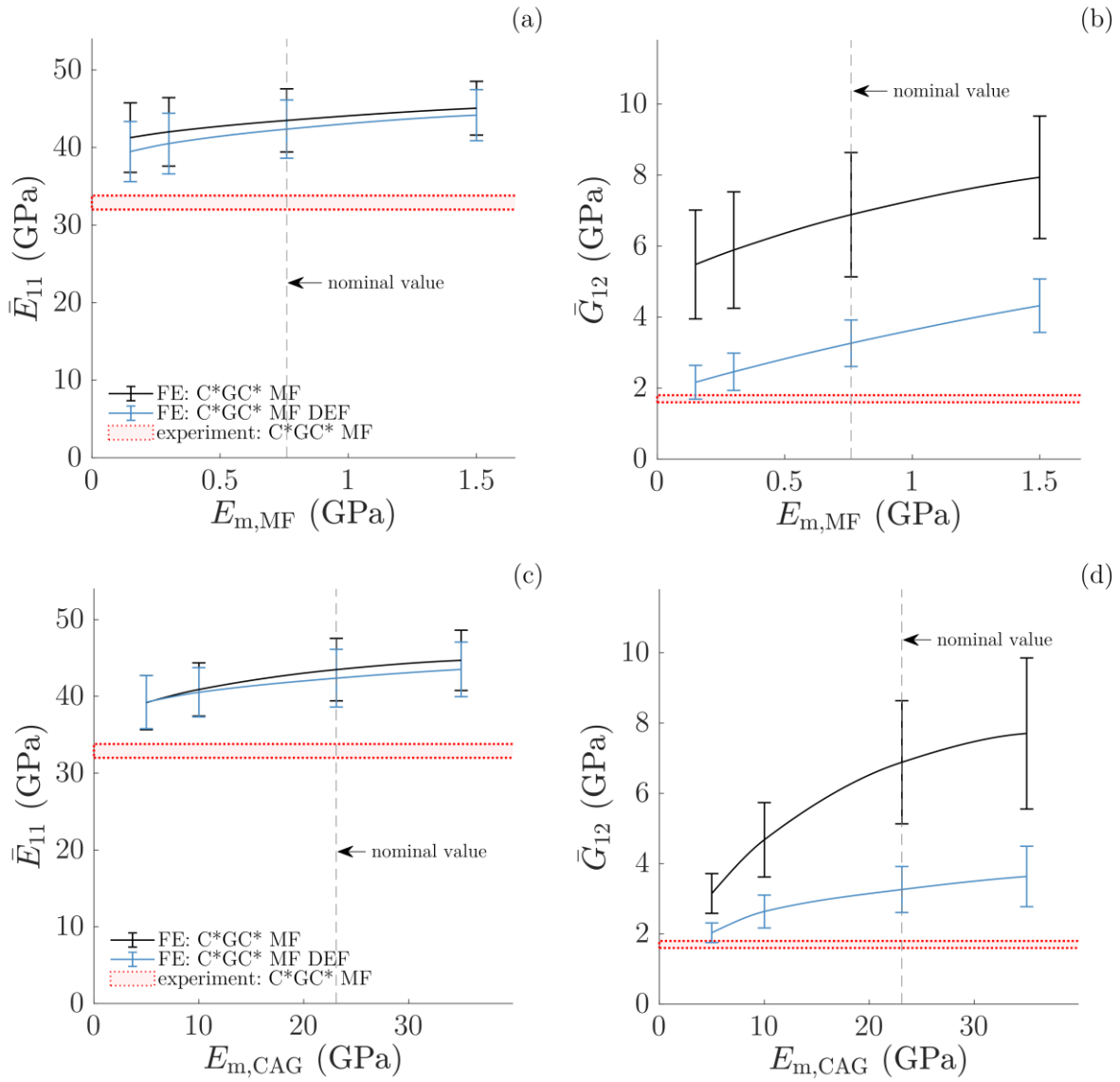

Figure 5.20. Predicted homogenised tensile and in-plane shear moduli, $\overline{E}_{11}$ (left) and $\overline{G}_{12}$ (right) for the C*GC* MF laminates: (a) and (b) effect of the elastic modulus of the structural electrolyte ($E_{m,MF}$), and (c) and (d) effect of the elastic modulus of the carbon aerogel ($E_{m,CAG}$).

5.6 Summary of results

A device-level finite element model for the prediction of the mechanical response of SSCs was developed. Unlike existing models in the literature [115], the present model does not rely on calibration of material parameters, and uses a realistic quasi-mesoscale representation of the fabric architecture. The latter was obtained by modifying the methodology developed in Chapter 4, exploiting size scale differences in the fabrics to minimise computational cost. The numerical predictions of elastic properties were compared with recent experimental results [47] and combined with detailed microstructural characterisation to aid interpretation of experimental results. The main findings of the present chapter were as follows:

- Intralaminar pre-cracks and voids, as well as gross interlaminar voidage of the matrix were discovered in the CAG-modified structural and multifunctional specimens, and characterised using optical, scanning electron and X-ray imaging methods.
- Scanning electron imaging of the CAG-modified structural specimens failed in tension indicated that poor CAG precursor infusion resulted in a broom-like fracture morphology; whilst good CAG precursor infusion resulted in flat fracture surfaces.
- FE models generated assuming neat constituent properties and defect-free microstructures resulted in overly optimistic predictions of the tensile and shear elastic responses of the CAG-modified structural and multifunctional laminates.
- Further numerical studies associated the pre-cracks with significant decreases in the in-plane shear stiffness of CAG-modified laminates.
- The ply offset was found to significantly influence the elastic properties for all material configurations.
- The in-plane shear modulus of the multifunctional laminates was significantly influenced by the elastic modulus of the structural electrolyte.
- The numerical results suggest that SSCs based on CAG-modified carbon fabrics could deliver equivalent, and even improved, elastic properties compared to conventional woven composites, provided defects can be avoided.

The results and their implications are discussed in detail in Section 8.2.

6 Current collection performance analysis and prediction

6.1 Introduction

The gravimetric mechanical properties and power density of the structural supercapacitors is presently limited by high internal resistance and parasitic weight. Addressing the geometric design of current collectors is a compelling, yet unexplored, route to performance improvement. This chapter evaluates the role of current collection design in determining performance, and addresses the following aims:

- to develop a three-dimensional electrical conduction model for the analysis of power losses due to internal resistances within the electrodes and current collectors, in the existing generation structural supercapacitors;
- to use the model to evaluate power loss and parasitic mass over a range of operating conditions;
- to formulate principles for the design of efficient current collectors for structural supercapacitors and assess the potential impact of the proposed design strategies.

This chapter is organised as follows: in Section 6.2, the key electrical conductivity parameters governing power losses in the electrode/current collector assembly are identified and the experimental procedures by which they are characterised are described. Section 6.3 reports the development of the three-dimensional electrical conduction model. Section 6.4 presents the results of parametric studies evaluating the influence of current collector design on the tradeoff between resistive power losses and mass. These results are later discussed in Chapter 8.

6.2 Materials and characterisation methods

6.2.1 Materials

This work focused on the contribution of the electrode and current collector sub-system to the performance of the Group's CAG-modified carbon fabric-based SSCs . The electrode considered was the C* fabric (Chapter 4, Table 4.1). The current collector was a commercially available copper tape with a one-sided conductive acrylic adhesive layer (AT526, Advance Tapes International [246]) with 10 mm width and 35 μm foil thickness.

The copper tape was bonded to the electrode via vacuum-assisted resin infusion under flexible tooling at a pressure of one bar, and cured at 130°C for 2 hours. 'Case I' is used to denote the combination of the above electrode and current collector materials. Measurement of the electrical conductivity of the electrode, and the electrode/current collector contact conductivity is detailed in Section 6.2.2.

Additional studies focused on two proposed device fabrication strategies for improving the contact properties between the C* fabric electrodes and the current collector foils: (a) selective masking of the CAG-modified fabric (see Appendix C.4) enabling direct contact of the current collector material to pyrolised carbon fibres (Case II), and (b) an electrically conductive surface treatment containing colloidal copper, which has shown promising results for Li-ion battery contacts [247] (Case III). In Case II, the contact and intrinsic conductivity of the pyrolised carbon fabric was characterised (Section 6.2.2) to provide the local material parameters. In Case III, the contact properties of the surface treatment were not experimentally characterised, and reported values [247] were used instead.

6.2.2 Intrinsic and contact conductivity characterisation

The electrical design of cells involves co-optimisation of several resistive components [248], requiring (in the case of SSC electrode and current collectors) knowledge of the conductivity of the electrode/current collector contact interface, σ_C, and the intrinsic conductivity of the electrode material, σ_e. Due to the anisotropic crystal structure of carbon fibres [249], the aligned architecture of the fabric weave, and the reliance of charge transfer on fibre-to-fibre contacts (illustrated in Figure 6.1), an anisotropic electrical conductivity of the electrode was expected.

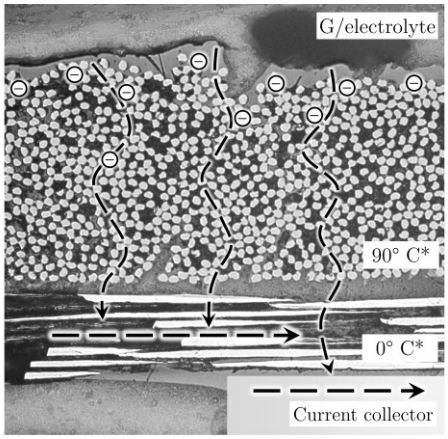

Figure 6.1. Cross-section view through the C*GC* MF laminate, showing the separator, electrode and current collector regions, and schematic of the electron path from the electrode/electrolyte interface to the current collector.

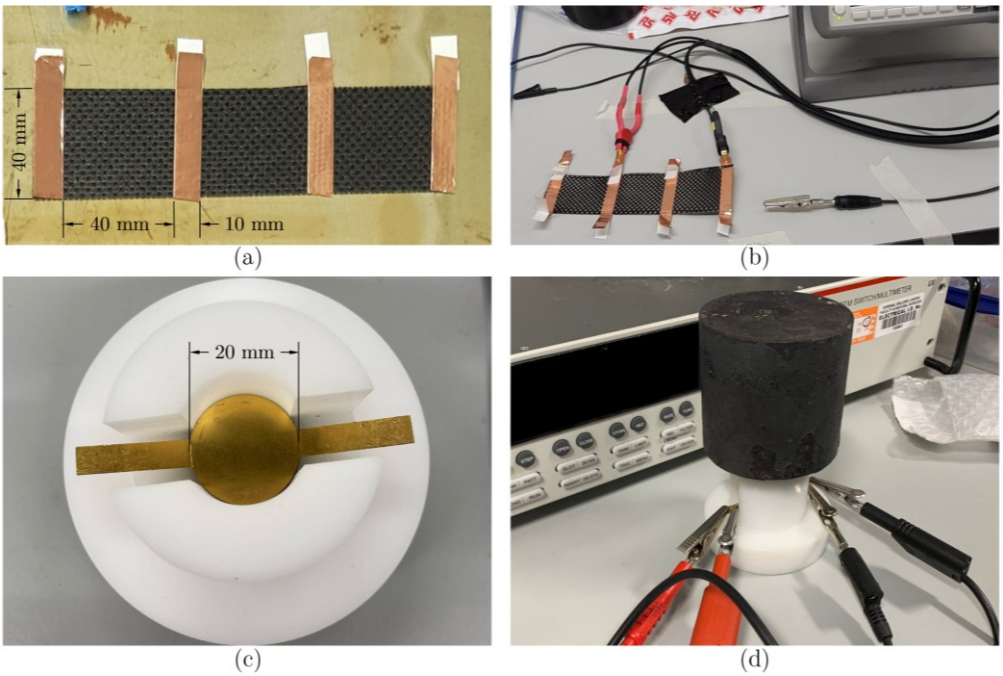

Figure 6.2. Experimental measurement of (a) and (b) in-plane, and (c) and (d) through-thickness electric resistance.

Electrode conductivity was therefore characterised along the longitudinal ($\sigma_{e,1}$) and transverse ($\sigma_{e,3}$) fabric directions (see Figure 6.3). Transmission line measurements (outlined in Section 2.5.1) were performed on 0/90 C* fabric specimens with cured copper current collectors (Figure 6.2(a) and Figure 6.2(b)) to determine the lateral electrode conductivity and contact conductivity. Assuming uniform sheet and contact conductivity, and uniform thickness (320 μm, as measured from compaction experiments (Appendix C.1)) across the specimen, the lateral electrode conductivity and the contact conductivity were calculated from the linear fit of this data as $\sigma_{e,1} = 156 \pm 26$ S/cm and $\sigma_C = 0.95 \pm 0.27$ S/cm², respectively. The conductivity of the pyrolised carbon fabric without CAG was

also characterised to obtain the material parameters for the Case II models. In this case, no change was observed in the lateral conductivity compared to the C* fabric, while contact conductivity was improved (ca. +280%) to 3.58 S/cm². The low effective contact conductivity, relative to the in-plane electrode conductivity validates the underlying assumption in the TLM method that negligible current entered intermediate fingers.

The through-thickness conductivity of C* and pyrolised C fabric specimens was characterised by a four-wire method using a 20 mm diameter piston-type cell, shown in Figure 6.2(c) and Figure 6.2(d). The current and voltage probes were attached to gold foil contacts, sandwiching the specimen. To minimise contact resistance within the stack, a layer of Pyrolytic Graphite Sheet (PGS, EYGS121807 70 μm, Panasonic) was placed between the C* fabric and gold foils. To promote contact between the layers, compression was applied by adding a 2 kg weight to the top of the piston, corresponding to 60 kPa applied pressure.

A Keithley 3706A System switch/multimeter was used to make the measurements in four-probe mode. It was assumed that the contact resistance of the gold/PGS and PGS/C* interfaces could be neglected, and therefore that the measured resistance could be purely attributed to the electrode. This assumption was verified by measuring the resistance of the gold/gold contact (that is, without a specimen in between), and that of a gold/PGS/gold stack, which were both negligible compared to the resistance of the fabrics.

The total through-thickness resistance measured for the C* fabric was $0.058 \pm 0.002\ \Omega$, leading to $\sigma_{e,3} = 0.165$ S/cm and a ratio of lateral to transverse electrode conductivity $\frac{\sigma_{e,1}}{\sigma_{e,3}} = 945$. For the pyrolised C fabric without CAG, the measured transverse resistance was $0.053 \pm 0.005\ \Omega$, leading to $\sigma_{e,3} = 0.151$ S/cm and $\frac{\sigma_{e,1}}{\sigma_{e,3}} = 1033$.

6.3 Electrical model development

6.3.1 Geometry and boundary conditions

The analysis in this work was restricted to the domain including a single electrode/current collector assembly, to understand the importance of electrical resistive losses in isolation. The computational expense of modelling the architecture of the fabric electrode at the mesoscale, as had been previously done in Chapters 4 and 5, could not be justified in this particular case, especially due to the availability of appropriate constitutive data. The resistance measurements gathered on macro-scale samples (Section 6.2.2) was considered

the most accurate source of material data, therefore the electrode was modelled as a continuous layer with homogenised properties. The domain was modelled in 3D, as shown in Figure 6.3, to account for the effects of finite electrode thickness and material orthotropy.

Given the above assumption of uniform active material volume per unit area, it was reasonable to further assume a uniform surface current density, j_s, acting over the electrode/separator interface plane, to represent the active current density. Whilst the active currents may not necessarily be uniform in the real devices, this condition is expected to hold true in an ideal electrode, where the active material is fully utilised; optimising the device in this best case, highest energy density, scenario should be appropriate more generally. The electrode domain can, therefore, be thought of as a representation of the transport limitation through the active layer. The separator was assumed to be sufficiently conductive in the transverse direction, such that lateral transport in this layer was negligible. The effect of modifying the current collector geometry could therefore be assessed by analysing the current distributions and heat dissipated within this domain.

In most practical applications several structural supercapacitor cells would typically be stacked and therefore, the following design constraints were assumed: (i) uniform thickness of the current collectors, and (ii) external connection made through a single junction at the cell edge (referred to as the end-tab). In the models, the end tab extended a small distance from the cell edge and a fixed electric potential (ground, $\psi_s = 0$) was specified at the end-tab cross-section. All other external surfaces were assumed electrically insulated. For simplicity, the analysis was restricted to a square electrode geometry.

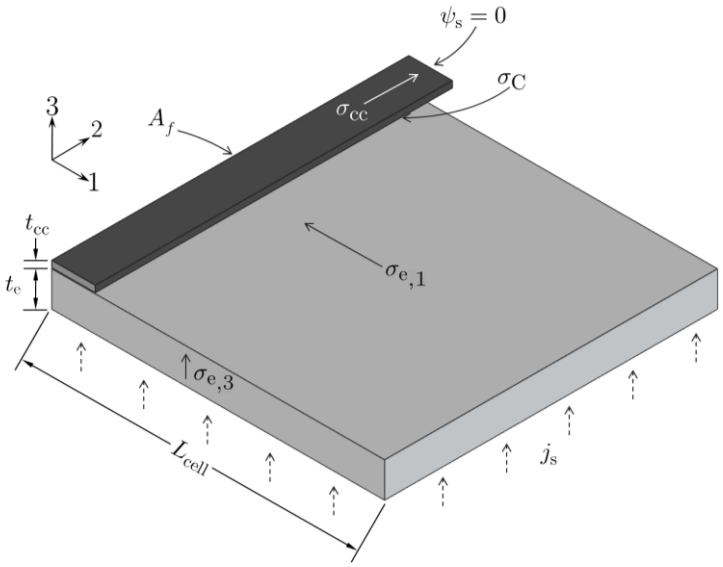

Figure 6.3. Domain and boundary conditions for the current collection model (electrode in light grey, and current collector in dark grey).

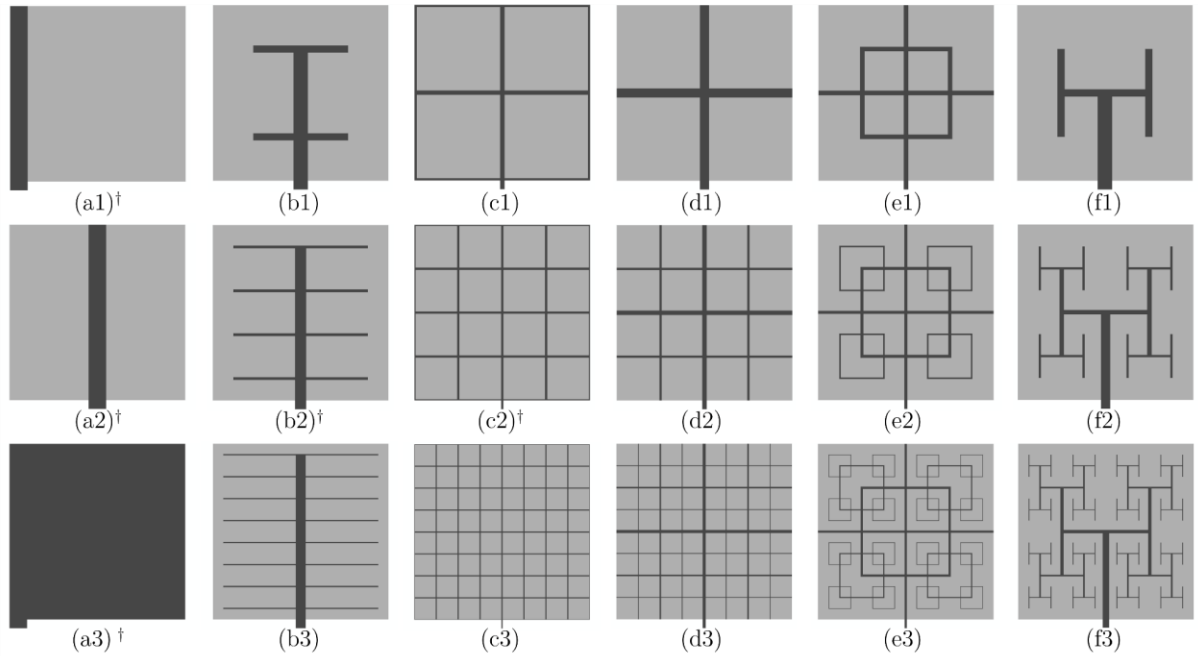

Figure 6.4. Current collector geometries with $A_f = 10\%$: (a1) side-strip, (a2) centre-strip, (b*i*) busbar and fingers, (c*i*) simple grid, (d*i*) fractal cross grid, (e*i*) fractal square grid, (f*i*) fractal H-tree grid. $i = 1 \ldots 3$ denotes the grid density. (a3) side-tabbed plate with $A_f = 100\%$. † denotes the geometries considered in case I and II.

In non-mass-critical applications, where current collection design is driven by the sole objective of minimising resistive loss, a planar sheet collector with full area coverage, shown in Figure 6.4(a3), represents the optimal solution [156]. However, in mass-critical applications, where the current collector mass must simultaneously be minimised with resistive losses, geometries with partial coverage may be advantageous. In the latter case, it is possible to co-optimise mass and resistive losses by modifying the geometric design of the current collector. In this work, simple strips used in existing devices, and alternative current collector grids of varying geometric complexity, depicted in Figure 6.4, were considered:

- single rectangular strips located either along the edge or central axis of the cell, referred to as 'side-strip' (a1) and 'centre-strip' (a2), respectively;
- 'busbar and fingers' grids [155] with a central busbar ((b1) to (b3));
- 'simple grids' ((c1) to (c3));
- space-filling fractal grids [213,250,251], with 'cross' ((d1) to (d3)), 'square' ((e1) to (e3)) and 'H-tree' ((f1) to (f3)) geometries.

Parametric studies were performed considering the three case studies (I, II and III) representing different values of contact conductivity at the electrode/current collector

interface (further details of which are given in Section 6.3.3). For the baseline case I, the parametric studies were performed to analyse the influence of the following cell parameters:

- the current collector coverage ratio (area fraction), defined as $A_f = A_{\mathrm{cc}}/A_{\mathrm{cell}}$,
- the current collector thickness, t_{cc},
- the active current density, j_{s},
- the absolute electrode side length, L_{cell}.

These parameters were individually varied. Their values are given in Table 6.1, with nominal values used in the models shown in bold. The nominal current collector thickness of 35 μm was chosen to reflect the available copper tape material, with lower thicknesses (down to 1 μm) investigated as potentially more efficient solutions. It is anticipated that thicknesses <5 μm would imply a change of application method, for instance via screen printing [154] or direct-ink printing [252] due to the poor handleability of thin films.

Nevertheless, these low thicknesses may be beneficial not only for reducing the parasitic mass of current collectors, but may also result in improved contact properties if conductive particles are able to penetrate the electrode surface and achieve closer contact with the CAG and carbon fibres. In this work, however, the electrical conductivities were assumed to not vary with current collector thickness, and the influence of the electrical conductivities was investigated independently (see Section 6.3.3).

The values of side lengths were chosen to reflect device geometries typically characterised by the Group, for which recent experimental data was available. Geometric surface area equivalent to those of a 1 cm diameter coin cell and an A4 sheet, were achieved using 0.886 cm and 25 cm side lengths, whilst the intermediate value of 10 cm was chosen as the nominal value to allow straightforward numerical conversion between resistance and power loss. The active current density was kept constant for the different device sizes to permit performance comparisons (that is, scale-up analysis).

The nominal active current density of $j_{\mathrm{s}} = 1$ mA/cm² was selected in line with typical current densities used in experiments and demonstrator components, for which published data [47] was available. The additional value of $j_{\mathrm{s}} = 10$ mA/cm² was chosen to represent a more demanding electrical loading condition, which may be suitable for devices requiring more efficient current collection to maintain power density (Section 0), as well as for ease of numerical conversion as above.

To keep the number of variables in the parametric studies to a minimum, the analyses for Cases I and II were restricted to the subset of geometries including (a1), (a2), (a3), (b2) and (c2) (denoted by † in Figure 6.4). For cases II and III, the cell parameters were: $L_{\text{cell}} = 10$ cm, $j_{\text{s}} = 10$ mA/cm^2 , $A_f = 10\%$, and $t_{\text{cc}} = 35$ μm. For case III, the parametric study was expanded to consider all geometries in Figure 6.4.

Table 6.1. List of geometric and cell parameter values used in the current collection models.

Symbol	Quantity	Value	Unit
t_{e}	Electrode thickness	320	μm
t_{cc}	Current collector thickness	1,5,10,**35**	μm
L_{cell}	Cell length	0.886, **10**, 25	cm
A_f	Current collector area fraction	**10**…100	%
j_{s}	Active current density	**1**, 10	mA/cm^2
V_{R}	Rated voltage	1	V

Nominal parameter values in bold.

6.3.2 Domain discretisation

In the present work, the development of a finite element model for the analysis of current collection performance was selected over that of a theoretical analysis framework. It was judged that the former approach would: (i) significantly reduce the timescales for model development and investigation, (ii) provide more accurate predictions of the complex 3D current distribution, and (iii) provide greater flexibility with regards to geometric complexity.

The geometries were discretised using solid quadratic (20-node) hexahedral thermal-electric elements (DC3D20E) to capture potential gradients accurately. The meshes were structured using the volume partitioning technique to ensure a rectangular element shape. The use of biased (variable density) meshes was initially explored; however, due to time constraints on implementation, simple unbiased meshes were ultimately used. Mesh sensitivity studies were performed to ensure solution convergence (see Section 6.4.1). The numerical results were verified against 1D solutions for the plate and side-strip geometries. The models were generated within Abaqus and solved in a coupled thermal-electrical analysis procedure.

6.3.3 Constitutive model

Based on the electrode conductivity measurements (Section 6.2.2), an orthotropic conductivity model was assumed in the electrode domain. An isotropic material model was

assumed in the current collector domain. A surface-based contact interaction [253] was used to specify uniform contact conductivity at the electrode/current collector interface. In the baseline constitutive model (Case I), the measured contact conductivities measured for the C* fabric and the cured copper current collector were used.

Additional case studies focused on the effects on current collection performance of selective masking of the C* fabric (Case II), and the use of an electrically conductive surface treatment (Case III) (see Section 6.2.1). In these studies, the measured (Section 6.2.2) and reported values of the contact conductivities were respectively used to define the electrical contact. For the Case II models, the electrode conductivity in the regions directly underneath the contact zones were locally modified to reflect those measured on the pyrolised fabric (Section 6.2.2). All constitutive parameter values are listed in Table 6.2.

Table 6.2. List of electric conductivities used in the three case studies.

Symbol	Quantity	Value			Unit
		Case I	Case II	Case III	
$\sigma_{\mathrm{e,l}}$	Lateral conductivity of electrode	**156.25**	156.25	156.25	S/cm
$\sigma_{\mathrm{e,t}}$	Transverse conductivity of electrode	**0.165**	0.151‡	0.165	S/cm
σ_{cc}	Conductivity of current collector	**5.95×10^5**	5.95×10^5	5.95×10^5	S/cm
σ_{C}	Effective contact conductivity	**0.945**	3.58‡	14.45‡ [247]	S/cm²

Nominal parameter values in bold; ‡ refers to regions directly underneath current collectors.

6.3.4 Performance evaluation

Within the domain considered, the electrode, current collector and their contact interface contribute to the total power dissipation due to resistive losses, also known as Joule heating [34], $P_{\mathrm{J,total}}$, through the respective contributions $P_{\mathrm{J,e}}$, $P_{\mathrm{J,cc}}$ and $P_{\mathrm{J,C}}$:

$$P_{\mathrm{J,total}} = P_{\mathrm{J,e}} + P_{\mathrm{J,cc}} + P_{\mathrm{J,C}} \quad . \tag{6.1}$$

The generalised Ohm's law was assumed within the electrodes and current collector:

$$\mathbf{J} = \boldsymbol{\sigma}^{\mathbf{E}} \cdot \mathbf{E} \quad , \tag{6.2}$$

where matrix notation is used, and $\mathbf{J} = \mathbf{J}(\mathbf{x})$ is the electric current density, $\boldsymbol{\sigma}$ is the electrical conductivity matrix, $\mathbf{E} = \mathbf{E}(\mathbf{x})$ is the electric field intensity, $\mathbf{E}(\mathbf{x}) = -\frac{\partial\psi(\mathbf{x})}{\partial\mathbf{x}}$, and $\psi(\mathbf{x})$ is the electric potential. The Joule heat per unit volume is given by Joule's law:

$$\frac{dP_{\mathrm{J}}}{dV} = \mathbf{J}\cdot\mathbf{E} = \mathbf{E}\cdot\boldsymbol{\sigma}^{\mathbf{E}}\cdot\mathbf{E} \quad . \tag{6.3}$$

Joule heating was calculated from the finite element solutions by integrating the element-wise power dissipation, P_J^e, as per Eqn. (6.3) over the elements, e:

$$P_{\mathrm{J}} = \sum_n \sum_i \sigma_i^{\mathrm{E},e}\ E_i^e\ {}^2V_e = \sum_n \sum_i P_{\mathrm{J},i}^e = \sum_n P_{\mathrm{J}}^e \quad , \tag{6.4}$$

where n is the number of elements, V^e is the element volume and $i = 1,2,3$ denotes the three-dimensional Cartesian coordinate directions. The above expression was verified against the Abaqus energy field output variable ALLJD (electric energy dissipated due to flow of electric current). The benefit of this post-processing step was the ability to calculate the orthogonal components of the total power dissipation in each direction, $P^e_{\mathrm{J},i}$, allowing comparisons of the relative power loss contributions due to lateral and transverse currents within the electrode. The component and total power dissipation in the electrode and current collector domains were calculated by summation of P^e_{J} over the respective sets of elements. The power dissipation contributions from the electrode and current collector domains were calculated by integration over the relevant element sets. Ohm's law was also assumed to govern the current flow across the contact interface:

$$j_{\mathrm{C}} = \sigma^{\mathrm{E}}_{\mathrm{C}} \, \psi_{\mathrm{A}} - \psi_{\mathrm{B}} \quad , \tag{6.5}$$

where j_{C} is the electric current density perpendicular to the contact interface, $\sigma^{\mathrm{E}}_{\mathrm{C}}$ is the contact conductivity, and ψ_{A} and ψ_{B} are the electric potentials at corresponding points on the two contact surfaces [253]. The effective resistance of the electrode/current collector assembly was calculated from the total power dissipation according to:

$$R_{\mathrm{eff}} = \frac{P_{\mathrm{J,total}}}{i_{\mathrm{s}}^2} \quad , \tag{6.6}$$

where i_{s} is the total active current. The power loss coefficient was defined as:

$$P^* = 2P_{\mathrm{J}}/i_{\mathrm{s}}V_{\mathrm{R}} \quad , \tag{6.7}$$

where the power dissipated from a pair of electrodes and current collectors is considered, and V_{R} is the rated voltage of the cell, assumed 1 V. It should be noted that this voltage rating corresponds to aqueous devices, whilst voltages between 2.5 V and 4 V would be expected for ionic liquids. 1 V was chosen to enable easy extrapolation of the performance to a range of electrolyte systems. A current collector mass fraction was defined as:

$$m_f = 2m_{\mathrm{cc}}/m_{\mathrm{active}} \quad , \tag{6.8}$$

where m_{cc} is the mass of a single current collector and m_{active} is the mass of active materials in the cell, including the two electrodes, separator, and electrolyte filling the pore space. For the constant thickness, constant volumetric density, current collectors studied here, the current collector m_f was directly proportional to A_f. The mass fraction and the power loss coefficient were used to evaluate and compare the current collector designs in Figure 6.4.

6.4 Results

6.4.1 Mesh convergence

Mesh sensitivity analyses were performed to ensure solution convergence. The maximum element side length was varied between 10 mm and 0.6125 mm, while component thicknesses were discretised using between 2 and 20 elements. The overall power dissipation (P_{total}) and the maximum electric potential gradients (E_{max}) were obtained using the above mesh densities. An element side length of 1.25 mm was sufficient for reasonable numerical convergence of P_{total} (Figure 6.5(a)) and its components (results omitted here for brevity).

Convergent behaviour was also observed for E_{max} (Figure 6.5(b)). The moderate increase in the value of E_{max} was not correlated with an appreciable effect on the overall power losses of the whole model, due to the fact that large potential gradients were confined to a small volume of elements compared to the volume of the whole model. Meshes with ca. 1×10^5 elements were therefore deemed acceptable for further analysis.

6.4.2 Relative contributions to resistive loss and effect of current density

Following the methodology described in Section 6.3.4, the power loss contributions due to the effective resistances of the electrode (partitioned into lateral and transverse components), current collector and the electrode/current collector contact interface were calculated for the 'Case I' geometries in Figure 6.4. The corresponding power loss coefficients obtained for the nominal model parameters are shown in Figure 6.6(a).

Contact resistance was the dominant source of power dissipation in all cases, and (as expected) scaled inversely with the current collector area fraction, leading to a contact power loss coefficient ca. 0.2% and ca. 2% for the full and partial (A_f = 10%) coverage current collector geometries, respectively. The power losses were directly proportional to the current density, with contact resistance accounting for over 20% of the losses in the partial coverage geometries at j_{s} = 10 mA/cm² (Figure 6.6(b)). The relative contributions of the loss components remained constant. Amongst the partial coverage geometries, lateral resistive losses in the electrode varied significantly, decreasing by 98% between the 'side-strip' and 'simple grid' geometries.

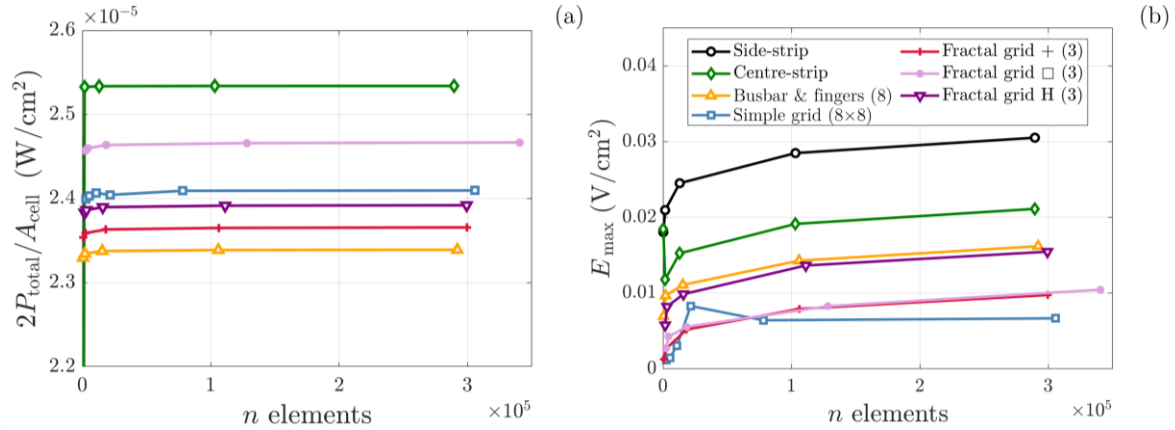

Figure 6.5. Numerical convergence of (a) total power losses, and (b) maximum potential gradient for different current collector geometries (nominal parameter values).

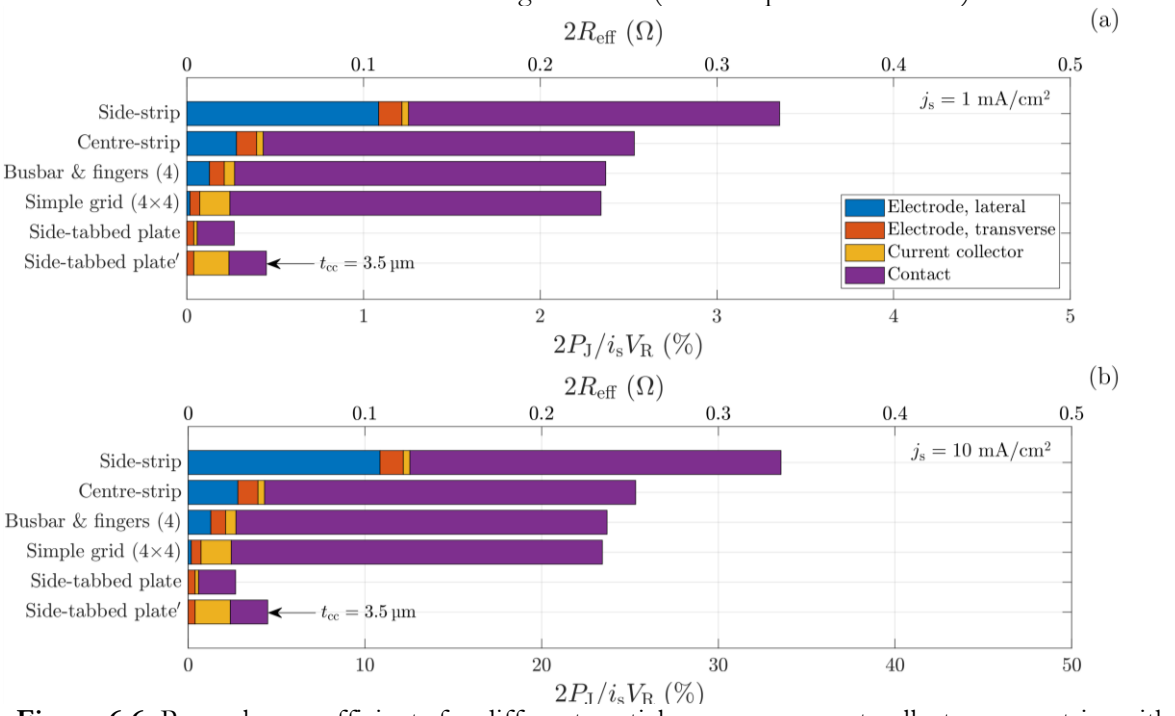

Figure 6.6. Power loss coefficients for different partial coverage current collector geometries with $A_f = 10\%$ (with side-tabbed plate solutions shown for comparison) computed at (a) $j_s = 1$ mA/cm², and (b) $j_s = 10$ mA/cm². Case I, $L_{cell} = 10$ cm, $t_{cc} = 35$ µm unless otherwise indicated.

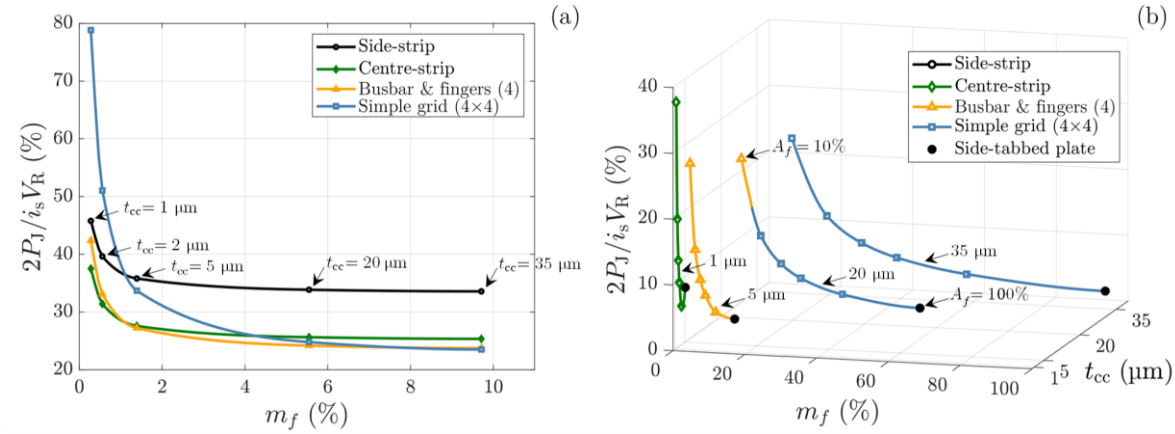

Figure 6.7. (a) Total power loss coefficient and current collector mass fraction for different partial coverage current collector geometries with $A_f = 10\%$, across a range of thicknesses. (b) Pareto frontiers across a range of current collector thicknesses. Case I, $j_s = 10$ mA/cm² and $L_{cell} = 10$ cm.

6.4.3 Effect of current collector thickness and area fraction

The power loss coefficient and mass fraction performance indices were calculated for the different partial coverage current collector geometries with $A_f = 10\%$, across a range of area thicknesses (Figure 6.7(a)). For a given current collector thickness, reductions in power loss could be made by switching to a more efficient geometry, for example, from a side-strip to a busbar and fingers grid at $t_{\mathrm{cc}} = 35$ μm. The data also showed that it was possible to achieve mass savings at no significant penalty to the power loss coefficient (that is, achieve 'Pareto improvements') by reducing the current collector thickness.

For example, by switching from the 35 μm side strip to a 5 μm busbar and fingers grid, the current collector mass could be reduced by 86% without a significant increase in resistive losses. By considering a range of area fractions, in addition to thicknesses, it was possible to construct the Pareto frontiers of optimal solutions at each thickness, as shown in Figure 6.7(b). Note that the curves were constructed by selecting the minimum total power loss solution at each current collector thickness and area fraction. Note that reducing the thickness has the effect of 'jumping' to a new Pareto frontier.

6.4.4 Device scale-up

For a constant current density and current collector area fraction, the power dissipation due to contact resistance was expected to be directly proportional to cell area: $P_{\mathrm{J,C}} \propto A_{\mathrm{cell}}$, since $R_{\mathrm{C}} \propto 1/A_{\mathrm{cell}}$ and $i_{\mathrm{s}} \propto A_{\mathrm{cell}}$. Based on initial analysis of the limiting case where current is collected from one edge of the cell, the lateral power dissipation in the electrodes and current collector scales as $P_{\mathrm{J,e,l}} \propto A_{\mathrm{cell}}^2$ and $P_{\mathrm{J,cc}} \propto A_{\mathrm{cell}}^2$. In the limiting case where transverse current in the electrode is uniformly collected across its surface area $P_{\mathrm{J,e,t}} \propto A_{\mathrm{cell}}$. For the partial current collector geometries studied here, the proportionality was expected to be approximately linear for $P^*_{\mathrm{J,e,l}}$ and $P^*_{\mathrm{J,cc}}$, whilst $P^*_{\mathrm{J,e,t}}$ and $P^*_{\mathrm{J,C}}$ were expected to stay relatively constant with area.

The computed power losses and effective resistances for surface areas equivalent to those of a 1 cm diameter coin cell and an A4 sized sheet were plotted in Figure 6.8. These results confirmed the above relationships held for the electrode/current collector assemblies. The relative increase in the power loss coefficient with cell area was more severe for current collector geometries with less efficient lateral current collection, such as the side strip collector (Figure 6.8 (a)), where lateral losses in the electrode outstrip contact losses

for $A_{cell} > 200$ cm². On the other hand, full coverage current collectors did not accumulate lateral losses (Figure 6.8 (b)), and the slight increase in the power loss coefficient was instead due to power dissipation within the current collector.

6.4.5 Comparisons with ionic resistive losses and experimental data

The overall resistance of an SSC cell includes the electronic resistances in the electrode and current collector pairs, and the ionic resistance in the electrode and separator layers. Combining these contributions would enable comparisons with experimental ESR measurements from real SSC cells.

The migration of ions through a porous layer is a diffusion-limited process, which is sensitive to both experimental conditions and microstructural characteristics [254]. To estimate ionic resistance, the effective ionic conductivities within the porous electrode and separator layers must be known, that is, the bulk ionic conductivity must be corrected for the porosity and tortuosity of the porous layer. The Bruggeman relation, presented in its standard form in Appendix A.3, is the most widely used such correction. It is sometimes modified using fitting parameters to obtain better agreement with experiments; however, the exact values of the fitting parameters vary widely between different electrode and separator materials [254,255]. In the absence of direct experimental data or literature data on fitting parameters for electrode and separator materials of sufficiently similar microstructure to those studied in this work, the use of modified corrections could not be justified on accuracy grounds. Therefore, the Bruggeman correction was used in its standard form here to provide a first estimate of ionic resistance contributions in SSCs.

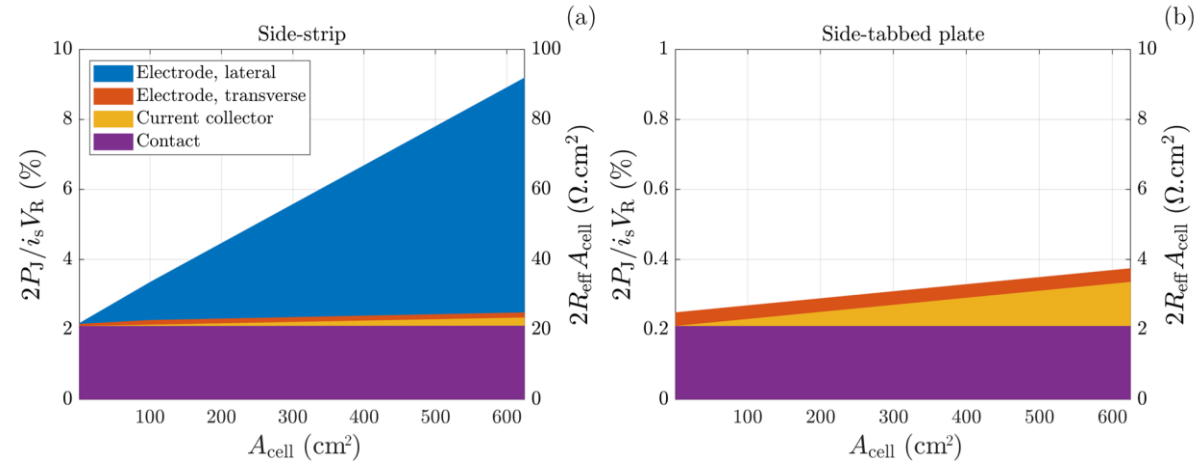

Figure 6.8. Power loss coefficient and area-normalised resistance as a function of electrode surface area for: (a) side-strip with $A_f = 10\%$, and (b) side-tabbed plate current collector geometries. Case I, $L_{cell} = 0.9, 10, 25$ cm, $j_s = 1$ mA/cm², $t_{cc} = 35$ µm.

For the monofunctional (semi-structural) devices using pure ionic liquid electrolyte, the ionic conductivity of neat EMIM-TFSI (9 mS/cm [256]) and the porosity of the glass fibre fabric ply (61%, calculated from the total fibre volume fraction of the ply) were used to obtain an effective ionic conductivity of the separator layer, $\kappa_{\mathrm{sep,eff}} = 4.3$ mS/cm. Using the separator thickness of 53 μm, and assuming negligible in-plane current within the separator layer, the effective resistance of the separator was calculated as $R_{\mathrm{sep,IL,eff}} = \frac{t_{\mathrm{sep}}}{\kappa_{\mathrm{sep,eff}} A_{\mathrm{cell}}}$. Note that this underlying assumption was verified by a 'full cell' simulation, which included the separator layer in between two electrodes.

For the CAG-modified electrodes, the overall porosity (30%) was calculated from the porosity of the CAG monolith (47%, Section 5.2.1.2) and the total fibre volume fraction of the carbon fabric (36%) at the specified thickness of 320 μm. The effective ionic conductivity within the electrode, $\kappa_{\mathrm{e,eff}} = 1.5$ mS/cm, was approximately three times lower than that in the separator. Assuming the ions were able to penetrate the full thickness of the electrode and are uniformly distributed across it, the average distance travelled by ions within the electrode ($t_{\mathrm{e}}/2$) was used to calculate the effective ionic resistance contribution from the electrode: $R_{\mathrm{e,IL,eff}} = \frac{t_{\mathrm{e}}}{2\kappa_{\mathrm{e,eff}} A_{\mathrm{cell}}}$.

For the multifunctional devices, the effective ionic conductivities in the separator and electrodes, 0.18 mS/cm and 0.06 mS/cm, respectively, were similarly calculated using the ionic conductivity of the structural electrolyte with 34 vol.% EMIM-TFSI (0.38 mS/cm, interpolated data from literature [241]). The calculated ionic resistances were combined with the numerical predictions of electronic resistance for Swagelok and A4 size devices, and plotted against available area-normalised ESR values from literature [47] and unpublished work by the Group (Figure 6.9).

For the monofunctional devices, the ionic resistance in the electrodes was predicted to dominate the overall resistance for all configurations, except the A4 sized device with a side-strip current collector, where lateral losses dominated. In the multifunctional devices, for all configurations the predicted ionic resistance was very large, and the power loss factor was greater than 100%, implying that useful capacitive energy storage would not be possible due to the large Ohmic potential drop at a current density of 1 mA/cm^2. The ionic resistance in the separator was the second largest source of loss, for all but the A4 sized device with a side-strip collector.

When compared with experimental monofunctional and multifunctional Swagelok cell measurements, which represent a 'plate' current collector solution, the overall resistance was overpredicted by 49% and 85%, respectively. In both cases, the ionic resistance contribution from the electrode alone was greater than the total measured resistance. Experimental data from A4 size devices was only available for the monofunctional case with a strip-like collector. The overall resistance in that case was underpredicted by 87%. The possible causes of these experimental-numerical 'performance gaps', and the influence of pressure on resistance measurements and predictions are discussed in Section 8.3.1.

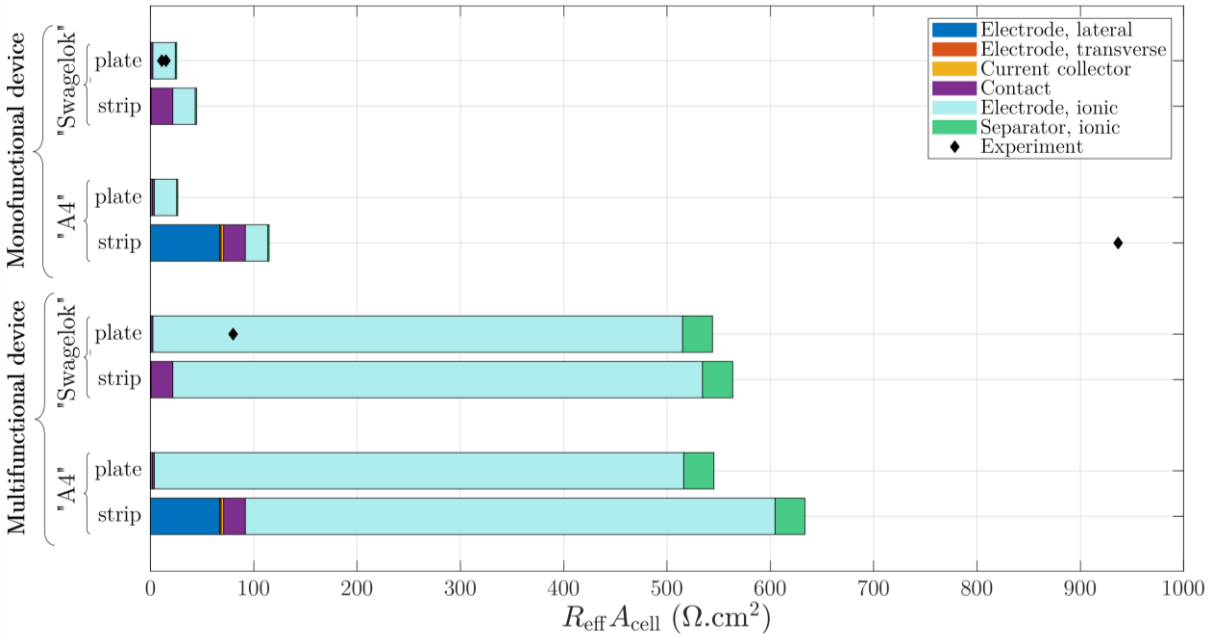

Figure 6.9. Predicted area-normalised resistances of monofunctional (above) and multifunctional (below) devices, computed for Swagelok and A4 sized devices, and side-strip ($A_f = 10\%$) and plate current collector geometries (Case I, $j_s = 1$ mA/cm^2, $t_{cc} = 35$ µm), compared with available experimental values from literature [47] and unpublished work by the Group.

6.4.7 Effect of contact properties

The contact resistance was inversely proportional to the contact conductivity (Figure 6.10). Therefore, the effect of modifying the contact conductivity was to change the importance of contact losses relative to the other loss sources components. While contact losses could be reduced by ca. 74% through selective masking (Case II), these were still predicted to dominate the overall losses (at the nominal thickness) in all but the least efficient current collector geometry (side-strip). On the other hand, by reducing contact losses by ca. 93%, the colloidal copper surface treatment (Case III) could bring the magnitude of the contact losses on par with that of the other sources of loss.

Case III was further examined to understand the impact of the geometric design of the current collector, in the regime of low contact losses. In this regime, the relative performance gains, which can be obtained by modifying the current collector geometry were seen more clearly (Figure 6.11(a)): for instance, the total power loss could be reduced by 60% or more by moving away from a side-strip to a grid collector.

The differences in overall power loss between the various grids were marginal. The busbar and finger design generally performed better than the simple or space-filling fractal grids. Whilst the simple and fractal grids generally had lower lateral electrode losses, this gain was offset by higher current collector losses. The latter were exacerbated as the grid density (or number of finger elements, n_f) was increased due to the reduced width of grid elements (illustrated in Figure 6.11(b) and (c)). The opposite was true for the lateral losses.

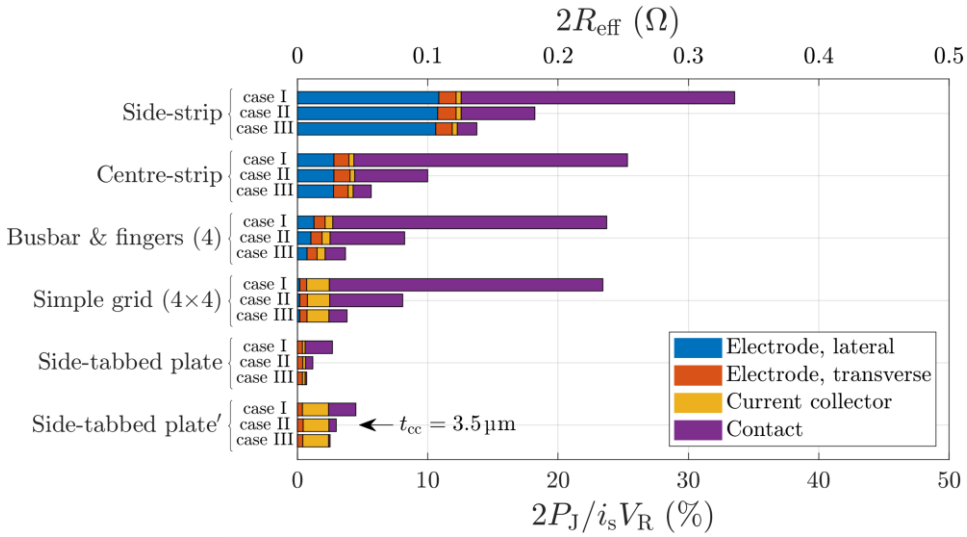

Figure 6.10. Effect of contact properties on power loss coefficient and effective resistance. $L_{\mathrm{cell}} = 10$ cm, $j_s = 10$ mA/cm², $A_f = 10\%$, $t_{cc} = 35$ µm, unless otherwise indicated.

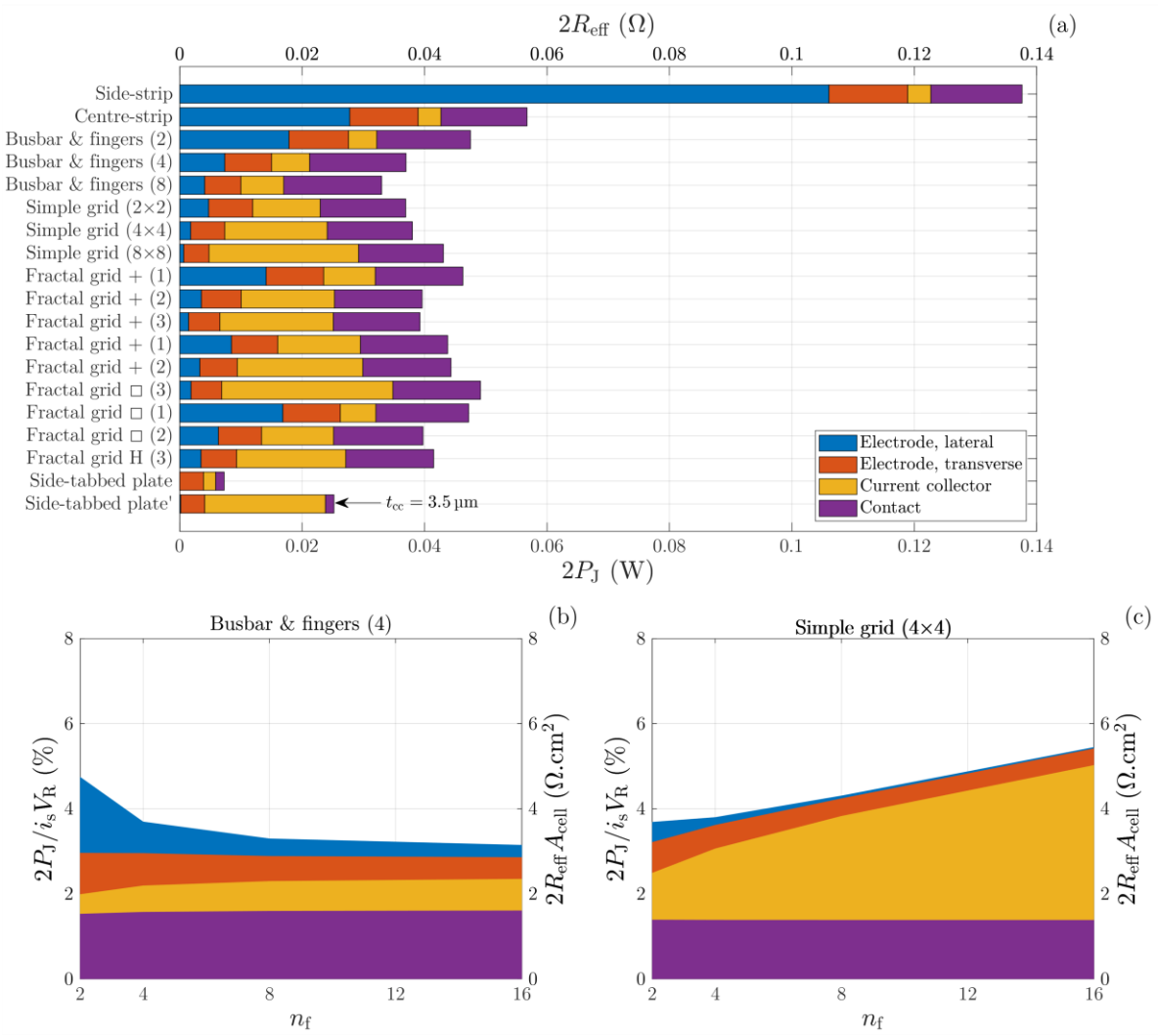

Figure 6.11. Power loss coefficient and effective resistance for various partial coverage current collector geometries (with side-tabbed plate for comparison); and effect of grid density (number of fingers n_{f}) on power loss contributions in (b) busbar and fingers, and (c) simple grid current collectors. Case III, $L_{\text{cell}} = 10$ cm, $j_{\text{s}} = 10$ mA/cm², $A_f = 10\%$, $t_{\text{cc}} = 35$ µm.

6.5 Summary of results

A finite element model of direct current electrical conduction through the electrodes and current collectors in structural supercapacitors was developed. The model enables the evaluation of power loss due to Joule heating. The total power loss includes contributions due to bulk electrical resistance within the electrodes and current collectors, and due to contact resistance at the electrode/current collector interface. The power loss is therefore governed by the respective electrical conductivities, active current density, device area and current collector geometry, which are specified as model inputs. The relative importance of these parameters was explored through parametric studies, which found:

- At present, the principal source of resistive power loss in the electrodes and current collectors in structural supercapacitor devices is the high contact resistance between those components.
- Therefore, the most effective near-term strategy for the mitigation of resistive losses lies in improving the contact at the electrode/current collector interface or else, increasing the areal coverage and reducing the thickness of current collector foils.
- When considering the combined electric and ionic resistance contributions, the actual resistance of Swagelok devices was overpredicted, and that of freestanding A4 devices was significantly underpredicted.
- Contact resistance could be reduced substantially through either selective CAG masking or conductive surface treatment of the electrodes, with the latter strategy predicted to deliver greater performance gains.
- In the regime where the overall power loss is not dominated by contact losses, hierarchically structured collector geometries with wider elements near the end tabs (such as busbar and fingers) were shown to be preferable to geometries with narrow grid elements (such as simple grids).
- The performance benefits associated with current collector grids increase with increasing active current densities and device area, and decreasing foil thickness, due to rising lateral losses in the electrode and current collector.

These results are discussed in detail in Section 8.3.

7 Electrochemical and multiphysics modelling

7.1 Introduction

A holistic and efficient approach to the analysis and design of SSCs requires numerical simulation software suites to evolve [25] to support multiphysics (mechanical-electrochemical) modelling workflows. To encourage a more seamless adoption of SSCs by the aviation industry, this chapter focused on developing such a capability within the widely used software suite Abaqus, via an electrochemical user-defined element subroutine (UEL) and accompanying model. Additionally, it was deemed sensible to maintain consistency with the existing mechanical model (Chapter 5), to ensure their future compatibility, allowing multiphysics analyses to be eventually performed through procedures such as sequential coupling [257]. Previous experience from the development of a user material subroutine (Chapter 4), and implementation of a sequentially coupled electro-mechanical model via a UEL by Matos *et al.* [199] (Section 2.6.2.2) further motivated the use of this approach. The aim of this chapter was therefore:

- to develop a UEL subroutine for steady-state and transient ion transport analysis;
- to apply the UEL within existing analysis procedures, enabling new electrochemical and multiphysics capabilities in Abaqus, relevant to SSCs.

Based on the theoretical background on physics-based electrochemical models of supercapacitors presented in Chapter 2, an ion transport finite element subroutine was developed. Note that the terms 'electrochemical' and 'ion transport' are used interchangeably here. This chapter is structured as follows: Section 7.2 details the development of a FORTRAN UEL subroutine based on the finite element equations and boundary conditions for ion transport in supercapacitors. Section 7.3 details the implementation of the ion transport element within a thermal-electrical analysis procedure. Section 7.4 presents initial results from the subroutine implementation and testing. The findings of this work are later discussed in Section 8.4.

7.2 Development of ion transport user element subroutine

7.2.1 Formulation of ion transport element

In a supercapacitor cell, ions are transported through the electrolyte under the combined forces of mass diffusion and electromigration. Theoretical models for these processes were reviewed in Section 2.6.2.2. For clarity, the physics-based governing equations are briefly summarised here. From the Poisson's equation (Eqn. (2.9)) the definition of free charge density (Eqn. (2.10)), the following PDE governing the potential field is obtained:

$$\varepsilon_0 \varepsilon_r \nabla^2 \psi + \sum_s e z_s c_s = 0 \quad . \tag{7.1}$$

Combining the Nernst-Planck equation for the mass flux (Eqn. (2.14)), with the mass conservation statement (Eqn. (2.16)), yields the following PDE:

$$\frac{\partial c_s}{\partial t} + \nabla \cdot \left(-D_s \nabla c_s - z_s u_s F c_s \nabla \psi \right) = 0 \quad , \tag{7.2}$$

where $s = 1, 2$ for a binary electrolyte. The formulation of the finite element equations for ion transport, based on the weighted residual approach applied to the above PDEs, was previously outlined by Lim [164], and can be found in Appendix D.1.

7.2.2 Domain discretisation

In contrast to the cubic Hermite discretisation used by Lim [164], which includes first derivatives of the field variables as auxiliary nodal variables, here, a quadratic Lagrange discretisation was selected. The latter was deemed simpler to implement, whilst also being closely matched in computational time and accuracy [258] for similar second order PDEs; it is also the one used in heat and mass transfer element formulations in Abaqus. Using the Lagrangian definition in this thesis, only the electric potential and concentrations of the two ion species are included in the vector of field variables of the system, which reads: $\mathbf{u} = \{\psi, c_1, c_2\}$. For the finite element, the vector of nodal field variables reads:

$$\mathbf{q}^{(k)} = \{q\}^{(k)} = \left\{ \psi^{(k)}, c_1^{(k)}, c_2^{(k)} \right\}^{\mathrm{T}} \quad , \tag{7.3}$$

where k is the node number. The vector of nodal variables for each element was defined in a consecutive manner according to standard conventions used in Abaqus [257]:

$$\mathbf{q}^{(e)} = \{q\}^{(e)} = \left\{ \psi^{(k)}, c_1^{(k)}, c_2^{(k)}, \psi^{(k+1)}, c_1^{(k+1)}, c_2^{(k+1)}, \ldots \right\}^{\mathrm{T}} \quad , \tag{7.4}$$

where e is the element number.

The global displacement vector $\{Q\} = \mathbf{Q}$ can be obtained by assembly of all $\{q\}^{(e)}$. In the following, the gradient notation ($\nabla\mathbf{q} = \nabla\{q\}$**)** has been used to denote spatial derivatives and dot notation ($\mathbf{q} = \{q\}$**)** has been used for temporal derivatives.

The continuous field variables $\mathbf{u}$ are approximated within the finite element as:

$$\mathbf{u}\ \mathbf{x}\ = \mathbf{N}\mathbf{q}^{\,e} \quad , \tag{7.5}$$

where $\mathbf{N}$ is the matrix of interpolation functions (see Section 7.2.3). This interpolation applies to each of the field variables, as well as the rate of change of concentration:

$$\psi = \mathbf{N}\boldsymbol{\psi}^{(e)} \quad , \quad c_s = \mathbf{N}\mathbf{c}_s^{(e)} \quad \text{and} \quad c_s = \mathbf{N}\mathbf{c}_s^{(e)} \quad ,$$
$$\text{where} \qquad \boldsymbol{\psi}^{(e)} = \left\{\psi^{(k)}, \psi^{(k+1)}, \ldots\right\}^{\mathrm{T}} \quad \text{and} \quad \mathbf{c}_s^{(e)} = \left\{\ c_s^{(k)}, c_s^{(k+1)}, \ldots\right\}^{\mathrm{T}} . \tag{7.6}$$

Since $\mathbf{q}^{(k)}$ contains three field variables, $\mathbf{N}$ can be rewritten as a $3 \times 3\alpha$ matrix:

$$\mathbf{N} = \begin{bmatrix} N_1 & 0 & 0 & N_2 & 0 & 0 & \cdots & N_\alpha & 0 & 0 \\ 0 & N_1 & 0 & 0 & N_2 & 0 & \cdots & 0 & N_\alpha & 0 \\ 0 & 0 & N_1 & 0 & 0 & N_2 & & 0 & 0 & N_\alpha \end{bmatrix} \quad , \tag{7.7}$$

where α is the number of shape functions. The derivative of the field variables is obtained from the displacement differentiation matrix, $\mathbf{B} = \boldsymbol{\nabla}\mathbf{N}$:

$$\nabla\mathbf{u} = \boldsymbol{\nabla}\mathbf{N}\mathbf{q}^{(e)} = \mathbf{B}\mathbf{q}^{(e)} \quad . \tag{7.8}$$

After applying the interpolation to the weighted residual equations (Appendix D.1), the element equations are rewritten in the following algebraic form, following Lim [164]:

$$\mathbf{R}^{\,e} = \mathbf{M}^{(e)}\mathbf{q}^{(e)} - \left(\mathbf{G}^{\,e} - \mathbf{F}^{\,e}\right) \quad . \tag{7.9}$$

The expanded components of the discretised finite element equation above are given in Appendix D.1. The global residual vector, $\mathbf{R}$, can be obtained by assembly (adding all element contributions, resulting in 3α equations). The value of the global displacement vector $\mathbf{Q}$ can then be sought, which satisfies in an integral sense a zero valued residual:

$$\mathbf{R} = \mathbf{M}\mathbf{Q} - \ \mathbf{G} - \mathbf{F}\ = 0 \quad , \tag{7.10}$$

where $\mathbf{G}$ is the global vector of internal loads. $\mathbf{F}$ is the global load vector associated with the boundary conditions specified on the element boundaries. It can be shown that [259], following assembly of $\mathbf{F}$, terms associated with the internal nodes of the mesh vanish, leaving only the terms associated with the nodes at the mesh boundary (electrode/electrolyte interfaces, denoted $\mathbf{x_1}$ and $\mathbf{x_2}$. Since there is no mass flux at these interfaces, only two non-zero terms remain**:**

$$\mathbf{F}_{\psi}^{\mathbf{x_1}} = -\varepsilon_0\varepsilon_{\mathrm{r}}\nabla\psi_{\mathrm{s}}^{\mathbf{x_1}} \qquad \text{and} \qquad \mathbf{F}_{\psi}^{\mathbf{x_2}} = \varepsilon_0\varepsilon_{\mathrm{r}}\nabla\psi_{\mathrm{s}}^{\mathbf{x_2}} \quad , \tag{7.11}$$

which are evaluated using the prescribed boundary conditions. These depend on the electrochemical experiment being simulated (see Appendix A.2).

7.2.3 Interpolation

For an 8-node quadratic 2D element, the Lagrange interpolation functions are expressed in natural coordinates ξ,η as:

$$\begin{aligned} N_1\ \xi,\eta\ &= \frac{1}{4}\ 1-\xi\ \ \eta-1\ \ \xi+\eta+1 & N_5\ \xi,\eta\ &= \frac{1}{2}\ 1-\eta\ \ 1-\xi^2 \\ N_2(\xi,\eta) &= \frac{1}{4}\ 1+\xi\ (\eta-1)(\eta-\xi+1) & N_6(\xi,\eta) &= \frac{1}{2}(1+\xi)(1-\eta^2) \\ N_3(\xi,\eta) &= \frac{1}{4}\ 1+\xi\ (\eta+1)(\xi+\eta-1) & N_7(\xi,\eta) &= \frac{1}{2}(1+\eta)(1-\xi^2) \\ N_4\ \xi,\eta\ &= \frac{1}{4}\ \xi-1\ \ \eta+1\ \ \xi-\eta+1 & N_8\ \xi,\eta\ &= \frac{1}{2}\ 1-\xi\ \ 1-\eta^2\ . \end{aligned} \tag{7.12}$$

As a result of this discretisation scheme, the element potential and concentration vectors, $\psi^{(e)}$ and $\mathbf{c}_s^{(e)}$, are 8×1, and the element vector of field variables, $\mathbf{q}^{(e)}$, is therefore 24×1. The element matrices $\mathbf{M}^{(e)}$ and $\frac{\partial \mathbf{G}^{\,e}}{\partial \mathbf{q}}$ are 24×24 and the force vectors $\mathbf{G}^{(e)}$ and $\mathbf{F}^{(e)}$ are 24×1. The element matrices were derived as part of this work and are listed in Appendix D.2.

7.2.4 Numerical integration

Numerical integration in the natural coordinate system was used to evaluate the volume integrals in the FE equations (Appendix D.1). The field variable transformation from global (x,y) to natural ξ,η coordinates was performed via the Jacobian matrix, **J**:

$$\begin{Bmatrix} \frac{\partial q}{\partial \xi} \\ \frac{\partial q}{\partial \eta} \end{Bmatrix} = \begin{bmatrix} \frac{\partial x}{\partial \xi} & \frac{\partial y}{\partial \xi} \\ \frac{\partial x}{\partial \eta} & \frac{\partial y}{\partial \eta} \end{bmatrix} \begin{Bmatrix} \frac{dq}{dx} \\ \frac{dq}{dy} \end{Bmatrix} = \mathbf{J} \begin{Bmatrix} \frac{dq}{dx} \\ \frac{dq}{dy} \end{Bmatrix} \text{ and } \begin{Bmatrix} \frac{\partial N_i}{\partial \xi} \\ \frac{\partial N_i}{\partial \eta} \end{Bmatrix} = \mathbf{J} \begin{Bmatrix} \frac{dN_i}{dx} \\ \frac{dN_i}{dy} \end{Bmatrix},$$

where

$$\begin{aligned} \frac{\partial x}{\partial \xi} &= \sum_{i=1}^{\alpha} \frac{\partial N_i}{\partial \xi} x_i \quad , \quad \frac{\partial x}{\partial \eta} = \sum_{i=1}^{\alpha} \frac{\partial N_i}{\partial \eta} x_i \quad , \\ \frac{\partial y}{\partial \xi} &= \sum_{i=1}^{\alpha} \frac{\partial N_i}{\partial \xi} x_i \quad , \quad \frac{\partial y}{\partial \eta} = \sum_{i=1}^{\alpha} \frac{\partial N_i}{\partial \eta} x_i \quad . \end{aligned} \tag{7.13}$$

For the arbitrary function $f\ x,y$, the above leads to:

$$\int_{y_1}^{y_2}\int_{x_1}^{x_2} f\ x,y\ dxdy = \int_{-1}^{1}\int_{-1}^{1} f\ \xi,\eta\ \det\mathbf{J}\, d\xi d\eta \quad ,$$

where

$$\det\mathbf{J} = \frac{\partial x}{\partial \xi}\frac{\partial y}{\partial \eta} - \frac{\partial y}{\partial \xi}\frac{\partial x}{\partial \eta} \quad . \tag{7.14}$$

Gaussian quadrature was used to evaluate integrals over the domain of the natural element:

$$\int_{-1}^{1}\int_{-1}^{1} f\ \xi,\eta\ d\xi d\eta = \sum_{i=1}^{n}\sum_{j=1}^{n} f(\xi_i,\eta_j) w_i w_j \quad , \tag{7.15}$$

where n is the number of points along each axis in the Gauss quadrature, ξ_i and η_j are their natural coordinates, and w_i and w_j are their weights. Three-point quadrature was used, with $\xi_i = \eta_j = [-\ \sqrt{3/5}\ 0,\ \ \sqrt{3/5}\ ]$ and $w_i = w_j = [5/9, 8/9, 5/9]$, and nine integration points in 2D.

7.2.5 Time integration and numerical solution

The incremental solution can be obtained by approximating the time dependence of the governing equation using the backward difference scheme [257] and derivations of this procedure are given in Appendix D.3. In Abaqus/Standard, the overall system of equations above is solved iteratively using Newton's method [257]. The general form of the element system of equations may (Eqn. (7.9)) can be rewritten as:

$$\{R\} = [C]\{u\} + [K]\{u\} - \{F\} \quad . \tag{7.16}$$

The element's contribution to the total residual, through the stiffness matrix and vector of nodal forces (AMATRX and RHS), must be defined within the UEL subroutine as [260]:

$$\text{AMATRX} = [K] + \left(\frac{1}{\Delta t}\right)[C] \quad \text{and} \quad \text{RHS} = \{F\} \quad ,$$

where

$$[K] = -\frac{d\{F\}}{d\{u\}} \quad \text{and} \quad [C] = -\frac{\partial\{F\}}{\partial\{u\}} \quad . \tag{7.17}$$

In a transient heat transfer analysis, $[C]$ is the heat capacity matrix, while in the ion transport analysis, it is the damping matrix associated with mass diffusion. Note that the terms 'thermal' and 'heat transfer' are used interchangeably in this Chapter, to maintain consistency with the terminology used in Abaqus [260]. The implementation of AMATRX and RHS can be found in Appendix D.4. The structure of the subroutine code closely followed that of a thermal element subroutine given in the Abaqus documentation [260].

7.3 Implementation of user element within a thermal-electrical analysis

7.3.1 Analysis procedure

Considering the nodal variables and form of the incremental solution (Section 7.2.5), the transient coupled thermal-electrical analysis (Abaqus/Standard) [257] procedure type provides the closest analogue in the commercial code to the ion transport problem. The thermal-electrical analysis type considers only two active degrees of freedom: electric potential and temperature, denoted as degrees of freedom 9 and 11, respectively, according to the Abaqus naming convention [257]. However, degree of freedom 11 is also reserved for the normalised concentration variable used in mass diffusion procedures, whilst degree of freedom 12 is available as a second temperature, which can be activated if required.

The analysis input file for the ion transport model (Appendix D.5) was therefore written to call a thermal-electrical analysis, with active degrees of freedom specified as 9,

11, 12, corresponding $\mathbf{u} = \{\phi, c_1, c_2\}$. This analysis procedure uses the backward difference scheme for time integration and Newton's solution method, with automatic convergence checks are applied to the current density residuals corresponding to degree of freedom 9, and to the heat (mass) flux residuals corresponding to degrees of freedom 11 and 12 [260]. The analysis workflow is illustrated in Figure 7.1.

7.3.2 Model geometry and discretisation

A 2D element (Figure 7.2) was chosen for the initial implementation and testing. It was anticipated that, upon successful subroutine validation in 2D, the additional effort required for extension to 3D would be negligible by comparison. For the initial testing, the electrolyte domain was considered in isolation, and a regular 1×5 mesh was generated (see Appendix D.5), as shown in Figure 7.3.

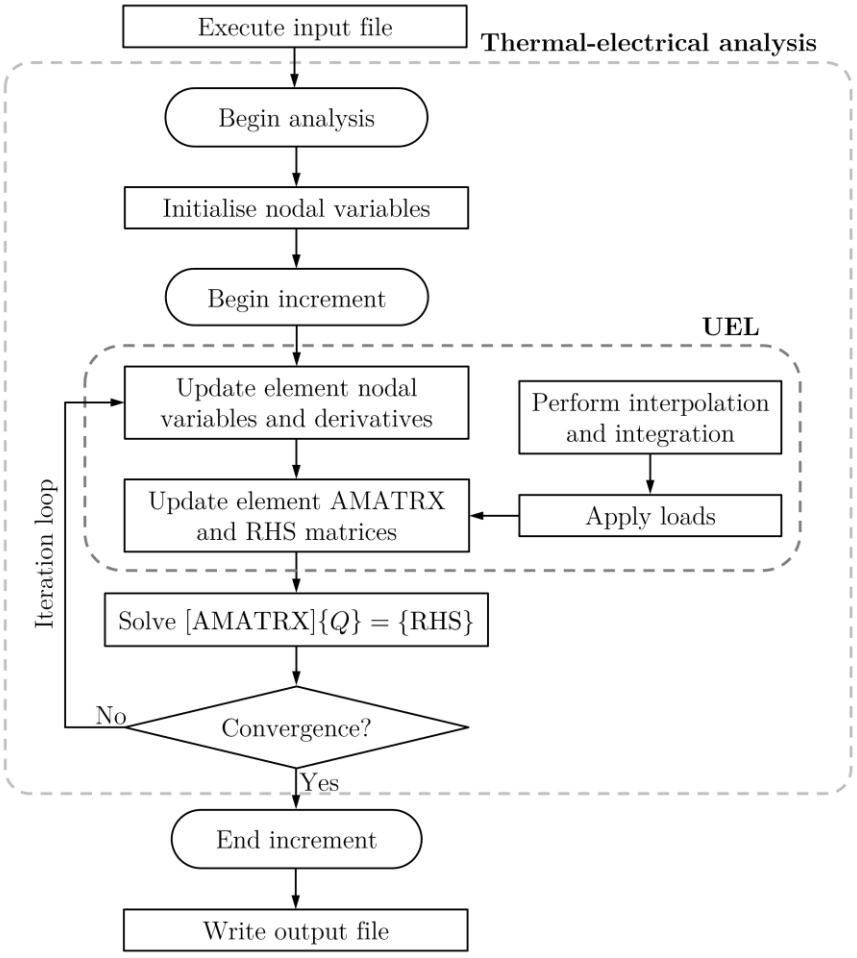

Figure 7.1. Flow chart of the thermal-electrical analysis procedure with an ion transport UEL.

7.3.3 Constitutive model

As required [260], all material behaviour was defined within the UEL subroutine (Appendix D.4), based on the user-defined parameter inputs and the solution-dependent state variables. The input variables defining material parameters and physical constants are listed in Table 7.1, and were chosen to enable validation of the subroutine against the 1D numerical solutions obtained by Lim [164].

7.3.4 Initial, boundary conditions and loads

For initial subroutine validation, a simple boundary value problem was considered, in which a fixed potential ψ_s was applied at the mesh boundary surfaces, shown in Figure 7.3, to simulate potentiostatic charge (Appendix A.2). The boundary surfaces were defined through node-based sets to ensure compatibility with the UEL [260]. Since a zero-mass flux condition was also required at the boundaries, these sets were also used to specify a node-based distributed flux of type Un, where $n = 1 \ldots 4$, refers to the element faces, as shown in Figure 7.2.

The user-subroutine file was modified accordingly to allow for any $n = 1 \ldots 4$ being specified by the input file, and the implementation of the different cases was confirmed in preliminary tests performed on a heat transfer user element subroutine [260]. These were compared to solutions obtained using the built-in heat transfer element (DC2D8). The initial potential was zero everywhere, whilst the concentrations for both ion species were initialised at the bulk concentration c_∞. The syntax used to specify these conditions in the analysis input file are given in Appendix D.5.

7.3.5 Post-processing

To record and access the simulation results, solution dependent (state) variables were defined (STATEV). The number of state variables requested was equal to the number of nodes per element multiplied by the variables of interest [260] (the spatial gradients of the field variables, $\nabla \mathbf{u}$). For the 8-node quadratic 2D element, the number of variables requested was 8×3×2 (48). To visualise the field variables, these nodal outputs were exported to MATLAB for interpolation and plotting.

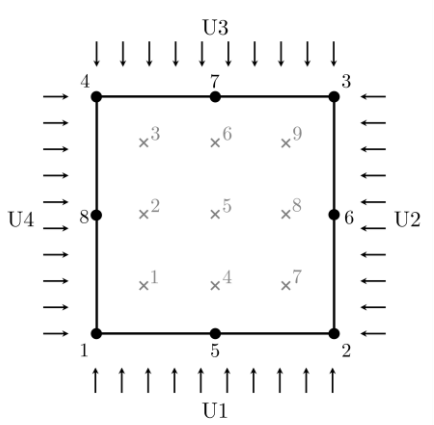

Figure 7.2. Node, integration point and distributed flux numbering over a finite element.

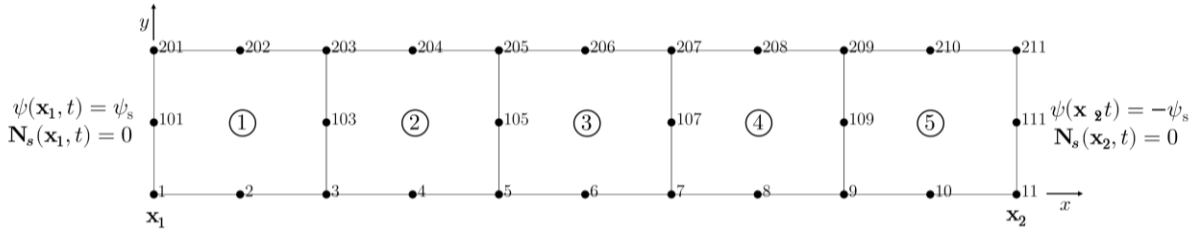

Figure 7.3. Five-element mesh and boundary conditions for ion transport model.

Table 7.1. List of input values used to test the ion transport model [164].

Symbol	Quantity	Value	Unit
$D_s = D$	Diffusivity	2×10^{-9}	m^2/s
c_∞	Bulk concentration	1	mol/m^3
L	Electrolyte layer thickness	3×10^{-7}	m
T_{abs}	Temperature	300	K
$u_s = u$	Mobility	8.02×10^{-13}	m^2mol/Js
ψ_s	Surface potential	0.02	V

7.4 Implementation results

7.4.1 Testing of ion transport subroutine

The potential and concentration fields obtained from the above implementation of the ion transport model were plotted against the analytical Poisson-Boltzmann steady state solution (Eqn. (2.12), Section 2.6.2.2) in Figure 7.4. The results showed that, despite the potential and concentration appearing to be correctly initialised, the solution was not updated over time. This problem was traced to the vector of nodal variables being passed into the ion transport subroutine as 'NaN' (not-a-number/undefined) values, in the first increment after initialisation.

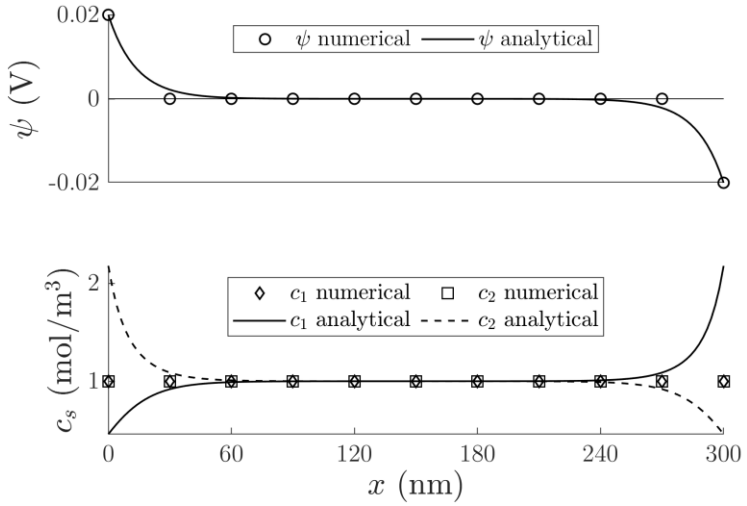

Figure 7.4. Ion transport model results, using nominal input values.

7.4.2 Testing of thermal subroutine

To understand the cause of the problem identified in the previous Section, further testing was carried out using the thermal element subroutine provided in the Abaqus documentation [260] (hereafter referred to as UELHT), as well as the inbuilt quadratic 2D thermal element (DC2D8) and thermal-electrical element (DC2D8E), in both the heat transfer and coupled thermal-electrical analysis procedures. The element/analysis combinations tested are listed in Table 7.2. In these tests, a simple boundary value problem was considered, with arbitrary values of nodal temperature specified at the mesh boundaries, over a two-element domain, as shown in Figure 7.5(a).

The results of these tests are plotted in Figure 7.5(b). All of the models listed in Table 7.2, except the UELHT_TE model produced the expected linear temperature distribution. In the UELHT_TE model (similarly to the ion transport model (Figure 7.4)) the solution did not update after the field variable initialisation. The numerical implementation of the ion transport and thermal subroutines is discussed in Section 8.4.

Table 7.2. List of elements and analysis procedures considered in the thermal subroutine testing.

Model code	Element type	Analysis procedure
UELHT_T	Thermal element subroutine (UELTRAN1)	Heat transfer
UELHT_TE	Thermal element subroutine (UELTRAN1)	Coupled thermal-electrical
DC2D8_T	Thermal element (DC2D8)	Heat transfer
DC2D8_TE	Thermal element (DC2D8)	Coupled thermal-electrical
DC2D8E_TE	Thermal-electrical element (DC2D8E)	Coupled thermal-electrical

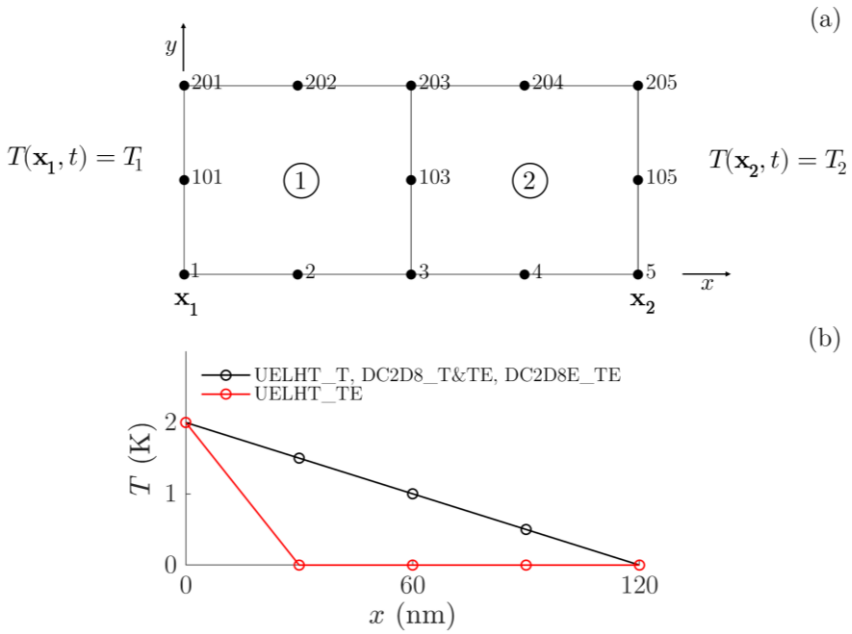

Figure 7.5. (a) Two-element mesh and boundary conditions for the thermal model, and (b) thermal element and subroutine testing results.

8 Discussion

In this Chapter, the research findings presented in Chapters 4 to 7, corresponding to Phases 1 to 4, are discussed. The results from each Phase are interpreted in the context of the relevant background literature and experimental data. Findings which relate across multiple Phases are examined. The limitations and wider relevance of the methodologies used in this thesis are evaluated.

8.1 Compaction analysis and prediction

8.1.1 Model limitations and practical variability

The recommendations of a recent benchmark exercise [61], with regards to the use of self-aligning spherical seating platens and direct thickness measurement methods (Section 2.3.1), were taken into account in the experimental part of the present work. It was therefore assumed that the remaining scatter in the experimental measurements could be primarily attributed to variability of the specimens themselves. For the multilayer specimens, the scatter was primarily attributed to differences in nesting due to the arbitrary ply offset of each specimen, which was not controlled during layup.

The results in Section 4.4.1 confirmed that the IP and 90°OP limit models of specimens C_2, G_2 and CGC predict the range, within which the compressibility responses of the physical specimens lie, and their predictions compared well with those reported for monolithic twill weave fabric stacks [57]. The observed experimental scatter in the compressibilities of these specimens was significantly narrower however, suggesting that the limit case models represent conditions less likely to occur in practice, while intermediate cases present a greater statistical likelihood. Furthermore, the experimental compressibility of these specimens tended towards the IP model predictions, where minimum nesting occurs. This tendency implies that physical multilayer specimens were subject to conditions limiting their compressibility, which were not considered in the models. These conditions may include i) global fabric pre-shear or relative misalignment of the fabric plies [55,57]; ii) local misalignment of the yarn directions within plies [57]; (iii) local deviation from the average geometric parameters (variability) [261]. In each case, deviation from the assumed idealised geometry would prevent the occurrence of complete nesting as predicted at the

90°OP limit, reducing the effective compressibility. This effect is expected to be especially significant for finer weaves, such as the glass fabric used in this study, since the geometric 'defect' count is expected to scale with the UC count per unit area; meanwhile, handling-induced shear and distortion is also more likely for this fabric. The narrow experimental compressibility range observed for the bilayer G_2 appears to support the above statement.

Compressibility predictions based on idealised geometric and nesting configuration assumptions are judged to be of limited direct use. They provide a bounding interval of compressibility since they assume a level of material uniformity and process control that is not achieved in practice. As evidenced by the μCT, some degree of geometric non-uniformity as well as pre-shear in the glass fabric (Figure 4.9(b) and Figure 4.11(d)) was apparent even at the local scale of a few unit cells. UC models with a random ply offset offer only a small improvement in this aspect, since they retain an implicit assumption of global geometric uniformity. The alternative would be to consider a stochastic model, where geometric variabilities are randomly distributed across a much larger representative volume element [261]. However, the computational cost associated with the application of such a scheme to meso-scale models with consistent meshes is judged to be prohibitive at present. Moreover, challenges related to ensuring model periodicity [57] and robustness in models considering fabric pre-shear and yarn misalignment require further attention.

While the IP models did provide a closer agreement with the experimental compressibility curves than the 90°OP models, neither of the predicted internal morphologies corresponded closely to those observed in physical specimens (Figure 4.11). It is therefore more likely that misalignment and geometric variability were instead responsible for the low apparent compressibility of physical specimens, particularly since a finite (non-zero) phase shift between the carbon plies was consistently observed in μCT and optical microscopy. The numerical findings underline the sensitivity of the internal morphology of WFRCs to the local ply offset. It is consequently not surprising that, in the literature, evidence from static compression tests [135,262] and static and fatigue delamination tests [263] suggests an important influence of nesting on the damage mechanisms and failure properties of monolithic WFRCs. To understand the ply offset sensitivity of the mechanical response of the SSC system under investigation, as well as other hybrid WFRCs, future mechanical analyses should consider a range of ply offset cases.

8.1.2 Effect of hybridisation of the stacking sequence

It is widely recognised that interply nesting increases the compressibility of monolithic multilayer stacks, compared to that of single layers [57]. In this work, the experimental data (Figure 4.4 and Figure 4.8(a)) further indicated that the scatter in compressibility was also greater for the multilayer stacks compared to that of single layers. The large difference in the compressibility predicted for the limit nesting configurations of the monolithic stacks (Figure 4.8(a)) further indicated that the experimental scatter had been primarily caused by variability in the ply offset introduced during hand layup.

It was initially hypothesised that hybridisation of the stacking sequence would reduce the effective compressibility of the stack by inhibiting interply nesting. Comparison between the compressibility curves of the $C_{2,90°OP}$ and $CGC_{90°OP}$ models (Figure 4.8(a) and (b)) indicated that hybridisation slightly reduced the average total fibre volume fraction (ca. −2% at 1 MPa); meanwhile, the experimental data presented a similar reduction (−1.6% at 1 MPa), supporting this hypothesis. This relatively small reduction was initially surprising, however further analysis of the compressibility curves and the internal morphology of the physical specimen provided an explanation.

The greater experimental scatter in the CGC response, compared to those in the remaining hybrid multilayer and the single layer specimens, suggested that some C/C nesting was present in the CGC specimens, despite the presence of the G ply. The optical and μCT observations (Figure 4.9(b), Figure 4.10, Figure 4.11(d) and (h)) confirmed that through-thickness waviness was introduced in the G ply, with a period and amplitude of the order of those of the C plies. This geometry was indicative of C/C nesting, made possible by the relatively low areal weight and bending rigidity (improved conformability) of the G fabric.

In contrast, the low scatter in the compression curves obtained for the CG and GCG stacking sequences indicated that interply nesting had a negligible influence on the compression response in those cases. In the former case, no matching fabric counter-surfaces were present in the layup, while in the latter, the matching counter-surfaces of the outer G plies were separated by the thicker and more rigid C ply. These results lead to the conclusion that some loss of nesting, resulting from the loss of matching fabric counter-surfaces, could be expected in stacking sequences combining dissimilar weaves; however, this effect is specific to the stacking sequence and likely depends on the degree of geometric

dissimilarity between the weaves, their relative thicknesses and bending rigidities. The choice of constituent fabrics may, therefore, influence the attainable fibre volume fractions and local architecture in the final hybrid WFRCs. It is interesting to note that a similar loss of nesting has been reported in the case of monolithic fabric stacks containing off-axis plies [57], suggesting the influence of hybridisation may not be so apparent in laminates with quasi-isotropic layups.

8.1.3 Effect of CAG modification

The out-of-plane compression tests confirmed the qualitative finding of preliminary optical microscopy imaging that compressibility was markedly reduced by CAG modification of the carbon fabric. An absolute change in the total fibre volume fraction obtained at 1 MPa applied pressure ca. −13% was measured for both the single fabric plies and device stacks (Figure 4.12). This reduction was much more significant than that due to stacking sequence hybridisation in the multi-layer specimens (as discussed in Section 8.1.2).

The findings of this experiment are in qualitative agreement with those reported for CNT-reinforced carbon fabrics [204,205]. As the authors of that study have remarked, the manufacture of composites containing nanomodified fibres should take this change of fabric behaviour into account. It is also apparent that, in the absence of compensatory modifications to the present manufacturing process, the fibre-dominated mechanical properties of these composites could be significantly inferior to those of traditional WFRCs.

8.1.4 Computational cost

The 1:5 ratio in unit cell sizes in the hybrid system studied here, coupled with the demanding mesh size requirements for convergence, resulted in a very large FE mesh, exceeding 200,000 elements for a bilayer hybrid model. Furthermore, the numerous contact interactions necessitated the use of an explicit solution scheme, placing restrictions on the maximum allowable time increment. The solution of such a model is at present only feasible with the use of high-performance computing (HPC). Adoption of these mesoscale models outside research settings is therefore judged unlikely. Even with HPC, the computational cost would quickly become prohibitive for meso-models with less favourable tessellation ratios or thicker stacks. For this reason, the present study was limited to few plies only; however, out-of-plane symmetry or periodicity boundary conditions [116,134] could be applied to reduce the problem size for thicker stacks.

8.2 Mechanical performance analysis and prediction

8.2.1 Effect of ply offset

Firstly, it should be emphasised that during laminate manufacture the ply offset was not controlled, therefore the panels would have contained arbitrary ply offsets. The three idealised ply offset models studied in Chapter 5 were therefore analysed with the aim of providing an indicative range of elastic properties that could be expected from physical specimens. The numerical results (Table 5.4) confirmed that ply offset could be a source of significant variability in the mechanical properties of a series of statistically independent samples, agreeing with the results of the compaction studies in Chapter 4.

This variability was not observed in the experimental study in Ref. [47] most likely because the samples were not statistically independent: test coupons were cut from the same laminate, with one laminate produced per specimen orientation and material configuration. Some care should therefore be exercised when comparing the experimental performances across the different material configurations, as the reported scatter in the experimental measurements does not include variations associated with ply offset variation.

When analysing the effect of ply offset on the tensile and in-plane shear elastic properties, it is important to note that the mechanical responses varied under the combined (and coupled [132]) influence of both geometric/material symmetry (or lack thereof) and free surface effects. The former was determined by the ply offset, while the latter was controlled by the through-thickness boundary conditions. The influence of through thickness boundary conditions is reported in Appendix B.2. The work in Chapter 5 modelled single cell laminates using in-plane periodicity and free lateral surface boundary conditions with constrained out-of-plane rotation, to ensure the models were representative of the experimental conditions in Ref. [47], whilst keeping computational cost low.

In woven composite laminates, ply offset determines the mutual mechanical support provided by adjacent yarns, resulting in variation in the internal stress distribution between the different geometric configurations [134,136]. For both the tensile and shear load cases (Figure 5.19(a) and (b)), the highest apparent stiffnesses were generally produced by the 90°OP model. While this configuration was unsymmetric, the compaction models in Chapter 4 showed that it had a more homogenous local fibre volume fraction distribution and smaller resin pockets, which may have enhanced the load distribution across the

laminate. Comparing the results of the IP (asymmetric) and 180°OP (symmetric) stacking sequences, it could be concluded that asymmetry in the IP case led to a lower apparent tensile modulus, whilst the shear modulus was negligibly affected.

8.2.2 Model limitations and effect of constituents and defects

Before discussing the limitations of the finite element models developed in Chapter 5, it is important to note that the use of FEM for the prediction of the mechanical properties of woven composites overcomes many of the shortcomings of alternative analytical models. Analytical models based on orientation averaging and classical laminate theory, such as the slice array model (Section 5.4.5), are generally unsuitable for the prediction of the through-thickness elastic properties or failure properties [124] due to their reliance on geometric and stress-state idealisations. In contrast, the three-dimensional stress-state predictions obtained by FEM increase both the accuracy and versatility of these models.

Indeed, extending the presently developed elastic models to the nonlinear regime in future would be relatively straightforward, and was the primary motivation for pursuing the approach. Even in the linear elastic regime, which was the focus of this work, FEM was instrumental in enabling investigations of the influence of complex microstructural features such as nesting and defects. The considerable variability in mechanical properties which arises due to differences in ply offset discussed above could not have been captured by analytical models, in which ply thicknesses are uniform and nesting is neglected. Likewise, the development cost associated with modelling discontinuous features such as defects is minimal.

Many of the numerical findings in Chapter 5 were qualitatively anticipated based on the elastic properties of the constituent materials under investigation. The relatively higher elastic modulus of the CAG (23 GPa) compared to the STR epoxy system (2.7 GPa) was expected to result in increases in the elastic moduli, with larger increases in matrix-dominated properties, such as the shear modulus [245]. The degradation of the mechanical performance of the CAG-modified structural laminates reported from the experiments in Ref. [47] was therefore surprising, and indicated that the microstructure and composition of these laminates was insufficiently understood. The above research gap motivated the more detailed microstructural characterisation presented in Section 5.3.1, and subsequent modelling of defects in Section 5.5.3 in an attempt to explain the performance gap between the experimental results and the numerical predictions obtained from the defect-free

models. Accounting for the presence of transverse cracks (DEF models) did not sufficiently explain the elastic performance degradation, though it accounted for a large portion of it, particularly in the in-plane shear case.

The latter could be explained by considering the orientation of the transverse crack plane, which is perpendicular to the plane of shear. This situation can be represented by the iso-stress model, with springs k_1 and k_2 in series, where $k_1<k_2$ (as shown in Figure 8.1(a)). The effective shear response of this system is dominated by the most compliant spring (the pre-crack). In isolation, interyarn delaminations do not have the same effect on shear modulus since they are oriented parallel to the shearing plane. In this case, the iso-strain (springs-in-parallel) model applies (Figure 8.1(b)), where the shear response is dominated by the stiffest spring. The response of the composite laminate would in reality be a complex combination of the two cases (simplified in Figure 8.1(c)) that is slightly more compliant than the iso-stress model.

Propagation of inaccuracies in the constitutive properties of the fibres and matrices used in the micromechanics equations may have also contributed to the discrepancies; nevertheless, it is unlikely that they could have been the primary source of error. On the other hand, it is well known that voidage results in stress concentrations and loss of load-carrying capacity, which particularly affect matrix- and interface-dominated composite properties [100]. It is therefore likely that voidage of the considerable extent observed in the C*GC* STR laminates, alongside poor wetting of the CAG with epoxy (and therefore poor load transfer), would have been responsible for further degradation in elastic properties.

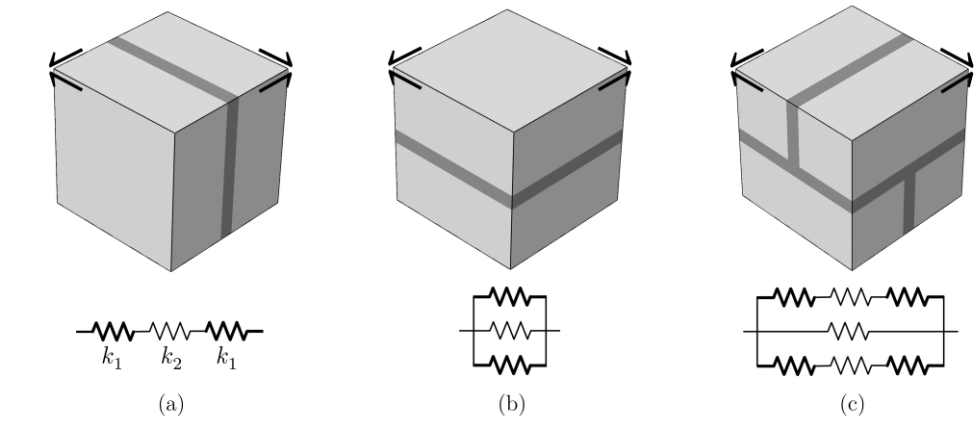

Figure 8.1. Schematic drawing illustrating the effect of pre-cracks with different orientations (dark grey) on the shear response of a composite volume, with equivalent spring network models shown

By neglecting voidage, the present models overpredict the mechanical properties by assuming: (i) a higher volume content of CAG than would have been present in the real laminates; and (ii) a continuous stress distribution throughout the yarns. Voidage was not accounted for in this work for the following reasons: (i) unlike the approximately periodic transverse cracks, the observed intrayarn and interlaminar voids represented large, geometrically irregular, and localised defects, which the mesoscale unit cell modelling approach is ill-suited to; and (ii) it is expected that in the near future, process-induced defects can be significantly reduced in the SSC laminates, leading to improvements in the predictive accuracy of the present models. Furthermore, a review of the literature (Sections 2.4.1.2 and 2.4.2.2) indicated that predicting the effects of voids on mechanical properties is complex and challenging, not least due to the critical influence of void size and shape on local stress concentrations.

Another factor which may have contributed to overprediction of the elastic properties of the CAG-modified laminates was the use of input material properties obtained from experimental characterisation of monolithic, rather than *in situ,* CAG. To verify this assumption, high magnification scanning electron micrographs of the monolithic and *in situ* CAG microstructures were compared in Section 5.3.3. The conclusions of this comparison were uncertain due to general variability of the morphology observed across the dry CAG-modified fabric, as well as differences in the viewing angle. However, there were qualitative indications of a subtle difference in morphology, with the microstructure of the monolithic CAG appearing less tortuous, which may indicate it had a higher density.

In the wider literature, the elastic modulus of unpyrolised CAG [75] and silica aerogels [113] has been reported to increase with aerogel density. Therefore, a denser monolithic CAG would imply that device-level stiffnesses would have been overestimated in the model. However, the magnitude of this potential error in the CAG properties is unknown. Accounting for a moderate percentage error, the overall conclusions of the numerical predictions are expected to remain qualitatively unchanged. Further investigations are recommended in Chapter 10.

Finally, it is acknowledged that in the real specimens, the geometry and distribution of pre-cracks was somewhat irregular. In the DEF models, a regular and periodically distributed geometry was assumed, with two cracks per yarn based on the X-ray

observations in Section 5.3.1.1. This simplification serves as a reminder that the DEF model results should be interpreted qualitatively.

In the multifunctional composite configuration, the validity of the assumption of a homogenous isotropic matrix and the use of neat, rather than *in situ,* matrix properties was clearly undermined by the observed voidage and possible phase separation of the structural electrolyte in the laminates in Ref. [47]. Since the *in situ* mechanical properties of the structural electrolyte are unknown at present, the FE predictions should be treated as indicative guidelines, reflecting the performance of ideal, defect-free composites. These guidelines can be useful to researchers developing future generations of SSCs and/or at early stages of constituent formulation. In future, experimental characterisation of the *in situ* microstructure and properties of the structural electrolyte is recommended (Chapter 10).

The present lack of experimental data on the *in situ* elastic properties and the non-linear mechanical response of the constituent materials and their mutual interfaces remains an obstacle to modelling progress. For this reason, and due to the presence of defects, the failure behaviour of SSC laminates was not modelled in this work. However, with increased availability of constitutive data, combined with measures to mitigate defects, in future, the models developed in this work could be readily adapted to simulate the response of SSCs beyond the linear regime. For example, the use of a surface-based interaction formulation (Section 5.4.3) at the yarn/yarn and yarn/matrix interfaces, enables delaminations of these interfaces to be modelled through a cohesive surface interaction.

An important next step towards a more complete understanding of the mechanical behaviour of SSCs (and one where computational modelling may prove useful) would focus on identifying the causes of their relatively poor tensile strength and shear strain to failure [47]. Finally, the models developed here, though focused on SSCs, are also relevant to a range of SPC systems that include common features, such as interply hybridisation, structural electrodes and separators with different characteristic length scales, electrodes featuring stiff electrochemically-active nanocarbon networks, and complex structural electrolytes. They may also assist the development and interpretation of bicontinuous aerogel-reinforced structural composites.

8.2.3 Tensile strength reduction in CAG-modified laminates

Whilst the experimental results from baseline and CAG-modified structural laminates (Table 5.3 and Figure 2.3) showed a relatively small reduction in tensile modulus (1%), the accompanying tensile strength reduction was unprecedented (69%). The fractographic analysis in Section 5.3.2 demonstrated that multiple interacting processes had contributed to the final failure of this laminate. The micrographs also offer clues regarding the reason for the poor tensile strength.

The combination of the two distinct 'broom-like' and 'flat' failure morphologies in different regions (Figure 5.12) of the carbon yarns was considered to be evidence of intrayarn voidage, as a result of poor infusion of both CAG precursor and epoxy into the interior of the carbon yarns. This conclusion was supported not only by the fractographic analysis above, but also by the optical, scanning electron and X-ray observations from the untested laminates (Section 5.3.1.1). From the quantitative X-ray analysis, it was discovered that the voids were elongated over a considerable distance along the yarns. The fibre bundles would have been unsupported by matrix over these long segments, and consequently, these regions would have been (i) the cause of stress concentrations in neighbouring well-infused regions, and (ii) unable to effectively redistribute additional stresses resulting from a fibre break in a nearby region.

For the failure sequence described in Section 5.3.2, where failure proceeded right-to-left across the zones A, B and C, the above suggests that zone B would have been unable to absorb the additional stresses resulting from the significant loss of load-carrying capacity in region A. As a result, intact fibres in region C, immediately adjacent to region B, would have experienced very large stresses due to (i) the pre-existing stress concentration due to the intrayarn void B, and (ii) the cumulative increase in stress concentration resulting from the large number of fibre breaks [264,265] in region A. This situation would have likely resulted in an unstable propagation of the crack front across the yarn. The slight change of depth in the fracture surface suggests that the first failure in region C was triggered from a critical fibre flaw at this depth.

Comparing the strain to failure reported in the literature for CAG/epoxy monoliths (0.35% [78]) with that of the T300 carbon fibres (1.5%, [91]), suggests that failure initiation may have been through the formation of transverse cracks in the CAG. These cracks may have initiated in CAG-rich skin regions or near the free surface and would have propagated

by brittle cleavage, creating stress concentrations, and promoting early fibre breakage. Considering the bundle failure sequence proposed above, it could be concluded that the brittleness of the CAG could have contributed to early catastrophic failure of the laminate.

The planar failure morphology of the well-infused regions A and B is indicative of either a strong fibre/matrix interface [104,238], or a low fibre strength relative to interfacial strength [238]. The latter explanation was discounted in recent fractographic analysis, which showed identical radial patterns at the carbon fibre ends in the baseline and CAG-modified laminates [47], whereas a larger 'mirror' zone would have been expected for CAG-modified fibres if they had been degraded [104]. Meanwhile, the fractographs in Section 5.3.2 (Figure 5.12) showed regions where continuity of the fracture plane had been preserved when failure had propagated from a fibre break into the CAG, as evidenced by radial riverlines. This continuity of the fracture plane and lack of interfacial debonding suggests a strong fibre/matrix interface [104].

Given the above findings, it is interesting to consider whether the large decrease in the composite tensile strength can be directly traced to the strength of the carbon fibre/matrix interface. Insights regarding this relationship can be obtained from the analytical model of Pimenta and Pinho [266] for the strength of infused UD fibre bundles. The analytical predictions link a high fibre/matrix yield stress, τ_{SL}, to a high mean bundle strength, $X_m^{[i]}$, where i denotes the bundle hierarchy level, with $n^{[i]} = 2^i$ filaments. The model contains an *a priori* assumption regarding the value of the stress concentration factor, k, associated with a fibre break: nominally $k = 2$; however, as the authors noted: the true value of k near a cluster of fibre breaks depends on local geometry, the size of broken clusters, matrix response and dynamic response.

In conventional polymer matrix composites, the presence of a plastic zone ahead of the crack tip relaxes the stress singularity near the fibre break [265]. In contrast, in the system studied here, the stiff and brittle CAG is unlikely to have undergone significant plastic yielding, suggesting that local stress concentrations near a single fibre break could have been larger than in conventional polymer matrix composites. Analytical stress field solutions by Beyerlein and Phoenix [265] suggest that the stress concentration factor for the fibre ahead of a crack rapidly increases with the number of contiguous fibre breaks, n_{b} (clusters of broken fibres), and takes a value of 5 for $n_{\mathrm{b}} = 31$ in composites with limited plastic yielding or interfacial debonding.

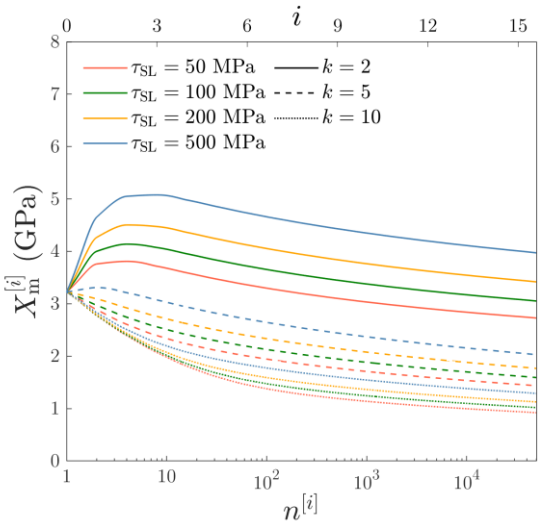

Figure 8.2. Bundle strength scaling for several shear-lag strengths τ_{SL}, and stress concentration factors k, calculated using the model of Pimenta and Pinho [266]. T300 fibres, $V_f = 60\%$.

Furthermore, it is important to note that the analytical models above consider only stress concentrations due to fibre breaks, that is, voids, geometric variability and other discontinuities in the microstructure are not considered; therefore, they offer only partial explanations of the failure mechanisms in the composites studied here. As discussed in the previous Section, the influence of voids on mechanical response is complex, and specific to the composite and void geometry. Examples of composites containing intralaminar voids of the size observed in this work (Section 5.3.1.1) are difficult to find in the literature, and models of the effects of voids focus instead on micro-voidage [137]; therefore it is not possible to make quantitative statements on their effects on stress concentrations.

One possible way to account for the low ductility of CAG, cumulative effect of fibre breaks and presence of voids in the bundle strength model in Ref. [266], is through the stress concentration factor. To study the significance of the magnitude of k in the CAG-modified composite system, the model was implemented in MATLAB and bundle strengths were evaluated over a range of values of k. As the matrix and interfacial strengths were also unknown for this material, a range of values of τ_{SL} were considered. Figure 8.2 illustrates the strength decrease associated with larger concentration factors. For all values of the carbon fibre/CAG interface strengths, the strength of a 3k bundle was reduced by ca. 65% when the value of the stress concentration factor increased from 2 to 10.

An energy-based fracture mechanics approach can also be useful in interpreting the flat fracture morphology observed in the well-infused carbon fibre bundles, since interfacial debonding and fibre pull-out are important energy-dissipating mechanisms during tensile

failure [265]. An analytical model for the translaminar fracture toughness by Pimenta and Pinho [267] offers quantitative insights on the relationship between fibre/matrix interface properties and debonding and pull-out toughnesses for various bundle sizes.

Model predictions for a 3k carbon fibre bundle, suggest that the toughening effect associated with fibre debonding sharply decreases for values of the mode II delamination toughness, $G_{II} > 1$ kJ/m^2, whilst the toughness component associated with fibre pull-out is also significantly diminished. As the delamination toughness of CAG-modified carbon fibre composites is unknown at present, it is difficult to generalise these findings to the presently considered composite system, however a high interfacial toughness could potentially be a contributing factor in the brittle tensile fracture.

In agreement with the literature [105], high fibre/matrix friction coefficient was also linked by the above model to reductions in the toughness components for the 3k bundle size. It is likely that the friction coefficient between debonded carbon fibres and CAG would be higher than that of epoxy, due to the hardness and porous nature of CAG, which would promote mechanical keying and prevent pull-out. Furthermore, shrinkage of the CAG around CFs during drying and pyrolysis is likely to have resulted in residual thermal compressive stresses on the fibre/matrix interface [105], enhancing its strength.

8.3 Current collection performance analysis and prediction

8.3.1 Model limitations and remaining research questions

The model presented in this chapter assumed a uniform electrode geometry and active current density. This approach was taken due to a present lack of electrical conductivity data at the micro- or meso- scales, as well as the increased computational expense associated with lower length scales. The active current was assumed to be injected at the electrode/electrolyte interface only, while in reality, provided sufficiently low scan rates, charge accumulation should occur at pore surfaces throughout the electrode interior; nevertheless, there the balance of transverse and lateral electronic conductivity would be evident. This electrical loading condition was therefore taken as a representation of the electrical transport limitation in the electrode layer, rather than an explicit representation of the double layer geometry.

Additionally, the model assumed a simple transversely isotropic material model for the electrodes, which was parametrised using the effective lateral conductivity measured from 0°/90° fabric specimens. In reality, due to the biaxial fabric architecture, the effective lateral conductivity at intermediate angles would be reduced from this maximum value, with a minimum at around ±45°. Unpublished experimental work by the Group has shown that the latter is approximately 45% lower than the maximum value. Despite the simplification, the numerical results represent a useful initial estimate of `losses in the electrode/current collector assembly, and deviations from the assumed behaviour are expected to be low, particularly when current collector elements are aligned with the fibre axes.

Future work could improve on the present model by employing either (a) a more accurate constitutive model of the fabrics, or (b) a mesoscale model, such as the one developed in this thesis (Chapter 4). The latter approach would require constitutive data to be measured for single yarns and their mutual interfaces, which may be challenging due to the lower magnitudes of resistance at this scale. In principle, there are opportunities to improve performance by designing current collector geometries, which complement the fabric directionality, but the manufacturing complications may not justify the effort.

Another limitation of the present model relates to the pressure applied during the resistance measurement. An influence of pressure on contact conductivity and the bulk conductivity of porous cell materials has been previously reported for traditional Li-ion batteries and supercapacitors [148,247]. This influence has not been discussed in the structural power literature despite being experimentally observed in unpublished work by the Group at ICL. It is possible that the defects observed in the carbon fabric electrodes (Section 5.3.1) may be partly responsible for the pressure dependence of electrical conductivity. For instance, pressure may improve internal electrical contact by closing yarn crossover delaminations, thereby improving the effective conductivity of this layer.

To assess the above issues, resistance measurements under controlled pressure were planned as part of this thesis; however, due to time and pandemic-related constraints, it was not possible to carry out these measurements. The available experimental data used in this work corresponded to slightly different applied pressures: 100 kPa for the lateral electrode conductivity and contact conductivity, and 62 kPa for the transverse electrode conductivities. The mixing of input parameters obtained from these two conditions was

justified by unpublished ESR measurements collected by the Group, which found a stable plateau in the overall conductivity above a pressure ca. 20 kPa.

Implicit in the use of 'plateau' value electrical conductivities is that the numerical predictions of the effective resistance of the electrode/current collector assembly also correspond to these conditions. Therefore, care must be taken when making comparisons with experimental measurements, such as those plotted in Figure 6.9 (Section 6.2.2). The applied pressure in the A4 cell measurements was 0.26 kPa, while that in the Swagelok cell measurements was unknown since the experimental setup did not allow pressure to be measured or controlled, thought it is likely to have been higher due to the small surface area. This mismatch may explain why, when ionic resistance contributions are taken into account, the measured resistance of the A4 devices was significantly underpredicted, whilst that of Swagelok devices was overpredicted.

Another factor complicating comparisons with experimental measurements from full cells relates to the contribution of ionic resistance to the total cell ESR. The effective ionic conductivity in the separator and electrode layers depends on the respective microstructures and the quality of infiltration of the pores with electrolyte. Incomplete infiltration would imply shorter average ion paths within the electrode, which may partially explain why the resistance measured from Swagelok devices was significantly lower than that estimated assuming complete infiltration of the electrode. Furthermore, the use of the standard form of the Bruggeman correction to estimate the effective ionic conductivity carries large uncertainties; therefore, these estimates should be treated with caution, and experimental characterisation of this parameter should be sought in future.

8.3.2 General design rules for current collectors in mass-sensitive applications

To aid the interpretation of the numerical results presented in Chapter 1, the design space for current collectors was analytically constructed, considering the dimensionless conductivity parameters σ_e/σ_{cc} and $\sigma_C L_{cell}/\sigma_e$ describing the relative importance of bulk electrode, bulk current collector and contact losses in the system. The analysis assumes that the density of the current collector material is greater than that of the electrode material, as is typical for electrochemical cells; and, for simplicity, that electrode conductivity is isotropic. Several regimes of interest were identified in this design space, illustrated schematically in Figure 8.3. In the theoretical limit $\sigma_{\mathrm{e}}/\sigma_{\mathrm{cc}} \geq 1$, assuming good contact

between the electrode and the external circuit connections, no current collector is needed at all. In practice, the use of a current collector is necessitated by the limited conductivity of most electrode materials, particularly for supercapacitors, where currents are larger than for batteries. In the limits $\sigma_e/\sigma_{cc} \to 0$ and/or $\sigma_C L_{cell}/\sigma_e \to 0$, a plate current collector is necessary to minimise bulk electrode and contact losses, respectively. In this case, mass reduction can only be achieved by reducing the current collector thickness as far as possible, dictated by the current collector conductivity, and practical fabrication methods.

For all intermediate conductivity ratios, it is possible to optimise the current collector area fraction and thickness by considering the tradeoff between current collector mass and total resistive losses. In the regime of low device active current density, simple strip current collector geometries (Figure 8.3, region in green) may be sufficient to ensure resistive power losses remain low. The conductivity ratios of the specific system under consideration would dictate the most appropriate design strategy.

In the regime of high device active current density, current collection is more demanding ($P^* \propto j_s$); therefore, more sophisticated grid current collector geometries (Figure 8.3, region in blue) are advantageous. When high current density is compounded with a large cell area, the need for grid solutions increases ($P^* \propto A_{cell}$). At very low current collector thicknesses, collector geometries with a hierarchical structure, where element width progressively increases towards the end tab, emerge as more efficient solutions.

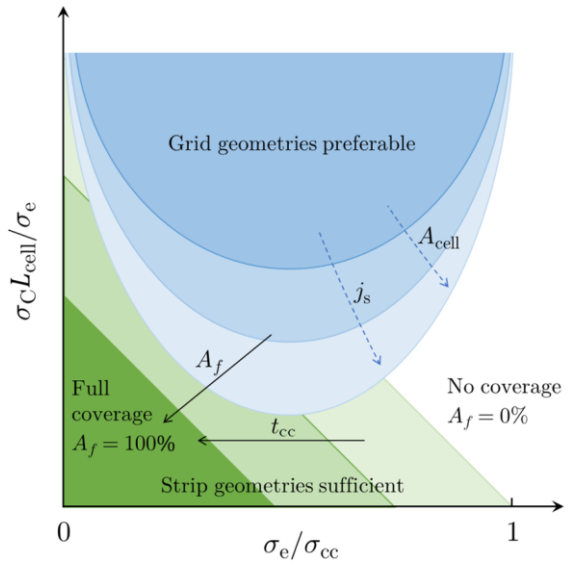

Figure 8.3. Schematic representation of dimensionless current collector design space, illustrating the parameter regimes where strip (green) or grid (blue) geometries are preferred. Solid arrows indicate recommended parameter selection; dash arrows indicate parameter influence over the size of the design regions.

8.3.3 Design implications for structural supercapacitors

This work demonstrated that, at present, power performance is limited chiefly by the poor contact conductivity of the electrode/current collector interface, and somewhat by the lateral electrode conductivity (Figure 6.6). Therefore, the most effective route to minimise resistive power losses is to maximise the current collector area fraction (Figure 8.3, region in green). To ensure parasitic mass is kept low, the foil thickness should be simultaneously reduced.

The numerical results suggest that resistive losses would remain acceptably low for foil thicknesses as low as 1 μm. However, practical considerations may prevent the use of ultra-thin foils: for instance, due to poor handleability, scale-up difficulties or pore access requirements. The latter is currently true for the SSCs under investigation, which require post-infusion of IL to improve capacitance. In this case, geometries with partial area fractions can offer a good compromise between mass and power losses, provided they are appropriately designed.

The quantitative findings challenge the prevailing design strategies for current collectors in SSCs and other SPC embodiments, demonstrating that the side-strip collectors currently used in SSCs represent an inefficient current collection solution, due to high lateral losses in the electrode (Figure 6.6). For a 10% current collector fraction, these losses could be reduced by 98% by replacing the side-strip with the simple grid, which can be attributed to the reduced lateral current path. This reduction is slightly offset by an increase in current collector resistance, attributed to the reduced width of grid elements. This width is particularly important in locations where the current is largest, such as near end tabs.

To obtain a simultaneous reduction in the current collector mass, alternative designs with hierarchical structures are advantageous. Figure 6.7(a) shows that, with a busbar and fingers design, which is wider near the end tab, thicknesses as low as 5 μm could be achieved (a current collector mass reduction of 86% compared to the nominal thickness) without significantly increasing overall power loss. This explains why in the Pareto frontiers in Figure 6.7(b) as the thickness is reduced, the minimum power loss solutions transition from the ‘simple grid’ to the ‘busbar and fingers’, to the ‘centre-strip’ geometries, and why the Pareto frontier eventually collapses onto the plate solution.

The above findings may be used to rank the key current collector design parameters in order of their importance for the overall performance(that is, their general capacity to reduce parasitic mass and/or effective resistance) of the SSCs studied here:

1) Area fraction: should be increased as far as practicable.
2) Thickness: should be decreased as far as practicable, and subject to the bulk resistance of the current collector remaining acceptably low.
3) Grid density: should be increased. This parameter rises in importance as cell area and current density are increased, or contact conductivity is improved.
4) Width of central grid element: should be sized to ensure bulk current collector losses remain acceptably low. This parameter rises in importance as thickness is reduced.
5) Geometric pattern: assuming the above parameters have been appropriately selected, the geometric pattern can be optimised for small additional efficiency improvements.

Section 6.4.7 investigated how the design problem may change in the near future if contact resistance ceases to be the dominant source of loss in low area fraction current collectors. This study showed that, when dense grids were considered, the space-filling fractal grids did not present an advantage over busbar and fingers grid. This finding was explained by the larger width of the central element (busbar) in the latter.

The busbar and fingers class of geometries is therefore considered the ideal candidate for future SSC current collectors, and future work should aim to reduce the foil thickness and explore grid elements with a tapered geometry or variable thickness. Adopting thin, current collector grids would imply changes to the present device fabrication routes: most likely screen printing [154], direct-ink printing [252], evaporation, or the transfer of pre-cut foils, though the latter may be unsuitable for ultra-low thicknesses. The choice of fabrication route should consider cost and efficiency of material use, as well as the delamination properties and conductivity of the materials used. Contact conductivity is likely to be improved through printing techniques.

Finally, the conductivity measurements presented in Section 6.2.2 raise an important question regarding the performance benefits afforded by modifying the carbon fabric with CAG. It has been established in the literature that the ratio between the longitudinal to transverse electrical conductivity of single carbon fibres is around 6 [268]. Therefore, a noticeable improvement in the effective transverse conductivity of a carbon

fabric would be expected upon the addition of a more conductive matrix between the carbon fibres. Comparing the pyrolised carbon fabric without CAG with the CAG-modified fabric, it was found that the effective lateral conductivity was unaffected, whilst the effective transverse conductivity was improved only by 9%. This relatively modest increase suggests that the electrical conductivity of CAG is too low to produce a meaningful performance improvement in the composite. It may therefore be desirable to seek alternative, more highly conductive materials to either replace or supplement the CAG matrix. Potential candidate materials include, among others, CNTs, graphene and activated carbon.

8.4 Electrochemical and multiphysics modelling

8.4.1 Implementation of the ion transport model

The implementation of the ion transport model in Abaqus could not be concluded within the timeframe of this thesis. At present, the subroutine has been implemented in a thermal-electrical analysis, however the solution is not updated following variable initialisation, due to NaN-valued nodal variable inputs, resulting in zero-valued residual vectors (Section 7.4.1). Further testing is recommended as future work (Chapter 10) to understand the exact causes of this problem.

In the present work, additional testing was carried out on the thermal element subroutine provided in the software documentation [260] in combination with the thermal-electrical analysis procedure (Section 7.4.2). The tests revealed that the problem was shared between the two subroutines, implying either (i) incorrect syntax used across the subroutine or input files, or (ii) a general incompatibility between the thermal-electrical procedure type with the use of element subroutines; however, further testing is required to verify the above.

The thermal-electrical analysis workflow proposed in this thesis offers a promising eventual route to multiphysics (mechanical-electrochemical) analysis of SSCs within Abaqus/Standard, as a fully coupled thermal-electrical-structural procedure is also available [257]. The latter shares many similar features with the thermal-electrical analysis, suggesting that, once the workflow has been validated, the ion transport subroutine could be implemented within a coupled multiphysics analysis with relative ease. The proposed simulation framework aims to promote the certification and deployment of SSCs in aviation, by establishing relevant analysis capabilities in the Abaqus FEA software used by key players in the industry [215].

8.5 Novel achievements and impact

This thesis develops and applies new computational models for the mechanical, electrical, and electrochemical response of structural supercapacitors. The key contributions and impact of each chapter are summarised as follows:

Phase 1: Compaction analysis and prediction

- For the first time, the effects of CAG and stacking sequence hybridisation on fabric and stack compressibility were experimentally determined. The key finding that the present CAG-modification process restricts the attainable fibre volume fractions. This informs the future development of nanomodified structural electrodes with improved fibre packing.
- The fabric compaction model developed is the first in the literature to tackle hybrid multi-layer fabric stacks and allows systematic investigation into the effects of hybridisation and ply offset on compressibility and final composite microstructure.
- The model serves as an automated geometric pre-processor for realistic finite element models of SSCs.
- The present modelling methodology eliminates the need for extensive characterisation of physical specimens, and is widely applicable to many other composites with hybridised fabric stacking sequences, which receive growing interest [141,143].

Phase 2: Mechanical performance analysis and prediction

- The mechanical model of SSCs developed represents the first attempt in the literature to predict their device-level mechanical performance based on constituent properties.
- This work also presents the most comprehensive microstructural analysis yet performed of CAG-modified and SSC composites, drawing together optical, scanning electron and μCT observations to link processing defects to measured mechanical properties and observed fracture morphologies.
- A direct relationship was numerically demonstrated between pre-crack defects and reduced in-plane shear stiffness, and for the first time, a link was suggested between gross voidage and additional stiffness and strength reductions in SSCs.

- These important insights advance the state-of-the-art with regards to the analysis of the mechanical behaviour of SSCs. Additionally, they offer guidance for future material development and inspire optimisation for enhancing mechanical performance.

Phase 3: Current collection performance analysis

- This work is the first to analyse resistive power dissipation in SSCs and demonstrate that current collection is an important factor in the scale-up of these devices.
- A variety of strategies to improve current collection, particularly while minimising total weight, were evaluated numerically. Key material properties were measured and used to parametrise novel conduction analyses. Contact resistance emerged as the primary source of electrical resistive loss in the SSCs studied here.
- The results demonstrated quantitatively that the prevailing 'side-strip' design of current collectors is damaging to SSC performance, due to high lateral resistive losses.
- More efficient current collector geometries were identified by evaluating the tradeoff between power loss and parasitic mass over a range of conditions. These findings have extended the state-of-the-art in SSC design and informed the manufacture of demonstrator components.
- The methodology and findings are more widely applicable to other SPCs, batteries and fuel cells in mass-critical applications, such as EVs, drones, and satellites.

Phase 4: Electrochemical and multiphysics

- An original user element subroutine for ion transport was proposed to extend multiphysics analysis capabilities in the Abaqus finite element simulation package.
- An implementation of the subroutine within a thermal-electrical analysis procedure was proposed to enable ion transport analysis. Further work is required to validate this implementation and guidance has been offered for future development.
- The ion transport element subroutine represents a first step towards the demonstration of a multiphysics modelling framework for SSCs. The proposed simulation workflow would enable the analysis of SSCs with complex 3D microstructures.

9 Conclusions

In the preceding chapters, predictive finite element models were developed for the compacted morphology of structural supercapacitors and aspects of their mechanical, electrical, and electrochemical behaviour. These Phases were linked by the common research aim of predicting the performance of SSCs, and the strong need to identify design strategies for its improvement. The key conclusions are summarised in the following:

Phase 1: Compaction analysis and prediction

- The compaction of fabric reinforcements used as electrodes and separators in SSCs has direct implications for the final composite geometry, and ultimately, performance. Limited understanding of the effects of hybridisation and CAG modification on the compaction of SSC reinforcements motivated an experimental-numerical study.
- The compaction experiments demonstrated a substantial reduction in the attainable fibre volume fraction for CAG-modified fabrics (ca. –13% absolute reduction at 1 MPa), which would negatively impact on the fibre-dominated properties of SSCs.
- An original mesoscale model for dry fabric stacks with hybridised stacking sequences was proposed and validated, expanding the state-of-the-art in this field, which has so far focused on monolithic fabric stacks. The model provided information about the hybrid composite micro- and mesostructure, underlining the importance of ply offset.
- The compaction model addressed the need for realistic models of the complex geometry of SSCs, to enable future predictions of their mechanical and electrochemical behaviour.

Phase 2: Mechanical performance analysis and prediction

- Computational modelling offers a valuable means to analyse the mechanical behaviour of SSCs, troubleshoot performance issues and identify strategies for improvement. This work addressed the development of the first predictive models for SSC devices.
- This work demonstrates that, at present, the principal challenges for the performance and predictive modelling of SSCs stem from the presence of manufacturing defects, such as pre-cracks and gross voidage, and a lack of *in situ* material data.

- The predictions of the tensile and initial in-plane shear elastic moduli of the baseline laminates were conservative, and within 10% of the measured values. In contrast, models of the CAG-modified laminates assuming neat material properties and defect-free microstructure overpredicted the above performance by approximately 24% and 180% for the structural, and 35% and 280% for the multifunctional laminates.
- A significant degradation of shear stiffness, related to the presence of pre-cracks, was demonstrated numerically. However, discrepancies in the tensile and shear moduli remained: 22% and 81% for the structural, and 32% and 82% for the multifunctional laminates, and were attributed to intrayarn and interlaminar voids. Predictive accuracy should improve as measures are taken to mitigate process-induced defects. Crucially, this work suggests that CAG-modified SSCs could soon deliver equivalent, or even improved, elastic properties, compared to those of conventional woven composites.
- Extensive microstructural and fractographic analyses were performed to interpret the unprecedented strength reductions reported for CAG-modified laminates. Several contributing factors were identified: the presence of stress concentrations near voids, the brittle response of the CAG, and the likelihood of a strong CAG/CF interface.
- The mechanical model developed here is a starting point for the future development of multiphysics models for the combined mechanical and electrochemical performance of SSCs. Such models could examine the effects of mechanical deformation and damage on the electrochemical response. The present work offers important insights on the former

Phase 3: Current collection performance analysis and prediction

- SSCs must provide high gravimetric electrical and mechanical properties; however, their performance is currently limited by internal resistance and mass. Considering the importance of the current collectors, this chapter proposed their re-design in SSCs.
- A new three-dimensional electrical conduction model was proposed for SSC electrodes and current collectors to analyse the tradeoff between resistive losses and parasitic mass. This work challenged the prevailing ‘side-strip’ current collector design by demonstrating that it is associated with increased lateral losses in the electrode, which could be reduced by 98% by switching to a ‘simple grid’ current collector design. Significant mass reductions of 86% are predicted to be obtained by using thin

'busbar and fingers' current collectors. The benefits of current collector grids with greater width near end tabs increase for larger current densities and device areas.

- It was demonstrated that, at present, high contact resistance is the principal performance limiting factor for current collection in SSCs. The most effective near-term strategy for the mitigation of losses lies in improving contact conductivity, for example through conductive surface treatments; or else, increasing the area fraction and reducing the thickness of foils.
- Experimental uncertainties regarding the pressure dependence of conductivity, and the effective ionic conductivity of the electrodes, made validation of the model challenging. Further experiments are required for validation (outlined in Chapter 10).
- The tradeoff analysis methodology proposed here is applicable not only to the development of other SPCs, but also monofunctional supercapacitors, batteries, and fuel cells, and is relevant to many mass-critical energy storage applications.

Phase 4: Electrochemical and multiphysics modelling

- Predictive modelling has immense potential to accelerate the development and deployment of SSCs. To ensure progress unfolds rapidly, existing simulation tools must evolve to provide a unified approach to electrochemical and mechanical analysis.
- In this thesis, an original user element subroutine for ion transport was proposed to extend the multiphysics analysis capabilities of the Abaqus software suite. Further work is still required to validate the implementation of the subroutine.
- The ion transport element subroutine represents a first step towards the demonstration of a multiphysics modelling framework for SSCs. The simulation workflow proposed here would enable the analysis of SSCs with complex three-dimensional microstructures.

This thesis has identified many exciting opportunities for the application of computational models to complement experimental research and advance the development of structural supercapacitors. The models proposed and developed here are the first to address the strong need for such predictive tools, advancing the state-of-the-art in this promising class of multifunctional materials.

10 Future work and implications

The findings of this thesis have several important implications for the manufacture of SSCs which are associated with the optimisation and control of key processing steps. This work has also opened many avenues for future experimental and numerical investigations in relation to mechanical, current collection, and electrochemical performance. This chapter offers some perspectives on the above areas and outlines recommendations for future work:

Manufacture of structural supercapacitors

- A continuous theme within this work is the intrinsic link between manufacturing processes and conditions and the final performance of SSCs. The present work therefore suggests that the mechanical, electrical, and electrochemical properties of the constituents may be better leveraged by a careful optimisation of fabrication processes and design philosophies.
- The compaction experiments (Chapter 4) showed that the present CAG-modification process significantly limits the attainable fibre volume fraction in CAG-modified composites (ca. −13% absolute reduction at 1 MPa). Microstructural characterisation of the CAG-modified laminates (Chapter 5) showed evidence of incomplete infusion of CAG precursor into the carbon fabric. Future developments could explore the use of high-pressure consolidation of the C* fabrics, for instance via resin transfer molding, to produce higher volume fraction, void-free fabrics.
- Mechanical modelling (Chapter 5) further showed that process-induced pre-cracks in the CAG-modified fabric negatively impact composite shear properties. Drying conditions could be further optimised to reduce the occurrence of pre-cracks.
- Microstructural characterisation (Chapter 5) also showed that large interlaminar voids are present in SSCs, resulting either from phase separation of the structural electrolyte, or air entrapment. These potential material compatibility and manufacturability issues should be investigated further by performing detailed microstructural characterisation using scanning electron microscopy.

- Current collection modelling (Chapter 1) demonstrated that more efficient current collector geometries can be employed in SSCs to minimise charge collection losses. Future development should explore the use of thin 'busbar and fingers' current collectors to minimise parasitic mass and improve charge collection efficiency.

- Electrochemical characterisation performed within the group has demonstrated a pressure-dependence of conductivity and overall electrochemical behaviour, contributing to performance variability. It is therefore important that future characterisation protocols ensure consistency in test conditions, and the latter should reflect in-service conditions. Further research is needed to understand whether the compaction achieved for SSCs *in situ* is sufficient for adequate cell operation.

- The *in situ* mechanical behaviour of the current collectors also deserves attention. Delamination issues have already been reported for SSCs with aluminium current collectors [37]. As the technology readiness of SPCs progresses, greater attention will be given to their long-term performance and integrity. Mechanical degradation due to the cyclic heat generation and structural loading are likely to increase delamination risk; therefore, developing strategies for delamination resistance will be important.

- Experimental trials could explore strategies to improve the contact and bulk electrical conductivities of the CAG-modified fabric electrodes, such as: local infusion of the dry carbon fabric with a more conductive matrix; conductive additives in CAG; process modifications to minimise electrode defects, such as interyarn delaminations and intrayarn pre-cracks; alternative electrode chemistries; other measures to exploit the higher axial conductivity of carbon fibres.

Mechanical performance analysis and prediction

- At present, the prediction of the linear elastic response of SSCs is challenging due to: (i) the presence of large-scale defects in the CAG-modified carbon fabric and structural electrolyte *in situ*, (ii) uncertainty regarding the elastic properties (and variability thereof) of the structural electrolyte and CAG *in situ*, and (ii) uncertainty regarding the extent of infusion of epoxy into CAG. Work must be undertaken to (i) minimise the presence of defects, (ii) characterise *in situ* constituent properties, perhaps through nanoindentation testing of fibre-reinforced microcomposite specimens, and (iii) develop an imaging technique allowing visual differentiation

between dry and filled CAG, for instance through the use of suitable contrast agents, with a fine enough particle size to infiltrate CAG nanopores, and minimal effect on the viscosity of the carrier resin.

- At present, the issues identified above, combined with the near-complete lack of data on the failure properties of the constituent materials and their interfaces, represent major stumbling blocks for the prediction of the non-linear and damage response of SSCs. Provided these obstacles are addressed by experimental work, the mechanical model developed in this thesis could be readily adapted to simulate the non-linear response. Reduced unit cells could be developed to increase computational efficiency.
- More work is needed to confirm the hypotheses that the presence of voids and a strong CAG/CF interface encourages early failure of the CAG-modified laminates. Further tensile testing of baseline and CAG-modified structural composites could help understand the role of the fibre/matrix interface properties on longitudinal strength and translaminar toughness. For proper interpretation of these experiments, fibre undulation, voids and other defects should be minimised. Therefore, the ideal specimen geometry would be a unidirectional single yarn microcomposite with a low filament count. Researchers should verify complete infusion of CAG precursor and epoxy into the yarns, by utilising high resolution scanning electron microscopy of polished cross-sections or high resolution μCT.
- To support the investigations above, the interfacial strength and frictional stress of the CAG/carbon fibre interface could also be characterised in micromechanical tests, such as fibre push-through, pull-out or fragmentation. These tests could also support further analysis of process-induced fibre damage [36]. The data would also enable prediction of strength and fracture toughness. Achieving an optimal combination of matrix strain to failure and fibre/matrix interface values is an important issue deserving further attention. It is also a key issue for the adoption of CAG-modified structural composites since failure properties have critical importance in many structural applications.

Current collection performance analysis and prediction

- Formal optimisation of individual current collector geometries was outside the scope of this work, however in future, geometries of interest, such as the space-filling fractal

grids could be optimised. Their performance can be evaluated through the spatial power loss distributions, rather than total power loss factors, of the various sources of losses. The geometric parameters, such as the number of hierarchical levels and the element width and spacing, can be adjusted to address current collection 'hot spots' and reduce redundancy. Topology optimisation algorithms may be relevant here. Future work should consider tapered elements, and other typical device geometries.

- To enable quantitative experimental validation of the present model, a protocol for the measurement of the effective electrical resistance of the electrode/current collector assembly could be developed. Otherwise, qualitative validation of the numerical findings could be achieved through full cell resistance measurements, in which only the current collector geometry is varied. Direct characterisation of the effective ionic conductivities of the electrode and separator is also recommended.

- In future, the cost, carbon competitiveness and corrosion resistance of current collectors for structural power applications should be considered in addition to mass. Material choice could be made based on a wider range of current collector material candidates. Materials which could be of interest in the present application include carbon-based materials (such as graphene and CNT veils) and conductive polymers (such as polypyrrole and polyaniline), which are gaining popularity in research [251,252]. The work in this chapter focused on metallic current collectors, since in the near term they are likely to remain the material of choice for SSCs fabricated by the Group. The present model is nevertheless readily applicable to non-metallic or anisotropic materials, such as aligned CNT veils.

- The proposed methodology for the analysis of power and mass efficiency tradeoffs could be applied in many other mass-critical applications of energy storage, for example next generation supercapacitors, batteries, fuel cells, as well as other SPCs, with applications in EVs, drones, satellites, and portable electronics. Additional design concerns associated with cost and sustainability further motivate such an analysis.

Electrochemical and multiphysics modelling

- More work is required to validate the implementation of the ion transport model, ideally with the engagement of Abaqus FEA developers. Upon successful validation of the model, there are many potential further applications to explore, outlined below.

- The ion transport model should be extended to the porous electrode domains for full cell analysis. This could be achieved using porous electrode theory (Appendix A.3).
- The ion transport user element subroutine should be extended to 3D. This is expected to require marginal effort. The scalability of the model to larger, more complex 3D geometries, such as the mesoscale models analysed in Chapters 4 and 5, should be assessed. Novel meshing methodologies with locally dense meshes at electrode/electrolyte interfaces may be required to reduce the problem size.
- Standard electrochemical experiments, such as CV and GCD, should be simulated to enable validation of the model. Further work should determine as to whether incorporating the Stern layer/steric corrections improves the predictive accuracy.
- Heat generation during device operation should be examined. This could be achieved through a 1D sequentially coupled electrochemical-thermal analysis.
- Multifunctional performance optimisation studies could be performed by implementing the ion transport element within a sequentially coupled structural-electrochemical analysis. This would enable systematic interrogation of the available design space for SSC devices. Alternatively, a combined structural-electrochemical element subroutine could be developed for these purposes, by extending the ion transport element. Optimisation procedures could be used to identify the optimal combinations of geometric parameters and constituent properties, which would strike the desired balance between mechanical and electrochemical performance.
- The coupling between mechanical deformation and damage, and the electrochemical response of SSCs should be analysed. The modelling methodologies suggested above could be applied here. Additionally, the development of new mechanical-electrical interaction models may be appropriate: for example, infiltration of ionic liquid into cracks and delaminations could be modelled using modified traction-separation type models, which update the local electrical and ionic conductivity based on current damage level. Progress in this area is contingent on an increased availability of experimental data, both at constituent and device level, to enable model parametrisation and validation.

References

[1] European Commission. Reducing emissions from aviation 2015. http://ec.europa.eu/clima/policies/transport/aviation/index_en.htm (accessed July 7, 2018).

[2] Lee DSL, Forster P. Calculating the true climate impact of aviation emissions. Carbon Br 2020. https://www.carbonbrief.org/guest-post-calculating-the-true-climate-impact-of-aviation-emissions (accessed June 15, 2021).

[3] Tsotsis T. Challenges and Opportunities for Composite Materials Transitions in Aerospace. ECCM18 Conf. Proc., 2018.

[4] Royal Netherlands Aerospace Centre, SEO Amsterdam Economics. Destination 2050: A route to net zero European aviation. 2021.

[5] Air Transport Action Group. Facts & figures 2020. https://www.atag.org/facts-figures.html (accessed August 20, 2021).

[6] McKinsey. McKinsey electric vehicle index: Europe cushions a global plunge in EV sales 2020. https://www.mckinsey.com/industries/automotive-and-assembly/our-insights/mckinsey-electric-vehicle-index-europe-cushions-a-global-plunge-in-ev-sales.

[7] Automotive News Europe. Norway's EV sales rise to record 54% market share 2021. https://europe.autonews.com/automakers/norways-ev-sales-rise-record-54-market-share (accessed January 7, 2021).

[8] Schäfer AW, Barrett SRH, Doyme K, Dray LM, Gnadt AR, Self R, *et al.* Technological, economic and environmental prospects of all-electric aircraft. Nat Energy 2019;4:160–6. https://doi.org/10.1038/s41560-018-0294-x.

[9] Pejman R, Kumbur EC, Najafi AR. Multi-physics design optimization of structural battery. Multifunct Mater 2021;4. https://doi.org/10.1088/2399-7532/abf158.

[10] Bockenheimer C, Speckmann H. Validation, verification and implementation of SHM at Airbus. Proc 9th Int Work Struct Heal Monit (IWSHM 2013), Stanford, CA, USA 2013:5.

[11] Pearce R. NASA's Aeronautics research strategy: a reflection of research continuity, strategic analysis, and community dialogue 2013. https://www.nasa.gov/sites/default/files/files/CSC_ARMD_July2013.pdf (accessed May 1, 2020).

[12] Volvo. Tomorrow's Volvo car: body panels serve as the car battery 2013. https://www.media.volvocars.com/ca/en-ca/media/pressreleases/35026 (accessed August 12, 2019).

[13] Perkins C. Future Tesla cars will use batteries for shell structure. Road Track 2020. https://www.roadandtrack.com/new-cars/car-technology/a34115181/tesla-structural-batteries/ (accessed May 1, 2020).

[14] Automobili Lamborghini. Hybrid Lamborghinis: supercapacitor technology patented with MIT 2019. https://www.lamborghini.com/en-en/news/hybrid-lamborghinis-supercapacitor-technology-patented-mit (accessed May 1, 2020).

[15] Advanced Propulsion Centre, UK Automotive Council. Electrical energy storage roadmap 2020 2021. https://www.apcuk.co.uk/app/uploads/2021/09/https-__www.apcuk_.co_.uk_app_uploads_2021_02_Exec-summary-Technology-Roadmap-Electrical-Energy-Storage-final.pdf (accessed September 1, 2021).

[16] Shirshova N, Qian H, Houllé M, Steinke JHG, Kucernak ARJ, Fontana QPV, *et al.*

Multifunctional structural energy storage composite supercapacitors. Faraday Discuss 2014;172:81–103. https://doi.org/10.1039/c4fd00055b.

[17] Asp LE, Johansson M, Lindbergh G, Xu J, Zenkert D. Structural battery composites: a review. Funct Compos Struct 2019;1:042001. https://doi.org/10.1088/2631-6331/ab5571.

[18] Xu Y, Lu W, Xu G, Chou T. Structural supercapacitor composites: a review. Compos Sci Technol 2021;204:108636. https://doi.org/10.1016/j.compscitech.2020.108636.

[19] BAE Systems. Frontline military technology promises battery revolution 2012. https://www.baesystems.com/en/article/frontline-military-technology-promises-battery-revolution (accessed September 1, 2020).

[20] Greenhalgh ESG, Ankersen J, Asp LE, Bismarck A, Fontana QPV, Houlle M, *et al.* Mechanical, electrical and microstructural characterisation of multifunctional structural power composites. J Compos Mater 2015;49:1823–34. https://doi.org/10.1177/0021998314554125.

[21] Asp LE, Bouton K, Carlstedt D, Duan S, Harnden R, Johannisson W, *et al.* A structural battery and its multifunctional performance. Adv Energy Sustain Res 2021;2:2000093. https://doi.org/10.1002/aesr.202000093.

[22] Qian H, Kucernak A, Greenhalgh E, Bismarck A, Shaffer M. Multifunctional structural supercapacitor composites based on carbon aerogel modified high performance carbon fiber fabric. ACS Appl Mater Interfaces 2013;5:6113. https://doi.org/10.1021/am400947j.

[23] Greenhalgh ES, Shirshova N, Kucernak ARJ, Shaffer MSP, Teixeira R, Bismarck A, *et al.* Recent advances in structural supercapacitors for transport applications. 20th Int. Conf. Compos. Mater., Copenhagen: 2015.

[24] Asp LE, Greenhalgh ES. Structural power composites. Compos Sci Technol 2014;101:41–61. https://doi.org/10.1016/j.compscitech.2014.06.020.

[25] Ferreira ADBL, Nóvoa PRO, Marques AT. Multifunctional Material Systems: A state-of-the-art review. Compos Struct 2016;151:3–35. https://doi.org/10.1016/j.compstruct.2016.01.028.

[26] Chan KY, Jia B, Lin H, Hameed N, Lee JH, Lau KT. A critical review on multifunctional composites as structural capacitors for energy storage. Compos Struct 2018;188:126–42. https://doi.org/10.1016/j.compstruct.2017.12.072.

[27] Thomas JP, Qidwai MA. The design and application of multifunctional structure-battery materials systems. JOM 2005;57:18–24. https://doi.org/10.1007/s11837-005-0228-5.

[28] Zhang Y, Ma J, Singh AK, Cao L, Seo J, Rahn CD, *et al.* Multifunctional structural lithium-ion battery for electric vehicles. J Intell Mater Syst Struct 2017;28:1603–13. https://doi.org/10.1177/1045389X16679021.

[29] Pereira T, Guo Z, Nieh S, Arias J, Hahn HT. Embedding thin-film lithium energy cells in structural composites. Compos Sci Technol 2008;68:1935–41. https://doi.org/10.1016/j.compscitech.2008.02.019.

[30] Ladpli P, Nardari R, Kopsaftopoulos F, Chang FK. Multifunctional energy storage composite structures with embedded lithium-ion batteries. J Power Sources 2019;414:517–29. https://doi.org/10.1016/j.jpowsour.2018.12.051.

[31] Wong EL, Baechle DM, Xu K, Carter RH, Snyder JF, Wetzel ED. Design and processing of structural composite batteries. Int SAMPE Symp Exhib 2007;52.

[32] Snyder JF, Wetzel ED, Watson CM. Improving multifunctional behavior in structural electrolytes through copolymerization of structure- and conductivity-promoting monomers. Polymer (Guildf) 2009;50:4906–16. https://doi.org/10.1016/j.polymer.2009.07.050.

[33] Asp LE, Leijonmarck S, Carlson T, Lindbergh G. Realisation of structural battery composite materials. ICCM Int. Conf. Compos. Mater., 2015. https://doi.org/10.13140/RG.2.1.2029.1922.

[34] Berrueta A, Ursua A, Martin IS, Eftekhari A, Sanchis P. Supercapacitors: electrical characteristics, modeling, applications, and future trends. IEEE Access 2019;7:50869–96. https://doi.org/10.1109/ACCESS.2019.2908558.

[35] Bismarck A, Blaker JJ, Anthony DB, Qian H, Maples HA, Robinson P, *et al.* Development of novel composites through fibre and interface/interphase modification. IOP Conf Ser Mater Sci Eng 2016;139. https://doi.org/10.1088/1757-899X/139/1/012001.

[36] Qian H, Bismarck A, Greenhalgh ES, Shaffer MSP. Carbon nanotube grafted silica fibres: Characterising the interface at the single fibre level. Compos Sci Technol 2010;70:393–9. https://doi.org/10.1016/j.compscitech.2009.11.014.

[37] Hudak NS, Schlichting AD, Eisenbeiser K. Structural supercapacitors with enhanced performance using carbon nanotubes and polyaniline. J Electrochem Soc 2017;164:A691–700. https://doi.org/10.1149/2.0721704jes.

[38] Qi G, Nguyen S, Anthony DB, Kucernak ARJ, Shaffer MSP. The influence of fabrication parameters on the electrochemical performance of multifunctional structural supercapacitors The influence of fabrication parameters on the electrochemical performance of multifunctional structural supercapacitors. Multifunct Mater 2021;4. https://doi.org/10.1088/2399-7532/ac1ea6.

[39] Ciocanel C, Browder C, Simpson C, Colburn R. The challenges of achieving good electrical and mechanical properties when making structural supercapacitors. Proc SPIE - Int Soc Opt Eng 2013;8689:1–9. https://doi.org/10.1117/12.2009738.

[40] Amplianitis A, Masouras A, Gkikas G, Kalogridi Z, Baltopoulos A, Vavouliotis A, *et al.* Graphene-based systems for enhanced energy storage. E3S Web Conf 2017;16:09006. https://doi.org/10.1051/e3sconf/20171609006.

[41] Muralidharan N, Teblum E, Westover AS, Schauben D, Itzhak A, Muallem M, *et al.* Carbon Nanotube Reinforced Structural Composite Supercapacitor. Sci Rep 2018;8:1–9. https://doi.org/10.1038/s41598-018-34963-x.

[42] Deka BK, Hazarika A, Kim J, Park Y-B, Park HW. Recent development and challenges of multifunctional structural supercapacitors for automotive industries. Int J Energy Res 2017;41:1397–411. https://doi.org/10.1002/er.3707.

[43] Senokos E, Ou Y, Torres JJ, Sket F, González C, Marcilla R, *et al.* Energy storage in structural composites by introducing CNT fiber/polymer electrolyte interleaves. Sci Rep 2018;8:1–10. https://doi.org/10.1038/s41598-018-21829-5.

[44] Rana M, Ou Y, Meng C, Sket F, González C, Vilatela JJ. Damage-tolerant, laminated structural supercapacitor composites enabled by integration of carbon nanotube fibres. Multifunct Mater 2019;3. https://doi.org/10.1088/2399-7532/ab686d.

[45] Deka BK, Hazarika A, Kim J, Park Y Bin, Park HW. Multifunctional CuO nanowire embodied structural supercapacitor based on woven carbon fiber/ionic liquid-polyester resin. Compos Part A Appl Sci Manuf 2016;87:256–62. https://doi.org/10.1016/j.compositesa.2016.05.007.

[46] Greenhalgh ES, Kucernak A, Shaffer MSP, Bismarck A, Shirshova. Beyond structural : multifunctional composites that store electrical energy. EPSRC Reference: EP/P007465/1. 2016.

[47] Pernice MF, Qi G, Senokos E, Anthony DB, Nguyen S, Valkova M, *et al.* Mechanical, electrochemical and multifunctional performance of a CFRP/carbon aerogel structural supercapacitor and its corresponding monofunctional equivalents. Prep 2021.

[48] Snyder JF, Gienger EB, Wetzel ED. Performance metrics for structural composites with electrochemical multifunctionality. J Compos Mater 2015;49:1835–48. https://doi.org/10.1177/0021998314568167.

[49] Javaid A, Ho KKC, Bismarck A, Steinke JHG, Shaffer MSP, Greenhalgh ES. Carbon fibre-reinforced poly(ethylene glycol) diglycidylether based multifunctional structural supercapacitor

composites for electrical energy storage applications. J Compos Mater 2016;50:2155–63. https://doi.org/10.1177/0021998315602324.

[50] Gereke T, Döbrich O, Hübner M, Cherif C. Experimental and computational composite textile reinforcement forming: a review. Compos Part A Appl Sci Manuf 2013;46:1–10. https://doi.org/10.1016/j.compositesa.2012.10.004.

[51] Verleye B, Croce R, Griebel M, Klitz M, Lomov SV V, Morren G, *et al.* Permeability of textile reinforcements: Simulation, influence of shear and validation. Compos Sci Technol 2008;68:2804–10. https://doi.org/10.1016/j.compscitech.2008.06.010.

[52] Charmetant A, Vidal-Sallé E, Boisse P. Hyperelastic modelling for mesoscopic analyses of composite reinforcements. Compos Sci Technol 2011;71:1623–31. https://doi.org/10.1016/j.compscitech.2011.07.004.

[53] Mohammed U, Lekakou C, Dong L, Bader MG. Shear deformation and micromechanics of woven fabrics. Compos Part A Appl Sci Manuf 2000;31:299–308. https://doi.org/10.1016/S1359-835X(99)00081-0.

[54] Potluri P, Sagar TV. Compaction modelling of textile preforms for composite structures. Compos Struct 2008;86:177–85. https://doi.org/10.1016/j.compstruct.2008.03.019.

[55] Ivanov DS, Lomov SV. Compaction behaviour of dense sheared woven preforms: Experimental observations and analytical predictions. Compos Part A Appl Sci Manuf 2014;64:167–76. https://doi.org/10.1016/j.compositesa.2014.05.002.

[56] Swery EE, Allen T, Kelly P. Predicting compaction-induced deformations of meso-scale textile models efficiently. J Compos Mater 2016:0021998316671572. https://doi.org/10.1177/0021998316671572.

[57] Nguyen QT, Vidal-Sallé E, Boisse P, Park CH, Saouab A, Bréard J, *et al.* Mesoscopic scale analyses of textile composite reinforcement compaction. Compos Part B Eng 2013;44:231–41. https://doi.org/10.1016/j.compositesb.2012.05.028.

[58] Tavana R, Najar SS, Abadi MT, Sedighi M. Meso/macro-scale finite element model for forming process of woven fabric reinforcements. J Compos Mater 2013;47:2075–85. https://doi.org/10.1177/0021998312454034.

[59] Lin H, Sherburn M, Crookston J, Long AC, Clifford MJ, Jones IA. Finite element modelling of fabric compression. Model Simul Mater Sci Eng 2008;16:35010. https://doi.org/http://dx.doi.org/10.1088/0965-0393/16/3/035010.

[60] Naouar N, Vidal-Salle E, Maire E, Schneider J, Boisse P. Meso F.E. simulation of composite reinforcement deformation based on X-ray computed tomography. Mater Tech 2016;104:165–76. https://doi.org/10.1051/mattech/2016029.

[61] Yong AXH, Aktas A, May D, Endruweit A, Lomov S V., Advani SG, *et al.* Experimental characterisation of textile compaction response: a benchmark exercise. Compos - Part A Appl Sci Manuf 2021;142. https://doi.org/10.1016/j.compositesa.2020.106243.

[62] van Wyk CM. Note on the compressibility of wool. J Text Inst Trans 1946;37:T285–92. https://doi.org/10.1080/19447024608659279.

[63] Gutowski TG, Dillon G. The elastic deformation of lubricated carbon fiber bundles: Comparison of theory and experiments. J Compos Mater 1992;26:2330–47. https://doi.org/10.1177/002199839202601601.

[64] Manson JE. Elastic compression of a fiber network. J Appl Mech 1995;62:1993–6. https://doi.org/10.1115/1.2895906.

[65] Lomov SV, Verpoest I. Compression of woven reinforcement: a mathematical model. J Reinf Plast Compos 2000;19:1329--1350. https://doi.org/https://doi.org/10.1106/50RF-DQJ7-9RN3-6CPX.

[66] Lomov S V., Ivanov DS, Verpoest I, Zako M, Kurashiki T, Nakai H, *et al.* Meso-FE modelling

of textile composites: road map, data flow and algorithms. Compos Sci Technol 2007;67:1870–91. https://doi.org/10.1016/j.compscitech.2006.10.017.

[67] Camanho PP, Hallett SR. Numerical modelling of failure in advanced composite materials. Woodhead Publishing: 2015.

[68] Lin H, Sherburn M, Crookston J, Long AC, Clifford MJ, Jones IA. Finite element modelling of fabric compression. Model Simul Mater Sci Eng 2008;16:35010. https://doi.org/10.1088/0965-0393/16/3/035010.

[69] Gasser A, Boisse P, Hanklar S. Mechanical behaviour of dry fabric reinforcements. 3D simulations versus biaxial tests. Comput Mater Sci 2000;17:7–20. https://doi.org/10.1016/S0927-0256(99)00086-5.

[70] Thompson AJ, El Said B, Ivanov D, Belnoue JPH, Hallett SR. High fidelity modelling of the compression behaviour of 2D woven fabrics. Int J Solids Struct 2017. https://doi.org/10.1016/j.ijsolstr.2017.06.027.

[71] Shirshova N, Bismarck A, Carreyette S, Fontana QP V, Greenhalgh ES, Jacobsson P, *et al.* Structural supercapacitor electrolytes based on bicontinuous ionic liquid–epoxy resin systems. J Mater Chem A 2013;1:15300. https://doi.org/10.1039/c3ta13163g.

[72] Wendong Q, Dent J, Arrighi V, Cavalcanti L, Shaffer MSP, Shirshova N. Structural electrolytes: using multifunctional block-copolymers to control the morphology of epoxy-IL formulations. Prep 2021.

[73] Singh A. Carbon aerogel reinforced hierarchical carbon fiber multifunctional composite material. Imperial College London, 2013.

[74] Elkhatat AM, Al-muhtaseb SA. Advances in tailoring resorcinol-formaldehyde organic and carbon gels 2011:2887–903. https://doi.org/10.1002/adma.201100283.

[75] Schwan M, Naikade M, Raabe D, Ratke L. From hard to rubber-like: mechanical properties of resorcinol–formaldehyde aerogels. J Mater Sci 2015;50:5482–93. https://doi.org/10.1007/s10853-015-9094-x.

[76] Petričević R, Glora M, Fricke J. Planar fibre reinforced carbon aerogels for application in PEM fuel cells. Carbon N Y 2001;39:857–67. https://doi.org/10.1016/S0008-6223(00)00190-1.

[77] Al-muhtaseb BSA, Ritter JA. Preparation and properties of resorcinol-formaldehyde organic and carbon gels. Adv Mater 2003;15:101–14. https://doi.org/https://doi.org/10.1002/adma.200390020.

[78] Anthony DB, Bismarck A, Shaffer MSP. HiPerDuCT programme grant report on carbon aerogel-monolith modified matrix properties in compression. 2015.

[79] Lamy-Mendes A, Silva RF, Durães L. Advances in carbon nanostructure-silica aerogel composites: A review. J Mater Chem A 2018;6:1340–69. https://doi.org/10.1039/c7ta08959g.

[80] Pekala RW, Alviso CT, LeMay JD. Organic aerogels: microstructural dependence of mechanical properties in compression. J Non Cryst Solids 1990;125:67–75. https://doi.org/10.1016/0022-3093(90)90324-F.

[81] Moner-Girona M, Martínez E, Esteve J, Roig A, Solanas R, Molins E. Micromechanical properties of carbon-silica aerogel composites. Appl Phys A Mater Sci Process 2002;74:119–22. https://doi.org/10.1007/s003390100986.

[82] Fan Z, Gong F, Nguyen ST, Duong HM. Advanced multifunctional graphene aerogel - Poly (methyl methacrylate) composites: experiments and modeling. Carbon N Y 2015;81:396–404. https://doi.org/10.1016/j.carbon.2014.09.072.

[83] Shokrieh MM, Hosseinkhani MR, Naimi-Jamal MR, Tourani H. Nanoindentation and nanoscratch investigations on graphene-based nanocomposites. Polym Test 2013;32:45–51. https://doi.org/10.1016/j.polymertesting.2012.09.001.

[84] VanLandingham MR. Review of instrumented indentation. J Res Natl Inst Stand Technol 2003;108:249–65. https://doi.org/10.6028/jres.108.024.

[85] Fischer-Cripps AC. Nanoindentation. Third. Springer; 2011.

[86] Hay J, Crawford B. Measuring substrate-independent modulus of thin films. J Mater Res 2011;26:727–38. https://doi.org/10.1557/jmr.2011.8.

[87] Xu ZH, Rowcliffe D. Finite element analysis of substrate effects on indentation behaviour of thin films. Thin Solid Films 2004;447–448:399–405. https://doi.org/10.1016/S0040-6090(03)01071-X.

[88] Gregory JR, Spearing SM. Nanoindentation of neat and in situ polymers in polymer – matrix composites. Compos Sci Technol 2005;65:595–607. https://doi.org/10.1016/j.compscitech.2004.09.001.

[89] Davidson DL, Pharr GM. Matrix properties of textile reinforced ceramic matrix composites measured by nanoindentation. J Compos Technol Res 2001;23:102–10. https://doi.org/http://dx.doi.org/10.1520/CTR10918J.

[90] Nguyen S, Anthony DB, Qian H, Yue C, Singh A, Bismarck A, *et al*. Mechanical and physical performance of carbon aerogel reinforced carbon fibre hierarchical composites. Compos Sci Technol 2019;182. https://doi.org/10.1016/j.compscitech.2019.107720.

[91] Toray Carbon Fibers America inc. T300 data sheet n.d.

[92] Aveston J, Cooper GA, Kelly A. The properties of fibre composites. Proc. Conf. Natl. Phys. Lab., IPC Science and Technology Press Ltd; 1971, p. 15–26.

[93] Hull D, Clyne T. Fibres and matrices. An Introd. to Compos. Mater., 1996, p. 9–38. https://doi.org/https://doi.org/10.1017/CBO9781139170130.004.

[94] Naslain RR. The design of the fibre-matrix interfacial zone in ceramic matrix composites. Compos Part A Appl Sci Manuf 1998;29:1145–55. https://doi.org/10.1016/S1359-835X(97)00128-0.

[95] Senokos E, Reguero V, Cabana L, Palma J, Marcilla R, Vilatela JJ. Large-area, all-solid, and flexible electric double layer capacitors based on CNT fiber electrodes and polymer electrolytes. Adv Mater Technol 2017;2:1–10. https://doi.org/10.1002/admt.201600290.

[96] Medina C, Canales C, Arango C, Flores P. The influence of carbon fabric weave on the in-plane shear mechanical performance of epoxy fiber-reinforced laminates. J Compos Mater 2014;48:2871–8. https://doi.org/10.1177/0021998313503026.

[97] Fouinneteau MRC, Pickett AK. Shear mechanism modelling of heavy tow braided composites using a meso-mechanical damage model 2007;38:2294–306. https://doi.org/10.1016/j.compositesa.2006.12.006.

[98] Karahan M. Investigation of damage initiation and propagation in 2x2 twill woven carbon/epoxy multi-layer composites. Text Res J 2011;81:412–28. https://doi.org/10.1177/0040517510395996.

[99] Mclendon WR, Whitcomb JD. Characteristic progressive damage modes in a plain weave textile composite under multiaxial loads. J Compos Mater 2017;51:1539–56. https://doi.org/10.1177/0021998316662132.

[100] Mehdikhani M, Gorbatikh L, Verpoest I, Lomov S V. Voids in fiber-reinforced polymer composites: A review on their formation, characteristics, and effects on mechanical performance. J Compos Mater 2019;53:1579–669. https://doi.org/10.1177/0021998318772152.

[101] Goodwin AA, Howe CA, Paton RJ. The role of voids in reducing the interlaminar shear strength of RTM laminates. Proc. ICCM11, Gold Coast: 1997.

[102] Nikishkov Y, Seon G, Makeev A. Structural analysis of composites with porosity defects based

on X-ray computed tomography. J Compos Mater 2014;48:2131–44. https://doi.org/10.1177/0021998313494917.

[103] Naganuma T, Naito K, Kyono J, Kagawa Y. Influence of prepreg conditions on the void occurrence and tensile properties of woven glass fiber-reinforced polyimide composites. Compos Sci Technol 2009;69:2428–33. https://doi.org/10.1016/j.compscitech.2009.06.012.

[104] Greenhalgh ES. Failure analysis and fractography of polymer composites. Woodhead Publishing; 2009. https://doi.org/https://doi.org/10.1533/9781845696818.356.

[105] Chawla KK. Composite materials. 2012. https://doi.org/10.1007/978-0-387-74365-3.

[106] Peng HX, Fan Z, Evans JRG. Bi-continuous metal matrix composites. Mater Sci Eng A 2001;303:37–45. https://doi.org/https://doi.org/10.1016/S0921-5093(00)01879-7.

[107] Tuchinskii LI. Elastic constants of pseudoalloys with a skeletal structure. Sov Powder Metall Met Ceram 1983;22:588–95. https://doi.org/10.1007/BF00805660.

[108] Lee C, Greenhalgh ES, Shaffer MSP, Panesar A. Optimized microstructures for multifunctional structural electrolytes. Multifunct Mater 2019;2:045001. https://doi.org/10.1088/2399-7532/ab47ed.

[109] Tu V, Asp LE, Shirshova N, Larsson F, Runesson K, Janicke R. Performance of bicontinuous structural electrolytes. Multifunct Mater 2020;3. https://doi.org/https://doi.org/10.1088/2399-7532/ab8d9b.

[110] Ma HS, Prévost JH, Jullien R, Scherer GW. Computer simulation of mechanical structure-property relationship of aerogels. J Non Cryst Solids 2001;285:216–21. https://doi.org/10.1016/S0022-3093(01)00456-2.

[111] Lu Z, Yuan Z, Liu Q, Hu Z, Xie F, Zhu M. Multi-scale simulation of the tensile properties of fiber-reinforced silica aerogel composites. Mater Sci Eng A 2015;625:278–87. https://doi.org/10.1016/j.msea.2014.12.007.

[112] Liu Q, Lu Z, Zhu M, Yuan Z, Yang Z, Hu Z, *et al*. Simulation of the tensile properties of silica aerogels: the effects of cluster structure and primary particle size. Soft Matter 2014;10:6266–77. https://doi.org/10.1039/C4SM01074D.

[113] Ma H, Zheng X, Luo X, Yi Y, Yang F. Simulation and analysis of mechanical properties of silica aerogels: from rationalization to prediction. Materials (Basel) 2018;11:1–12. https://doi.org/10.3390/ma11020214.

[114] Morales-Flórez V, De La Rosa-Fox N, Piñero M, Esquivias L. The cluster model: a simulation of the aerogel structure as a hierarchically-ordered arrangement of randomly packed spheres. J Sol-Gel Sci Technol 2005;35:203–10. https://doi.org/10.1007/s10971-005-2363-4.

[115] Ricks TM, Lacy TE, Santiago D, Bednarcyk BA. NASA/TM—2016-219391 Mechanical model development for composite structural supercapacitors 2016. https://ntrs.nasa.gov/api/citations/20160013861/downloads/20160013861.pdf.

[116] Wehrkamp-Richter T, De Carvalho N V., Pinho ST. Predicting the non-linear mechanical response of triaxial braided composites. Compos Part A Appl Sci Manuf 2018;114:117–35. https://doi.org/10.1016/j.compositesa.2018.08.011.

[117] Asp LE, Marklund E, Varna J, Olsson R. Multiscale modelling of non-crimp fabric composites. ASME Int. Mech. Eng. Congr. Expo. Proc., Houston: 2012. https://doi.org/10.1115/IMECE2012-89236.

[118] Ishikawa T, Chou TW. Stiffness and strength behaviour of woven fabric composites. J Mater Sci 1982;17:3211–20. https://doi.org/10.1007/BF01203485.

[119] Raju IS, Wang JT. Classical laminate theory models for woven fabric composites. J Compos Technol Res 1994;16:289–303. https://doi.org/10.1520/ctr10589j.

[120] Naik NK, Ganesh VK. Prediction of on-axes elastic properties of plain weave fabric

composites. Compos Sci Technol 1993;45:135–52. https://doi.org/https://doi.org/10.1016/0266-3538(92)90036-3.

[121] Kregers AF, Melbardis YG. Determination of the deformability of three-dimensionally reinforced composites by the stiffness averaging method. Polym Mech 1978;14:1–5. https://doi.org/https://doi.org/10.1007/BF00859550.

[122] Cox BN. Macroscopic Elasticity of 3D woven composites. J Compos Mater 1994;29. https://doi.org/https://doi.org/10.1177%2F002199839502900606.

[123] Pastore CM, Gowayed YA. Self-consistent fabric geometry model: modification and application of a fabric geometry model to predict the elastic properties of textile composites. J Compos Technol Res 1994;16:32–6. https://doi.org/10.1520/ctr10392j.

[124] Prodromou AG, Lomov S V, Verpoest I. The method of cells and the mechanical properties of textile composites. Compos Struct 2011;93:1290–9. https://doi.org/10.1016/j.compstruct.2010.09.022.

[125] Green SD, Matveev MY, Long AC, Ivanov D, Hallett SR. Mechanical modelling of 3D woven composites considering realistic unit cell geometry. Compos Struct 2014;118:284–93. https://doi.org/10.1016/j.compstruct.2014.07.005.

[126] Sharma R, Mahajan P, Mittal RK. Fiber bundle push-out test and image-based finite element simulation for 3D carbon/carbon composites. Carbon N Y 2012;50:2717–25. https://doi.org/10.1016/j.carbon.2012.02.030.

[127] Patel DK, Waas AM. Damage and failure modelling of hybrid three-dimensional textile composites: a mesh objective multi-scale approach. Philos Trans R Soc A Math Phys Eng Sci 2016;374. https://doi.org/10.1098/rsta.2016.0036.

[128] Wehrkamp-Richter T, Hinterhölzl R, Pinho ST. Damage and failure of triaxial braided composites under multi-axial stress states. Compos Sci Technol 2017;150:32–44. https://doi.org/10.1016/j.compscitech.2017.07.002.

[129] Ahmed S, Zheng X, Wu T, Bhatti NA. Meso-scale damage modeling of hybrid 3D woven orthogonal composites under uni-axial compression. Proc. 13th Int. Conf. Damage Assess. Struct. DAMAS 2019, Porto, Portugal: 2020, p. 816–26.

[130] Tang X, Whitcomb JD. General techniques for exploiting periodicity and symmetries in micromechanics analysis of textile composites. J Compos Mater 2003;37:1167–89. https://doi.org/10.1177/0021998303033467.

[131] De Carvalho N V., Pinho ST, Robinson P. Reducing the domain in the mechanical analysis of periodic structures, with application to woven composites. Compos Sci Technol 2011;71:969–79. https://doi.org/10.1016/j.compscitech.2011.03.001.

[132] Owens BC, Whitcomb JD, Varghese J. Effect of finite thickness and free edges on stresses in plain weave composites. J Compos Mater 2010;44:675–92. https://doi.org/10.1177/0021998309347571.

[133] Ivanov DS, Lomov S V., Ivanov SG, Verpoest I. Stress distribution in outer and inner plies of textile laminates and novel boundary conditions for unit cell analysis. Compos Part A Appl Sci Manuf 2010;41:571–80. https://doi.org/10.1016/j.compositesa.2010.01.004.

[134] Ivanov DS, Ivanov SG, Lomov S V., Verpoest I. Unit cell modelling of textile laminates with arbitrary inter-ply shifts. Compos Sci Technol 2011;72:14–20. https://doi.org/10.1016/j.compscitech.2011.08.003.

[135] De Carvalho NV, Pinho ST, Robinson P. An experimental study of failure initiation and propagation in 2D woven composites under compression. Compos Sci Technol 2011;71:1316–25. https://doi.org/10.1016/j.compscitech.2011.04.019.

[136] De Carvalho N V, Pinho ST, Robinson P. Analytical modelling of the compressive and tensile response of woven composites. Compos Struct 2012;94:2724–35.

https://doi.org/10.1016/j.compstruct.2012.03.036.

[137] Broucke B Van Den, Hegemann J, Das R, Oster R, Hackl K. Modelling of textile reinforced composites using finite element tools and investigation of the influence of porosity on mechanical properties. Finite Elem. Model. Text. Text. Compos., St-Petersburg: 2007.

[138] Xu K, Qian X. An FEM analysis with consideration of random void defects for predicting the mechanical properties of 3d braided composites. Adv Mater Sci Eng 2014;2014. https://doi.org/10.1155/2014/439819.

[139] Rajpurohit A, Joannès S, Singery V, Sanial P, Laiarinandrasana L. Hybrid effect in in-plane loading of carbon/glass fibre based inter- and intraply hybrid composites. J Compos Sci 2020;4:6. https://doi.org/10.3390/jcs4010006.

[140] Swolfs Y, Geboes Y, Gorbatikh L, Pinho ST. The importance of translaminar fracture toughness for the penetration impact behaviour of woven carbon/glass hybrid composites. Compos Part A J 2016;103:1–8. https://doi.org/10.1016/j.compositesa.2017.09.009.

[141] Cheon J, Lee M, Kim M. Study on the stab resistance mechanism and performance of the carbon, glass and aramid fiber reinforced polymer and hybrid composites. Compos Struct 2020;234:111690. https://doi.org/10.1016/j.compstruct.2019.111690.

[142] Sun G, Tong S, Chen D, Gong Z, Li Q. Mechanical properties of hybrid composites reinforced by carbon and basalt fibers. Int J Mech Sci 2018;148:636–51. https://doi.org/10.1016/j.ijmecsci.2018.08.007.

[143] Chen D, Luo Q, Meng M, Sun G. Low velocity impact behavior of interlayer hybrid composite laminates with carbon/glass/basalt fibres. Compos Part B Eng 2019;176:107191. https://doi.org/10.1016/j.compositesb.2019.107191.

[144] Sevkat E, Liaw B, Delale F, Raju BB. Drop-weight impact of plain-woven hybrid glass-graphite/toughened epoxy composites. Compos Part A Appl Sci Manuf 2009;40:1090–110. https://doi.org/10.1016/j.compositesa.2009.04.028.

[145] Enfedaque A, Molina-Aldareguía JM, Gálvez F, González C, Llorca J. Effect of glass fiber hybridization on the behavior under impact of woven carbon fiber/epoxy laminates. J Compos Mater 2010;44:3051–68. https://doi.org/10.1177/0021998310369602.

[146] Kim BK, Sy S, Yu A, Zhang J. Electrochemical supercapacitors for energy storage and conversion. Handb Clean Energy Syst 2015:1–25. https://doi.org/10.1002/9781118991978.hces112.

[147] D'Entremont A, Pilon L. First-principles thermal modeling of electric double layer capacitors under constant-current cycling. J Power Sources 2014;246:887–98. https://doi.org/10.1016/j.jpowsour.2013.08.024.

[148] Tammela P, Olsson H, Strømme M, Nyholm L. The influence of electrode and separator thickness on the cell resistance of symmetric cellulose-polypyrrole-based electric energy storage devices. J Power Sources 2014;272:468–75. https://doi.org/10.1016/j.jpowsour.2014.08.041.

[149] Maxwell Technologies. Datasheet: 2.7V 100F ultracapacitor cell. 2018.

[150] Cusenza MA, Bobba S, Ardente F, Cellura M, Di Persio F. Energy and environmental assessment of a traction lithium-ion battery pack for plug-in hybrid electric vehicles. J Clean Prod 2019;215:634–49. https://doi.org/10.1016/j.jclepro.2019.01.056.

[151] Maxwell Technologies. Ultracapacitor safety data sheet. 2018.

[152] Pereira AI, Martins J, Tavares CJ, Andrade L, Mendes A. Development of stable current collectors for large area dye-sensitized solar cells. Appl Surf Sci 2017;423:549–56. https://doi.org/10.1016/j.apsusc.2017.06.194.

[153] Holmes-Gentle I, Agarwal H, Alhersh F, Hellgardt K. Assessing the scalability of low conductivity substrates for photo-electrodes: via modelling of resistive losses. Phys Chem Chem Phys 2018;20:12422–9. https://doi.org/10.1039/c8cp01337c.

[154] Johannisson W, Carlstedt D, Nasiri A, Buggisch C, Linde P, Zenkert D, *et al.* A screen-printing method for manufacturing of current collectors for structural batteries. Multifunct Mater 2021;4. https://doi.org/10.1088/2399-7532/ac2046.

[155] Serreze HB. Optimizing solar cell performance by simultaneous consideration of grid pattern design and interconnect configuration. Conf. Rec. IEEE Photovolt. Spec. Conf., 1978, p. 609–14.

[156] Handy RJ. Theoretical analysis of the series resistance of a solar cell. Solid State Electron 1967;10:765–75. https://doi.org/https://doi.org/10.1016/S0263-8223(00)00056-8.

[157] Hauser JR, Dunbar PM. Performance limitations of silicon solar cells. IEEE Trans Electron Devices 1977;ED-24:305–21. https://doi.org/10.1109/T-ED.1977.18734.

[158] Noh HS, Hwang J, Yoon K, Kim BK, Lee HW, Lee JH, *et al.* Optimization of current collection to reduce the lateral conduction loss of thin-film-processed cathodes. J Power Sources 2013;230:109–14. https://doi.org/10.1016/j.jpowsour.2012.12.059.

[159] Lee WJ, Shinde PS, Go GH, Ramasamy E. Ag grid induced photocurrent enhancement in WO3 photoanodes and their scale-up performance toward photoelectrochemical H2 generation. Int J Hydrogen Energy 2011;36:5262–70. https://doi.org/10.1016/j.ijhydene.2011.02.013.

[160] Abdi FF, Gutierrez Perez RR, Haussener S. Mitigating voltage losses in photoelectrochemical cell scale-up. Sustain Energy Fuels 2020. https://doi.org/10.1039/d0se00246a.

[161] Hankin A, Bedoya-Lora FE, Ong CK, Alexander JC, Petter F, Kelsall GH. From millimetres to metres: the critical role of current density distributions in photo-electrochemical reactor design. Energy Environ Sci 2017;10:346–60. https://doi.org/10.1039/c6ee03036j.

[162] Farivar F. CFD simulation and development of an improved photoelectrochemical reactor for H2 production. Int J Hydrogen Energy 2015;41:882–8. https://doi.org/10.1016/j.ijhydene.2015.11.045.

[163] Madabattula G, Wu B, Marinescu M, Offer G. How to design lithium ion capacitors: modelling, mass ratio of electrodes and pre-lithiation. J Electrochem Soc 2020;167:013527. https://doi.org/10.1149/2.0272001jes.

[164] Lim JI. Transient finite element analysis of electric double layer using Nernst-Planck-Poisson equations with a modified Stern layer. Texas A&M University, 2006. https://doi.org/10.1016/j.jcis.2006.08.049.

[165] Pilon L, Wang H, D'Entremont A. Recent advances in continuum modeling of interfacial and transport phenomena in electric double layer capacitors. J Electrochem Soc 2015;162:A5158–78. https://doi.org/10.1149/2.0211505jes.

[166] Rieger B, Erhard S V., Kosch S, Venator M, Rheinfeld A, Jossen A. Multi-dimensional modeling of the influence of cell design on temperature, displacement and stress inhomogeneity in large-format lithium-ion cells. J Electrochem Soc 2016;163:A3099–110. https://doi.org/10.1149/2.1051614jes.

[167] Meier DL, Schroder DK. Contact resistance: its measurement and relative importance to power loss in a solar cell. IEEE Trans Electron Devices 1984;31:647–53. https://doi.org/10.1109/T-ED.1984.21584.

[168] Dubal DP, Ayyad O, Ruiz V. Chem Soc Rev Hybrid energy storage : the merging of battery and supercapacitor chemistries. Chem Soc Rev 2015;44:1777–90. https://doi.org/10.1039/C4CS00266K.

[169] Kroupa M, Offer GJ, Kosek J. Modelling of supercapacitors: factors influencing performance. J Electrochem Soc 2016;163:A2475–87. https://doi.org/10.1149/2.0081613jes.

[170] Yassine M, Fabris D. Performance of commercially available supercapacitors. Energies 2017;10. https://doi.org/10.3390/en10091340.

[171] Burt R, Birkett G, Zhao XS. A review of molecular modelling of electric double layer capacitors. Phys Chem Chem Phys 2014;16:6519–38. https://doi.org/10.1039/c3cp55186e.

[172] Burke A, Liu Z, Zhao H. Present and future applications of supercapacitors in electric and hybrid vehicles. 2014 IEEE Int Electr Veh Conf 2014:1–8. https://doi.org/10.1109/IEVC.2014.7056094.

[173] Matheson R. New applications for ultracapacitors. MIT News 2016. http://news.mit.edu/2016/new-applications-ultracapacitors-drilling-aerospace-electric-cars-0907 (accessed September 1, 2019).

[174] O'Brien DJ, Baechle DM, Yurchak OB, Wetzel ED. Effect of processing conditions and electrode characteristics on the electrical properties of structural composite capacitors. Compos Part A Appl Sci Manuf 2015;68:47–55. https://doi.org/10.1016/j.compositesa.2014.09.003.

[175] Shirshova N, Qian H, Shaffer MSP, Steinke JHG, Greenhalgh ES, Curtis PT, *et al.* Structural composite supercapacitors. Compos Part A 2013;46:96–107. https://doi.org/10.1016/j.compositesa.2012.10.007.

[176] Fujimoto T, Awaga K. Electric-double-layer field-effect transistors with ionic liquids. Phys Chem Chem Phys 2013;15:8983–9006. https://doi.org/10.1039/c3cp50755f.

[177] Ho C, Raistrick ID, Huggins RA. Application of A-C techniques to the study of lithium diffusion in tungsten trioxide thin films. J Electrochem Soc 1980;127:343–50. https://doi.org/10.1149/1.2129668.

[178] Randles JEB. Kinetics of rapid electrode reactions. Faraday Discuss 1947;1:11–9. https://doi.org/10.1039/DF9470100011.

[179] Mei BA, Munteshari O, Lau J, Dunn B, Pilon L. Physical interpretations of Nyquist plots for EDLC electrodes and devices. J Phys Chem C 2018;122:194–206. https://doi.org/10.1021/acs.jpcc.7b10582.

[180] Lukács Z, Kristóf T. A generalized model of the equivalent circuits in the electrochemical impedance spectroscopy. Electrochim Acta 2020;363:137199. https://doi.org/10.1016/j.electacta.2020.137199.

[181] Zubieta L, Bonert R. Characterization of double-layer capacitors for power electronics applications. IEEE Trans Ind Appl 2000;36:199–205. https://doi.org/10.1109/28.821816.

[182] De Levie R. On porous electrodes in electrolyte solutions. Electrochim Acta 1964;9:1231–45. https://doi.org/10.1016/0013-4686(64)85015-5.

[183] Drummond R, Howey DA, Duncan SR. Low-order mathematical modelling of electric double layer supercapacitors using spectral methods 2014. https://doi.org/10.1016/j.jpowsour.2014.11.116.

[184] Iozzo DAB, Tong M, Wu G, Furlani EP. Numerical analysis of electric double layer capacitors with mesoporous electrodes: effects of electrode and electrolyte properties. J Phys Chem C 2015;119:25235–42. https://doi.org/10.1021/acs.jpcc.5b08409.

[185] Johnson AM, Newman J. Desalting by Means of Porous Carbon Electrodes. J Electrochem Soc 1971;118:510–7. https://doi.org/10.1149/1.2408094.

[186] Newman JS, Thomas-Alyea KE. Electrochemical Systems. 3rd. ed. New York: Wiley; 2004.

[187] Wang H, Pilon L. Mesoscale modeling of electric double layer capacitors with three-dimensional ordered structures. J Power Sources 2013;221:252–60. https://doi.org/10.1016/j.jpowsour.2012.08.002.

[188] Campillo-Robles JM, Artetxe X, del Teso Sánchez K, Gutiérrez C, Macicior H, Röser S, *et al.* General hybrid asymmetric capacitor model: validation with a commercial lithium ion capacitor. J Power Sources 2019;425:110–20. https://doi.org/10.1016/j.jpowsour.2019.03.121.

[189] Biesheuvel PM, Bazant MZ. Nonlinear dynamics of capacitive charging and desalination by porous electrodes. Phys Rev E 2010;81:1–12. https://doi.org/10.1103/PhysRevE.81.031502.

[190] Wang Y, Zhang C, Qiao X, Mansour AN, Zhou X. Three-dimensional modeling of mediator-enhanced solid-state supercapacitors. J Power Sources 2019;423:18–25. https://doi.org/10.1016/j.jpowsour.2019.03.012.

[191] Cagle C, Feng G, Qiao R, Huang J, Sumpter BG, Meunier V. Structure and charging kinetics of electrical double layers at large electrode voltages. Microfluid Nanofluidics 2010;8:703–8. https://doi.org/10.1007/s10404-009-0542-2.

[192] Schiffer J, Linzen D, Sauer DU. Heat generation in double layer capacitors. J Power Sources 2006;160:765–72. https://doi.org/10.1016/j.jpowsour.2005.12.070.

[193] Lee J, Yi J, Kim D, Shin CB, Min KS, Choi J, *et al.* Modeling of the electrical and thermal behaviors of an ultracapacitor. Energies 2014;7:8264–78. https://doi.org/10.3390/en7128264.

[194] Parvini Y, Siegel JB, Stefanopoulou AG, Vahidi A. Supercapacitor electrical and thermal modeling, identification, and validation for a wide range of temperature and power applications. IEEE Trans Ind Electron 2016;63:1574–85. https://doi.org/10.1109/TIE.2015.2494868.

[195] Ai W, Kraft L, Sturm J, Jossen A, Wu B. Electrochemical thermal-mechanical modelling of stress inhomogeneity in lithium-ion pouch cells. J Electrochem Soc 2020;167:013512. https://doi.org/10.1149/2.0122001jes.

[196] Zhu J, Li W, Wierzbicki T, Xia Y, Harding J. Deformation and failure of lithium-ion batteries treated as a discrete layered structure. Int J Plast 2019;121:293–311. https://doi.org/10.1016/j.ijplas.2019.06.011.

[197] Bahei-El-Din Y a. Modelling electromechanical coupling in woven composites exhibiting damage. Proc Inst Mech Eng Part G J Aerosp Eng 2009;223:485–95. https://doi.org/10.1243/09544100JAERO435.

[198] Xia Z, Sujidkul T, Niu J, Smith CE, Morscher GN. Modeling of electromechanical behavior of woven SiC/SiC composites. Compos. Part A Appl. Sci. Manuf., vol. 43, Elsevier Ltd; 2012, p. 1730–7. https://doi.org/10.1016/j.compositesa.2012.03.020.

[199] Matos MAS, Tagarielli VL, Baiz-Villafranca PM, Pinho ST. Predictions of the electro-mechanical response of conductive CNT-polymer composites. J Mech Phys Solids 2018;114:84–96. https://doi.org/10.1016/j.jmps.2018.02.014.

[200] Carlstedt D, Asp LE. Thermal and diffusion induced stresses in a structural battery under galvanostatic cycling. Compos Sci Technol 2019;179:69–78. https://doi.org/10.1016/j.compscitech.2019.04.024.

[201] Golmon S, Maute K, Dunn ML. Numerical modeling of electrochemical-mechanical interactions in lithium polymer batteries. Comput Struct 2009;87:1567–79. https://doi.org/10.1016/j.compstruc.2009.08.005.

[202] Xu J, Varna J. Matrix and interface cracking in cross-ply composite structural battery under combined electrochemical and mechanical loading. Compos Sci Technol 2020;186:107891. https://doi.org/10.1016/j.compscitech.2019.107891.

[203] Carlstedt D, Runesson K, Larsson F, Xu J, Asp LE. Electro-chemo-mechanically coupled computational modelling of structural batteries. Multifunct Mater 2020;3. https://doi.org/10.1088/2399-7532/abc60d.

[204] Lomov S V., Gorbatikh L, Kotanjac Ž, Koissin V, Houlle M, Rochez O, *et al.* Compressibility of carbon woven fabrics with carbon nanotubes/nanofibres grown on the fibres. Compos Sci Technol 2011;71:315–25. https://doi.org/10.1016/j.compscitech.2010.11.024.

[205] Aravand MA, Shishkina O, Straumit I, Liotta AH, Wicks SS, Wardle BL, *et al.* Internal geometry of woven composite laminates with "fuzzy" carbon nanotube grafted fibers. Compos

Part A 2016;88:295–304. https://doi.org/10.1016/j.compositesa.2016.06.010.

[206] Carlstedt D, Marklund E, Asp LE. Effects of state of charge on elastic properties of 3D structural battery composites. Compos Sci Technol 2019;169:26–33. https://doi.org/10.1016/j.compscitech.2018.10.033.

[207] Xu J, Lindbergh G, Varna J. Multiphysics modeling of mechanical and electrochemical phenomena in structural composites for energy storage: single carbon fiber micro-battery. J Reinf Plast Compos 2018;37:701–15. https://doi.org/10.1177/0731684418760207.

[208] Dionisi F, Harnden R, Zenkert D. A model to analyse deformations and stresses in structural batteries due to electrode expansions. Compos Struct 2017;179:580–9. https://doi.org/10.1016/j.compstruct.2017.07.029.

[209] Nguyen S, Anthony DB, Qian H, Yue C, Singh A, Bismarck A, *et al*. Mechanical and physical performance of carbon aerogel reinforced carbon fibre hierarchical composites. Compos Sci Technol 2019;182:1–36. https://doi.org/10.1016/j.compscitech.2019.107720.

[210] Choudhry RS, Khan KA, Khan SZ, Khan MA, Hassan A. Micromechanical modeling of 8-harness satin weave glass fiber-reinforced composites. J Compos Mater 2017;51:705–20. https://doi.org/10.1177/0021998316649782.

[211] Wehrkamp-Richter T. Multiscale analysis of the mechanical response of triaxial braided composites. Technische Universität München, 2018.

[212] ToolBox E. Metals and Alloys - Densities 2004. https://www.engineeringtoolbox.com/metal-alloys-densities-d_50.html (accessed October 12, 2020).

[213] Hurst D, Vassilicos JC. Scalings and decay of fractal-generated turbulence. Phys Fluids 2007;19. https://doi.org/10.1063/1.2676448.

[214] Siemens. Airbus Helicopters: simulation and virtual aircraft. Siemens Blog 2021. https://blogs.sw.siemens.com/simcenter/airbus-helicopters-simulation-and-virtual-aircraft/ (accessed February 26, 2021).

[215] Dassault Systèmes. Airbus selects Dassault Systèmes' SIMULIA realistic simulation solutions for nonlinear FEA of aircraft structures 2007. https://www.theengineer.co.uk/airbus-selects-dassaults-simulia-realistic-simulation-solutions/ (accessed September 9, 2018).

[216] Chomarat. Composites Reinforcements C-weave™ 200P 3K HS n.d. http://composites.chomarat.com/en/product/c-weave-200p-3k-hs/ (accessed February 7, 2018).

[217] Gividi Fabrics srl. Data sheet and product information. 2016.

[218] Shirshova N, Rogaume T, Najmi H, Poisson M. The combustion behavior of epoxy-based multifunctional electrolytes. Fire Mater 2021:1–13. https://doi.org/10.1002/fam.2967.

[219] De Carvalho NV, Pinho ST, Robinson P. Numerical modelling of woven composites: Biaxial loading. Compos Part A Appl Sci Manuf 2012;43:1326–37. https://doi.org/10.1016/j.compositesa.2012.03.017.

[220] Tan P, Tong L, Steven GP. Micromechanics models for the elastic constants and failure strengths of plain weave composites. Compos Struct 1999;47:797–804. https://doi.org/doi.org/10.1016/S0263-8223(00)00056-8.

[221] Lomov SV, Verpoest I, Cichosz J, Hahn C, Ivanov DS, Verleye B. Meso-level textile composites simulations: open data exchange and scripting. J Compos Mater 2014;48:621–37. https://doi.org/10.1177/0021998313476327.

[222] Dassault Systèmes Simulia Corp. Abaqus user's manual 2016.

[223] Cornelissen B, Sachs U, Rietman B, Akkerman R. Dry friction characterisation of carbon fibre tow and satin weave fabric for composite applications. Compos Part A Appl Sci Manuf 2014;56:127–35. https://doi.org/10.1016/j.compositesa.2013.10.006.

[224] Badel P, Gauthier S, Vidal-Sallé E, Boisse P. Rate constitutive equations for computational analyses of textile composite reinforcement mechanical behaviour during forming. Compos Part A Appl Sci Manuf 2009;40:997–1007. https://doi.org/10.1016/j.compositesa.2008.04.015.

[225] Mimaroglu A, Unal H, Arda T. Friction and wear performance of pure and glass fibre reinforced poly-ether-imide on polymer and steel counterface materials. Wear 2007;262:1407–13. https://doi.org/10.1016/j.wear.2007.01.015.

[226] Boisse P, Gasser A, Hagege B, Billoet J-L. Analysis of the mechanical behavior of woven fibrous material using virtual tests at the unit cell level. J Mater Sci 2005;40:5955–62. https://doi.org/10.1007/s10853-005-5069-7.

[227] Lin H, Clifford MJ, Long AC, Sherburn M. Finite element modelling of fabric shear. Model Simul Mater Sci Eng 2009;17. https://doi.org/10.1088/0965-0393/17/1/015008.

[228] Dassault Systèmes Simulia. Abaqus benchmarks guide (6.13). 2013.

[229] Boisse P, Hamila N, Guzman-Maldonado E, Madeo A, Hivet G, dell'Isola F. The bias-extension test for the analysis of in-plane shear properties of textile composite reinforcements and prepregs: a review. Int J Mater Form 2017;10:473–92. https://doi.org/10.1007/s12289-016-1294-7.

[230] Daniel IM, Ishai O. Engineering mechanics of composite materials. vol. 3. 2nd ed. Oxford University Press; 2006. https://doi.org/10.1016/B978-1-84569-385-5.50021-0.

[231] Krucinska I, Stypka T. Direct measurement of the axial poisson's ratio of single carbon fibres. Compos Sci Technol 1991;41:1–12. https://doi.org/10.1016/0266-3538(91)90049-U.

[232] Quorum Technologies. K575X sputter coater instruction manual. 2008.

[233] Micro Materials Limited. NanoTest user manual. 2007.

[234] Oliver WC, Pharr GM. An improved technique for determining hardness and elastic modulus using load and displacement sensing indentation experiments 1992. https://doi.org/https://doi.org/10.1557/JMR.1992.1564.

[235] The University of Texas High-Resolution X-ray Computed Tomography Facility. Artifacts and partial-volume effects n.d. http://www.ctlab.geo.utexas.edu/about-ct/artifacts-and-partial-volume-effects/ (accessed February 8, 2021).

[236] Yang B, Zhao CY, Bi FY, Wang SB, Ma C, Wang SL. Effect of horizontal shift between fabric layers on the meso-scale-void formation in liquid composite molding. Express Polym Lett 2019;13:501–11. https://doi.org/10.3144/expresspolymlett.2019.42.

[237] Zhao C, Yang B, Wang S, Ma C, Wang S, Bi F. Three-dimensional numerical simulation of meso-scale-void formation during the mold-filling process of LCM. Appl Compos Mater 2019;26:1121–37. https://doi.org/10.1007/s10443-019-09770-w.

[238] Hull D, Clyne T. Strength of composites. An Introd. to Compos. Mater., Cambridge: Cambridge University Press; 1996, p. 158–207. https://doi.org/doi:10.1017/CBO9781139170130.010.

[239] Arvai K. K-means clustering in Python: a practical guide n.d. https://realpython.com/k-means-clustering-python/ (accessed August 1, 2021).

[240] Graham RL, Yao FF. Finding the convex hull of a simple polygon. J Algorithms 1983;4:324–31. https://doi.org/https://doi.org/10.1016/0167-8655(82)90016-2.

[241] Wendong Q, Dent J, Arrighi V, Cavalcanti L, Shaffer MSP, Shirshova N. Biphasic epoxy-ionic liquid structural electrolytes: Minimising feature size through cure cycle and multifunctional block-copolymer addition. Multifunct Mater 2021;4. https://doi.org/10.1088/2399-7532/ac1ea7.

[242] Chamis CC. Simplified composite micromechanics for predicting microstresses. J Reinf Plast

Compos 1987;6:268–89. https://doi.org/10.1177/073168448700600305.

[243] Bard S, Demleitner M, Weber R, Zeiler R, Altstädt V. Effect of curing agent on the compressive behavior at elevated test temperature of carbon fiber-reinforced epoxy composites. Polymers (Basel) 2019;11. https://doi.org/10.3390/polym11060943.

[244] Oral I, Guzel H, Ahmetli G. Determining the mechanical properties of epoxy resin (DGEBA) composites by ultrasonic velocity measurement. J Appl Polym Sci 2013;127:1667–75. https://doi.org/10.1002/app.37534.

[245] Jones RM, Bert CW. Mechanics of composite materials. Taylor & Francis; 1999. https://doi.org/10.1016/B978-0-444-99713-5.50002-6.

[246] Advance Tapes International Limited. Technical data AT528 50 micron copper foil shielding tape 2021. https://docs.rs-online.com/0acf/0900766b8079dba7.pdf.

[247] Taheri P, Hsieh S, Bahrami M. Investigating electrical contact resistance losses in lithium-ion battery assemblies for hybrid and electric vehicles. J Power Sources 2011;196:6525–33. https://doi.org/10.1016/j.jpowsour.2011.03.056.

[248] Janoch R, Gabor AM, Anselmo A, Dube CE. Contact resistance measurement - observations on technique and test parameters. IEEE 42nd Photovolt. Spec. Conf., New Orleans: 2015, p. 1–6. https://doi.org/10.1109/PVSC.2015.7355851.

[249] Alarifi IM. Investigation the conductivity of carbon fibercomposites focusing on measurement techniquesunder dynamic and static loads. J Mater Res Technol 2019;8:4863–93. https://doi.org/10.1016/j.jmrt.2019.08.019.

[250] Verbeek AA, Willems PA, Stoffels GGM, Geurts BJ, van der Meer TH. Enhancement of turbulent flame speed of V-shaped flames in fractal-grid-generated turbulence. Combust Flame 2016;167:97–112. https://doi.org/10.1016/j.combustflame.2016.02.022.

[251] Hearst RJ, Lavoie P. Decay of turbulence generated by a square-fractal-element grid. J Fluid Mech 2014;741:567–84. https://doi.org/10.1017/jfm.2013.684.

[252] Gu Y, Federici JF. Fabrication of a flexible current collector for lithium ion batteries by inkjet printing. Batteries 2018;4. https://doi.org/10.3390/batteries4030042.

[253] Dassault Systèmes Simulia. Analysis user's manual 2012;V:831.

[254] Tjaden B, Brett DJL, Shearing PR. Tortuosity in electrochemical devices: a review of calculation approaches. Int Mater Rev 2018;63:47–67. https://doi.org/10.1080/09506608.2016.1249995.

[255] Cannarella J, Arnold CB. Ion transport restriction in mechanically strained separator membranes. J Power Sources 2013;226:149–55. https://doi.org/10.1016/j.jpowsour.2012.10.093.

[256] BASF. Ionic liquids as electrolytes n.d. http://www.intermediates.basf.com/chemicals/web/en/function/conversions:/publish/content/news-and-publications/brochures/download/BASF_Ionic_Liquids_Electrolytes.pdf.

[257] Dassault Systèmes. Abaqus 2016 analysis user's guide. 2015.

[258] Zhang L, Tonks MR, Gaston D, Peterson JW, Andrs D, Millett PC, *et al.* A quantitative comparison between C0 and C1 elements for solving the Cahn-Hilliard equation. J Comput Phys 2013;236:74–80. https://doi.org/10.1016/j.jcp.2012.12.001.

[259] The-Crankshaft Publishing. FEM for heat transfer problems 2020. http://what-when-how.com/the-finite-element-method/fem-for-heat-transfer-problems-finite-element-method-part-3/ (accessed October 1, 2019).

[260] Dassault Systèmes. Abaqus 2016 user subroutines reference guide. 2015.

[261] Matveev M, Long A, Brown L, Jones I. Effects of layer shift and yarn path variability on mechanical properties of a twill weave composite. J Compos Mater 2017;51:913–25.

https://doi.org/10.1177/0021998316655870.

[262] Breiling KB, Adams DO, Verhulst MA. Effects of nesting on compression-loaded 2-D woven textile composites. J Compos Mater 1996;30:1710–28. https://doi.org/10.1177/002199839603001505.

[263] Irizar MO. Quasi-static and fatigue delamination characterisation for carbon fibre reinforced woven laminates: Investigation into the nesting effect between layers. Mondragon Unibertsitatea, 2016. https://doi.org/http://hdl.handle.net/20.500.11984/1196.

[264] Lomov S V., Breite C, Melnikov A, Mesquita F, Swolfs Y, Abaimov SG. Clusters and avalanches of fibre breaks in a model of an impregnated unidirectional fibre bundle under tension. Int J Solids Struct 2021;225:111061. https://doi.org/10.1016/j.ijsolstr.2021.111061.

[265] Beyerlein IJ, Phoenix SL. Stress concentrations around multiple fiber breaks in an elastic matrix with local yielding or debonding using quadratic influence superposition. J Mech Phys Solids 1996;44:1997–2039. https://doi.org/10.1016/S0022-5096(96)00068-3.

[266] Pimenta S, Pinho ST. Hierarchical scaling law for the strength of composite fibre bundles. J Mech Phys Solids 2013;61:1337–56. https://doi.org/10.1016/j.jmps.2013.02.004.

[267] Pimenta S, Pinho ST. An analytical model for the translaminar fracture toughness of fibre composites with stochastic quasi-fractal fracture surfaces. J Mech Phys Solids 2014;66:78–102. https://doi.org/10.1016/j.jmps.2014.02.001.

[268] Matsuo S, Sottos NR. Single carbon fiber transverse electrical resistivity measurement via the van der Pauw method. J Appl Phys 2021;130. https://doi.org/10.1063/5.0060126.

[269] Hu C, Zhang G, Li H, Zhang C, Chang Y, Chang Z, *et al.* Thin sandwich graphene oxide@N-doped carbon composites for high-performance supercapacitors. RSC Adv 2017;7:22071–8. https://doi.org/10.1039/c7ra00909g.

[270] Chen GZ. Supercapacitor and supercapattery as emerging electrochemical energy stores. Int Mater Rev 2017;62:173–202. https://doi.org/10.1080/09506608.2016.1240914.

[271] Gamry Instruments. Testing electrochemical capacitors. 2018.

[272] Doyle CM. Design and simulation of lithium rechargeable batteries. University of California at Berkeley, 1995.

[273] Newman J. Electrochemical Systems. 2nd ed. NJ: Prentice Hall; 1991.

[274] Rawat P, Singh KK. Mechanical characterization of symmetrical and asymmetrical glass woven composite laminates. Int. Conf. Compos. Mater. Struct. ICCMS, Hyderabad: 2017.

A Electrochemistry background

A.1 Electrochemical characterisation methods

The specific differential capacitance of an electrode, C_s, (in F/mm²) is defined as the amount of charge stored per unit area, q_s, per unit surface electric potential, ψ_s:

$$C_s = q_s/\psi_s \quad . \tag{A.1}$$

The capacitance of an SC cell is related to those of its electrodes, $C_{s,1}$ and $C_{s,2}$, by

$$\frac{1}{C_{s,\text{cell}}} = \frac{1}{C_{s,1}} + \frac{1}{C_{s,2}} \quad . \tag{A.2}$$

Specific capacitance can be measured in a GCD experiment (Figure A.1(a)), where the cell is cyclically charged and discharged at a constant current, i_{GCD}, or constant current density, $j_{\text{GCD}} = j_s$, within a specified potential window, $\Delta\psi$. From the response $\psi(t)$, specific capacitance is calculated from the linear portion of the discharge curve, that is, after the initial (Ohmic/iR) voltage drop [269], $\Delta\psi_{iR}$, as:

$$C_{s,\text{cell}} = \frac{\Delta Q_s}{\Delta\psi - \Delta\psi_{iR}} = \frac{j_{\text{GCD}}\Delta t}{\Delta\psi - \Delta\psi_{iR}} \quad , \tag{A.3}$$

where ΔQ_s is the cell charge or capacity. The measured capacitance is reduced for high current densities (Figure A.1(b)), due to an increase in the Ohmic drop. The equivalent series resistance at direct current, ESR_{DC}, is extracted from the initial voltage drop through:

$$\text{ESR}_{\text{DC}} = \frac{\Delta\psi_{iR}}{i_{\text{GCD}}} \quad . \tag{A.4}$$

The maximum energy density at the cell rated voltage, V, is then calculated from (A.3) as:

$$E_{s,\max} = \frac{1}{2} C_{s,\text{cell}} V^2 \quad . \tag{A.5}$$

The maximum and usable power ratings [149] of a capacitor are commonly calculated as:

$$P_{\max} = \frac{V^2}{4\text{ESR}_{\text{DC}}} \quad \text{and} \quad P_{\text{u}} = \frac{V^2}{8\text{ESR}_{\text{DC}}} \quad . \tag{A.6}$$

Capacitance can also be calculated from a CV experiment (Figure A.1(c)), which measures cell current as the potential is cyclically swept over a range at a specified scan rate, $\frac{d\psi_s}{dt}$, (usually 0.1 mV/s to 1 V/s). In ideal EDLCs, the current is related to the scan rate through the capacitance, however series resistance and parasitic reactions cause non-linearity. The capacitance can be determined according to Eqn. (A.3) from the charge stored in one cycle:

$$\Delta Q = \frac{1}{2}\int \frac{i_{\text{CV}}}{\frac{d\psi_s}{dt}} d\psi_{\text{CV}} \quad . \tag{A.7}$$

For porous electrodes, pore accessibility is improved at lower scan rates, resulting in larger measured capacitance [270,271].

EIS experiments analyse the current response of the cell to an imposed electric potential, $\psi_s\ t$, composed of a time-independent DC potential and an oscillating AC potential of small amplitude (typically less than 10 mV) and varying frequency. The frequency sweep allows different physical processes to be partitioned based on their time constants [177]. It is the preferred method for measuring ESR and gives a measure of capacitance and non-ideality.

Impedance data can be represented in a Nyquist plot (Figure A.1(d)). Its typical shape consists of a semicircle between points A to B at the high frequency end, sloped portion B to C and near-vertical portion at C. The measured impedance spectrum is generally interpreted in terms of an equivalent circuit model (discussed in Section 2.6.2.2), whose parameter values are evaluated by data fitting. It has been observed, however, that the interpretation of EIS data across the literature is prone to inconsistencies and ambiguities [179].

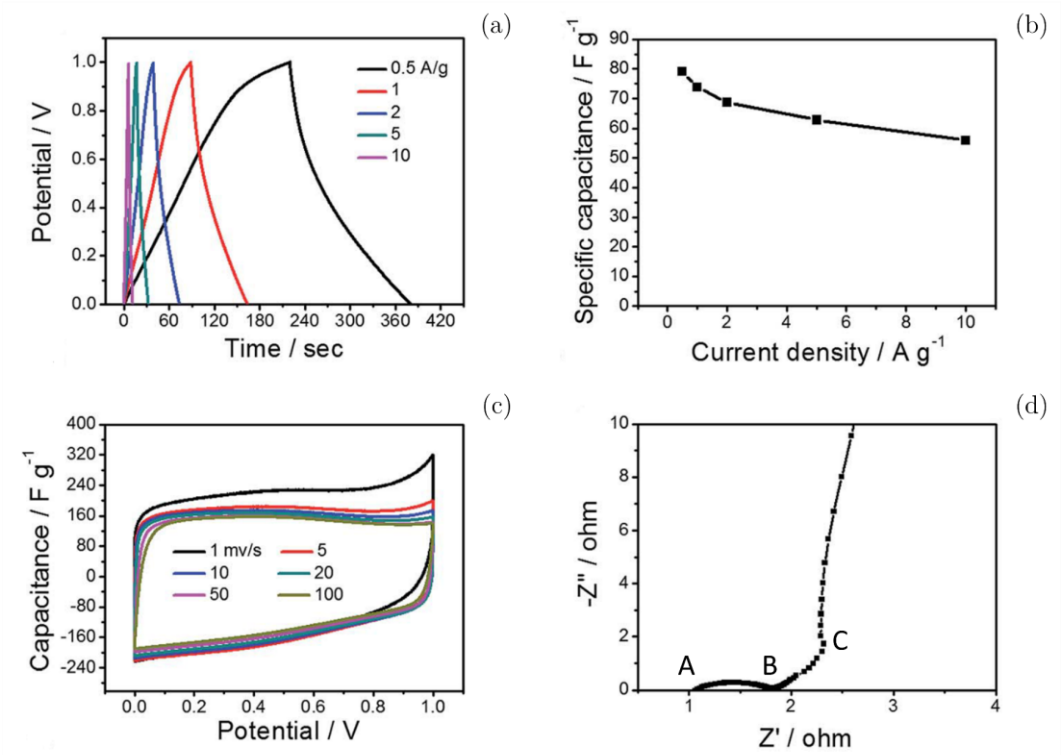

Figure A.1. Typical (a) GCD measurements, (b) current density-dependence of measured capacitance (c) CV measurements, and (c) EIS plot for a supercapacitor. Adapted from [269].

A.2 Boundary conditions in the transient PNP model

The mass conservation equation is a first order PDE in time and second order in space. It requires two boundary conditions for each ion species in the diffuse layer. A zero flux must be satisfied at the Stern/diffuse layer interfaces (illustrated in Figure 2.6) for each ion species. A zero ion concentration in the Stern layer is additionally imposed [165]:

$$\begin{aligned} \mathbf{N}_s(\pm\, L-H,t\,) &= 0 \quad , \\ \nabla c_s\; -L \le x \le -L+H,t\; &= 0 \quad \text{and} \quad \nabla c_s\; L-H \le x \le L,t\; = 0. \end{aligned} \tag{A.8}$$

Continuity of the potential and current density at the Stern/diffuse layer interfaces $x = \pm(L-H)$ is enforced:

$$\begin{aligned} \psi\; \pm(L-H)^-,t\; &= \psi\; \pm(L-H)^+,t \\ \nabla\psi\; \pm(L-H)^-,t\; &= \nabla\psi\; \pm(L-H)^+,t \end{aligned} \tag{A.9}$$

The electric potential boundary condition imposed at the current collector/electrode interface depends on the experiment being simulated, for example, CV, EIS or GC, typically taking the form:

$$\psi\; -L-L_\mathrm{s},t\; = \psi_\mathrm{s}(t) \quad \text{and} \quad \psi\; L+L_\mathrm{s},t\; = -\psi_\mathrm{s}(t) \tag{A.10}$$

In CV, the potential is prescribed at the current collector/electrode interface as follows:

$$\psi_\mathrm{s}\; t\; = \begin{cases} \psi_\mathrm{max} - \nu[t - 2\; m-1\; \tau_\mathrm{CV} & \text{for} \quad 2\; m-1\; \tau_\mathrm{CV} \le t \le\; 2m-1\; \tau_\mathrm{CV} \\ \psi_\mathrm{min} + \nu[t - 2\; m-1\; \tau_\mathrm{CV} & \text{for} \quad 2m-1\; \tau_\mathrm{CV} \le t \le 2m\tau_\mathrm{CV} \end{cases} \tag{A.11}$$

where $\psi_{max} - \psi_{min}$ is the potential window, ν is the scan rate, m is the cycle number and $\tau_{CV} = \frac{\psi_{max} - \psi_{min}}{\nu}$ is half the time period.

In EIS, an oscillating potential is prescribed:

$$\psi_s\; t\; = \psi_\mathrm{DC} + \psi_0 e^{i2\pi ft} \quad . \tag{A.12}$$

where ψ_{DC} is the direct potential, ψ_0 is the amplitude of the AC potential oscillations and f is the frequency. In GCD, a constant surface current density, j_s, is imposed, corresponding to the Neumann boundary condition:

$$\nabla\psi_\mathrm{s}\; t\; = \begin{cases} -j_\mathrm{s}/\sigma_\mathrm{s} & \text{for} \quad m-1\; \tau_\mathrm{GCD} \le t \le\; m-1/2\;\; \tau_\mathrm{GCD} \\ j_\mathrm{s}/\sigma_\mathrm{s} & \text{for} \quad m-1/2\; \tau_\mathrm{GCD} \le t \le m\tau_\mathrm{GCD} \end{cases} \tag{A.13}$$

where τ_GCD is the time period.

A.3 Porous electrode theory

Porous electrode theory [163,272,273] is an extension of the transient model, in which the electrode domain is represented as a superposition of solid- (s) and electrolyte- (l) phase continua, responsible for electronic and ionic transport, respectively. The effective transport properties of the two phases are most commonly calculated by Bruggeman's correction, which accounts for the porosity, ε_{e}, (the proportion of volume taken up by the liquid phase) and tortuosity (the degree of lengthening of ion paths) of the porous network [273]:

$$\sigma^{\mathrm{E}}_{\mathrm{s,eff}} = \sigma^{\mathrm{E}}_{\mathrm{s}}\ 1-\varepsilon_{\mathrm{e}}\ ^{1.5} \quad , \tag{A.14}$$

$$\kappa_{s,\mathrm{eff}} = \kappa_s \varepsilon_{\mathrm{e}}^{1.5} \quad , \tag{A.15}$$

$$D_{s,\mathrm{eff}} = D_s \varepsilon_{\mathrm{e}}^{1.5} \quad . \tag{A.16}$$

It should be noted that the general form of the correction above uses an exponent value of 1.5, derived from the analysis of spherical particle networks; however, the exponent is sometimes used as a fitting parameter to ensure correlation with experimental measurements [254].

The corresponding solid- and electrolyte-phase potentials and current densities in the electrode domain are assumed continuous and defined as:

$$j_{\mathrm{s}} = -\sigma^{\mathrm{E}}_{\mathrm{s,eff}} \nabla \psi_{\mathrm{s}} \quad , \tag{A.17}$$

$$j_{\mathrm{l}} = -F \sum\ z_s D_{s,\mathrm{eff}} \nabla c_s - \kappa_{s,\mathrm{eff}} \nabla \psi_{\mathrm{l}} \quad . \tag{A.18}$$

Thus, the solid phase potential is defined over the two electrode domains, while the liquid phase potential is defined over all three domains. Discontinuities in the spatial variation of electrolyte concentration are neglected. Electroneutrality is satisfied through:

$$\nabla \cdot j_{\mathrm{s}} + \nabla \cdot j_{\mathrm{l}} = 0 \quad , \tag{A.19}$$

$$\nabla \cdot j_{\mathrm{s}} = -a j_n \quad , \tag{A.20}$$

where a is the pore wall surface area per unit volume of electrode and j_n is the average transfer current density from the electrolyte to the solid phase (also pore wall flux). The latter is calculated from the double layer capacitance (per unit interfacial area) of the electrode active material and the overpotential:

$$j_n = -\mathrm{C}_{\mathrm{DL}} \frac{\partial\ \psi_{\mathrm{s}} - \psi_{\mathrm{l}}}{\partial t} \quad . \tag{A.21}$$

The mass conservation equation in the electrolyte phase of the electrode becomes:

$$\varepsilon_{\mathrm{e}} \frac{\partial c_i}{\partial t} = a \mathbf{N}_n - \nabla \cdot \mathbf{N}_i \quad , \tag{A.22}$$

where $\mathbf{N}_n$ is the average flux due to double layer charging [186].

B Boundary conditions in mesoscale unit cells

B.1 Implementation of periodic boundary conditions

The elastic deformations of the mesoscale periodic unit cells studied in Chapters 4 and 5 were simulated through periodic boundary conditions, implemented as multi-point constraint equations. Table B.1 and Table B.2 list the equations used to simulate the principal tensile and shear strains, respectively.

Table B.1. Periodic boundary conditions used to simulate principal tensile strains.

Face pair	ε_{11}	ε_{22}	ε_{33}
x^+/x^-	$u_1^{x^-} = u_1^{x^+} + \varepsilon_{11} L_x$ $u_2^{x^-} = u_2^{x^+} + a_2$ $u_3^{x^-} = u_3^{x^+} + a_3$	$u_1^{x^-} = u_1^{x^+} + a_1$ $u_2^{x^-} = u_2^{x^+} + \varepsilon_{22} L_y$ $u_3^{x^-} = u_3^{x^+} + a_3$	$u_1^{x^-} = u_1^{x^+} + a_1$ $u_2^{x^-} = u_2^{x^+} + a_2$ $u_3^{x^-} = u_3^{x^+} + a_3$
y^+/y^-	$u_1^{y^-} = u_1^{y^+} + b_1$ $u_2^{y^-} = u_2^{y^+} + b_2$ $u_3^{y^-} = u_3^{y^+} + b_3$	$u_1^{y^-} = u_1^{y^+} + b_1$ $u_2^{y^-} = u_2^{y^+} + b_2$ $u_3^{y^-} = u_3^{y^+} + b_3$	$u_1^{y^-} = u_1^{y^+} + b_1$ $u_2^{y^-} = u_2^{y^+} + b_2$ $u_3^{y^-} = u_3^{y^+} + b_3$
z^+/z^-	–	–	$u_3^{z^+} = u_3^{z^-} + \varepsilon_{33} L_z$

Table B.2. Periodic boundary conditions used to simulate principal shear strains.

Face pair	γ_{12}	γ_{13}	γ_{23}
x^+/x^-	$u_1^{x^-} = u_1^{x^+} + a_1$ $u_2^{x^-} = u_2^{x^+} - \frac{\gamma_{12}}{2} L_x$ $u_3^{x^-} = u_3^{x^+} + a_3$	$u_1^{x^-} = u_1^{x^+} + a_1$ $u_2^{x^-} = u_2^{x^+} + a_2$ $u_3^{x^-} = u_3^{x^+} - \frac{\gamma_{13}}{2} L_x$	$u_1^{x^-} = u_1^{x^+} + a_1$ $u_2^{x^-} = u_2^{x^+} + a_2$ $u_3^{x^-} = u_3^{x^+} + a_3$
y^+/y^-	$u_1^{y^-} = u_1^{y^+} - \frac{\gamma_{12}}{2} L_y$ $u_2^{y^-} = u_2^{y^+} + b_2$ $u_3^{y^-} = u_3^{y^+} + b_3$	$u_1^{y^-} = u_1^{y^+} + b_1$ $u_2^{y^-} = u_2^{y^+} + b_2$ $u_3^{y^-} = u_3^{y^+} + b_3$	$u_1^{y^-} = u_1^{y^+} + b_1$ $u_2^{y^-} = u_2^{y^+} + b_2$ $u_3^{y^-} = u_3^{y^+} - \frac{\gamma_{23}}{2} L_y$
z^+/z^-	–	$u_1^{z^+} = u_1^{z^-} + \frac{\gamma_{13}}{2} L_z$	$u_2^{z^+} = u_2^{z^-} + \frac{\gamma_{23}}{2} L_z$

B.2 Effect of through-thickness boundary conditions

The responses of the CGC STR and C*GC* STR models with free lateral surfaces (F) were compared to those of the models with (i) a combination of a symmetric and a free lateral surface (S), and (ii) lateral surfaces linked by a periodic boundary condition (P). These results are presented in Table B.3 and Figure B.1. The effect of the out-of-plane boundary conditions depended on the material and ply offset configuration, though the apparent laminate stiffness generally increased. In the tensile case, the largest change in modulus was observed for the anti-symmetric IP model, while under in-plane shear, both the IP and 90°OP models were similarly affected. In both loading conditions, the symmetric 180°OP model was negligibly changed. This relative insensitivity to out-of-plane boundary conditions was attributed to the absence of bending-extension coupling in this symmetric laminate [274].

Table B.3. Predicted homogenised tensile and in-plane shear moduli for the SSC laminates with free surface (F), symmetry (S) and periodicity (P) out-of-plane boundary conditions.

Laminate type	Boundary condition	E_{11} (GPa)				G_{12} (GPa)			
		IP	90°OP	180°OP	Δ_{max} (%)	IP	90°OP	180°OP	Δ_{max} (%)
CGC STR	F	38.4	44.5	39.3	16.0	2.7	2.7	2.8	1.1
	S	43.6	47.9	44.7	9.8	2.9	2.9	3.0	1.5
	P	45.2	45.6	46.5	2.9	2.7	2.7	2.7	0.0
C*GC* STR	F	44.3	48.7	45.1	9.8	7.7	7.8	8.2	6.0
	S	49.8	52.4	50.5	5.2	10.8	10.8	11.6	6.8
	P	49.3	49.7	50.5	2.5	7.5	7.6	7.5	0.3

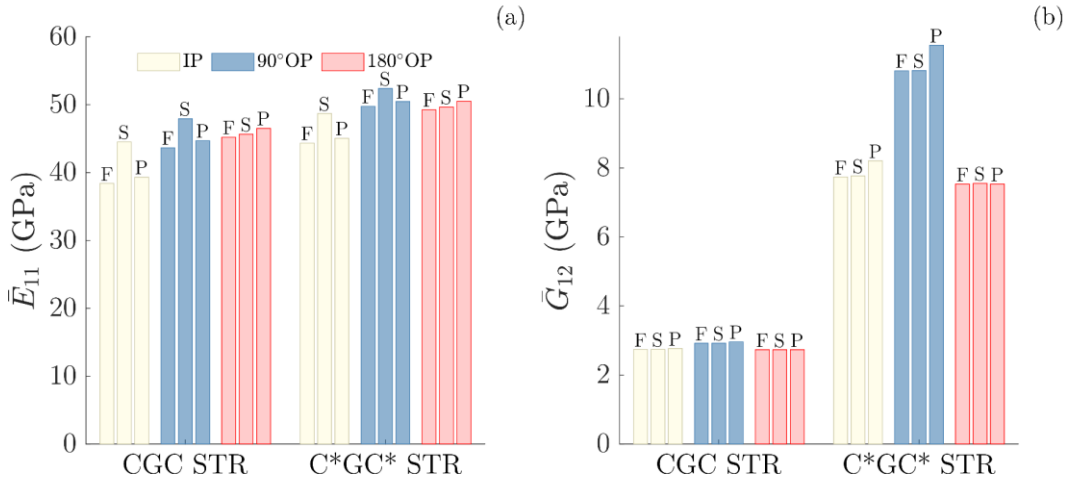

Figure B.1. Predicted homogenised (a) tensile and (b) in-plane shear moduli, for the CGC STR and C*GC* STR laminates with free surface (F), symmetry (S) and periodicity (P) out-of-plane boundary conditions.

C Supplementary characterisation of CAG-modified carbon fabric and CAG monoliths

C.1 Compaction of dry fabrics: cycling tests

Cyclic compaction experiments were performed on single layers of the C, G and C* fabrics (Table 4.1). The experimental procedure detailed in Section 4.2.1 was used with the following exceptions: the test procedure consisted of three loading-unloading cycles, with a linear loading ramp to a prescribed maximum load and linear unloading to zero-displacement; the load rate was 5 mm/min; three specimens were tested per fabric.

In the C* tests, the thickness was obtained from the crosshead displacement (corrected for the machine compliance), while in the rest, it was directly measured by the video gauge system. Both methods showed excellent repeatability, therefore representative compressibility curves are presented (Figure C.1). Significant softening in compressibility was observed in the C and G fabrics, compared to C*. For the latter, the second and third cycles were almost identical, unlike the other fabrics, whose relaxation continued, indicating a different softening mechanism.

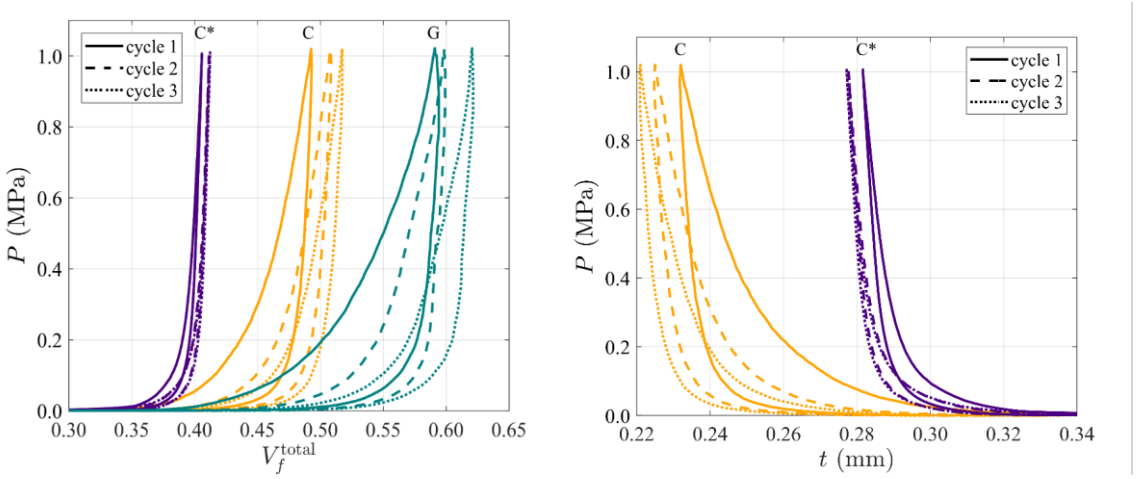

Figure C.1. Representative cyclic compressibility curves (three cycles) for the C, C* and G fabrics.

After the tests no obvious damage was observed with the naked eye in any of the specimens, however when C* specimens were removed, some CAG residue was left on the platens (note the platens were wiped clean between tests). To investigate this issue further, scanning electron microscopy was performed on a pristine and compacted C* sample (Figure C.2).

Qualitative observations revealed no substantial change following compaction in the quantity or size of the transverse cracks on the yarn surfaces, however interstitial void regions appeared to have been enlarged, as the observed residue would support. It was concluded that damage to the CAG, rather than relaxation of the fibre architecture, would have been the primary cause of softening of the C* fabric response, explaining why relaxation did not continue significantly after the second cycle.

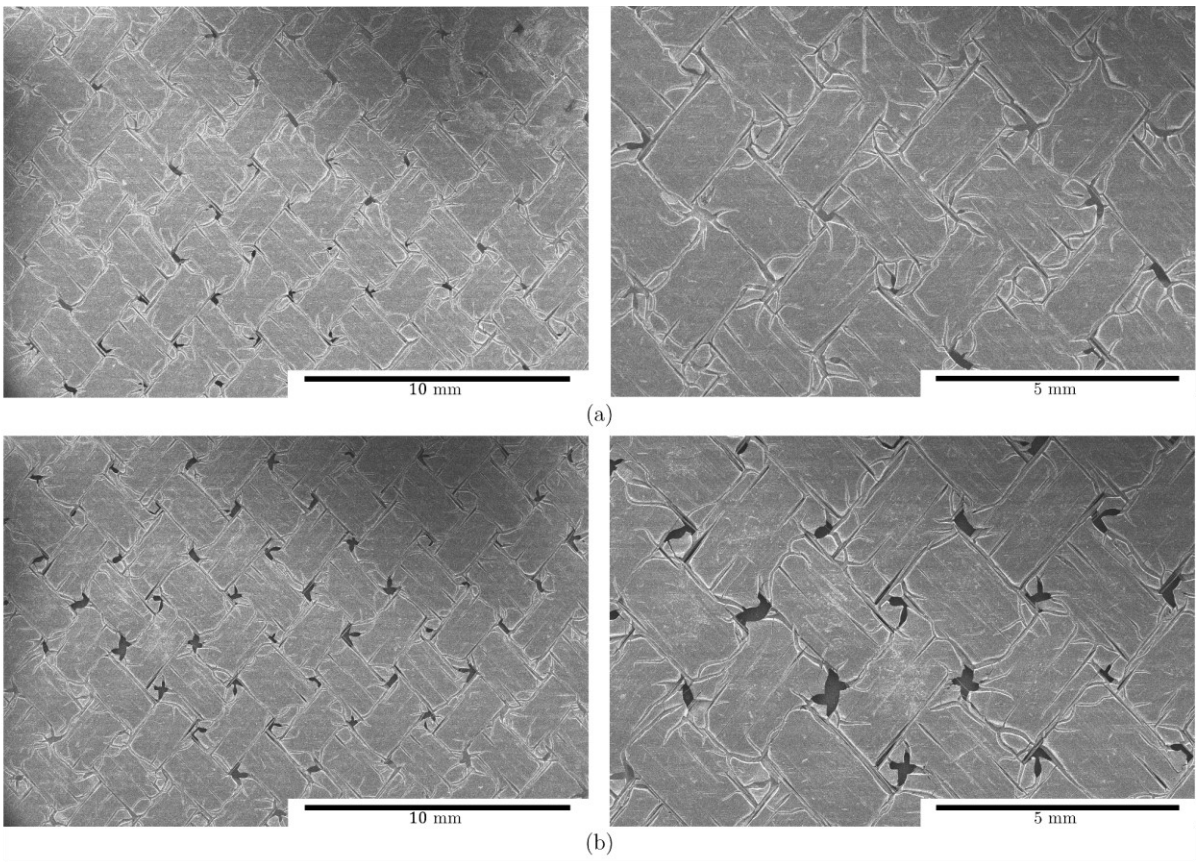

Figure C.2. Scanning electron micrographs of C* fabric (a) before, and (b) after cyclic compression tests.

C.2 Preliminary microindentation tests on CAG-modified carbon fabric

Preliminary indentations were performed on CAG-modified spread tow carbon fibre dry fabric (Textreme-CAG, Figure C.3(a) and (b)). Both a deadweight micro-hardness tester (Wilson Hardness Tukon 1102) and the instrumented nano-indenter (Section 5.2.3) were used at maximum loads between 100 and 500 mN. Several challenges to performing and interpreting indentations were identified: pre-damage made it difficult to identify suitable regions to probe; test repeatability was poor due to the heterogeneous sample architecture and presence of defects – for a given maximum load, the indentation size and damage varied dramatically; discontinuities in the recorded response indicated cracking and delamination, which was confirmed by scanning electron microscopy (Figure C.3(c) and (d)). These specimens were therefore deemed unacceptable for characterisation of the elastic modulus of CAG.

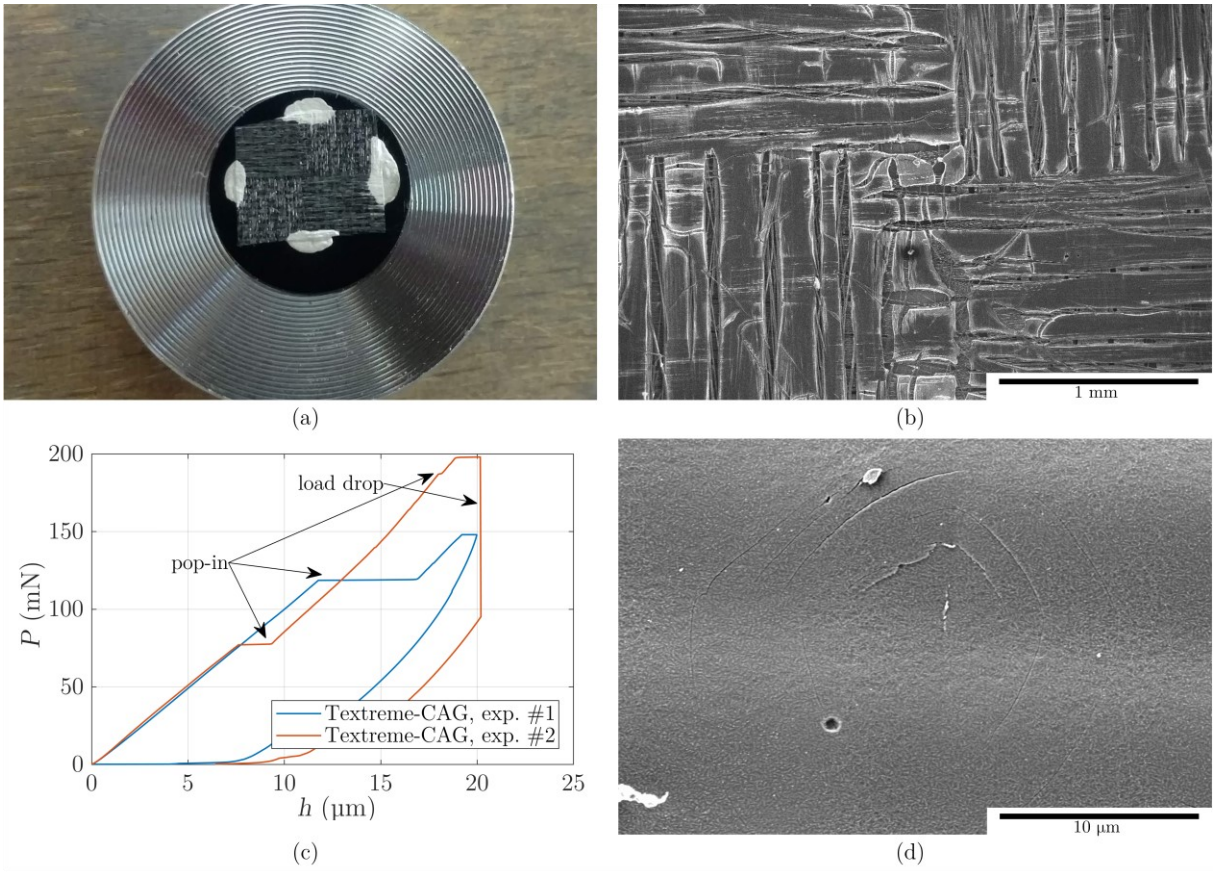

Figure C.3. (a) Textreme-CAG specimen, (b) scanning electron micrograph of specimen surface, (c) typical indentation force–displacement curves, (d) scanning electron micrograph of indentation imprint (P_{max} = 250 mN) showing radial cracking.

C.3 Manufacture and physical characterisation of monolithic CAG samples

The resorcinol-formaldehyde (RF) sol for the production of CAG-modified carbon fibre fabric samples has been described elsewhere in detail [90]. Modifications to that procedure are as follows for the production of monolithic carbon aerogel samples. Instead of a premixed solution, resorcinol (Sigma-Aldrich (GB), ReagentPlus®, 99%, 307521) and formaldehyde (Sigma-Aldrich, ACS reagent, 37 wt. % in H_2O, containing 10-15% methanol as stabilizer to prevent polymerization, 252549) were used directly from the manufacturers, in a R:F molar ratio of 1:2, and HPLC grade water (Sigma-Aldrich (GB), 270733) was added to obtain a 40 wt. % RF in the final solution. The RF, water mix was stirred until clear (ca. 15 min), then potassium hydroxide (Sigma-Aldrich (GB), ACS reagent, ≥85%, 221473), which acts as the catalyst (Cat), was added dropwise in a 1 M (aq) solution to achieve a R:Cat ratio of 50:1. The solution (900 ml in a sealed vessel) was then stirred continuously using a large magnetic stirrer bar at least 200 RPM for 6 h, maintaining a temperature between 10 °C and 20 °C for the first 3 h (to prevent thermal runaway) through the use of an ice bath, or 20 °C through the use of a jacket reaction vessel and refrigerated/heating circulating bath unit (Huber (DE), Ministat 230).

The sol was then heated to 30 °C for 3 h, and transferred to a fridge at 5 °C for 24 h (if made in the jacketed vessel the sol was cooled to 5 °C before transferring). Monolithic cubic samples were formed by pipetting in a silicon ice cube tray (OXO (GB), Covered Silicone Ice Cube Tray, 11154300MLNYKEU). The ice cube tray was sealed using a vacuum bagger (Buffalo (GB), Light duty chamber vacuum pack machine CD969) under reduced pressure (ca. 500 mbar). The sol was aged in the moulds contained within the sealed bags following the same procedure as previously described [14], 24 h at room temperature (RT), 24 h at 50 °C, and 24 h at 90 °C, in a programmable vacuum oven (Memmert VO400) at reduced pressure (500 mbar). Once aged, the samples were slowly cooled to RT in the oven, removed from the bag, and the mould was then placed in a bath of acetone to allow solvent exchange. Fresh acetone was replenished at least three times, for a minimum soak time of 24 h, whilst keeping the carbon aerogel precursor wet and submerged at all times. Samples were kept submerged until transferring to a CO_2 critical point drying (CPD), Leica Microsystems (GB) EM CPD300. In the CPD, samples were submerged in fresh HPLC

grade acetone, and then dried. Once dry, samples were removed from the CPD and kept at RT in ambient conditions until pyrolysis.

Pyrolysis was carried out in a high temperature furnace with an Inconel reaction chamber as previously described [90], on smooth alumina plates (Almath Crucibles Ltd (GB), 99%, SUB360360) at a heating rate of approximately 1-2 °C/min until 800 °C was achieved. Samples were then kept at 800 °C for an hour, before being cooled to RT overnight (ca. 15 h) in the furnace chamber. All pyrolysis processes were carried out under flow of nitrogen, 2 l/min at 2 bar, with the chamber purged at a higher flow rate of 4 l/min for a minimum of 30 minutes before heating commenced.

The weight of the CAG monolith sample used in nanoindentation tests was 0.7918 g before pyrolysis (after CPD) and 0.4077 g after pyrolysis, corresponding to a 51.5% yield. Density measurements were performed on samples from an equivalent batch using helium gas displacement (AccuPyc, Micromeritics Instruments) and solid particle displacement (GeoPyc, Micromeritics Instruments). Envelope and skeletal densities of 0.64 g/cm^3 and 1.21 g/cm^3, respectively, were obtained for the CAG monolith, corresponding to a total porosity of 47%.

C.4 Manufacture of selectively CAG-modified carbon fabric

A novel manufacturing method has been recently developed (unpublished work of D. B. Anthony and M. Turk), which allows carbon fabric to be selectively infused with CAG, leaving regions of the carbon fabric free of aerogel. This is achieved by using polylactic acid (PLA) as a masking material to prevent subsequent infusion with CAG precursor. The processing steps are outlined as follows.

PLA masking sheets are prepared by additive manufacturing. A pair of masking sheets is placed coincidently on either side of the as-received carbon fabric and the stack is placed in a hot press at 160°C and 0.4 MPa. The PLA-infused carbon fabric is post-infused with the resorcinol-formaldehyde precursor by resin infusion under flexible tooling. The sample is pyrolised in a furnace as described in Section C.3. At temperatures above 400°C the PLA mask is decomposed, leaving regions of pyrolised carbon fibres without CAG.

D Ion transport element implementation

D.1 Formulation of finite element equations

Eqns. (7.1) and (7.2) represent the system residuals. The weighted residuals have been derived by Lim [164] using Galerkin's method, outlined in the following. The method involves multiplying the residual statements by the arbitrary variations $\delta\psi$ and δc_s, and integrating over the domain V, such that the solution is sought in an integral sense:

$$\int \left(\varepsilon_0 \varepsilon_{\mathrm{r}} \nabla^2 \psi + \sum_s \; e z_s c_s \right) \delta\psi \; dV = 0 \tag{D.1}$$

$$\int \left(\frac{\partial c_s}{\partial t} + \nabla \cdot \mathbf{N}_s \right) \delta c_s \; dV = 0 \tag{D.2}$$

Applying the divergence theorem to the first term in Eqn. (D.1) and second term in Eqn. (D.2), the following integral equations are obtained:

$$\int \sum_s \; \delta\psi (e z_s c_s) \, dV + [\delta\psi (\varepsilon_0 \varepsilon_{\mathrm{r}} \nabla\psi)]_{\mathbf{x_1}}^{\mathbf{x_2}} - \int \delta(\nabla\psi) \; \varepsilon_0 \varepsilon_{\mathrm{r}} \nabla\psi \quad dV = 0 \tag{D.3}$$

$$\int \delta c_s c_s \; dV + [\delta c_s \mathbf{N}_s]_{\mathbf{x_1}}^{\mathbf{x_2}} - \int \delta(\nabla c_s) \mathbf{N}_s \, dV = 0 \tag{D.4}$$

Substituting the field approximation

(7.6) into the weak forms (D.3) and (D.4), and factoring out the arbitrary variations, the discretised finite element residual equations are obtained:

$$\mathbf{R}_{\psi}^{(e)} = \int \sum_s \; \mathbf{N}^{\mathrm{T}} e z_s c_s \; dV + [\mathbf{N}^{\mathrm{T}} \varepsilon_0 \varepsilon_{\mathrm{r}} \nabla\psi \,]_{\mathbf{x_1}}^{\mathbf{x_2}} - \int \mathbf{B}^{\mathrm{T}} \; \varepsilon_0 \varepsilon_{\mathrm{r}} \nabla\psi \;\; dV = 0 \tag{D.5}$$

$$\mathbf{R}_{c_s}^{(e)} = \int \mathbf{N}^{\mathrm{T}} c_s \; dV + [\mathbf{N}^{\mathrm{T}} \mathbf{N}_s]_{\mathbf{x_1}}^{\mathbf{x_2}} - \int \mathbf{B}^{\mathrm{T}} \mathbf{N}_s \, dV = 0 \tag{D.6}$$

Applying the finite element interpolation to the element residuals (D.5) and (D.6), the element equations are rewritten in the following algebraic form, following Lim [164]:

$$\mathbf{R}^{\,e} = \mathbf{M}^{(e)} \mathbf{q}^{(e)} - (\mathbf{G}^{\,e} - \mathbf{F}^{\,e}) \tag{D.7}$$

The expanded components of the discretised finite element equations are expressed as:

$$\mathbf{M}_{c_s}^{\,e} \, \mathbf{q}^{(e)} = \int \mathbf{N}^{\mathbf{T}} c_s \; dV = \int \mathbf{N}^{\mathbf{T}} \mathbf{N} \mathbf{c}_s^{(e)} \; dV \tag{D.8a}$$

$$\mathbf{G}_{\psi}^{\,e} = \int \mathbf{B}^{\mathrm{T}} \; \varepsilon_0 \varepsilon_{\mathrm{r}} \nabla\psi \;\; dV + \int \sum_s \; \mathbf{N}^{\mathrm{T}} e z_s c_s \; dV \tag{D.8b}$$

$$\mathbf{G}_{c_s}^{\,e} = \int \mathbf{B}^{\mathrm{T}} \mathbf{N}_s \, dV = - \int \mathbf{B}^{\mathrm{T}} (D_s \nabla c_s) dV - \int \mathbf{B}^{\mathrm{T}} (z_s u_s F c_s \nabla\psi) dV \tag{D.8c}$$

$$\mathbf{F}_{\psi}^{\,e} = [\mathbf{N}^{\mathrm{T}} \varepsilon_0 \varepsilon_{\mathrm{r}} \nabla\psi]_{\mathbf{x_1}}^{\mathbf{x_2}} \quad \text{and} \quad \mathbf{F}_{c_s}^{\,e} = [\mathbf{N}^{\mathrm{T}} \mathbf{N}_s]_{\mathbf{x_1}}^{\mathbf{x_2}} \tag{D.8d}$$

D.2 Ion transport finite element matrices

$\boldsymbol{M}^{(e)}$ is the damping matrix associated with mass diffusion. For the eight-node 2D ion transport element, it is a 24×24 matrix. It was obtained from the vector of shape functions as follows:

$$\mathbf{M}^{e} = \mathbf{N}^{\mathbf{T}}\mathbf{N} = \begin{Bmatrix} 0 & 0 & 0 & & 0 & 0 & 0 \\ 0 & \int N_1^2\,dV & 0 & \cdots & 0 & \int N_1 N_\alpha\,dV & 0 \\ 0 & 0 & \int N_1^2\,dV & & 0 & 0 & \int N_1 N_\alpha\,dV \\ & \vdots & & \ddots & & \vdots & \\ 0 & 0 & 0 & & 0 & 0 & 0 \\ 0 & \int N_1 N_\alpha\,dV & 0 & \cdots & 0 & \int N_\alpha^2\,dV & 0 \\ 0 & 0 & \int N_1 N_\alpha\,dV & & 0 & 0 & \int N_\alpha^2\,dV \end{Bmatrix} . \quad \text{(D.9)}$$

The repeating unit of the mass matrix can be written in index notation:

$$\mathbf{M}_{ij}^{(e)} = \begin{bmatrix} 0 & 0 & 0 \\ 0 & \int N_i N_j dV & 0 \\ 0 & 0 & \int N_i N_j dV \end{bmatrix} , \quad \text{(D.10)}$$

where $i, j = 1,2 \ldots 8$. The element $\mathbf{B}$ matrix was obtained from the spatial derivatives of the shape functions:

$$\mathbf{B} = \begin{bmatrix} N_{1,x} & 0 & 0 & & N_{\alpha,x} & 0 & 0 \\ 0 & N_{1,x} & 0 & & 0 & N_{\alpha,x} & 0 \\ 0 & 0 & N_{1,x} & \cdots & 0 & 0 & N_{\alpha,x} \\ N_{1,y} & 0 & 0 & & N_{\alpha,y} & 0 & 0 \\ 0 & N_{1,y} & 0 & & 0 & N_{\alpha,y} & 0 \\ 0 & 0 & N_{1,y} & & 0 & 0 & N_{\alpha,y} \end{bmatrix} , \quad \text{(D.11)}$$

where $N_{i,x} = \frac{\partial N_i}{\partial x}$. The matrix $\partial\mathbf{G}/\partial\mathbf{q}$ is 24×24 and was obtained from $\mathbf{B}^{\mathrm{T}}\mathbf{B}$, with repeating unit:

$$\mathbf{B}^{\mathrm{T}}\mathbf{B}_{ij} = \begin{bmatrix} N_{1,x}N_{1,x} + N_{1,y}N_{1,y} & 0 & 0 \\ 0 & N_{1,x}N_{1,x} + N_{1,y}N_{1,y} & 0 \\ 0 & 0 & N_{1,x}N_{1,x} + N_{1,y}N_{1,y} \end{bmatrix} , \quad \text{(D.12)}$$

$\partial\mathbf{G}/\partial\mathbf{q}$ is obtained as:

$$\frac{\partial \mathbf{G}_{\psi}^{(e)}}{\partial \mathbf{q}} = \int \varepsilon_0 \varepsilon_{\mathrm{r}} \mathbf{B}^{\mathrm{T}} \frac{\partial \nabla \psi}{\partial \mathbf{q}}\, dV + \int \sum_s \mathbf{N}^{\mathrm{T}} e z_s \frac{\partial c_s}{\partial \mathbf{q}}\, dV = \int \varepsilon_0 \varepsilon_{\mathrm{r}} \mathbf{B}^{\mathrm{T}} \mathbf{B} \frac{\partial \boldsymbol{\psi}^{\,e}}{\partial \mathbf{q}}\, dV + \int e z_s \mathbf{N}^{\mathrm{T}} \mathbf{N} \frac{\partial \mathbf{c}_s^{\,e}}{\partial \mathbf{q}} dV$$

$$\frac{\partial \mathbf{G}_{c_s}^{\,e}}{\partial \mathbf{q}} = \int \mathbf{B}^{\mathrm{T}} \frac{\partial \mathbf{N}_s}{\partial \mathbf{q}} dV = -\int D_s \mathbf{B}^{\mathrm{T}} \frac{\partial \nabla c_s}{\partial \mathbf{q}} dV - \int z_s u_s F \mathbf{B}^{\mathrm{T}} \frac{\partial\, c_s \nabla \psi}{\partial \mathbf{q}} dV == -\int D_s \mathbf{B}^{\mathrm{T}} \mathbf{B} \frac{\partial \mathbf{c}_s^{\,e}}{\partial \mathbf{q}} dV - \int z_s u_s F \mathbf{B}^{\mathrm{T}} \mathbf{B} c_s \frac{\partial \boldsymbol{\psi}^{\,e}}{\partial \mathbf{q}} dV - \int z_s u_s F \mathbf{B}^{\mathrm{T}} \mathbf{N} \nabla \psi \frac{\partial \mathbf{c}_s^{\,e}}{\partial \mathbf{q}} dV.$$

Its repeating unit is rewritten in vector form as:

$$\frac{\partial \mathbf{G}}{\partial \mathbf{q}}_{ij} = \begin{bmatrix} \varepsilon_0 \varepsilon_{\mathrm{r}} \int (N_{i,x} N_{j,x} + N_{i,y} N_{j,y}) dV & e z_1 \int N_i N_j\, dV & e z_2 \int N_i N_j\, dV \\ -z_1 u_1 F \int c_1 (N_{i,x} N_{j,x} + N_{i,y} N_{j,y}) dV & -D_1 \int \big(N_{i,x} N_{j,x} + N_{i,y} N_{j,y}\big) dV & 0 \\ & -z_1 u_1 F \int N_i (N_{j,x} \psi_x + N_{j,y} \psi_y) dV & \\ -z_2 u_2 F \int c_2 (N_{i,x} N_{j,x} + N_{i,y} N_{j,y}) dV & 0 & -D_2 \int \big(N_{i,x} N_{j,x} + N_{i,y} N_{j,y}\big) dV \\ & & -z_2 u_2 F \int N_i (N_{j,x} \psi_x + N_{j,y} \psi_y) dV \end{bmatrix}. \tag{D.13}$$

The load vectors are 24×1. $\boldsymbol{F}^{(e)}$ is the vector of externally applied loads (nodal forces), associated with electric potential and concentration boundary conditions at the mesh boundaries (see Section 7.2.2). $\boldsymbol{G}^{(e)}$ is the internal load vector, defined as:

$$\mathbf{G}_{\psi}^{e} = \int \mathbf{B}^{\mathrm{T}}\ \varepsilon_0\varepsilon_{\mathrm{r}}\nabla\psi\ \ dV + \int \sum_{s}\ \mathbf{N}^{\mathrm{T}} e z_s c_s\ \ dV \quad ,$$

$$\mathbf{G}_{c_s}^{e} = \int \mathbf{B}^{\mathrm{T}}\mathbf{N}_s\, dV = -\int \mathbf{B}^{\mathrm{T}}\ D_s\nabla c_s\ \ dV - \int \mathbf{B}^{\mathrm{T}}\ z_s u_s F c_s \nabla\psi\ \ dV \quad . \tag{D.14}$$

The repeating unit of the internal load vector can be written in index notation:

$$\mathbf{G}_{ij}^{(e)} = \begin{Bmatrix} \varepsilon_0\varepsilon_{\mathrm{r}} \int (N_{i,x}\psi_x + N_{i,y}\psi_y)\, dV + e\int N_i(z_1c_1 + z_2c_2)\, dV \\ -D_1 \int (N_{i,x}c_{1,x} + N_{i,y}c_{1,y})dV - z_1u_1F\int c_1(N_{i,x}\psi_x + N_{i,y}\psi_y)dV \\ -D_2 \int (N_{i,x}c_{2,x} + N_{i,y}c_{2,y})dV - z_2u_2F\int c_2(N_{i,x}\psi_x + N_{i,y}\psi_y)dV \end{Bmatrix} \quad . \tag{D.15}$$

D.3 Numerical solution of the finite element equations

The derivation of the incremental solution using a backward difference scheme has been presented by Lim [164], and is summarised here. The time incrementation reads:

$$\mathbf{q}_{t+1} = \frac{\mathbf{q}_{t+1} - \mathbf{q}_t}{\Delta t_{t+1}} = \frac{\Delta\mathbf{q}_{t+1}}{\Delta t_{t+1}} \tag{D.16}$$

where subscripts t and $t+1$ denote consecutive time steps and Δt is the time increment between them. The residual equation is rewritten for the $t+1$ increment:

$$\mathbf{R}_{t+1}^{(e)} = \mathbf{M}^{(e)}\mathbf{q}_{t+1}^{(e)} - (\mathbf{G}_{t+1}^{e} - \mathbf{F}_{t+1}^{(e)}) \tag{D.17}$$

It is necessary to linearise the nonlinear terms in $\boldsymbol{G}^{(e)}$ and $\mathbf{F}^{e}$, via a Taylor expansion:

$$\begin{aligned} \mathbf{G}_{t+1}^{e} &= \mathbf{G}_{t}^{e} + \frac{\partial \mathbf{G}^{e}}{\partial \mathbf{q}}\Delta\mathbf{q}_{t+1} \\ \mathbf{F}_{t+1}^{e} &= \mathbf{F}_{t}^{e} + \frac{\partial \mathbf{F}^{e}}{\partial \mathbf{q}}\Delta\mathbf{q}_{t+1} = \mathbf{F}_{t}^{e} \end{aligned} \tag{D.18}$$

Substituting the above into Eqn. (D.17) and collecting terms, the incremental solution reads:

$$\overline{\mathbf{M}}_{t+1}^{(e)}\Delta\mathbf{q}_{t+1} = \overline{\mathbf{F}}_{t+1}^{(e)} \quad ,$$

where

$$\begin{cases} \overline{\mathbf{M}}_{t+1}^{(e)} = \mathbf{M}^{(e)} - \Delta t_{t+1}\dfrac{\partial \mathbf{G}^{e}}{\partial \mathbf{q}} \\ \overline{\mathbf{F}}_{t+1}^{(e)} = \Delta t_{t+1}(\mathbf{G}_{t}^{e} - \mathbf{F}_{t}^{e}) \end{cases} \tag{D.19}$$

D.4 Ion transport user-defined element subroutine

```
SUBROUTINE UEL(RHS,AMATRX,SVARS,ENERGY,NDOFEL,NRHS,NSVARS,PROPS, NPROPS,COORDS,
MCRD,NNODE,U,DU,V,A,JTYPE,TIME,DTIME,KSTEP,KINC,JELEM,PARAMS, NDLOAD,JDLTYP,
ADLMAG,PREDEF,NPREDF,LFLAGS,MLVARX,DDLMAG,MDLOAD,PNEWDT,JPROPS,NJPROP,PERIOD)
C   2D CONTINUUM UEL FOR TRANSIENT ION TRANSPORT 8-NODE BI-QUAD LAGRANGE, 3X3 GAUSS
        PTS
      INCLUDE 'aba_param.inc'
      PARAMETER(ZERO=0.D0,HALF=0.5D0,ONE=1.D0,TWOHUN=200.D0,FIVHUN=500.D0,CONDUC=204.D0)
      DIMENSION
        RHS(MLVARX,*),AMATRX(NDOFEL,NDOFEL),SVARS(NSVARS),ENERGY(8),PROPS(*),COORDS(MC
        RD,NNODE),U(NDOFEL),DU(MLVARX,*),V(NDOFEL),A(NDOFEL),TIME(2),PARAMS(3),JDLTYP(MDLO
        AD,*),ADLMAG(MDLOAD,*),DDLMAG(MDLOAD,*),PREDEF(2,NPREDF,NNODE),LFLAGS(*),JPROPS(*
        )
      DIMENSION GPX(9),GPY(9),GWEI(9),N(8),DNDX(8),DNDY(8),DNDXI(8),DNDETA(8),IFACE(9),GWE(3),
        NUMGPBFACE(3), NUMGPTFACE(3), NUMGPLFACE(3), NUMGPRFACE(3)
      DOUBLE PRECISION D1,D2,EL,Z1,Z2,FAR,EPS0,EPSR,MOB1,MOB2, SIGEL, DGDU(NDOFEL,NDOFEL)
      INTEGER i
      DATA IFACE/1,5,2,6,3,7,4,8,1/
      DATA NUMGPBFACE/1,4,7/
      DATA NUMGPRFACE/7,8,9/
      DATA NUMGPTFACE/9,6,3/
      DATA NUMGPLFACE/3,2,1/
C ---------------------------------------------------------------------------------------
C     -----ABAQUS VARIABLE DECLARATION-----
C     WRITE ONLY VARIABLES:
C        RHS                    vector of residual nodal forces (1X24)
C        AMATRX                 element Jacobian/stiffness matrix (24X24)
C        SVARS                  solution-dependent variables
C        ENERGY
C     OPTIONAL:
C        STATEV
C        PNEWDT
C     READ ONLY ARRAYS:
C        PROPS                  array containing the real property values, length NPROPS
C        JPROPS                 array containing the integer property values, length NJPROP
C        COORDS(K1,K2)          K1th (original) coor of the K2th node of the element
C        U(K1)                  total values of the variables at the end of the current increment i.e. t+dt
C        DU(K1,KRHS)            incremental values of the variable for the current increment for the RHS

C        V(K1)                  1st time derivative, dU/dt, for implicit dynamics only LFLAGS(1)=11/12
C        A(K1)                  2nd time derivative, dU/dt, for implicit dynamics only FLAGS(1)=11/12
C        JDLTYP(K1,K2)          array of integers to define distributed load types
C        ADLMAG(K1,1)           total load magnitude of the K1th distributed load at end of current
          increment
C        DDLMAG(K1,1)           increments in the magnitudes of the distributed loads ^
C        PREDEF(K1,K2,K3)                array of values of predefined field variables
C        PARAMS                 parameters for solution procedure
C        LFLAGS                 array of flags to define the procedure type
C        TIME(1)                current value of step time
C        TIME(2)                current value of total time
C     READ ONLY SCALAR PARAMETERS:
C        DTIME                  time increment dt
C        PERIOD                 time period of the current step
C        NDOFEL                 number of degrees of freedom in the element =24
C        MLVARX                 dimensioning parameter used when several RHS vectors are used
C        NRHS                   n of RHS vectors =1
C        NSVARS                 n of sol-dependent vars
C        NPROPS                 n of real property values
```

```
C       NJPROP                  n of integer property values
C       MCRD                    user-defined max n of coordinates needed at any node point
C       NNODE                   user-defined n nodes on the element
C       JTYPE                   integer defining the element type
C       KSTEP                   current step number
C       KINC                    current increment number
C       JELEM                   user-assigned element number
C       NDLOAD                  ID number of distributed load and/or flux currently active
C       MDLOAD                  total number of distributed loads and/or fluxes
C       NPREDF                  n of predefined field variables
C     ------------------------------------------------------------------------------------------
C     -----  ADDITIONAL VARIABLE DECLARATION ----- [SI UNITS]
C     PSI, C1, C2               potential, conc1, conc3 at a Gauss pt at time t + dt  [V] and [mol/m3]
C     PSIOLD, C1OLD, C2OLD      value of ^ at time t
C     DPSIDX, DC1DX, DC2DX      value of derivative of ^ wrt x  [V/m]   SVARS 1,2
C     DPSIDY, DC1DY, DC2DY      value of derivative of ^ wrt y   SVARS 3,4
C     DPSIDT, DC1DT, DC2DT      value of derivative of ^ wrt to time   SVARS 5,6
C     DGDU                      DGDU matrix used to calculate AMATRX (24X24)
C     G                         G vector used to calculate RHS (FBAR) (24x1)
C     XI                        isoparametric coordinate, xi
C     ETA                               isoparametric coordinate, eta
C     GWE(3)                    Gauss weight in 1D
C     GWEI(9)                   Gauss weight in 2D (FOR ALL EACH INTEGRATION PTS OF THE
          ELEMENT)
C     WE(1)                     Gauss weight at each int point multiplied by Jacobian
C     N(8)                      interpolation functions
C     DNDX                      derivative of N wrt x
C     DNDY                      derivative of N wrt y
C     DNDXI                     derivative of N wrt xi
C     DNDETA                    derivative of N wrt eta
C     DETJACOB                  determinant of the Jacobian
C     SVARS(7,8)                ion flux density N1 [mol/m^2.s] in x, y
C     SVARS(9,10)               ion flux density N2 [mol/m^2.s] in x, y
C     SVARS(11,12)              current density [A/m^2] in x, y
C ------------------------------------------------------------------------------------------
C     ==================MATERIAL PROPERTY DEFINITION==================
C     -----  mm, g, ms, mA, K, mmol, cd
C      D1 = PROPS(1)
C      D2 = PROPS(2)
C      Z1 = PROPS(3)
C      Z2 = PROPS(4)
C      MOB1 = PROPS(5)
C      MOB2 = PROPS(6)
C      RHO = PROPS(7)
      D1 = 2.0e-6
      D2 = 2.0e-6
      Z1 = 1.0
      Z2 = -1.0
      CI0 = 1.0e-6
      RHO = 0.00152
      ABST = 300.0
      EL = 1.602e-13
      KB = 1.38065e-20
      FAR = 96485300
      EPS0 = 8.85e-6
      EPSR = 78.5
      SIGEL = 2000.0
      MOB1 = D1*Z1*EL/(KB*ABST*FAR)
      MOB2 = D2*Z2*EL/(KB*ABST*FAR)
C     ----- units consistent with Newman's Electrochemical Systems book -----
C     ----- mobility in units [(m2/V.s).(mol/C)] = [m2.mol/J.s]-----
C     ----- ionic conductivity in units [A/V.m=S/m] -----
```

```
C     ==================INITIALIZATION OF MATRICES (NRHS=1)==================
      DO 6 K1 = 1,NDOFEL
        RHS(K1,NRHS) = ZERO
      DO 4 K2 = 1,NDOFEL
        AMATRX(K2,K1) = ZERO
        DGDU(K2,K1) = ZERO
    4 CONTINUE
    6 CONTINUE
C     RUN IF CORRECT LFLAGS SET
      IF (LFLAGS(3).EQ.1) RETURN
C     NORMAL IMPLICIT TIME INCREMENTATION PROCEDURE. DEFINE AMATRX & RHS
      IF (LFLAGS(1).EQ.76 .OR. LFLAGS(1).EQ.77) THEN
C     COUPLED THERMAL-ELECTRICAL ANALYSIS, TRANSIENT: FIXED 76 / AUTOMATIC 77 dt
C     DETERMINE GAUSS POINT LOCATIONS
      CALL GSPT(GPX,GPY)
C     DETERMINE GAUSS WEIGHTS
      CALL GSWT(GWEI,GWE)
C     ==================ASSEMBLE AMATRX AND RHS==================
C     ===LOOP THROUGH INTEGRATION POINTS (GAUSS PTS) K===
      DO 300 K = 1,9
        XI = GPX(K)
        ETA = GPY(K)
        CALL DER(XI,ETA,GPX,GPY,GWEI,N,DNDX,DNDY,DNDXI,DNDETA,DXDXI,DXDETA,DYDXI,DYDETA,
                 AJACOB,COORDS,MCRD,NNODE)
C     INITIALISE DOF VALUES
        PSI =ZERO
        DPSIDX=ZERO
        DPSIDY=ZERO
        PSIOLD=ZERO
        C1 =ZERO
        DC1DX=ZERO
        DC1DY=ZERO
        C1OLD=ZERO
        C2 =ZERO
        DC2DX=ZERO
        DC2DY=ZERO
        C2OLD=ZERO
C       EVALUATE DOF VALUES & GRADIENTS @ t+dt AT GAUSS PT K
C       AND DOF VALUES @ t (OLD)
          DO I=1,8
          PSI=PSI+U(1+3*(I-1))*N(I)
          DPSIDX=DPSIDX+U(1+3*(I-1))*DNDX(I)
          DPSIDY=DPSIDY+U(1+3*(I-1))*DNDY(I)
          PSIOLD=PSIOLD+(U(1+3*(I-1))-DU(1+3*(I-1),NRHS))*N(I)
          C1=C1+U(2+3*(I-1))*N(I)
          DC1DX=DC1DX+U(2+3*(I-1))*DNDX(I)
          DC1DY=DC1DY+U(2+3*(I-1))*DNDY(I)
          C1OLD=C1OLD+(U(2+3*(I-1))-DU(2+3*(I-1),NRHS))*N(I)
          C2=C2+U(3+3*(I-1))*N(I)
          DC2DX=DC2DX+U(3+3*(I-1))*DNDX(I)
          DC2DY=DC2DY+U(3+3*(I-1))*DNDY(I)
          C2OLD=C2OLD+(U(3*I)-DU((3*I),NRHS))*N(I)
        END DO
C       EVALUATE TIME DERIVATIVES
        DPSIDT=(PSI-PSIOLD)/DTIME
        DC1DT=(C1-C1OLD)/DTIME
        DC2DT=(C2-C2OLD)/DTIME
C       SAVE GRADIENTS IN DOFS AS SVARS
        SVARS(1)=DPSIDX
        SVARS(2)=DPSIDY
        SVARS(3)=DC1DX
        SVARS(4)=DC1DY
```

```
      SVARS(5)=DC2DX
      SVARS(6)=DC2DY
C -----------------------------------------------------------------------------
C     EVALUATE M MATRIX
      WE=GWEI(K)*DETJACOB
      DO KI=1,8
      DO KJ=1,8
      AMATRX(2+3*(KI-1),2+3*(KJ-1)) = AMATRX(2+3*(KI-1),2+3*(KJ-1)) + WE*(N(KI)*N(KJ))
      AMATRX(3+3*(KI-1),3+3*(KJ-1)) = AMATRX(3+3*(KI-1),3+3*(KJ-1)) + WE*(N(KI)*N(KJ))
      END DO
      END DO
C     EVALUATE DGDU
      DO KI=1,8
      DO KJ=1,8
      DGDU(1+3*(KI-1),1+3*(KJ-1)) = DGDU(1+3*(KI-1),1+3*(KJ-1)) + EPS0*EPSR*WE*(DNDX(KI)*DNDX(KJ)
         + DNDY(KI)*DNDY(KJ))
      DGDU(1+3*(KI-1),2+3*(KJ-1)) = DGDU(1+3*(KI-1),2+3*(KJ-1)) + EL*Z1*WE*(N(KI)*N(KJ))
      DGDU(1+3*(KI-1),3+3*(KJ-1)) = DGDU(1+3*(KI-1),3+3*(KJ-1)) + EL*Z2*WE*(N(KI)*N(KJ))
      DGDU(2+3*(KI-1),1+3*(KJ-1)) = DGDU(2+3*(KI-1),1+3*(KJ-1)) - Z1*MOB1*FAR*C1*WE*
         (DNDX(KI)*DNDX(KJ) + DNDY(KI)*DNDY(KJ))
      DGDU(3+3*(KI-1),1+3*(KJ-1)) = DGDU(3+3*(KI-1),1+3*(KJ-1)) - Z2*MOB2*FAR*C2*WE*
         (DNDX(KI)*DNDX(KJ) + DNDY(KI)*DNDY(KJ))
       DGDU(2+3*(KI-1),2+3*(KJ-1)) = DGDU(2+3*(KI-1),2+3*(KJ-1)) - D1*WE*(DNDX(KI)*DNDX(KJ)+
          DNDY(KI)*DNDY(KJ)) - Z1*MOB1*FAR*WE*(N(KI)*(DNDX(KJ)*DPSIDX + DNDY(KJ)*DPSIDY))
      DGDU(3+3*(KI-1),3+3*(KJ-1)) = DGDU(3+3*(KI-1),3+3*(KJ-1)) - D2*WE*(DNDX(KI)*DNDX(KJ)+
          DNDY(KI)*DNDY(KJ)) - Z2*MOB2*FAR*DPSIDX*WE*(N(KI)*(DNDX(KJ)*DPSIDX +
         DNDY(KJ)*DPSIDY))
      END DO
      END DO
C     EVALUATE MBAR=M-dt*dGdU
      DO KI=1,NDOFEL
      DO KJ=1,NDOFEL
      AMATRX(KI,KJ)= AMATRX(KI,KJ) - DTIME * DGDU(KI,KJ)
      END DO
      END DO
C -----------------------------------------------------------------------------
C     EVALUATE RHS=Fbar(t+1)=dt(t+1)*G(t)-dt(t+1)*F(t)
C     EVALUATE dt*G and add to RHS vector - where G is the vector of internal loads
      DO KI=1,8
      RHS(1+3*(KI-1),NRHS) = RHS(1+3*(KI-1),NRHS) + DTIME*WE*(EPS0*EPSR*(DNDX(KI)*DPSIDX +
         DNDY(KI)*DPSIDY) + EL*Z1*N(KI)*C1 + EL*Z2*N(KI)*C2)
      RHS(2+3*(KI-1),NRHS) = RHS(2+3*(KI-1),NRHS) - DTIME*WE*(- D1*(DNDX(KI)*DC1DX +
         DNDY(KI)*DC1DY) - Z1*MOB1*FAR*C1*(DNDX(KI)*DPSIDX + DNDY(KI)*DPSIDY))
      RHS(3*KI,NRHS) = RHS(3*KI,NRHS) - DTIME*WE*(-D2*(DNDX(KI)*DC2DX + DNDY(KI)*DC2DY)
         Z2*MOB2*FAR*C2*(DNDX(KI)*DPSIDX + DNDY(KI)*DPSIDY))
      END DO
C -----------------------------------------------------------------------------
C     EVALUATE dt*F and add to RHS vector - where F is the BC vector
C     BOUNDARY NODES: U20 (RHS boundary), U40 (LHS boundary) - EVALUATE F VECTOR
C     CV  exp. = prescribed potential      + zero distributed mass flux bc
      IF (JDLTYP(1,1).EQ.40) THEN
        DO KJ=7,9
          RHS(3*(IFACE(KJ)-1)+1,NRHS) = RHS(3*(IFACE(KJ)-1)+1,NRHS) - DTIME*EPS0*EPSR*DPSIDX
          RHS(3*(IFACE(KJ)-1)+2,NRHS) = RHS(3*(IFACE(KJ)-1)+2,NRHS) +
             DTIME*(D1*DC1DX+Z1*MOB1*FAR*C1*DPSIDX)
          RHS(3*(IFACE(KJ)-1)+3,NRHS) = RHS(3*(IFACE(KJ)-1)+3,NRHS)  + DTIME*(D2*DC2DX +
             Z2*MOB2*FAR*C2*DPSIDX)
         END DO
      END IF
C     RHS FACE Fpsi(RHS nodes)=eps0*epsr*sigel*Phi*dpsi(RHS nodes)
      IF (JDLTYP(1,1).EQ.20) THEN
        DO KJ=3,5
```

```
          RHS(3*(IFACE(KJ)-1)+1,NRHS) = RHS(3*(IFACE(KJ)-1)+1,NRHS) + (DTIME*EPS0*EPSR*DPSIDX)
          RHS(3*(IFACE(KJ)-1)+2,NRHS) = RHS(3*(IFACE(KJ)-1)+2,NRHS) - DTIME*(D1*DC1DX +
         Z1*MOB1*FAR*C1*DPSIDX)
          RHS(3*(IFACE(KJ)-1)+3,NRHS) = RHS(3*(IFACE(KJ)-1)+3,NRHS) - DTIME*(D2*DC2DX +
         Z2*MOB2*FAR*C2*DPSIDX)
        END DO
      END IF
C     ===END LOOP THROUGH GAUSS PTS K===
  300 CONTINUE
C ---------------------------------------------------------------------------
C    =============APPLIED DISTRIBUTED FLUX================
C     EVALUATE additional terms in dt*F and add to RHS vector
C     GCD exp. = prescribed distributed electric flux + zero distributed mass flux bc
C     READ ONLY ARRAYS:
C        JDLTYP(K1,K2)   array of integers to define distributed load types
C        For general nonlinear steps ADLMAG(K1,1) is the total load magnitude of
C        the K1th distributed load at the end of the current increment for distributed loads of type Un.
C        ADLMAG(K1,1)    total load magnitude of the K1th distributed load at the end of current increment
C        DDLMAG(K1,1)    increments in the magnitudes of the distributed loads ^
C     READ ONLY SCALAR PARAMETERS:
C        NDLOAD      ID number of distributed loads and/or fluxes currently active
C        MDLOAD      total number of distributed loads and/or fluxes
C     APPLIED DISTRIBUTED FLUX U1,U2,U3,U4 - CORRESPONDS TO GCD BCS
C     JDLTYP(1,1)=[1,2,3,4]=[BOT,RHS,TOP,LHS] FACE
C     IFACE=[1,5,2,6,3,7,4,8,1]   ORDERING OF NODES IN AC DIRECTION FROM BOT LEFT CORNER
C     BOT GAUSS PTS (1,4,7), NODES (1,5,2)  (FLUX U1)
C     RHS GAUSS PTS (7,8,9), NODES (2,6,3)  (FLUX U2)
C     TOP GAUSS PTS (9,6,3), NODES (3,7,4)  (FLUX U3)
C     LHS GAUSS PTS (3,2,1), NODES (4,8,1)  (FLUX U4)
      IF (JDLTYP(1,1).EQ.4) THEN
        XI=-1.0
        DO KI=1,3
          ETA=GPY(NUMGPLFACE(KI))
          CALL DER(XI,ETA,GPX,GPY,GWEI,N,DNDX,DNDY,DNDXI,DNDETA,DXDXI,DXDETA,DYDXI,DYDETA,
                   AJACOB,COORDS,MCRD,NNODE)
          DS=SQRT(DXDE*DXDE + DYDE*DYDE)
          DO KJ=7,9
            RHS(3*(IFACE(KJ)-1)+1,NRHS) = RHS(3*(IFACE(KJ)-1)+1,NRHS)
                   + (DTIME*EPS0*EPSR*SIGEL)*GWE(KI)*DS*PHI(IFACE(KJ))*ADLMAG(1,1)
          END DO
        END DO
      END IF
      IF (JDLTYP(1,1).EQ.2) THEN
        XI=1.0
        DO KI=1,3
          E=GPY(NUMGPRFACE(KI))
          CALL DER(XI,ETA,GPX,GPY,GWEI,N,DNDX,DNDY,DNDXI,DNDETA,DXDXI,DXDETA,DYDXI,DYDETA,
                   AJACOB,COORDS,MCRD,NNODE)
          DS=SQRT(DXDE*DXDE + DYDE*DYDE)
          DO KJ=3,5
            RHS(3*(IFACE(KJ)-1)+1,NRHS) = RHS(3*(IFACE(KJ)-1)+1,NRHS)
                   + (DTIME*EPS0*EPSR*SIGEL)*GWE(KI)*DS*PHI(IFACE(KJ))*ADLMAG(1,1)
          END DO
        END DO
      END IF
      IF (JDLTYP(1,1).EQ.1) THEN
        ETA=-1.0
        DO KI=1,3
          C=GPX(NUMGPBFACE(KI))
          CALL DER(XI,ETA,GPX,GPY,GWEI,N,DNDX,DNDY,DNDXI,DNDETA,DXDXI,DXDETA,DYDXI,DYDETA,
                   AJACOB,COORDS,MCRD,NNODE)
          DS=SQRT(DXDC*DXDC + DYDC*DYDC)
```

```
          DO KJ=1,3
            RHS(3*(IFACE(KJ)-1)+1,NRHS) = RHS(3*(IFACE(KJ)-1)+1,NRHS)
                  + (DTIME*EPS0*EPSR*SIGEL)*GWE(KI)*DS*PHI(IFACE(KJ))*ADLMAG(1,1)
          END DO
        END DO
       END IF
       IF (JDLTYP(1,1).EQ.3) THEN
         ETA=1.0
         DO KI=1,3
          C=GPX(NUMGPTFACE(KI))
          CALL DER(XI,ETA,GPX,GPY,GWEI,N,DNDX,DNDY,DNDXI,DNDETA,DXDXI,DXDETA,DYDXI,DYDETA,
                    AJACOB,  COORDS,MCRD,NNODE)
          DS=SQRT(DXDC*DXDC + DYDC*DYDC)
          DO KJ=5,7
            RHS(3*(IFACE(KJ)-1)+1,NRHS) = RHS(3*(IFACE(KJ)-1)+1,NRHS)
                  + (DTIME*EPS0*EPSR*SIGEL)*GWE(KI)*DS*PHI(IFACE(KJ))*ADLMAG(1,1)
          END DO
         END DO
       END IF
      END IF
      RETURN
      END
C     ========== DETERMINE GAUSS POINT LOCATIONS (3PT G QUADRATURE) ==========
      SUBROUTINE GSPT(GPX,GPY)
      INCLUDE 'aba_param.inc'
      DIMENSION AR(3),GPX(9),GPY(9)
      PARAMETER(ZERO=0.D0,ONENEG=-1.D0,ONE=1.D0,THREE=3.D0,FIVE=5.D0)
C     GPX, GPY: X , Y COORDINATES OF GAUSS PT NUMGP
      R=SQRT(THREE/FIVE)
      AR(1)=ONENEG
      AR(2)=ZERO
      AR(3)=ONE
      DO 10 I=1,3
      DO 10 J=1,3
      NUMGP=(I-1)*3+J
      GPX(NUMGP)=AR(I)*R
      GPY(NUMGP)=AR(J)*R
 10   CONTINUE
      RETURN
      END
C     ========== DETERMINE GAUSS WEIGHTS (3PT G QUADRATURE, 2D) ==========
      SUBROUTINE GSWT(GWEI,GWE)
      INCLUDE 'aba_param.inc'
      DIMENSION GWEI(9),GWE(3)
      PARAMETER(FIVE=5.D0,EIGHT=8.D0,NINE=9.D0)
      GWE(1)=FIVE/NINE
      GWE(2)=EIGHT/NINE
      GWE(3)=FIVE/NINE
      DO 10 I=1,3
      DO 10 J=1,3
      NUMGP=(I-1)*3+J
      GWEI(NUMGP)=GWE(I)*GWE(J)
 10   CONTINUE
      RETURN
      END
C     ======== CALCULATE SHAPE FUNCTION AND SHAPE FUNCTION DERIVATIVE VALUES =======
      SUBROUTINE DER(XI,ETA,GPX,GPY,GWEI,N,DNDX,DNDY,DNDXI,DNDETA,
           DXDXI,DXDETA,DYDXI,DYDETA,DETJACOB,COORDS,MCRD,NNODE)
      INCLUDE 'aba_param.inc'
      DIMENSION N(8),DNDX(8),DNDY(8),DNDXI(8),DNDETA(8),COORDS(MCRD,NNODE)
      PARAMETER(ZERO=0.D0,FOURTH=0.25D0,HALF=0.5D0,ONE=1.D0,TWO=2.D0)
C     2D QUADRATIC INTERPOLATION FUNCTIONS N
```

```
      N(1) = FOURTH*(ONE-XI)*(ONE-ETA)*(-XI-ETA-ONE)
      N(2) = FOURTH*(ONE+XI)*(ONE-ETA)*(XI-ETA-ONE)
      N(3) = FOURTH*(ONE+XI)*(ONE+ETA)*(XI+ETA-ONE)
      N(4) = FOURTH*(ONE-XI)*(ONE+ETA)*(-XI+ETA-ONE)
      N(5) = HALF*(ONE-XI*XI)*(ONE-ETA)
      N(6) = HALF*(ONE+XI)*(ONE-ETA*ETA)
      N(7) = HALF*(ONE-XI*XI)*(ONE+ETA)
      N(8) = HALF*(ONE-XI)*(ONE-ETA*ETA)
C     DERIVATIVES OF N WRT TO XI
      DNDXI(1) = FOURTH*(ONE-ETA)*(TWO*XI+ETA)
      DNDXI(2) = FOURTH*(ONE-ETA)*(TWO*XI-ETA)
      DNDXI(3) = FOURTH*(ONE+ETA)*(TWO*XI+ETA)
      DNDXI(4) = FOURTH*(ONE+ETA)*(TWO*XI-ETA)
      DNDXI(5) = -XI*(ONE-ETA)
      DNDXI(6) = HALF*(ONE-ETA*ETA)
      DNDXI(7) = -XI*(ONE+ETA)
      DNDXI(8) = -HALF*(ONE-ETA*ETA)
C     DERIVATIVES WRT OF N TO ETA
      DNDETA(1) = FOURTH*(ONE-XI)*(TWO*ETA+XI)
      DNDETA(2) = FOURTH*(ONE+XI)*(TWO*ETA-XI)
      DNDETA(3) = FOURTH*(ONE+XI)*(TWO*ETA+XI)
      DNDETA(4) = FOURTH*(ONE-XI)*(TWO*ETA-XI)
      DNDETA(5) = -HALF*(ONE-XI*XI)
      DNDETA(6) = -ETA*(ONE+XI)
      DNDETA(7) = HALF*(ONE-XI*XI)
      DNDETA(8) = -ETA*(ONE-XI)
C     INTERPOLATION DERIVATIVES
      DXDXI=ZERO
      DXDETA=ZERO
      DYDXI=ZERO
      DYDETA=ZERO
      DO 3 I=1,8
        DXDXI=DXDXI+COORDS(1,I)*DNDXI(I)
        DXDETA=DXDETA+COORDS(1,I)*DNDETA(I)
        DYDXI=DYDXI+COORDS(2,I)*DNDXI(I)
        DYDETA=DYDETA+COORDS(2,I)*DNDETA(I)
    3 CONTINUE
C     DETERMINANT OF JACOBIAN
      DETJACOB=(DXDXI*DYDETA-DXDETA*DYDXI)
C     DERIVATIVES OF N WRT TO X AND Y
      DO 5 I=1,8
        DNDX(I)=(DNDXI(I)*DYDETA-DNDETA(I)*DYDXI)/DETJACOB
        DNDY(I)=(DNDETA(I)*DXDXI-DNDXI(I)*DXDETA)/DETJACOB
5     CONTINUE
      RETURN
      END
```

D.5 Ion transport analysis input file

```
*Heading
** Job name: 5EL_REG_2D_CHARGE Model name: 5EL_REG_2D_CHARGE
** TRANSIENT THERMAL-ELECTRICAL ANALYSIS USING 2D 8-NODED UEL ELEMENT
** Generated by: Abaqus/CAE 2017
*Preprint, echo=NO, model=NO, history=NO, contact=NO
**
** PARTS
**
*Part, name=PART
*NODE,NSET=N1
1,
2,30.0e-6
3,60.0e-6
4,90.0e-6
5,120.0e-6
6,150.0e-6
7,180.0e-6
8,210.0e-6
9,240.0e-6
10,270.0e-6
11, 300.0e-6
101,0,25.0e-6
103,60.0e-6,25.0e-6
105,120.0e-6,25.0e-6
107,180.0e-6,25.0e-6
109,240.0e-6,25.0e-6
111, 300.0e-6,25.0e-6
201,0,50.0e-6
202,30.0e-6,50.0e-6
203,60.0e-6,50.0e-6
204,90.0e-6,50.0e-6
205,120.0e-6,50.0e-6
206,150.0e-6,50.0e-6
207,180.0e-6,50.0e-6
208,210.0e-6,50.0e-6
209,240.0e-6,50.0e-6
210,270.0e-6,50.0e-6
211, 300.0e-6,50.0e-6
*NSET,NSET=L1
1,101,201
*NSET,NSET=R1
11,111,211
*****
*****  UEL ELEMENT DEFINITI0N
***** 8-noded 2D quadilateral element, active dofs potential 9 (EPOT) & two concentrations 11,12 (NT11,NT12)
*USER ELEMENT, TYPE=U1, NODES=8, PROPERTIES=7, COORDINATES=2, VARIABLES=48, UNSYMM
9, 11, 12
**
*ELEMENT, TYPE=U1, ELSET=UEL_ELSET
** LINE TO DEFINE CONNECTIVITIES BELOW
1,1,3,203,201,2,103,202,101
2,3,5,205,203,4,105,204,103
3,5,7,207,205,6,107,206,105
4,7,9,209,207,8,109,208,107
5,9,11,211,209,10,111,210,109
*Elset, elset=UEL_ELSET
 1, 2, 3, 4, 5
```

```
**
*UEL PROPERTY, ELSET=UEL_ELSET
** LINE TO DEFINE VALUES OF D1, D2, Z1, Z2, MOB1, MOB2, RHO
2.0e-3,2.0e-3,1,-1,8.02e-16,-8.02e-16,0.00152
**
** Section: Section-dummy
*Solid Section, elset=UEL_ELSET, material=dummy
*End Part
**
** ASSEMBLY
**
*Assembly, name=Assembly
**
*Instance, name=PART-1, part=PART
*End Instance
**  generate edge node sets
*Nset, nset=B_EDGE, instance=PART-1
 1, 2, 3, 4, 5, 6, 7, 8, 9, 10, 11
*Nset, nset=L_EDGE, instance=PART-1
 1, 101, 201
*Nset, nset=R_EDGE, instance=PART-1
 11, 111, 211
*Nset, nset=T_EDGE, instance=PART-1
 201, 202, 203, 240, 205, 206, 207, 208, 209, 210, 211
*End Assembly
*Amplitude, name=Amp-1, definition=SMOOTH STEP
          0.,             0.,          0.001,             1.
*End Assembly
**
** MATERIALS
**
*Material, name=dummy
*CONDUCTIVITY
204.,
*DENSITY
2707.,
*SPECIFIC HEAT
896.,
**
** PREDEFINED FIELDS
**
** Name: INITIAL-C1-C2   Type: Temperature
*INITIAL CONDITIONS, type=TEMPERATURE
PART-1.N1, 1.0e-6, 1.0e-6
**
**
** STEP: Step-1
**
*Step, name=Step-1, nlgeom=NO
*Coupled Thermal-electrical, end=PERIOD, deltmx=1.0e-12
0.2, 1., 1e-05, 0.5,
**
** BOUNDARY CONDITIONS
**
** Name: BC_EP_R Type: Electric potential
*Boundary
R_EDGE, 9, 9, -2e5
** Name: BC_EP_L Type: Electric potential
*Boundary
L_EDGE, 9, 9, 2e5
**
** LOADS
```

```
**
**
**
** OUTPUT REQUESTS
**
*Restart, write, frequency=0
**
** FIELD OUTPUT: F-Output-1
**
*Output, field
*Node Output
NT, RFL, RFLE, CFL, EPOT, RECUR
*Element Output, directions=YES
HFL, TEMP, ECD, EPG, EVOL, SDV, SDV1, SDV2
*Contact Output
ECD,
**
*NODE PRINT, FREQUENCY=1
NT
*NODE PRINT, FREQUENCY=1
EPOT
*EL PRINT, POSITION=INTEGRATION POINTS, FREQUENCY=1
TEMP
*EL PRINT, POSITION=INTEGRATION POINTS, FREQUENCY=1
SDV1
*EL PRINT, POSITION=INTEGRATION POINTS, FREQUENCY=1
SDV2
*EL PRINT, POSITION=INTEGRATION POINTS, FREQUENCY=1
SDV3
*EL PRINT, POSITION=INTEGRATION POINTS, FREQUENCY=1
EPG
**
** HISTORY OUTPUT: H-Output-1
**
*Output, history
*Contact Output
HFLA,
*End Step
```